Searching for neutrinoless double-beta decay with scintillating bolometers

Dounia Lila Helis

université
PARIS-SACLAY

Searching for neutrinoless double-beta decay with scintillating bolometers

Recherche de la double désintégration bêta sans neutrinos avec des bolomètres scintillants

Thèse de doctorat de l'Université Paris-Saclay

École doctorale n°576 : Particules, hadrons, énergie et noyau : instrumentation, imagerie, cosmos et simulation (PHENIICS)
Spécialité de doctorat : Physique des Particules
Unité de recherche : Université Paris-Saclay, CEA, Département de Physique des Particules, 91191, Gif-sur-Yvette, France
Référent : Faculté des sciences d'Orsay

Thèse présentée et soutenue à Paris-Saclay, le 21 septembre 2021, par

Dounia Lila Helis

Composition du jury

Jules GASCON Professeur, Université Claude Bernard Lyon 1	Président
Susana CEBRIAN-GUAJARDO Professeure, Université de Saragosse	Rapporteur et examinatrice
Davide FRANCO Directeur de recherche, Université de Paris	Rapporteur et examinateur

Direction de la thèse

Claudia NONES Chercheuse-HDR, CEA/IRFU, Université Paris Saclay	Directrice de thèse
Emiliano OLIVIERI Ingénieur de recherche, Université Paris Saclay	Examinateur et co-encadrant

Thèse de doctorat

NNT : 2021UPASP073

A feu ma grand-mère Madeleine Marcilly parce que faire un doctorat sur quelque chose de plus petit que des petit pois c'est possible.

Résumé en Français

Les neutrinos sont les particules les plus abondantes de l'univers. Cette particule fut introduite par Pauli pour expliquer le continuum en énergie observé dans les spectres de la désintégration bêta. Le seul moyen de justifier ceci était de considérer une désintégration à trois corps avec trois particules émises dans l'état final: le noyau fille, un anti-électron (électron) et un neutrino (antineutrino). Ensuite, cette particule fut prise en compte par Fermi dans sa théorie de la désintégration bêta. Cowen et Reines furent les premiers a détecté expérimentalement le neutrino (antineutrino) donnant la preuve de son existence. Pourtant, cette particule reste l'une des plus mystérieuses du modèle standard de la physique des particules (SM). Ce dernier est construit tel que les neutrinos n'ont pas de masse ce qui fait d'eux les uniques leptons de spin ½ à ne pas en avoir. Grâce aux expériences d'oscillation de neutrinos nous savons aujourd'hui que les différences des masses entre les neutrinos sont non-nulles, ce qui implique qu'au moins deux d'entre eux ont bien une masse, très petite par rapport aux autres particules du SM. Pour avoir accès aux trois masses des neutrinos, il nous faut une information supplémentaire. L'état des connaissances actuel ne nous permet pas non plus d'expliquer par quel mécanisme ils acquièrent cette masse. Un autre mystère entourant les neutrinos est celui de leur nature : sont-ils des particules de Dirac (un neutrino et un antineutrino sont deux particules distinctes) ou des particules de Majorana (un neutrino et un antineutrino sont deux particules identiques) ? Une manière possible de répondre à toutes ces questions serait la détection expérimentale de la double désintégration bêta dans neutrinos.

La double désintégration bêta sans neutrinos ($0\nu\beta\beta$) est une transition nucléaire hypothétique dont la demi-vie serait supérieure à 10^{26} ans. Ce type de désintégration est possible, en théorie, pour les noyaux ayant un nombre pair de protons et de neutrons. Elle consiste en la transformation d'un noyau en un noyau plus léger après émission simultanée de deux électrons mais pas de neutrino. Ce processus est interdit par le SM car il viole la conservation du nombre leptonique (symétrie interne du SM). L'observation expérimentale de la $0\nu\beta\beta$ impliquerait que les neutrinos sont des fermions de Majorana et ce qui en ferait les premières particules de ce type jamais découvertes. La mesure du taux de désintégration de la $0\nu\beta\beta$ nous donne aussi l'information manquante qui nous permettra de connaître la masse de chacun des neutrinos, car le taux d'événement $0\nu\beta\beta$ est inversement proportionnel au carré de la masse effective des neutrinos de Majorana. L'observation de cette désintégration ne serait pas seulement utile pour mieux comprendre les neutrinos mais aussi pour expliquer l'asymétrie matière-antimatière dans l'univers. En effet, ce processus engendre une création de matière sans antimatière.

D'un point de vue énergétique, la transition $0\nu\beta\beta$ est possible pour 35 noyaux, mais sa recherche expérimentale n'est possible que pour 11 noyaux. Ceci est due à la prise en compte des contraintes expérimentales telles que: la possibilité d'enrichir l'isotope candidat pour augmenter la masse, la valeur de l'énergie de la transition ainsi que l'abondance isotopique. La signature expérimentale d'une telle désintégration serait un excès d'événement à la valeur de l'énergie de la réaction $Q_{\beta\beta}$ qui correspond à la somme des énergies cinétiques des deux électrons émis. Idéalement, ce pic serait bien visible au-dessus d'un bruit de fond causé par diverses sources. Cependant, de par la nature rare de cette désintégration, le taux d'événement attendu est très faible et on s'attend à ce que les événements recherchés soient "cachés" dans ce bruit de fond. Il est donc important de mettre tout en œuvre pour éliminer et contrôler au maximum toute source de contamination potentielle. Parmi les 11 candidats possibles, choisir les isotopes dont la $Q_{\beta\beta}$ est supérieure à 2.6 MeV, valeur limite de l'énergie des gammas issus de la radioactivité naturelle, permet déjà d'éliminer cette contamination. Ensuite, construire les dispositifs expérimentaux pour la recherche de $0\nu\beta\beta$ dans des laboratoires souterrains permet de réduire considérablement le flux de muons atmosphériques qui contaminent le spectre en énergie dans la région d'intérêt (valeur de l'énergie à laquelle le pic de la $0\nu\beta\beta$ est attendu). Le choix de la technologie de détection de ce processus est un point clé pour le contrôle du bruit de fond. En effet, avoir une méthode de détection qui permettrait de discriminer l'origine des différents types de particules peut être utilisé pour rejeter des événements appartenant au bruit de fond. L'une des technologies les plus prometteuses dans le domaine de la recherche de la désintégration $0\nu\beta\beta$ est celle basée sur les bolomètres scintillants, détecteurs utilisées dans cette thèse.

Un bolomètre est un détecteur fonctionnant à basse température (10-20 mK dans le cas des détecteurs utilisés dans cette thèse) composé de trois éléments principaux : un absorbeur, un capteur thermique et un bain thermique qui maintient le système à basse température. Le capteur thermique mesure l'augmentation de la température T induite par l'énergie E déposée d'une particule incidente dans l'absorbeur. Cette élévation de température est décrite par l'équation simplifiée TEC, où C est une capacité thermique de l'absorbeur. L'une des expériences les plus développés recherchant la $0\nu\beta\beta$ avec ce type de détecteur est l'expérience CUORE (Cryogenic Underground Observatory for Rare Event) situées au laboratoire souterrain du Gran Sasso en Italie (LNGS). Cette expérience nous a démontré la possibilité de construire une expérience bolométrique cryogénique à l'échelle de la tonne en exploitant 998 cristaux naturel de TeO_2 contenant du ^{130}Te (dont l'abondance isotopique naturelle est de 30%), candidat à la $0\nu\beta\beta$. Néanmoins, le niveau de bruit de fond atteint n'était pas assez bas avec ces bolomètres pour contraindre suffisamment la $0\nu\beta\beta$ du ^{130}Te. Ce bruit de fond étant limité par les contaminations de surface provenant des particules alphas issues des matériaux entourant les détecteurs ou des détecteurs eux-mêmes. Il est devenu nécessaire de

discriminer les différents types de particules interagissant dans le cristal afin de rejeter efficacement les alphas de surface. Dans ce but, l'utilisation d'un détecteur à double lecture est requis, l'un des détecteurs permettant ceci est le bolomètre scintillant.

Un bolomètre scintillant est composé d'un bolomètre principal contenant un cristal scintillant avec la source $0\nu\beta\beta$ couplé à un bolomètre auxiliaire qui agit comme photodétecteur. Ce type de détecteur est basé sur un concept simple: deux boulomètres sont couplés entre eux. L'un de ces deux boulomètres, qu'on appellera bolomètre principal, est composé d'un cristal à scintillation qui contient l'isotope candidat à la $0\nu\beta\beta$. Afin de récolter la lumière de scintillation, le bolomètre principal est couplé à un bolomètre auxiliaire qui va agir comme photodétecteur. L'interaction d'une particule dans le bolomètre principal réchauffe le cristal et le capteur thermique enregistre cette élévation de température, ce cristal était scintillant, l'interaction émet de la lumière qui sera enregistrée par le bolomètre auxiliaire. Utilisant le fait que les particules alphas n'émettent pas la même quantité de lumière que les particules gammas et bêtas, il est donc possible de les discriminer grâce à la voie lumière. Cette technologie de détection permet d'avoir un détecteur avec une double lecture : chaleur (particule en interaction dans le cristal) et lumière (lumière scintillante émise par la particule en interaction) lues en coïncidence afin de discriminer l'origine de la particule et donc l'origine du bruit de fond. De plus, ces détecteurs offrent la possibilité d'utiliser l'approche "source=détecteur", car le cristal qui compose le bolomètre principal contient l'isotope étudié, ce qui améliore l'efficacité de la détection.

Les bolomètres scintillants furent proposés comme ligne de base pour la future expérience à l'échelle de la tonne CUPID (CUORE Upgrade with Particle IDentification). Cette expérience étant proposée comme suite de l'actuelle expérience CUORE. La construction de CUPID passe par plusieurs étapes de recherche et développements, et par la construction de démonstrateurs de taille moyenne. CUPID a eu deux démonstrateurs: CUPID-0 au LNGS et CUPID-Mo au Laboratoire Souterrain de Modane (LSM). CUPID-0 a confirmé la possibilité de construire des bolomètres scintillants pour la $0\nu\beta\beta$ du ^{82}Se, le ^{82}Se étant intégré dans des cristaux de ZnSe. Cette expérience était composée de 26 cristaux de ZnSe arrangés en tour. Les résultats obtenus ont montré que les bolomètres scintillants permettent d'atteindre des niveaux de bruit de fond très bas, nécessaire pour la recherche d'événement rare tels que la $0\nu\beta\beta$. Cependant, les performances des détecteurs n'étaient pas assez élevées pour les critères de CUPID: la radioactivité des cristaux était trop élevée et la résolution en énergie pas assez satisfaisante. En parallèle, le projet LUMINEU (Luminescent Underground Molybdenum Investigation for NEUtrino mass and nature), visant à développer des bolomètres scintillants basés sur des cristaux enrichis en ^{100}Mo montra le potentiel de ces détecteurs pour la recherche de la $0\nu\beta\beta$. Le démonstrateur CUPID-Mo, basé sur la technologie de LUMINEU, fut installé au LSM. Le succès de cette expérience confirma le potentiel de ces détecteur, elle a permis d'atteindre une nouvelle limite de la demi-vie

de $0\nu\beta\beta$ du ^{100}Mo de $T_{1/2} > 1.8 \times 10^{24}$ ans à 90% C.I. (Confidence Interval), la meilleure jamais obtenue au niveau mondial sur cet isotope. La technologie utilisé par CUPID-Mo sera utilisée par CUPID.

Le travail de recherche présenté dans cette thèse recouvre un large horizon dans le domaine de la recherche expérimentale de $0\nu\beta\beta$: de la construction des détecteurs aux contraintes que l'on peut mettre sur la $0\nu\beta\beta$ en passant par l'analyse de données. Dans le cadre de l'expérience cryogénique de nouvelle génération à l'échelle de la tonne CUPID, des bolomètres scintillants composés de cristaux de molybdate de lithium ($Li_2^{100}MoO_4$) et tungstate de cadmium ($^{116}CdWO_4$) sont étudiés. Le molybdène-100 (^{100}Mo) et le cadmium-116 (^{116}Cd) étant les candidats à la $0\nu\beta\beta$ dont la $Q_{\beta\beta}$ est de 3043 keV et 2813 keV respectivement.

Comme mentionné plus haut, l'expérience CUPID-Mo située au LSM est un démonstrateur de CUPID. Elle est composée de 20 bolomètres scintillants contenant des cristaux de $Li_2^{100}MoO_4$ enrichis en ^{100}Mo afin de maximiser la quantité d'isotope candidate à la $0\nu\beta\beta$. Les 20 détecteurs sont répartis en 5 tours avec 4 bolomètres scintillants par tour. La prise de données a été faite entre mars 2019 et juillet 2020. Dans ce manuscrit, l'analyse des données qui a mené à la meilleure limite sur la durée de vie de la $0\nu\beta\beta$ jamais obtenue avec des cristaux de ^{100}Mo est présentée. Le succès de l'expérience a prouvé l'efficacité de la technologie des bolomètres scintillants contenant des cristaux de $Li_2^{100}MoO_4$ et a ouvert la voie à une expérience à bien plus grande échelle.

Dans le cadre de la R&D pour CUPID, des essais à basse température de deux cristaux de 0,6 kg de $^{116}CdWO_4$ enrichis en ^{116}Cd à 82% comme bolomètres scintillants ont été effectué. Ces détecteurs étaient exploités sous terre, dont un au LSM et le second au Laboratorio Subterraneo de Canfranc (LSC) en Espagne. Les résultats que nous avons obtenus ont montré que la technologie bolométrique basée sur le $^{116}CdWO_4$ offre une haute résolution énergétique (11-16 keV FWHM à 2615 keV) et une discrimination efficace du fond à 99.99%. Nous avons également montré qu'ils offrent une résolution en énergie d'un ordre de grandeur meilleure que lorsqu'ils sont utilisés comme des scintillateurs à température ambiante. Ces résultats obtenus confirment que la technologie de détection basée sur des bolomètres scintillants, offre la possibilité de se placer sur le devant de la scène dans le domaine de la recherche de la $0\nu\beta\beta$.

Ce manuscrit de thèse est structuré en six chapitres. Les deux premiers introduisent les objectifs physiques et les techniques appliquées, en présentant respectivement la pertinence de la double désintégration bêta sans neutrino et les bases de l'utilisation des bolomètres scintillants ; les quatre autres chapitres montrent la méthodologie et les résultats obtenus pour les différentes études entreprises.

Une brève introduction sur la physique des neutrinos et les recherches de désintégration double bêta sans neutrinos, couvrant à la fois les aspects théoriques

et les résultats expérimentaux, est présentée au chapitre 1. Dans le chapitre 2, le principe de fonctionnement et les avantages des bolomètres et, en particulier, des bolomètres scintillants, sont discutés ainsi que les trois différents dispositifs expérimentaux souterrains utilisés dans les travaux de thèse présentés dans ce manuscrit situés sont décrits.

Le chapitre 3 résume les travaux réalisés à l'aide de 20 bolomètres scintillants $Li_2^{100}MoO_4$ exploités dans le laboratoire souterrain de Modane au sein de CUPID-Mo, permettant d'obtenir la première limite supérieure mondiale de la demi-vie de la double désintégration bêta sans neutrino de ^{100}Mo. L'analyse de données présentée dans cette thèse correspond à 2.16 kg.yr d'exposition. Une description complète de l'expérience est présentée, avec un accent particulier sur la préparation des bolomètres et l'analyse des données pour l'optimisation du seuil d'énergie de déclenchement des détecteurs réalisée, pertinente pour l'analyse des coïncidences et la modélisation du bruit fond.

En effet, l'abaissement du seuil de détection a permis d'effectuer les premières recherches de matière noire avec les détecteurs CUPID-Mo, qui sont présentées dans le chapitre 4 après une brève introduction théorique sur la détection de la matière noire. L'interaction dépendante du spin (SD) sur ^{7}Li (J=3/2, Sp=1/2) peut être explorée. Deux ensembles de données (0.35 kg.yr) ont été analysés pour abaisser le seuil d'énergie en calculant de nouveaux paramètres d'impulsion pour construire des coupures de qualité afin de rejeter les événements non physiques. En considérant un seuil d'analyse de 20 keV et un niveau de bruit de fond d'environ 10-20 c/(keV kg d) au-dessus de cette énergie, des limites d'exclusion sur la section efficace pour le couplage SD en supposant séparément des interactions neutroniques et protoniques ont été dérivées; ces dernières sont prometteuses pour des masses de matière noire supérieures à 10 GeV et le potentiel a ensuite été évalué dans différentes conditions d'optimisation des détecteurs.

Les travaux développés à l'aide de bolomètres scintillants en $CdWO_4$ et les résultats obtenus pour la double désintégration bêta du ^{116}Cd sont présentés au chapitre 5. Deux cristaux différents, précédemment utilisés dans l'expérience Aurora, ont été exploités sur des montages différents dans les laboratoires souterrains de Modane et de Canfranc. La préparation des détecteurs et le traitement des données sont décrits en détail et les résultats obtenus pour les performances et la demi-vie de la désintégration double bêta du ^{116}Cd sont présentés; une limite (pour le mode sans neutrinos) et une valeur (pour le canal à deux neutrinos) similaires à celles établies par Aurora ont été dérivées avec une exposition plus faible. En outre, un cristal non enrichi a également été exploité à Canfranc et une optimisation du seuil de déclenchement du détecteur a été appliquée afin d'étudier une mesure possible du paramètre g_A en analysant la distorsion du spectre bêta de la désintégration bêta hautement interdite du ^{113}Cd. Bien qu'il n'ait pas été possible de dériver un résultat à partir des données disponibles, le potentiel de la technique a été exploré.

Enfin, les différents essais de R&D réalisés dans les laboratoires souterrains de Gran Sasso et de Canfranc avec les cristaux cubiques de $LiMoO_4$ enrichi prévus pour être utilisés dans CUPID, exploités dans différentes conditions, sont présentés au chapitre 6. La résolution énergétique et les rendements lumineux obtenus sont discutés. Les plans futurs et les perspectives de l'expérience de CUPID sont également commentés.

Acknowledgements

During my thesis, I have worked with wonderful people from all around the world. This Ph.D. work could not be done without them.

First, I would like to thank my thesis jury: Jules Gascon, Susana Cebrian, Davide Franco, and Emiliano Olivieri for accepting to evaluate my thesis.

I would like to express my immense gratitude to my supervisor Claudia Nones for giving me the opportunity to do a Ph.D. I could not dream of a better Ph.D. subject. I thank her for her support and her guidance through this Ph.D. journey.

I would like to thank Emiliano Olivieri for all the support, the endless hours dedicated to the detector construction and data analysis that we did together. I learned a lot from him.

I would like to thank my colleagues at IJCLab where I spent a lot of time. In particular, Anastasiia Zolotarova, my cleanroom mentor, for infinite hours in cleanrooms above and underground, Denys Poda for answering all my questions and making me guess the answers, Andrea Guiliani, Stefanos Marnieros, Pia Loiaza, and Pierre de Marcillac. A special mention to Hawraa Khalife, my co-bureau at IJCLab, my friend for helping me through my Ph.D. work. Another special mention to Riham Mariam my friend, for lending me her desk in the last days of my Ph.D., for long phone discussions during lockdowns, for coffee breaks, for advice, for everything.

During the multiple lockdowns, I have worked with many people remotely within the CUPID-Mo analysis team. I am grateful to all these people, especially Laura Marini. I would like to thank her for the long hours that she dedicated to the analysis that we did together. I would like to thank also Benjamin Schmidt and Bradley Welliver.

Thanks to my family, my everything, mama and papa, for always encouraging me to pursue my dreams. Thanks to my little brother, Farés, for always reminding me to take it easy.

Thanks to my grandparents: Zoulikha and Aissa, to whom I have always been a doctor. Thanks to grand-père Mohamed.

Many thanks to all my ants: Nabila, Wahiba, Sabira, Dr. Amel, Dr. Myriam, Louisa, Nadia, and especially Dr. Leila (I could not do this without her). Thanks to my uncles Fethi and Mohamed.

Thanks to all my adult cousins, all around the world, especially Sissi, Zizou, Ilyes, and Yacine.

Thanks to my friends: Amira, Laura, Louis, Elisabeth, Florian, Tim, Guilia and Martin. I hope we can continue having dinners all around the world this time.

Finally, a special thanks to Beatrice Mauri, my co-bureau, my favorite Italian, my friend. I am happy that I did a part of my Ph.D. journey with you. I'll miss you in my office...

Last but not least, I would like to thank Thomas Montandon for the endless support and for making me believe in me ...

Contents

Chapter 1

Neutrinos and neutrinoless double-beta decay

This chapter is dedicated to a brief overview of neutrino physics and the open questions related to this field. The actual knowledge about neutrinos is summarised in Sec. 1.1 and 1.2. The absolute mass scale of neutrinos and the problematic related to its measurement are discussed in Sec. 1.3. The experimental aspects of the neutrinoless double-beta decay, one of the most promising mechanisms to probe the neutrino mass and nature, is presented in Sec. 1.4. Finally, an overview of several neutrinoless double-beta decay experiments is given in Sec. 1.5.

1.1 Neutrino in the standard model

The Standard Model (SM) of particle physics is a theoretical framework that describes the twelve elementary particles and three of their fundamental interactions -electromagnetic, weak, and strong- carried with the three gauge bosons (see Fig 1.1 for a schematic view). Since the electromagnetic and weak interactions are unified, they are referred to as the electroweak interaction. Hence, the SM contains two distinct interactions: the strong interaction described by the quantum chromodynamics and the electroweak interaction described by the quantum electrodynamics [1]. The SM is a gauge theory and is invariant under the gauge group $SU(3)_C \otimes SU(2)_L \otimes U(1)_Y$. Each group is associated with an interaction: $SU(3)_C$ to the strong interaction, where the C stands for color, and the group $SU(2)_L \otimes U(1)_Y$ to the electroweak interactions, where L stands for left-handedness and Y for the hypercharge. To take into account the parity violation in the weak interaction, the left-handed particles belong to a doublet of $SU(2)_L$ and the right-handed particles to a singlet. In this context, the neutrino is described as a massless neutral Dirac left-handed particle. The only neutrino states, which couple to other fermions via weak interactions, are the left-handed neutrino and the right-handed anti-neutrino. Hence, neutrinos are singlet of the subgroup $SU(2)_L \otimes U(1)_Y$ and are part of the lepton doublet $L_{Ll} = \begin{pmatrix} \nu_l \\ l \end{pmatrix}_L$ where l is the lepton flavor and L is the left-handedness.

In the SM, the masses of fermions are generated via the Yukawa coupling by the Higgs mechanism; the doublet of the Higgs field couples to a fermion with left-handed and right-handed components, as shown in Eq. 1.1.

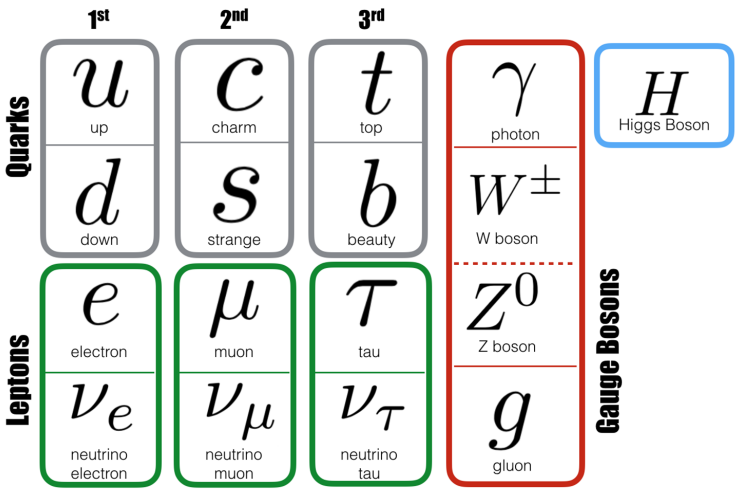

FIGURE 1.1: Schematic view of the particles of the SM classified with three generation family from the lightest to the heaviest fermion and the gauge bosons.

$$-\mathcal{L}_{Yukawa,leptons} = Y^{l}_{ij}\bar{L}_{Li}\phi E_{Rj} + hc.. \tag{1.1}$$

Since the SM does not take into account the right-handed neutrinos, such interaction cannot occur, and hence neutrinos are massless. Consequently, it is essential to understand how the neutrino mass is generated and thus go beyond the SM. There are several ways to construct a neutrino mass term in minimal extensions of the SM, but they need to contain the neutrino nature, which is still unknown [1].

1.2 Neutrino physics

1.2.1 History of neutrinos

The discovery of neutrinos is due to a kinematic problem. W. Pauli first introduced it to explain the energy continuum in the emitted electron spectra of β decays [2] (see Eq. 1.2 and 1.3 for the single β decay reactions). The energy spectra of α and γ decays, two-body decays, have a monochromatic peak (enlarged for several reasons) at the energy of the decay. β decay spectrum has a particularity: it is a continuum with a maximum at 1/3 of the transition energy (Q_β) of the decay. The only way to explain that was to use the kinematics of the decay, which requires a third particle, the neutrino. Indeed, the kinematics of a three-body decay explain perfectly the β decay spectrum. In 1930, Pauli introduced the neutrino, thinking that he did a terrible thing by adding an undetectable particle to solve the β spectrum kinematics problem, as he wrote in his famous letter to the scientific community reported in [2].

$$N(A,Z) \rightarrow N(A,Z+1) + e^{-} + \bar{\nu}_e \tag{1.2}$$

$$N(A,Z) \rightarrow N(A,Z-1) + e^{+} + \nu_e \tag{1.3}$$

After that, Fermi published his paper on the theory of β decays [3] where he included the neutrino predicted by Pauli. This missing particle in the β process had to be neutral and with a $1/2$ spin to conserve the angular momentum and the charge of the process.
In 1945, Pontecorvo proposed a reaction that allows to detect neutrinos [4], in the inverse electron capture of ^{37}Cl following the reaction in Eq.1.4:

$$\nu_e + ^{37}Cl \rightarrow e^{-} + ^{37}Ar \tag{1.4}$$

This reaction was very promising to detect neutrinos because the final state is easily identified from a chemical point of view since the ^{37}Ar is a noble gas and its extraction is straightforward.
Cowan and Reines saw the first evidence for neutrino in 1956 [5]. In their paper, they describe how they detected this undetectable particle, according to Pauli, in the inverse neutron β decay, following the reaction:

$$\bar{\nu}_e + p \rightarrow n + e^{+} \tag{1.5}$$

The anti-neutrinos were coming from a large nuclear reactor in Handford towards a cadmium-loaded scintillator solution [6].
In the following years and according to the experimental observations, many physicists tried to build a theory to describe neutrinos. In this theory, the neutrino is a massless two-component particle: the neutrino is defined as a left-handed particle and the anti-neutrino as a right-handed particle. It is considered as a Dirac particle and the lepton number was introduced to distinguish between the neutrino and the anti-neutrino as described in the SM.

Inspired by Pontecorvo's reaction, R. Davis build an experiment to detect neutrinos from the sun [7]. The experiment used 520 tons of chlorine in a tank and was located underground in Homestake mine in the USA [7]. The experiment results show a deficit of neutrinos coming from the sun with respect to the predicted flux by the Standard Solar Model (SSM). Other experiments observed the so-called solar neutrino problem: GALLEX [8], GNO [9] and SAGE [10] used a radio-chemical technique to detect solar neutrinos with the following reaction:

$$\nu_e + ^{71}Ga \rightarrow e^{-} + ^{71}Ge \tag{1.6}$$

The measured solar neutrino flux by these experiments was about two times lower than the expected one from SSM.
Pontecorvo proposed in [11] neutrino oscillations to solve the solar neutrino deficit problem. He proposed that a neutrino can change flavor while traveling from the sun to earth. The experimental observation of neutrino oscillations was first provided in 1998 by the Super-Kamiokande experiment [12]. The Super-Kamiokande exploited a water-Cherenkov detector that observed the disappearance of ν_μ from

atmospheric neutrinos. Other experiments followed this detection: the SNO experiment detected neutrino oscillations in neutrinos from the sun [13].

The experimental evidence of neutrino oscillations opens doors to new physics and provides essential information about the neutrino mass. However, the absolute mass measurement of neutrinos is not accessible through this process, and this will be explained in the next section.

1.2.2 Mass mixing and neutrino oscillations

As mentioned in the previous section, neutrino oscillations were first introduced by Pontecorvo, taking inspiration from the kaon oscillations [14]. His first hint came in 1957 when he advanced the idea of considering composite neutral particle muonium (μ^+-e^-) that could make a transition into an antimuonium (μ^--e^+). This idea was abandoned when we knew that ν_e and ν_μ were different particles [14]. After the measurement of the deficit of solar neutrinos, Pontecorvo gave a possible explanation of this phenomenon with the neutrino oscillations [11].

A neutrino of a specific flavor is defined by $W^\pm$ boson decays: $W^- \rightarrow e^-\bar{\nu}_e$, $W^- \rightarrow \mu^-\bar{\nu}_\mu$ and $W^- \rightarrow \tau^-\bar{\tau}_e$. As we know, neutrinos can change flavor and thus they need to have masses. This implies that neutrinos have a spectrum of mass eigenstate: a flavored neutrino is defined as superposition of three mass eigenstates in the mixing relation in Eq. 1.7 where $|\nu_i\rangle$ is the mass eigenstates.

$$|\nu_l\rangle = \sum_i^3 U_{il} |\nu_i\rangle \quad l = e, \mu, \tau \tag{1.7}$$

U is the Pontecorvo, Maki, Nakagawa, Sakata leptonic mixing matrix [15], so-called U_{PMNS} matrix. It is a 3×3 unitary matrix defined as

$$\begin{pmatrix} c_{12}c_{13} & s_{12}c_{13} & s_{13}e^{-i\delta} \\ -s_{12}c_{23} - c_{12}s_{23}s_{13}e^{i\delta} & c_{12}c_{23} - s_{12}s_{23}s_{13}e^{i\delta} & s_{23}c_{23} \\ s_{12}s_{23} - c_{12}c_{23}s_{13}e^{i\delta} & -c_{12}s_{23} - s_{12}c_{23}s_{13}e^{i\delta} & c_{23}c_{13} \end{pmatrix} \times \mathrm{diag}(e^{i\lambda_1}, e^{i\lambda_2}, 1) \tag{1.8}$$

where c_{ji}=cosθ_{ji} and s_{ji}=sinθ_{ji} with three mixing angles θ_{ij}. δ is the Dirac CP violation phase and λ_1 and λ_2 are the Majorana phases. One can summarize neutrino oscillations with three mass eigenstates and six parameters if the neutrino is a Majorana particle and with four parameters if the neutrino is a Dirac particle.

When a neutrino of a given flavor interacts with matter, it will always give a charged lepton with the same flavor: this is how a detector sees a neutrino of a given flavor. When a neutrino with flavor i propagates through a distance L, it can oscillate to another flavor f with a certain probability given in Eq. 1.9 where $\Delta m^2_{\alpha\beta} = m^2_\alpha - m^2_\beta$ is the squared mass difference between the mass eigenstates of the flavored neutrino, $U_{\alpha i}$ are the elements of the PMNS matrix, L is the traveled

distance between the neutrino source and the detector and $|\mathbf{p}|$ the neutrino momenta.

$$P(\nu_i \rightarrow \nu_f) = \sum_{\alpha,\beta} U^*_{i\alpha} U_{f\beta} U_{i\alpha} U^*_{f\beta} e^{-i\Delta m^2_{\alpha\beta} L/2|\mathbf{p}|} \tag{1.9}$$

In neutrino oscillation experiments, a disappearance or an appearance of a neutrino of a given flavor can be observed. The neutrino source can be the solar neutrinos, the atmospheric neutrinos, or an artificial source such as a nuclear reactor or an accelerator. Several experiments are studying neutrino oscillations; depending on the nature of the experiment, atmospheric, solar, accelerator or reactor, they can have access to a certain set of parameters of the PMNS matrix.

- The solar and atmospheric neutrino oscillation experiments measure the value of the sum of neutrino masses difference squared $(\Delta m^2)_{atm}$ and $(\Delta m^2)_{sol}$, and the two mixing angles θ_{12} and θ_{23}. Here one can cite here the Super-Kamiokande experiment [16] for atmospheric neutrinos and the SNO experiment [17] for the solar neutrinos.

- The mixing angle θ_{13} and the phase δ are measured by reactor experiments like Double Chooz [18] and accelerator neutrino oscillation experiments such as T2K [19] and NOvA [20]. These two latter experiments are both long baselines neutrino oscillation experiments. The T2K collaboration uses a scintillator as a near detector to measure the flux of muon neutrinos before the possible neutrino oscillations, just after producing the neutrino beam. The far detector is 295 km away from the near one; it is the Super-Kamiokande Cherenkov light detector. The NOvA experiment is using the same type of detector as far and near detectors. The distance between the near and the far detector in NoVA is about 800 km.

The most recent results on the measurement of the PMNS matrix parameters using the global analysis of neutrino oscillations [21] are summarised in Table 1.1.

	Best fit (3σ)	
Parameter	Normal hierarchy	Inverted hierarchy
Δm^2_{21} [$\times 10^{-5}$ eV^2]	7.56(7.05-8.14)	
$\lvert\Delta m^2_{31}\rvert$ [$\times 10^{-3}$ eV^2]	2.55(2.43-2.67)	2.47(2.34-2.59)
$\sin^2\theta_{12}$ [$\times 10^{-1}$]	3.21(2.73-3.79)	
$\sin^2\theta_{23}$[$\times 10^{-1}$]	4.30(3.84-6.35)	5.98(3.89-4.488 & 5.22-6.41)
$\sin^2\theta_{13}$ [$\times 10^{-2}$]	2.155(1.89-2.39)	2.155(1.9-2.38)
δ/π	1.40(0.00-2.00)	1.56(0.00-0.17 & 0.83-2.00)

TABLE 1.1: Best fit and 3σ range for PMNS matrix parameters obtained from neutrino oscillations global analysis [21].

From these experimental results, we know that depending on the sign of the square mass difference $|\Delta m^2_{31}|$ and considering the fact that there are two neutrinos

close in mass (m_1 and m_2) and the third one far away (m_3) we have two cases of the neutrino mass hierarchy, these cases are discussed in the next section.

1.3 Absolute mass scale of neutrino

Thanks to the observation of neutrino oscillations (described briefly in section 1.2.2), we know that neutrinos can mix and oscillate by a change of flavor. However, the mystery about the origin of their masses and their absolute mass scale remains complete.

1.3.1 Neutrino mass measurements

The measurement of the neutrino mass is one of the actual experimental and theoretical challenges. It is essential to have access to this crucial information to understand the mass generation process and many astrophysical processes since neutrinos are among the most abundant particles in the universe (about 330 ν/cm^3 today).

Neutrinos interact only via weak processes, which makes impossible the use of direct mass measurement through kinematics, the standard way to measure a particle mass. There are other ways to possibly measure neutrino masses:

- direct probes using the kinematics of weak decays (single β decays and electron capture);
- indirect probes through cosmological observations;
- neutrinoless double-beta decays.

Single β decay: it is one of the most promising approaches to probe neutrino mass. With a precise measurement of the electron energy spectrum, the investigation of the neutrino mass is possible in a model-independent way. Indeed, a spectral distortion occurs at the endpoint of the spectrum due to neutrino mass (see Fig. 1.2). The measurement of this distortion requires a low-energy endpoint and a good energy resolution. The β energy spectrum is obtained by the detection of the charged products in the single β decay. The spectral distortion of the decay gives access to the effective mass squared of the neutrino, given by Eq. 1.10.

$$m_\nu^2 = \sum_i |U_{ei}|^2 m_i^2 \tag{1.10}$$

One of the most promising experiments for direct neutrino mass measurement is the KArlsruhe TRItium Neutrino (KATRIN) experiment that studies the tritium β decay:

$$^3H \rightarrow ^3He + e^- + \bar{\nu}_e \tag{1.11}$$

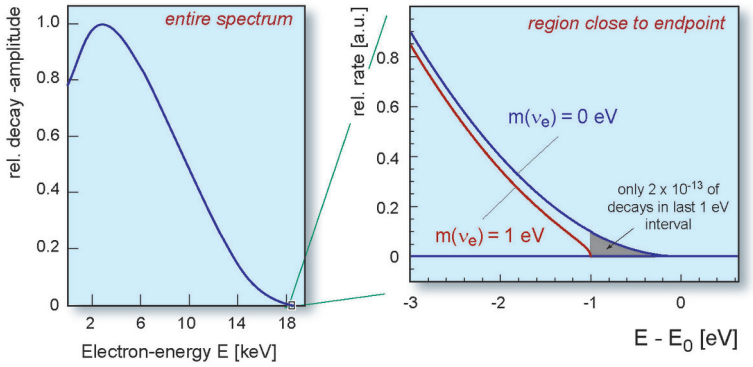

FIGURE 1.2: Tritium Beta decay spectrum (*left*) and the endpoint region (*right*) [26].

This decay is very interesting to probe the neutrino mass because it has low energy of transition (18.57 keV) and a relatively short half-life (12.32 yr). In [22], the collaboration reported the first results from four weeks of science data taking. An improved upper limit on the neutrino mass was set: 1.1 eV at 90% C.L. (confidence level). After 1000 days of data taking, the KATRIN experiment will be sensitive to neutrino effective mass of 0.2 eV at 90% C.L. [22].

Another process that is under study for a direct neutrino mass measurement is the electron capture of ^{163}Ho. The ECHo [23] and the HOLMES [24] experiments are using this process to probe the neutrino mass using bolometers where the ^{163}Ho is one of the components of the absorber. When an event occurs inside of the bolometers, the rise of temperature is measured by thermal sensors: transition-edge sensors (TES) for Holmes [24], or magnetic metallic calorimeters (MMC) for ECHo [23]. More details on the working principle of a bolometer will be given in Chapter 2.
The HOLMES experiment aims to directly measure the neutrino mass with a sensitivity below 0.2 eV [25].

Cosmology measurements: some of the neutrino properties can be studied by cosmology. This latter is sensitive to neutrino density, the number of neutrino species and the sum of their masses [15]. The latter is one of the most crucial parameters about neutrino masses. Neutrinos were produced in the early universe and contribute to the density of matter back then. Thanks to the Cosmic Microwave Background (CMB), the sum of neutrino masses is evaluated according to different cosmological models by looking at the temperature anisotropies to predict the low-redshift inhomogeneity spectrum as a function of neutrino mass.
The most recent limit on the sum of neutrino masses, given by the last results of the

Planck experiment assuming a spatially flat universe [27], is:

$$\sum_{i=3}^{3} m_i < 0.26 \text{ eV} \tag{1.12}$$

If the fluctuations of the density of the universe's visible baryonic matter which are known as the Baryonic Acoustic Oscillations are taken into account with Planck results, the sum of neutrino masses becomes [15]:

$$\sum_{i=1}^{3} m_i < 0.13 \text{ eV} \tag{1.13}$$

Another important indication about the neutrino mass will be given by future cosmological measurement: the mass hierarchy [28]. Indeed, the next-generation cosmological observations should lead to a limit that could distinguish between the normal and the inverted hierarchy. In [29], the impact of the cosmological measurements on the possible values of the light Majorana mass is investigated. The light Majorana mass is a parameter that neutrinoless double-beta decay experiments seek to measure. The authors in [29] quantified the discovery probabilities of neutrinoless double-beta decay (measurement of the light Majorana mass) based on cosmological data for the normal neutrino mass ordering.

In the light of what was described above, neutrino mass measurement is one of the experimental challenges of the century. Its measurement will provide crucial information to build a theoretical mass model. Another essential factor to be taken into account to build the neutrino mass theory is the nature of neutrino: Dirac or Majorana? One of the most promising processes that can solve the neutrino mass and nature mystery, if observed, is the neutrinoless double-beta decay described in Sec. 1.4.

1.3.2 The mass hierarchy

The measurement of the solar and atmospheric neutrino oscillations provides two important parameters about neutrino masses: $(\Delta m^2)_{atm}$ and $(\Delta m^2)_{sol}$. As mentioned above, there are two types of neutrino mass hierarchy derived from the experimental observations: the normal hierarchy and the inverted hierarchy. These two scenarios are obtained when we look at the sign of $(\Delta m^2)_{atm}$:

Normal hierarchy If $(\Delta m^2)_{atm} > 0$ then the lightest neutrino is m_1 so $m_1 < m_2 \ll m_3$, a schematic view of this hierarchy is given in Fig 1.3.

Inverted hierarchy If $(\Delta m^2)_{atm} < 0$ then the lightest neutrino is m_3 so the ordering becomes $m_3 \ll m_2 < m_1$ (refer to the right part of Fig 1.3).

In addition, if the square mass differences are negligible with respect to the neutrino masses this means that $m_1 \simeq m_2 \simeq m_3$, we have the degenerated hierarchy.

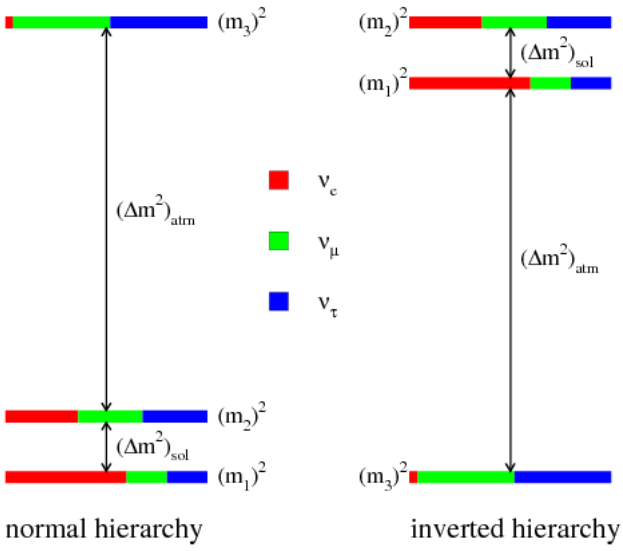

FIGURE 1.3: Neutrino mass hierarchy scheme. *Left*: normal hierarchy. *Right*: inverted hierarchy.

Hints for normal mass ordering have been reported by several neutrinos oscillation experiments [30] and the global fits of data show a preference for the normal ordering [31, 32].

1.3.3 Dirac or Majorana neutrinos

The SM formalism works perfectly with massless neutrinos (see section. 1.1), but it does not fit the experimental reality: the neutrino oscillates and hence has mass. A mass term for neutrinos in the SM is needed, but this is not easy since it has to contain the nature of neutrino, Dirac or Majorana. In the following, we will discuss three different scenarios for neutrino mass nature.

Dirac case

Let's consider that neutrinos have masses in the SM and the right-handed neutrino field can interact (in addition to the left-handed one already included in the SM), ψ_L and ψ_R. As for the other particles, the neutrino mass term is generated with the Yukawa couplings and the Higgs mechanism (described in 1.1), we obtain the following Lagrangian:

$$\mathcal{L} = m_D(\bar{\psi_L}\psi_R + \bar{\psi_R}\psi_L) \tag{1.14}$$

After the spontaneous breaking of the electroweak symmetry via the Higgs mechanism, we obtain a Dirac mass term for neutrino:

$$m_D = \frac{Y_{ll'}}{(\sqrt{2}G_F)^{1/2}} \tag{1.15}$$

where G_F is the Fermi constant and $Y_{ll'}$ are the Yukawa coupling constants. The problem with this mass term is that it does not explain why neutrino masses are so small with respect to the other particles of the SM.

Majorana case

If we consider that neutrinos are massive Majorana particles where two neutrinos field are taken into account, the right-handed one $\bar{\psi^C}\psi$ and the left-handed one $\bar{\psi}\psi^C$. The mass term is written as:

$$\mathcal{L} = \frac{1}{2}(m_M \bar{\psi}\psi^C + m_M^* \bar{\psi^C}\psi) \tag{1.16}$$

where m_M is the Majorana mass. This mass term violates the lepton number by a unit of two. This would imply that the neutrino and the anti-neutrino are identical.

Dirac and Majorana mass term or the see-saw mechanism

If we consider a more general case in which the neutrino Lagrangian contains both Dirac and Majorana mass terms: the Dirac mass term would be the link to the SM (without extension) through the mass generation via the Higgs mechanism and the Majorana mass terms would allow the coupling with left and right-handed neutrinos.
This case gives a natural explanation to the mass scale of the neutrino with respect to the other particles of the SM. This is the so-called see-saw mechanism [15], it gives the mass of neutrinos as a ratio between the Dirac neutrino mass m_D and the Majorana neutrino mass m_M:

$$m_\nu \sim \frac{m_M^2}{m_D} \tag{1.17}$$

1.4 Double-beta decays

We refer to double-beta decay to decays with two simultaneous β decays. Today, we assume two modes for this decay: the two neutrino mode ($2\nu\beta\beta$) and the zero neutrino mode, known as neutrinoless double-beta ($0\nu\beta\beta$) decay . These two modes are described in the following sections, particularly the $0\nu\beta\beta$ mode, subject of this thesis.

1.4.1 Two neutrino double-beta decay

After Fermi's development of single β decay theory [3], M. Goeppert-Mayer advanced the existence of a double-beta decay in 1935 [33]. This decay consists of the simultaneous emission of two electrons and two anti-neutrinos ($2\nu\beta\beta$) by nuclei with an even number of neutrons (n) and protons (p), following the reaction in 1.18

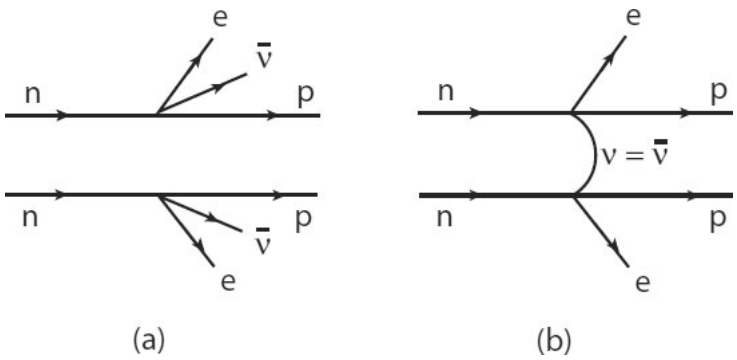

FIGURE 1.4: Feynman's diagram for $2\nu\beta\beta$ decay (left) and $0\nu\beta\beta$ (right).

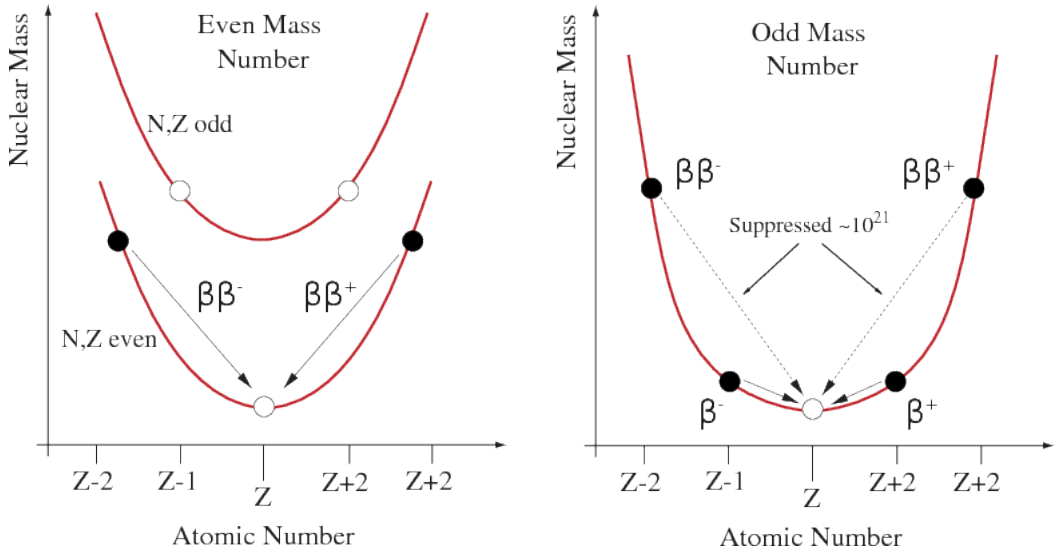

FIGURE 1.5: Isobaric mass parabola for an even isobar candidate (*left*) and for an odd isobar candidate (*right*).

and the Feynman diagram shown in Fig 1.4.

$$N(A,Z) \rightarrow N(A,Z+2) + 2e^- + 2\bar{\nu}_e \tag{1.18}$$

The $2\nu\beta\beta$ decay detection is favored when single β decay to the intermediate nucleus is energetically forbidden due to the pairing interaction or strongly suppressed by a large spin difference between N(A,Z) and N(A, Z+1). This can be illustrated by the mass isobaric parabola (see Fig 1.5) obtained from the Bethe-Weizsacker formula .

This decay is the rarest decay ever observed, it is allowed in the SM and is energetically possible for 35 nuclei. It was observed for 11 nuclei, with a half-life range of $T_{1/2} \approx 10^{18} - 10^{24}$ yr [34].

1.4.2 Neutrinoless double-beta decay

The neutrinoless double-beta decay mode was first proposed by Furry in 1939, assuming that neutrinos are Majorana particles [35]. The Feynman diagram of such decay is shown in Fig. 1.4. In $0\nu\beta\beta$ decay, two electrons are emitted in the final state with no neutrino following the reaction :

$$N(A,Z) \rightarrow N(A,Z+2) + 2e^{-} \tag{1.19}$$

This decay is a hypothetical one that has never been observed yet. It is not allowed by the SM as it violates the total lepton number and the B-L number (Baryon-Lepton number) by two units. This process is possible only if neutrinos are Majorana particles. If $0\nu\beta\beta$ decay is observed experimentally, it will imply the following:

- the neutrino absolute mass scale will be fixed;
- Majorana nature of neutrino will be proved;
- the experimental existence of a process violating the lepton number will open doors to physics beyond the SM;
- the violation of B-L number would help to understand the asymmetry of matter/antimatter in the universe.

The observable of $0\nu\beta\beta$ decay is its decay rate $(T^{0\nu}_{1/2})^{-1}$. In the case of a decay with an exchange of a light Majorana neutrino [15], the decay rate would be given by:

$$(T^{0\nu}_{1/2})^{-1} = G^{0\nu} g_A^4 |M^{0\nu}|^2 < m_{\beta\beta} >^2 \tag{1.20}$$

where $G^{0\nu}$ is the phase space factor, g_A is the axial coupling, $M^{0\nu}$ is the nuclear matrix element and $m_{\beta\beta}$ is the effective Majorana mass expressed as:

$$m_{\beta\beta} = |\sum_{i=1}^{3} U_{ei}^2 m_i| \tag{1.21}$$

To understand the experimental challenges related to the measurement of this decay rate, it is useful to give a brief description of each term of Eq. 1.20:

Phase space factor: it depends on the energy of the decay ($G^{0\nu} \sim Q^5_{\beta\beta}$) and on the charge of the daughter nucleus. It embeds the kinematics of the decay. $G^{0\nu}$ is calculated analytically and the most recent values obtained with high accuracy [36] are given in Table 1.2 for several $0\nu\beta\beta$ decay candidates.

Nuclear matrix element (NME): neutrinoless double-beta decay is a nuclear process where nucleon interactions are enclosed in the nuclear matrix element $M^{0\nu}$. The decay rate is strongly dependent on that so precise calculations of the NME are needed. Unfortunately, the evaluation of the nuclear matrix element is compli-

Nucleus	$G^{0\nu}$ [10^{-15} yr^{-1}]	$M^{0\nu}$
$^{48}Ca \rightarrow^{38} Ti$	26.32	0.9-3.0
$^{76}Ge \rightarrow^{76} Se$	26.15	2.8-6.2
$^{82}Se \rightarrow^{82} Kr$	11.52	2.6-5.4
$^{96}Zr \rightarrow^{96} Mo$	24.40	1.8-6.5
$^{100}Mo \rightarrow^{100} Ru$	18.90	3.9-7.2
$^{116}Cd \rightarrow^{116} In$	20.64	3.2-5.5
$^{130}Te \rightarrow^{130} Xe$	18.10	2.7-6.4
$^{136}Xe \rightarrow^{136} Ba$	18.83	2.2-4.8

TABLE 1.2: Phase space factor [36] and nuclear matrix elements [37] calculated for $0\nu\beta\beta$ decay candidates.

cated because it involves a many-body problem. This problem can be solved only by using nuclear models that contain the nuclear structure effects of the decay. In the case of $0\nu\beta\beta$, different models are used to calculate nuclear matrix elements:

- NSM: Nuclear Shell Model;
- QRPA: Quasi-particle Random Phase Approximation;
- IBM: Interacting Boson Model;
- EDF: Energy Density Functional;
- PHFB: Projected Hartree-Fock-Bogoliubov approach.

In Fig 1.6, the values of NME for these models are reported for several $0\nu\beta\beta$ decay candidates and the predicted half-life (inverse of the decay rate) is also given for each model [38] assuming that $g_A = 1.27$.

Weak axial-vector coupling g_A: the decay rate of $0\nu\beta\beta$ depends on the fourth power of g_A, so it is important to have a precise measurement of it to predict the decay rate. Indeed, suppose the value of g_A is smaller than the one that we use to evaluate the rate of $0\nu\beta\beta$ decay. In that case, this latter becomes longer and hence the sensitivity of an experiment is affected. In general, the value of g_A is taken as $g_A^{free} \approx 1.27$, in the case of a free nucleon approximation measured in neutron beta decay [15].

It turns out that g_A can be quenched in a way that in a nuclear interaction $g_A^{eff} = q \times g_A^{free}$ where q is a re-normalization factor. This deviation from the free nucleon value may result from nuclear medium and nuclear many-body effects [39]. The effective value g_A^{eff} depends on the model used to describe the studied β decay and on the process: the re-normalization of low momentum exchange process (β or $2\nu\beta\beta$ decays) can be different from the high momentum exchange processes ($0\nu\beta\beta$ decays) [39]. However, the information about this re-normalization factor is crucial

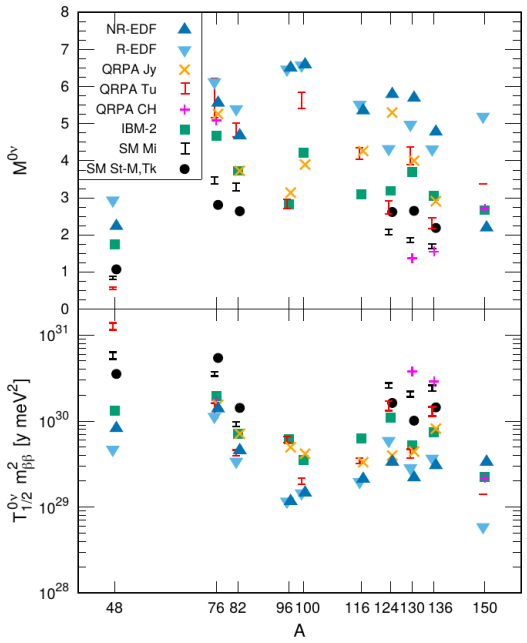

FIGURE 1.6: Nuclear matrix elements (*top panel*) and associated $T^{0\nu}_{1/2}$ scaled by the effective Majorana mass (*bottom panel*) as a function of the mass number A [38].

in any β decay. Forbidden non-unique β decays are the most interesting to probe the g_A^{eff} value for low momentum exchange β decays. In [40], a method to measure g_A^{eff} in such decay is presented: the spectral shape method (SSM). It consists of studying the shape of the β spectrum that is sensitive to the effective value of g_A. The authors in [41] applied this method on fourth-forbidden non-unique β decay of ^{113}Cd and ^{115}In. In this thesis, a preliminary analysis of the β decay of ^{113}Cd is performed with the goal of measuring g_A^{eff} value using this method with a low energy threshold scintillating bolometer. A full description of the experimental setup and method is presented in Chapter 5.

The search for neutrinoless double-beta decay faces theoretical challenges regarding the NME calculations and the g_A quenching factor, which are relevant parameters to evaluate the half-life of $0\nu\beta\beta$ decay, the experimental observable. Additionally, the search for $0\nu\beta\beta$ decay has challenging experimental issues that are presented in the next section.

1.4.3 Experimental point of view of neutrinoless double-beta decay

The last decades were fruitful in the field of neutrino oscillation experiments. It is now essential to try to understand the nature of neutrinos and their absolute mass scale. As discussed in the previous section, one of the most promising processes to probe the neutrino mass and nature is the search for $0\nu\beta\beta$ decay. The experimental

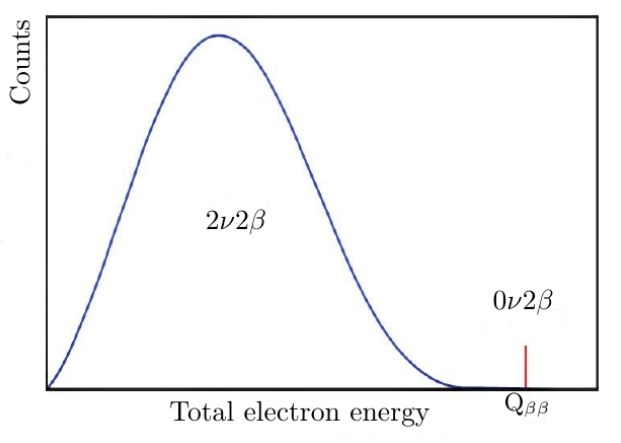

FIGURE 1.7: Schematic view of the $0\nu\beta\beta$ decay experimental signature. The $2\nu\beta\beta$ decay appears as a continuum.

observation of this process is challenging due to the very long half-life of the decay. The experimental signature of $0\nu\beta\beta$ decay is a monochromatic peak at the $Q_{\beta\beta}$ (energy of the decay) of the decay which is the sum of the energy of the two emitted electrons. In Fig 1.7, a schematic view of the spectrum is presented: the $2\nu\beta\beta$ mode appears as a continuum of the two electrons and the two neutrinos energy whereas the $0\nu\beta\beta$ mode appears as a monochromatic peak.

The number of candidates events N in the region of interest (ROI), where the $0\nu\beta\beta$ decay monochromatic peak is expected, can be written as follows:

$$N = ln(2)\frac{N_A}{m}\left(\frac{a\epsilon Mt}{T^{0\nu}_{1/2}}\right) \tag{1.22}$$

where N_A is the Avogadro number, m the molar mass, a the isotopic abundance, ϵ the detection efficiency of the signal in the ROI, M the mass of the source and t the exposure time. Of course, the sensitivity of an experiment to the half-life strongly depends on the total number of counts in the ROI, i.e., the number of background counts. This leads to the following:

$$T^{0\nu}_{1/2} \propto \begin{cases} a\ M\epsilon\ t & \text{background free} \\ a\ \epsilon\sqrt{\frac{M\ t}{BI\ \Delta E}} & \text{with background} \end{cases} \tag{1.23}$$

where ΔE is the energy resolution of the detector and BI is the background index, defined as:

$$BI = \frac{\text{number of background counts in the ROI}}{M\ \Delta E\ t} \tag{1.24}$$

From the formula 1.23, one can list the fundamental parameters to build a $0\nu\beta\beta$ decay experiment:

- the mass of the source has to be large to increase the sensitivity;

- isotopic abundance of the candidate element and possibility of enrichment, this point is related to the previous one. Indeed, to find a suitable candidate for $0\nu\beta\beta$ from an experimental point of view, it needs to have a relatively high isotopic abundance with an industrial possibility of enrichment at acceptable coast. This point will be discussed in Sec. 1.4.5;
- background index should be low; it provides the information on the background level in the ROI. The control of the background level and its origin is very important, and hence all background sources need to be known. A discussion about background sources is given in Sec. 1.4.4;
- the energy resolution and detector efficiency: it is important to build a detector with a high energy resolution in the ROI since the signature of $0\nu\beta\beta$ decay is a peak at $Q_{\beta\beta}$ above a flat background. Therefore, a good energy resolution and a background control are two important features for the $0\nu\beta\beta$ decay experiment. The energy resolution depends a lot on the chosen detection technology;
- the exposure time has to be sufficient to have enough data to increase the sensitivity. Most of the experiments achieved their sensitivity goal after 5-10 years of data taking. The background-free scenario in Eq. 1.23 is the ideal case translated experimentally by 0.1 counts in the live-time of the experiment in the ROI at 90% C.L.. In this case, the sensitivity is linear with the exposure time.

To summarise, the ingredients to build a successful $0\nu\beta\beta$ decay experiment are known and should be well controlled and determined. The choice of the source isotope is crucial because it is related to most of the parameters of Eq. 1.23. Besides, the detector technology is important to fully control the energy resolution, the detection efficiency and the background rejection.

1.4.4 Background sources

In a $0\nu\beta\beta$ decay experiment, the background can have different sources and origins. It is crucial to understand it to reduce its impact. The background sources can be divided into three categories, with respect to the detector:

- internal which can be controlled by choosing radio-pure materials that compose the detector;
- external which can be reduced by adding shielding around the detectors;
- surface contamination, which can be controlled by handling the detectors in a clean environment and surface treatment. For example, most of the experiments using copper as a detector holder have a special surface cleaning procedure. The choice of detection technology with a discrimination capability allows having a separation between the surface events and bulk events, which leads to a background level reduction.

The main background contributions are listed in the following.

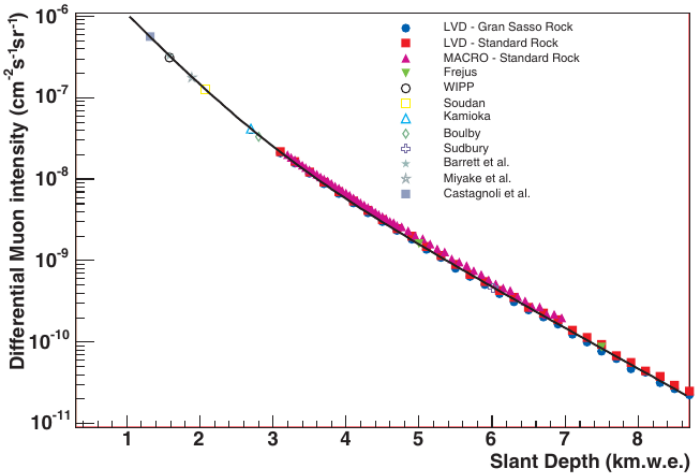

FIGURE 1.8: Measurements of the differential muon flux as a function of slant depth for different underground laboratories [42].

1.4.4.1 Natural radioactivity

One of the most important contributions for the background comes from the ^{232}Th and ^{238}U decay chains present in nature. The γ endpoint of this natural radioactivity is at 2615 keV, which corresponds to the decay of ^{208}Tl. It is important to choose a $0\nu\beta\beta$ decay candidate with a $Q_{\beta\beta}$ higher than this endpoint (see Sec. 1.4.5).

1.4.4.2 Cosmic muons

Muons are produced by the decay of charged pions created in the upper atmosphere by cosmic rays. The muon flux on earth is around one muons cm^{-2}.m^{-1}. The muon flux can be reduced considerably if the experiment is underground [42], the flux can drop up to 10^{-10} muons cm^{-2}.m^{-1} depending on the depth of the underground laboratory [42] as shown in Fig 1.8.

1.4.4.3 Cosmogenic activation

The cosmogenic activation is produced by the high-energy neutrons that come from the cosmic rays. The main issue with cosmogenic activation is that it produces long-lived isotopes that can contribute to the background in the ROI. To avoid this phenomenon, materials for detection should be stored within shields or underground. Moreover, the time spent by the detector above ground should be minimized, and the transportation of the detector material should not be done by flight.

In brief, all these background sources cited above can be significantly reduced and avoided by building the $0\nu\beta\beta$ decay experiment underground in a clean environment and adding radio-pure lead and copper shielding around the detectors. The environment around the detectors needs to be as much as possible radio-pure.

In addition, the detector technology and the data analysis chain play an essential role in reducing the background in the ROI.

1.4.5 Neutrinoless double-beta decay candidates

One can imagine the perfect experiment with a $0\nu\beta\beta$ decay candidate that has a high isotopic abundance a and can be enriched (large M), a high energy resolution detector at $Q_{\beta\beta}$ and a low counting background rate. Unluckily, the experimental reality is different. Among 35 $0\nu\beta\beta$ decay candidates, only 9 are relevant experimentally. These isotopes are listed in Table 1.3 with their isotopic abundance and $Q_{\beta\beta}$.

Isotope	Natural abundance (%)	$Q_{\beta\beta}$ (keV)
^{48}Ca	0.2	4263
^{76}Ge	7.8	2039
^{82}Se	9.2	2998
^{96}Zr	2.8	3348
^{100}Mo	9.6	3035
^{116}Cd	7.5	2813
^{130}Te	34.1	2527
^{136}Xe	8.9	2459
^{150}Nd	5.6	3371

TABLE 1.3: Isotopic abundance and $Q_{\beta\beta}$ for the most relevant candidates for $0\nu\beta\beta$.

The enrichment of the $0\nu\beta\beta$ decay candidate is an important issue: the method, the industrialization and the cost of the enrichment must be considered to choose an isotope. The enrichment by gas centrifuging is only possible for ^{76}Ge, ^{82}Se, ^{100}Mo,^{116}Cd, ^{130}Te and ^{136}Xe.

The choice of the isotope depends also on the $Q_{\beta\beta}$ of the decay that fixes two parameters: the phase space factor that is proportional to $Q_{\beta\beta}$ to the fifth power and the background. The latter can be drawn within two energy limits: the endpoint of the natural γ radioactivity at ^{208}Tl peak, at 2615 keV, and the ^{214}Bi β decay, at 3270 keV, that comes from the ^{222}Rn.

Out of the nine experimentally relevant candidates, three groups are distinguishable with respect to this two energy limits:

- $Q_{\beta\beta} < 2615$ keV: ^{76}Ge, ^{130}Te, ^{136}Xe, this group contains γ and radon background;
- 2615 keV $< Q_{\beta\beta} <$ 3270 keV: ^{82}Se, ^{100}Mo, ^{116}Cd, this group is γ free background but radon induced background can be an issue;
- $Q_{\beta\beta} > 3270$ keV: ^{48}Ca, ^{96}Zr, ^{150}Nd, this group is γ/β background free which is the ideal case but their enrichment is complicated.

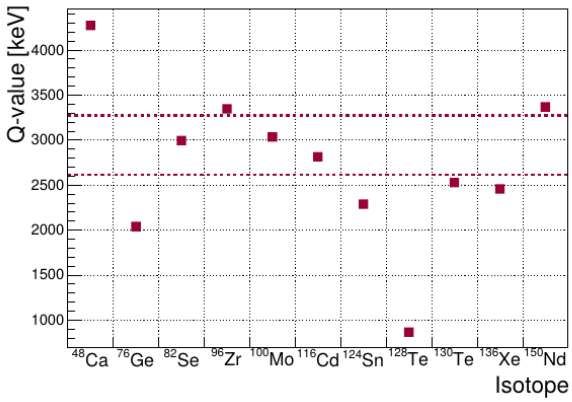

FIGURE 1.9: $Q_{\beta\beta}$ as a function of the isotopic abundance for the main $0\nu\beta\beta$ isotopes. The two horizontal dashed lines represent the two energy limits set by the background.

1.5 Experimental status for $0\nu\beta\beta$ decay searches

In this section, a brief overview of current $0\nu\beta\beta$ decay experiment (sorted by candidate for $0\nu\beta\beta$ decay) is given. In Table 1.4, the most stringent limits on the half-life of $0\nu\beta\beta$ decay for different isotopes are given.

Isotope	limit on $T^{0\nu}_{1/2}$ ($\times 10^{25}$)	$m_{\beta\beta}$ (eV)	Experiment	References
^{48}Ca	5.8×10^{-3}	< 3.5-22	ELEGANT-IV	[43]
^{76}Ge	18	< 0.07-0.16	GERDA	[44]
	2.7	< 0.2-0.43	MAJORANA	[45]
^{82}Se	3.5×10^{-1}	< 0.31-0.64	CUPID-0	[46]
^{96}Zr	9.62×10^{-4}	< 7.4-19.5	NEMO-3	[47]
^{100}Mo	1.4×10^{-1}	< 0.31-0.54	CUPID-Mo	[48]
^{116}Cd	2.2×10^{-3}	< 1.0-1.7	Aurora	[49]
^{130}Te	2.2	<0.090-0.350	CUORE	[50]
^{136}Xe	10.7	< 0.061-0.165	KamLAND-Zen	[51]
	3.5	< 0.093-0.286	EXO-200	[52]
^{150}Nd	2.0×10^{-3}	< 1.6-5.3	NEMO-3	[53]

TABLE 1.4: The most recent measurements on $T^{0\nu}_{1/2}$ limits at 90% C.L..

We distinguish two experimental approaches to search for $0\nu\beta\beta$ decay:

- calorimetric approach, i.e., homogeneous detector where the $0\nu\beta\beta$ decay candidate is embedded in the detector. This approach provides very high efficiency and good energy resolution. Most of the $0\nu\beta\beta$ decay experiments are using this approach.

- non-calorimetric approach, i.e., the source and the detector are separated. In this approach tracking systems are used. They provide a topological reconstruction of the events in the detector but the efficiency is reduced. It should be noted that the most advanced experiment that used this approach was the NEMO-3 experiment.

Experiments searching for $0\nu\beta\beta$ decay in ^{76}Ge

The $0\nu\beta\beta$ decay candidate ^{76}Ge belongs to the group of isotopes with a $Q_{\beta\beta}$ lower than the endpoint of the natural radioactivity. However, it is used in two leading experiments GERDA [44] and Majorana [45] that will merge and upgrade to LEGEND [54]. The isotope ^{76}Ge is exploited as a semiconductor detector widely used in experimental physics in general and has a good energy resolution which compensates the fact that ^{76}Ge has a low $Q_{\beta\beta}$.

GERDA: the GERmanium Detector Array experiment is based in the Hall A of Laboratori Nazionali del Gran Sasso (LNGS), in Italy, since 2004. It is an array of germanium diodes enriched in ^{76}Ge (~ 87 %). The detectors are in liquid argon that acts as a shielding against natural radioactivity and a thermal bath to cool down the system. GERDA uses 37 enriched detectors with two different geometries: coaxial and Broad Energy Ge (BEGe) detectors [55]. The latter allows having a pulse shape discrimination that leads to efficient background rejection. The GERDA experiment reached the lowest background index ever achieved $5.6^{+3.4}_{-2.4} \times 10^{-4}$ counts/(keV.kg.yr). The energy resolution FWHM at $Q_{\beta\beta}$ obtained by the experiment was 3.6 keV for coaxial and 3.0 keV for BEGe detectors [56]. With a total exposure of 103.7 kg.yr, the sensitivity assuming no signal is $T^{0\nu}_{1/2} > 1.8 \times 10^{26}$ yr [44]. the GERDA experiment is the first to be sensitive beyond 10^{26} yr.

Majorana: the MAJORANA collaboration is using high-purity germanium detectors to search for $0\nu\beta\beta$ decay in ^{76}Ge. The demonstrator is located at the Sanford Underground Research Facility in Lead in South Dakota, USA. The demonstrator contains an array of 44.1 kg of Ge detectors enriched to 88% in ^{76}Ge. The experiment is using pulse shape discrimination in a similar way to GERDA. In [45], the MAJORANA collaboration presents its results for an exposure of 26 kg.yr. They obtained the best energy resolution FWHM at $Q_{\beta\beta}$ (2.53 keV) ever achieved in $0\nu\beta\beta$ decay experiments. The MAJORANA demonstrator achieved a sensitivity on the half-life $T^{0\nu}_{1/2} > 2.7 \times 10^{25}$ yr (at 90% C.L.).

LEGEND: as mentioned, the MAJORANA demonstrator and the GERDA experiment achieved the best results among the $0\nu\beta\beta$ decay experiments in terms of FWHM, BI and sensitivity. The Large Enriched Germanium Experiment for Neutrinoless $\beta\beta$ Decay (LEGEND) collaboration aims to take the best of these two technologies and succeed in building a ton-scale experiment. LEGEND goal is to reach a sensitivity of 10^{28} yr [54]. The first phase of this experiment, LEGEND-200, is under construction at LNGS; it will contain 200 kg of Ge detectors and started in

February 2020. The next phase, LEGEND-1000, is at the design step, it will have one ton of Ge detectors.

Experiments searching for $0\nu\beta\beta$ decay in ^{82}Se

The ^{82}Se isotope has $Q_{\beta\beta} = 2998$ keV which is higher than the endpoint of the natural radioactivity. The isotope ^{82}Se has been chosen as a baseline for several experiments. This section will give a brief description of the NEMO-3, the SuperNEMO and the CUPID-0 experiments.

NEMO-3: the Neutrino Ettore Majorana Observatory experiment was located at Laboratoire Souterrain de Modane (LSM) in France. The data taking was from 2003 to 2011. Unlike most of $0\nu\beta\beta$ decay experiments, the NEMO-3 experiment used the inhomogeneous approach to probe the $0\nu\beta\beta$ decay with a tracking-calorimeter detector. The detector contains three main elements: the source foil, the tracking detector and the calorimeter. The source was a thin foil (60 mg/cm^2 of thickness) containing 7 enriched isotopes (^{48}Ca, ^{82}Se, ^{96}Zr, ^{100}Mo, ^{116}Cd, ^{130}Te and ^{150}Nd). The total mass of ^{82}Se in this foil is 0.932 kg. The source foil was located in the center of the tracking system that consists of a wire chamber composed of Geiger cells in counting mode. The wire chamber was placed in a magnetic field (25 G) produced by a solenoid surrounding the detector [57]. The magnetic field allows identifying the particle using the curvature of their trajectory while passing the tacking system. Finally, the calorimeter was around the wire chamber, made of plastic scintillators and photomultipliers [57]. The calorimeter allows the measurement of the energy of the particles. The whole detection system was surrounded by a passive shielding made of iron, borated water, paraffin and wood [57]. A schematic view of the detector is shown in Fig 1.10.
The NEMO-3 was the only detector that could provide a topological reconstruction of the events thanks to the combination of the tracking and calorimetric techniques, identifying different types of charged particles. The achieved limit on the $0\nu\beta\beta$ decay half-life for ^{82}Se was $T^{0\nu}_{1/2} > 2.5 \times 10^{23}$ yr at 90% C.L. for an exposure of 0.17 kg/yr [59].

SuperNEMO: the technology of SuperNEMO is based on the NEMO-3 experiment. The SuperNEMO demonstrator is also based on the tracking-calorimetric technique where a foil containing only ^{82}Se isotope is sandwiched between trackers and enclosed by calorimeters [60]. This design allows having a complete reconstruction of the tracks of the particles in the detector (see Fig. 1.11).

CUPID-0: the isotope ^{82}Se can be enclosed in a scintillating crystal such as ZnSe, used by the CUPID-0 collaboration as low-temperature scintillating bolometers. This detection technology will be deeply described in Chapter 2.
The CUPID-0 experiment is the first pilot experiment of the CUPID (CUORE Upgrade with Particle Identification) the next-generation experiment for $0\nu\beta\beta$ decay

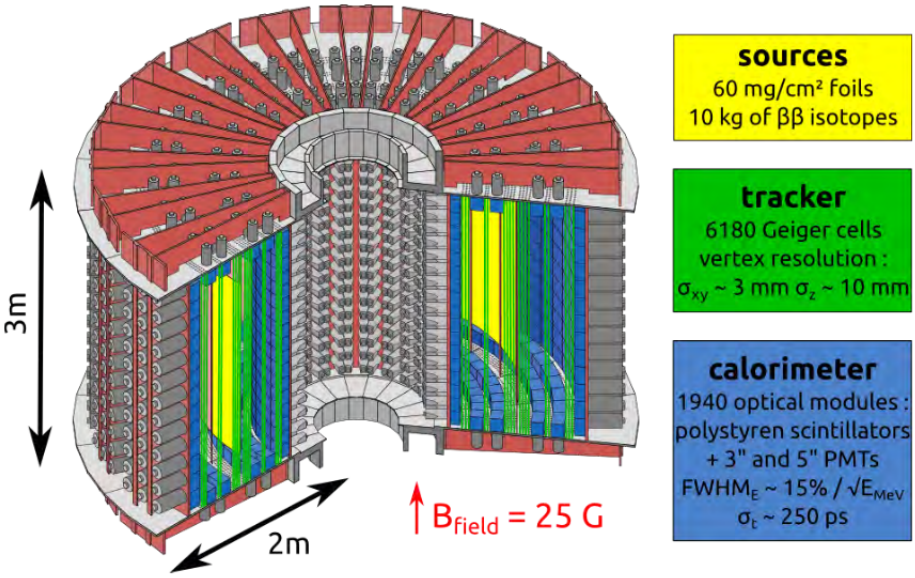

FIGURE 1.10: The NEMO-3 detector [58].

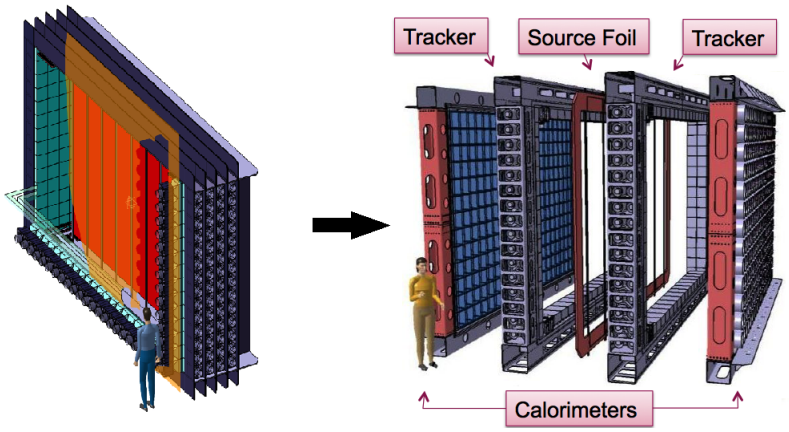

FIGURE 1.11: The SuperNEMO detector [58].

searches. It is an array of 26 scintillating bolometers made of ZnSe cylindrical crystals, 24 crystals were 96% enriched with ^{82}Se and two were natural crystals [46]. The experiment was located in the Hall A of LNGS and took data from June 2017 to December 2019. This pilot experiment showed that the CUPID technology allows reaching a low background of $3.5^{+1.0}_{-0.9} \times 10^{-3}$ counts/(keV.kg.yr). The most stringent limit was set on the half-life of the ^{82}Se $0\nu\beta\beta$ decay $T^{0\nu}_{1/2} > 3.5 \times 10^{24}$ yr at 90% C.L. [46].

Experiments searching for $0\nu\beta\beta$ decay in ^{100}Mo

The isotope ^{100}Mo is one of the most interesting candidates for $0\nu\beta\beta$ decay searches: it has good theoretical predictions on the half-life, it has a $Q_{\beta\beta}$ = 3034 keV higher than the endpoint of natural γ radioactivity, and it can be enriched at the industrial level with gas centrifugation. Besides, it is possible to make scintillating crystals containing ^{100}Mo, which is very useful in the case of a calorimetric approach. Several experiments studied this candidate; we cite the most important ones below.

NEMO-3: as mentioned above the NEMO-3 experiments studied the ^{100}Mo $0\nu\beta\beta$ decay. The thin foil containing the 7 isotopes had 6.914 kg of ^{100}Mo. In [61], the NEMO-3 collaboration gave the results of a total exposure of 34.3 kg.yr. The background level achieved, in the ROI, was 0.44±0.13 counts/(yr.kg). They achieved a limit on the half-life of the $0\nu\beta\beta$ decay of ^{100}Mo: $T^{0\nu}_{1/2} > 1.1 \times 10^{24}$ yr at 90% C.L. [61].

AMoRe: the Advanced Molybdenum-based Rare process Experiment is an experiment based on cryogenic scintillating bolometers operated at ∼10 mK made of ^{48depl}Ca^{100}MoO$_4$ crystals. Currently, this experiment is composed of an array of six crystals with a total mass of 1.9 kg (AMoRe-pilot). It is based in Yangyang underground laboratory in South Korea. In [62], the collaboration reported their first results: the limit on the half-life of the $0\nu\beta\beta$ decay of ^{100}Mo they obtained was $T^{0\nu}_{1/2} > 9.5 \times 10^{22}$ yr at 90% C.L.. The AMoRe-I is the next phase of the experiment and is currently being cooled down [63]. It exploits 13 ^{48depl}Ca^{100}MoO$_4$ and 5 Li$_2^{100}$MoO$_4$ crystals and is planning to take data for at least two years.

CUPID-Mo: the full description of this experiment will be given in Chapter 3 since it is an important part of this Ph.D. thesis.
CUPID-Mo is another pilot experiment of CUPID; it exploits 20 Li$_2^{100}$MoO$_4$ crystals enriched in ^{100}Mo operated as scintillating bolometers at 20 mK. The experiment was located at LSM and took science data from March 2019 to July 2020. With an exposure of 2.16 kg.yr the CUPID-Mo experiment archived the best limit on the $0\nu\beta\beta$ decay half-life of ^{100}Mo $T^{0\nu}_{1/2} > 1.4 \times 10^{24}$ yr at 90% C.L. [48]. The CUPID-Mo technology was chosen to be the baseline for CUPID.

Experiments searching for $0\nu\beta\beta$ decay in ^{116}Cd

The isotope ^{116}Cd is one of the favorable candidates for $0\nu\beta\beta$ decay searches. It has a good theoretical prediction on the half-life; $Q_{\beta\beta}$ = 2813.49 keV; an isotopic abundance of $I.A. = 7.5\%$; the possibility to produce enriched isotope by the centrifuge separation method; and finally, the ability to be embedded in $CdWO_4$ crystals, well-studied scintillators, which gave promising results in "source = detector" experiments.
The ^{116}Cd $0\nu\beta\beta$ decay was investigated by several experiments using different detection techniques.

NEMO-3: the NEMO-3 source foils, mentioned above, contained 0.410 kg of ^{116}Cd. In [64], the NEMO-3 collaboration set a new limit on the decay of ^{116}Cd to the ground state of ^{116}In: $T^{0\nu}_{1/2} > 1.0 \times 10^{23}$ yr at 90% C.L.

COBRA: the Cadmium-zinc-telluride 0-neutrino double-beta Research Apparatus (COBRA) is an experiment that uses CdZnTe semiconductor at room temperature, in which nine candidates for double-beta decays are contained. The CdZnTe semiconductors detectors are usually used in the detection of radiation. As mentioned, the semiconductor detectors provide good energy resolution, an important feature for $0\nu\beta\beta$ decay searches. The COBRA experiment is located at LNGS. The idea of COBRA is to use the semiconductor detectors as a source and a detector, so they have a high detection efficiency. Hence, an event in crystal A can be detected by crystal B. In this way, COBRA takes advantage of two basic detector concepts where the "source=detector" and "source≠detector". The COBRA demonstrator consists of an array of 64 cubics CdZnTe detectors [65]. Each detector has a size of $1\times1\times$ cm^3 and a mass of 5.9 g. In [66], the COBRA collaboration reported the limit archived on the different isotopes under study within the experiment. The limit on on the half-life of the $0\nu\beta\beta$ decay of ^{116}Cd they obtained was $T^{0\nu}_{1/2} > 1.6 \times 10^{21}$ yr at 90% C.L..
This experiment is also studying the single β-decay of ^{113}Cd, which is highly suppressed. The aim of this study is the measurement of the axial coupling g_A quenching through a prise measurement of the β spectrum of ^{113}Cd [67].

Aurora: the Aurora experiment took place in the DAMA/R&D setup at LNGS. It took data from 2011 to 2017 [49]. Aurora used 1.162 kg enriched cadmium tungstate $^{116}CdWO_4$ crystal as scintillators at room temperature to investigate the $0\nu\beta\beta$ decay in ^{116}Cd. Two $^{116}CdWO_4$ crystals with a mass of 580 g and 582 g (produced from the same crystal boule) were used to perform this measurement [68]. The scintillators were fixed to a Teflon container in a bath of ultra-pure pseudocumene-based liquid scintillator (LS). Photomultipliers and a light guide were added to read the two scintillating materials (crystals and the liquid). The whole system was surrounded by a passive shielding made of copper, lead, cadmium and polyethylene/paraffin to reduce the external background. In addition, the crystals and the shielding were inside a Plexiglas box flushed by nitrogen gas [49].

The results achieved were auspicious and they were reported in [49]. The energy resolution at $Q_{\beta\beta}$ was about 160 keV and an improved limit on the the half-life of the $0\nu\beta\beta$ decay of ^{116}Cd was set $T^{0\nu}_{1/2} > 2.2 \times 10^{23}$ yr at 90% C.L..

The two crystals used by the Aurora experiment are studied in this thesis as cryogenic scintillating bolometers. The study and the obtained results will be presented in Chapter 5.

Experiments searching for $0\nu\beta\beta$ decay in ^{130}Te

The isotope ^{130}Te is the only $0\nu\beta\beta$ decay candidate that does not need to be enriched thanks to its high isotopic abundance (34.1 % [69]). However, the energy of $0\nu\beta\beta$ decay for this isotope is lower than the endpoint of the natural γ radioactivity ($Q_{\beta\beta}$=2557 keV), which gives extra background in the ROI. This isotope was the first to be studied by $0\nu\beta\beta$ decay experiments. We present here briefly the notable current experiments.

CUORE: the Cryogenic Underground Observatory for Rare Event experiment is located in the Hall A of LNGS. It is the first-ton scale experiment using bolometers at low temperature ($\sim$11.8 mK). One of the biggest successes of CUORE is showing the ability to cool one ton of detectors to cryogenic temperature [70]. CUORE is composed of 988 natural TeO_2 crystals arranged in 19 towers. The towers are inside a cryostat that is surrounded by roman lead shielding. A schematic view of the CUORE cryostat with the bolometers inside is shown in Fig. 1.12. The CUORE collaboration published their latest results in [50]. The detectors showed excellent energy resolution (less than 10 keV FWHM) in the ROI and large detection efficiency. The background in the ROI is estimated at $(1.41\pm0.04)\times10^{-2}$ counts/(keV.kg.yr). The limit on the half-life of the $0\nu\beta\beta$ decay of ^{130}Te obtained was $T^{0\nu}_{1/2} > 2.2 \times 10^{25}$ yr at 90% C.L. for a total exposure of 1000 kg.yr [50].

SNO+: it is an experiment that will use the infrastructure of the Sudbury Neutrino Observatory (SNO) experiment at SNOLAB in Canada [71]. The detector will be filled with acrylic vessel and a liquid scintillator loaded with ^{130}Te surrounded by 9400 PMTs. The experiment will start with a loading of 0.5 % of ^{130}Te [72]. The expected sensitivity with this loading is $T^{0\nu}_{1/2} > 1.9 \times 10^{26}$ after 5 years of data taking [73].

Experiments searching for $0\nu\beta\beta$ decay in ^{136}Xe

Despite the low $Q_{\beta\beta}$ = 2459 keV of the $0\nu\beta\beta$ decay candidate ^{136}Xe, it has been chosen as a baseline for several experiment searching for $0\nu\beta\beta$ decay. It has a low cost and easy enrichment. It can be used as liquid Xenon (LXe) in large-scale experiments to be both the source and the detector.

Exo-200: the Enriched Xenon Observatory EX0-200 is an experiment based underground at the Waste Isolation Pilot Plant in the USA. EXO-200 used 200 kg of LXe

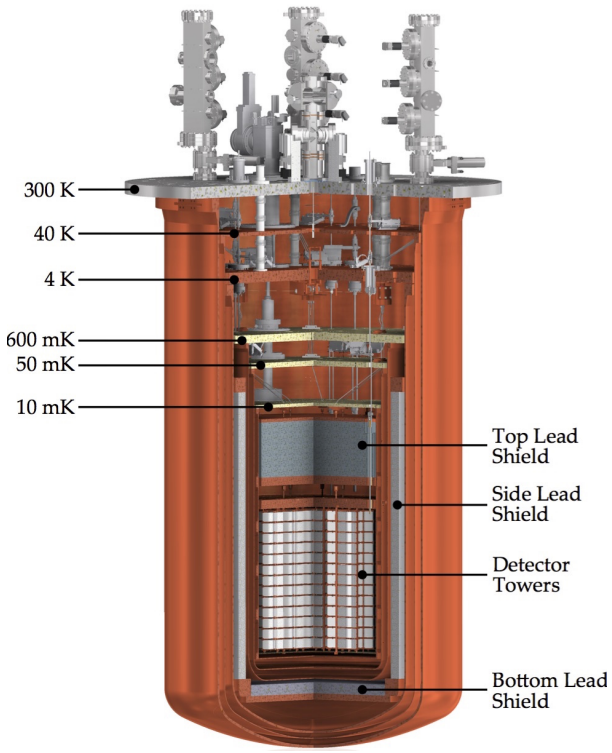

FIGURE 1.12: The CUORE cryostat [70].

enriched to 80% in ^{136}Xe. The LXe was in a time projection chamber (TPC) and all the system was operating at 167 K. The detector is made of almost two identical TPC with a shared cathode which creates two drifts regions [74]. The TPC is designed to collect ionization and scintillation signals: the scintillation is detected by the avalanche of the photodiodes and the ionization is detected by the drifts along the wire planes. The double readout scintillation-ionization provides a full reconstruction of the energy of each particle interaction in the detector [74]. This allows the discrimination between the different types of particles that interact in the liquid.
EXO-200 took data between 2011 and 2018, in two phases: Phase I 2011-2014 and Phase II 2016-2018. In [52], the EX0-200 collaboration reported their latest results with a total exposure of 234.1 kg.yr. The sensitivity on the half-life of $0\nu\beta\beta$ decay obtained was $T^{0\nu}_{1/2} > 3.5 \times 10^{25}$ yr at 90% C.L..

nEXO: the next-generation Enriched Xenon Observatory (nEXO) is the proposed follow up of EXO. The nEXO experiment will reuse the EXO technology with five tones of LXe TPC. The only difference is that the double TPC structure will be removed. The expected sensitivity on the half-life of $0\nu\beta\beta$ decay to be reached is about 10^{28} yr [75].

NEXT: another experiment using Xe TPC is the Neutrino Experiment with a Xenon TPC (NEXT). It will be located at the Laboratorio Subterraneo de Canfranc (LSC) in Spain. It will use high-pressured gaseous Xe in a TPC and tracking-calorimetric technology.
The NEXT collaboration built several prototypes to validate this technology; the last one is NEXT-White that is taking data since 2016 [76]. It is a prototype version of NEXT-100 that contains 5 kg of Xe. The results achieved with this prototype are very promising: the energy resolution at $Q_{\beta\beta}$ is about 1% FWHM [77]. The NEXT-100 experiment will be operated with 97 kg of Xe and will reach the sensitivity of 2.8×10^{25} yr at C.L. for exposure of 100 kg.yr [77].

KamLAND-Zen: this experiment exploits the existing infrastructure Kamioka Liquid scintillator Anti-Neutrino Detector (KamLAND) used for neutrino oscillations detection. It is located in the Kamioka mine in Japan. The KamLAND-Zen detector is composed of 13 tons of LXe (enriched in ^{136}Xe at ∼90%) in a 3 meters diameter inner balloon in the center of the detector. An outer balloon (13 m diameter) is surrounding the inner one, it is filled with a liquid scintillator that acts as an active shielding and the system is viewed by ∼ 2000 PMTs [51]. The total mass of ^{136}Xe is about 380 kg. With this mass, the achieved sensitivity was $T^{0\nu}_{1/2} > 1.07 \times 10^{26}$ yr [51].
The KamLAND-Zen experiment is currently running with 750 kg of ^{136}Xe, the goal is to reach a sensitivity of $T^{0\nu}_{1/2} > 4.6 \times 10^{26}$ yr.

1.5.1 Summary

Of course, in this brief overview of the past, current and future experiments, we did not cite all the existing ones. Also, not all the candidate isotopes for $0\nu\beta\beta$ decay were covered. For example, the ELEGANT-IV [43] is studying the isotope ^{48}Ca, The NEMO-3 experiment set the most stringent limit on ^{96}Zr [47] and ^{150}Nd [53].
Although $0\nu\beta\beta$ decay is not discovered yet, the development and enhancement of the detection technologies would make this possible with the next-generation experiments pushing the limits toward the normal ordering region.

1.6 Where are we in the neutrino mass hierarchy?

With the current experimental results, one can draw a state of art of what did the $0\nu\beta\beta$ decay experiments probe with respect to the neutrino mass hierarchy. The effective Majorana mass in Eq. 1.21 for all the possible hierarchies can be graphically represented as a function of the lightest neutrino mass [79] as shown in Fig. 1.13 where the excluded regions experimentally are highlighted [78]. As mentioned before, clues from the neutrino oscillation experiments and the cosmological observations showed a disfavoring regarding the inverted hierarchy. Therefore, if it is the case, the next-generation experiments will confirm that by probing the inverted

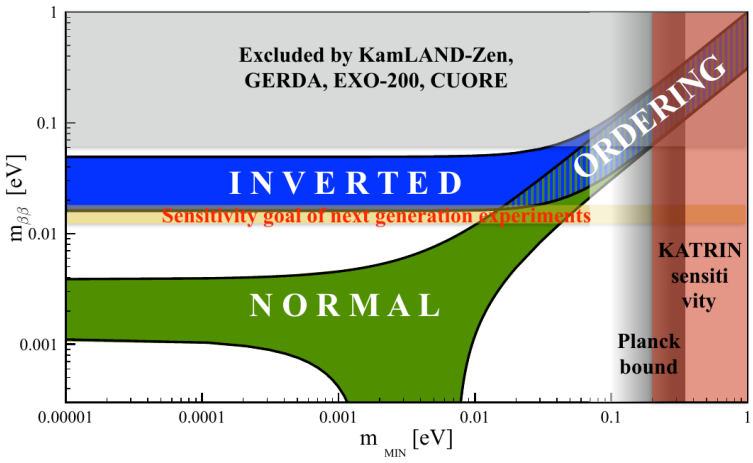

FIGURE 1.13: The effective Majorana mass $m_{\beta\beta}$ as a function of the lightest neutrino mass m_{MIN} [78].

hierarchy ultimately. One of these next-generation experiments is the CUPID experiment using scintillating bolometers (Chapter 6). This detection technology is described in the next Chapter 2.

Chapter 2

Scintillating bolometers

A very promising approach to study neutrinoless double-beta decay is the bolometric technology. Bolometers are known to be very efficient detectors and to provide high energy resolution. In this chapter, an overview of the bolometric technology and its working principle is given. The motivations to use scintillating bolometers for neutrinoless double-beta decay experiments are presented. Finally, the cryogenic facilities that have been used for the detectors and results presented in this thesis are briefly described.

2.1 Bolometers through a brief history

A bolometer (from $\beta o\lambda\acute{\eta}$, "ray," and $\mu\acute{\epsilon}\tau\rho o\nu$, "measure") is a device that sees a particle interaction as a rise of temperature due to the energy release of the particle interaction in the detector. The first idea of a bolometer was born in 1878 to study solar electromagnetic radiation. In his paper [80], Langley proposed a detector that converts the incident electromagnetic energy of the solar radiation into internal energy of the material that composes the bolometer. Historically, the use of bolometers started with astrophysics, where they were dedicated to measure the electromagnetic flux in the CMB. The first mobilization of a bolometer for nuclear detection was made by Curie and Laborde in 1903 when they measured the heat produced by radium salts [81].
The usage of bolometers for nuclear and particle physics started to become interesting when Simon, in 1934, advanced that the sensitivity of calorimetric detectors can be increased by many orders of magnitude if they were kept at very low temperatures [82]. From here, bolometers became cryogenic detectors working at temperatures of the order of the mK. The cryogenic bolometric approach, very similar to what we have today, for $0\nu\beta\beta$ decay searches were introduced by E. Fiorini and T. O. Niinikoski in 1984 [83].

2.2 How does a bolometer work?

In a bolometer, particle detection occurs when the deposited energy of interaction is converted into phonons measured as a temperature variation. This allows converting a large fraction of released energy into phonon excitation whereas other detectors like the scintillator lose a fraction of this energy into heat.

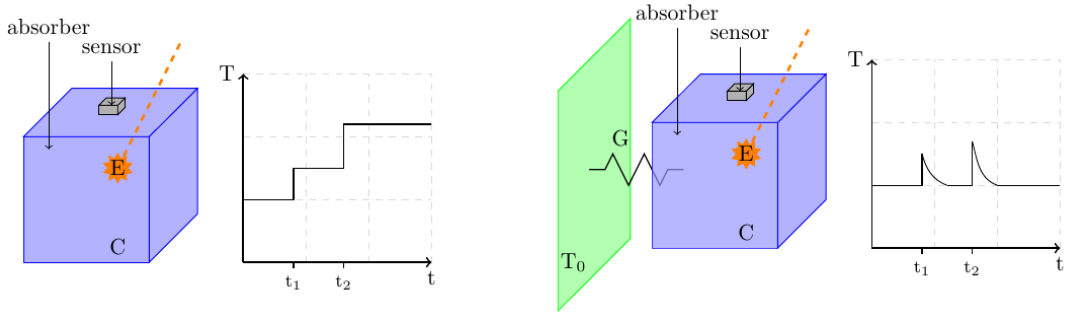

FIGURE 2.1: Schematic view of the working principle of a bolometer and the importance of the heat sink. *Left panel*: the bolometer is not linked to a thermal bath; the plot shows the temperature versus time. In this case, t_1 and t_2 represent the time of the energy deposition. *Right panel*: schematic view of the working principle of a bolometer linked to a thermal bath; the plot shows how the temperature recovers after each particle interaction thanks to the thermal bath. Figure from [84].

A bolometer is a low-temperature detector composed of three main elements: an absorber, a thermal sensor, and a thermal bath that keeps the system at low temperatures. The system is linked to a thermal bath because the detector needs to release the heat produced by the particle interaction in the absorber. In this way, after each interaction in the material, the detector will recover its initial temperature. Without a thermal bath, the detector will continuously warm up. A schematic view of these processes is given in Fig. 2.1.

The thermal sensor measures the rise in temperature ΔT induced by the deposited energy ΔE of an incident particle in the absorber. This temperature rise is described by the simplified equation:

$$\Delta T = \Delta E / C \tag{2.1}$$

where C is the heat capacity of the material that composes the detector. A schematic view of the working principle of this detector is shown in the right panel of Fig. 2.1. The working principle of a bolometer (also named in literature micro-calorimeter or thermal detector) allows to have:

- a wide choice of materials that compose the absorber and this is the key point to build a double readout bolometer that will be described later in this chapter;
- a low energy threshold and a high energy resolution. The minimum quantum excitation that transforms the energy release in the detector to phonons is very low, 10^{-5} eV at 100 mK, and it scales with energy [85];
- universal detector. The idea of the particle interaction detected as a rise of temperature implies, in theory, that a low-temperature calorimeter can detect any kind of interaction or particle.

It is important to point out that one of the drawbacks of this kind of detector is that they have a slow response and hence they are better adapted for experiments searching for rare events with a low signal rate, such as $0\nu\beta\beta$ decay searches. Another drawback of the bolometers is the necessity to operate them at very low temperatures, which requires cryogenic devices.

2.2.1 Energy resolution of a bolometer

As mentioned, bolometers can provide an excellent energy resolution (less than 1‰ at 2.6 MeV in most cases) when they are operated in good conditions in terms of the quality of the material used to construct the detector and the cryogenics employed to cool down. Like any other detector, several contributions cause the enlargement of a micro-calorimeter resolution. This limitation is drawn by the detector's thermodynamic fluctuation caused by the random exchange of phonons with the thermal bath. The energy excitation to produce a thermal phonon is $E_{phonon} = k_B T$, with k_B is the Boltzmann constant. From Eq. 2.1, the number of phonons is hence given by $N = C/k_B$. Therefore, the root means square (RMS) noise resulting from the internal energy is:

$$\Delta E_{int} = \sqrt{N} k_B T = \sqrt{k_B C T^2} \tag{2.2}$$

According to Eq. 2.2, the intrinsic noise of a $Li_2^{100}MoO_4$ crystal used by the CUPID-Mo experiment at 20 mK would be 17 eV, but this is not what we observe in practice. Another intrinsic noise contribution is the Johnson noise. It comes from the fact that the thermistor is a resistor with resistance R.
However, these two intrinsic noise contributions are not the main reasons for the observed spectral broadening. External noise contributions cause the enlargement of the detector resolution, such as the vibration from the cryogenic system where the detector is cooled down. These vibrations induce micro-phonic noise. Furthermore, electronic noise and temperature variations add extra spectral enlargement. In real life, the typical energy resolutions of the baseline of a bolometer are of the order of a few keV; for example, the median value of the baseline resolution of the CUPID-Mo detectors is 1.97 keV [86].

2.2.2 Absorber

The absorber is where the incident particle deposes its energy of interaction. The selection of the material that composes it is crucial because it will guide the ability to detect a signal from the nuclear event that occurs in the detector. Moreover, a wide choice of absorber material is available, which permits the embed of the $0\nu\beta\beta$ decay candidate and provides a very high detection efficiency (close to 100 %). Another critical point to consider when choosing a suitable material for the absorber is the heat capacity: it has to be low at cryogenic temperatures. The lower is the heat capacity C(T), the higher is the rise of temperature at a given energy release.

The heat capacity $C(T) = Mc(T)$ of a material, where M is the number of moles and $c(T)$ the specific molar heat, can be written as the sum of the lattice heat capacity $C_l(T)$ and the electrons heat capacity $C_e(T)$ at low temperature: $C(T) = C_l(T) + C_e(T)$. The absorber is usually a dielectric and diamagnetic crystal because only the lattice specific molar heat contributes to $c(T)$ at low temperature following:

$$c_l(T) = \frac{12\pi^2}{5} N_A k_B \left(\frac{T}{T_D}\right)^3 \tag{2.3}$$

where N_A is the Avogadro number and T_D the Debye temperature.

As mentioned before, the selection of a given absorber will guide and drive the performance of the detector in terms of light yield and radio-purity. Furthermore, it is observed that the quality of the crystal that composes the absorber influences the detector performance. The impurities can cause an energy loss in the detection, and the poly-crystals give a slow detector response.

2.2.3 Thermal sensor

The thermal sensor acts like a thermometer that will register the rise of temperature released by the particle interaction. It is the element that will convert this rise of temperature into an electrical signal exploitable by the physicist. Several types of sensors are used where usually their observable is a physical quantity that varies when the temperature does. At low temperature, the particle event in the absorber can be registered using:

- **Neutron Transmutation Doped (NTD) Ge sensors**: it is a resistive sensor where the energy release in the absorber is seen as a resistance variation. The CUORE [87] and the CUPID-Mo experiments [86] are using NTDs. A detailed description of these sensors will be given later in the text since the bolometers studied in this thesis are equipped with NTDs;
- **Metallic Magnetic Calorimeters (MMC)**: the deposit of energy is measured via the measure of the magnetization. These sensors are used by several experiments searching for rare decays with bolometers such as the AMoRe experiment [63];
- **Transistor Edge Sensors (TES)**: they are based on the superconducting transition of a thin layer deposited on the absorber. They work at their transition temperature, and the particle interactions are seen by a strong resistance variation. Experiments such CRESST-III [88] are using this kind of thermistor.

NTD sensors

NTDs are made by doping critically a semiconductor (usually Ge) with thermal neutrons [89]. This is done by bombarding a pure germanium crystal with neutrons (at a nuclear reactor), which produces dopants: ^{75}As from the β decay of ^{75}Ge

and ^{71}Ga from the electronic capture of ^{71}Ge. The doped crystals are then cut in small parallelepiped, which makes the NTDs nicely reproducible. In theory, this is an excellent and convenient feature to have a large number of identical and well-performing bolometers for a ton-scale experiment, but the reality is quite different. To have identically performing NTDs, the doping must be homogeneous along with the crystals, which is very hard to achieve in practice.

To characterize the performance of an NTD, we use the sensitivity that gives crucial information on the ability of the thermal sensor to transform the temperature variation in the crystal into a measurable resistance variation. It is defined as:

$$A = \frac{dlog(R(T))}{dlog(T)} = \frac{T}{R}\frac{dR(T)}{dT} \tag{2.4}$$

The sensitivity of the NTD depends strongly on the concentration of dopant impurities and hence the doping. Indeed, the higher is the concentration of impurities, the lower is the resistivity of the semiconductor, which can create energy levels below the conductance band or above the valence one. Beyond the Metal-Insulator-Transition (MIT) concentration, the behavior of the doped crystal becomes metallic and completely independent of the temperature. For low dopant concentration, the dopant behaves as an insulator at low temperatures. For a concentration just below the MIT, the dopant becomes close to the metal-insulator transition. This allows the material to change its properties as a function of the temperature. At very low temperatures (T<10 K), the conduction in the dopant is due to a quantum-mechanical tunneling effect through the potential barriers separating the dopant sites. This conduction regime is named Variable Range Hopping (VRH) and is characterized by phonons "jumping" between two energetically separated sites. In this case, the variation of the resistance as a function of the temperature is given in Eq. 2.5 where $\gamma = 1/2$. NTDs are characterized by their T_0 and R_0 that can be extracted experimentally.

$$R(T) = R_0 exp\left(\frac{T_0}{T}\right)^{\gamma} \tag{2.5}$$

In the detectors studied during this thesis, the resistance variations of the NTDs are measured via electrical contacts done with gold pads deposited on the two opposite sides of the NTD. Usually, the readout is done with a fixed current, so the voltage varies to get the information about the signal.

2.2.4 Heater

As bolometers are cryogenic detectors, they are submitted to cryogenic devices, which can affect their performances. These devices are subject to temperature variations that act on the detector's thermal response and provoke a shift in the amplitude. Due to the temperature variations, the thermal response can slightly differ for the same energy deposit, leading to a drift in the baseline, which can cause an energy resolution enlargement. It is shown that correcting this drift can significantly improve the resolution of the detector [90]. For this purpose, bolometers are usually equipped with the so-called heater. It is a heavily doped silicon chip glued

directly on the absorber, used to inject permanently pulses at given energy with a similar shape to the physical pulses. These pulses are used to stabilize the baseline response offline. A description of the stabilization procedure will be provided in Chapter 5.

2.3 Scintillating bolometers

The component of the bolometer, the absorber, provides freedom in choosing a crystal that can scintillate and contain the $0\nu\beta\beta$ decay candidate. It is possible to take advantage of this scintillating light by collecting it with the help of an auxiliary bolometer. This provides a double readout detector: a scintillating bolometer.

The use of luminescent bolometers by reading out the emitted light from the crystal was first introduced for solar neutrinos experiments in the 1980s [91]. In the early 2000s, a proposal to register the scintillation light with the help of an auxiliary bolometer was made [92]. The idea was to use scintillating crystals where the embedded $0\nu\beta\beta$ decay candidate has a $Q_{\beta\beta}$ higher than the endpoint of the natural γ radioactivity at 2.6 MeV to overcome both the surface α and the natural γ background. [93].

2.3.1 Why using scintillating bolometers?

As seen in Chapter 1, the control and the knowledge of the background is very important regarding the fact that the $0\nu\beta\beta$ decay signal is a peak over a flat background. Of course, the "flat background" is not that flat in real life and needs to be reduced and rejected. The dominant background above 2.6 MeV is coming from α particles: even if the $Q_{\beta\beta}$ of the candidate isotope is higher than 2.6 MeV, the background remains dominant. This was highlighted by the CUORE experiment [94] where the background model showed that the dominant component in the ROI is the energy-degraded α particles that originate from the materials around the detectors or from their surface. Therefore, it was important to develop a technology that reduces and rejects the background coming from α particles. This is the aim of the CUPID experiment, which is the CUORE upgrade with the possibility of particle identification based on scintillating bolometers. This particle identification provides a strong weapon to mitigate the background in the ROI. One of the baseline parameters of CUPID is to reach 10^{-4} counts/(keV.kg.yr) in the ROI [95].

A scintillating bolometer is based on a simple idea where the absorber of the main bolometer, made of a crystal scintillator, is coupled to an auxiliary thin bolometer to detect scintillation signals. The simultaneous detection of the deposited heat and the emitted light caused by a particle interaction in the crystal allows discrimination between different types of particles. This is possible because the emitted light is different for α and γ/β events for the same energy. The dual readout provides two distinct particle bands in practice: the γ/β band and the α band. A scheme of these bands is given in Fig. 2.2 where it is clear that a light yield cut can be applied to reject α events from the ROI.

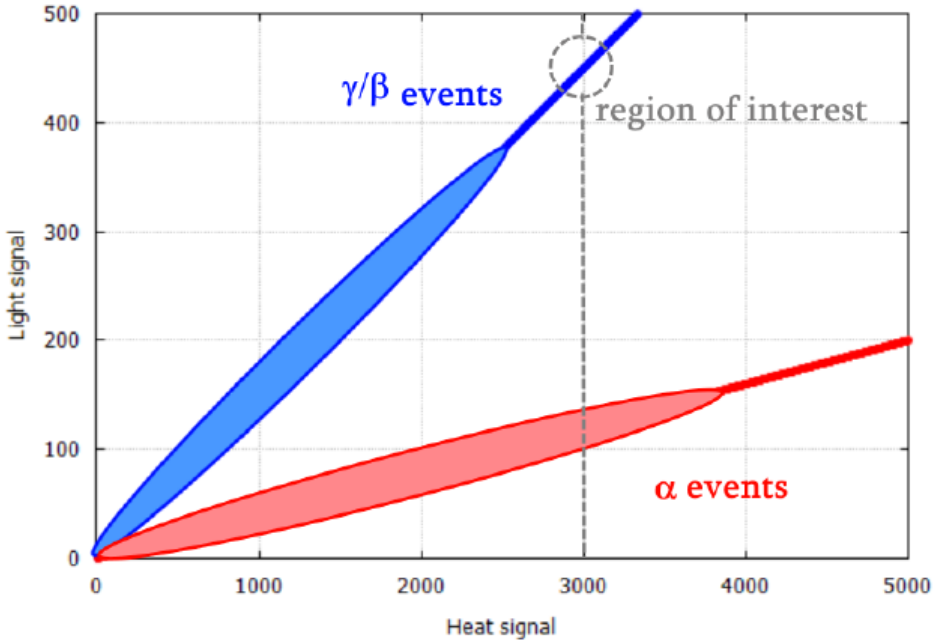

FIGURE 2.2: Schematic scatter plot: the light signal is represented on the y axis and the heat signal is represented in the x axis.

2.3.2 Scintillation mechanism

The scintillation mechanism of inorganic crystals is a complicated and not fully understood process. It uses the fact that the scintillating material contains different bands (valence and conduction bands). The mechanism is triggered by an energy deposition, and it is usually described as follows [96]:

- a primary electron-hole pair (e-h) is created by the absorption of the deposited energy by the interacting particle in the crystal. The multiplication of the e-h pairs occurs via radiative and non-radiative processes and by inelastic electron-electron scattering. The thermalization of the e-h pairs arrives when the energy of the electrons becomes smaller than the ionization threshold: the electrons go toward the conduction band and the holes toward the valence band;
- usually, the position of the absorption is different from the final emission state. Hence the energy has to migrate to the luminescent centers;
- the last process occurring during the scintillation mechanism is the emission of a photon by the excited center.

A useful quantity to describe the scintillation light is the light yield (LY). It quantifies the efficiency to convert the energy deposited by an event in the crystal to an

emitted light (photon). It can be defined as follows:

$$LY = \frac{dL}{dE} \tag{2.6}$$

where E is the total energy deposited and L is the amount of produced light by scintillation. The light yield depends on the stopping power $\frac{dE}{dr}$ of the interacting particle. The active centers in the crystal are homogeneously distributed, but not the way they are excited: heavy particles (α, neutron,..) release their energy in a smaller volume than the light ones (γ, β,...). This can be quantified by the semi-empirical formula [97]:

$$\frac{dL}{dE} = \frac{S\frac{dE}{dr}}{1 + kB\frac{dE}{dr}} \tag{2.7}$$

where S is the scintillation efficiency and kB is the Birks factor that depends on the number of activation centers. Depending on the type of particle, Eq. 2.7 can be simplified into two limit cases:

- the case of light particles like γ and β that have a small stopping power

$$LY_{\gamma(\beta)} = S\frac{dE}{dr} \tag{2.8}$$

- the case of heavy particles like α that have a large stopping power

$$LY_{\alpha} = \frac{S}{kB} \tag{2.9}$$

This difference in the light yield is used to discriminate the different types of particles with scintillating bolometers. The discrimination capability is defined in Eq. 2.10, it is the so-called discrimination power $DP_{\gamma(\beta)/\alpha}$. It allows quantifying the fact that the discrimination power is higher when the distance between the $\gamma(\beta)$ and the α band is higher with small width for each band.

$$DP_{\gamma(\beta)/\alpha} = \frac{LY_{\gamma(\beta)} - LY_{\alpha}}{\sqrt{\sigma^2_{\gamma(\beta)} + \sigma^2_{\alpha}}} \tag{2.10}$$

The quenching factor of α particles with respect to $\gamma(\beta)$ ones is defined as the ratio between their two light yields:

$$QF_{\alpha/\gamma(\beta)} = \frac{LY_{\alpha}}{LY_{\gamma(\beta)}} \tag{2.11}$$

2.3.3 Standard and enhanced Light Detectors

In this thesis, the scintillating bolometers studied are coupled to high purity Ge-based light detectors (LD) operated as bolometers to register the scintillation light. These thin bolometers are usually coupled to smaller NTDs to enhance the sensitivity (about a few hundreds of nV/keV). The LDs are coated with SiO to reduce light

reflection by the Ge and increase the light collection. This anti-reflective coating is based on index matching [98].

The typical baseline noise of these detectors is less than 1 keV. An example of a light detector used in this work is shown in Fig. 2.3.

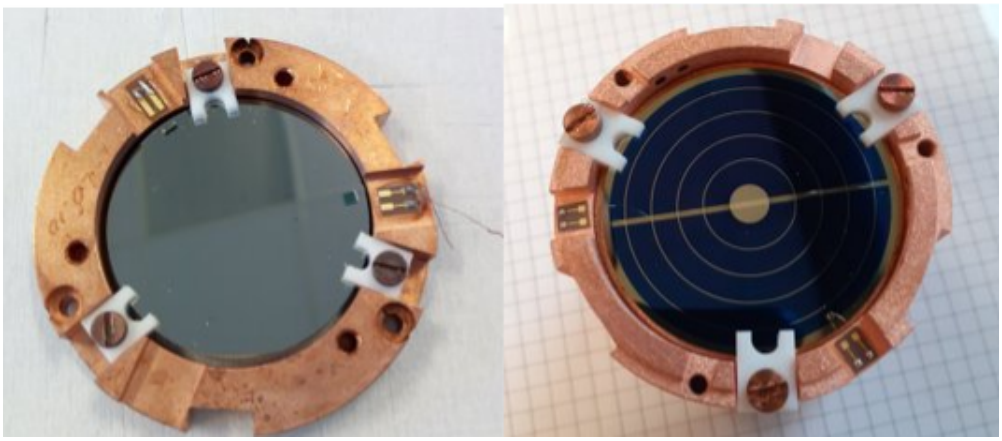

FIGURE 2.3: *Left:* standard Ge light detector. *Right:* Neganov-Trofimov-Luke light detector. In both detectors, a small NTD is glued on the edge.

It is possible to enhance the performances of the Ge LDs by boosting the signal using the Neganov-Trofimov-Luke effect [99, 100]. This effect is obtained when a semiconductor is placed in a stationary electric field, which amplifies the calorimetric measurement of the ionizing radiation at low temperatures. This electrical field is applied to the detector via aluminum electrodes evaporated directly on the Ge (see Fig. 2.3). With this method, the signal-to-noise ratio is improved thanks to the amplification of the signal. This kind of detector is required to register small light signals such as Cherenkov light [84]. When the detector is submitted to an electrical field generated by the voltage bias V_{el}, the deposited energy in the Ge E_0 will create electron-hole pairs that will drift under the effect of the electrical field. The total deposited heat in the LD, in this case, is written as:

$$E = E_0 + \eta \frac{qV_{el}}{\epsilon} E_0 \tag{2.12}$$

where q is the electron charge, ϵ is the minimum needed energy to create an electron-hole pair and η is a coefficient that takes into account the charge recombination and trapping. As mentioned, the Neganov-Trofimov-Luke effect provides better signal-to-ratio via a certain gain that characterizes a high number of produced electron-hole pairs when the energy of the incident photon is higher than the energy of the gap. This makes the calibration of a LD in a Neganov-Trofimov-Luke effect mode complicated as the gain depends on the energy of the event [84].

2.3.4 How to build a scintillating bolometer in the CUPID framework?

In this section, the basic steps to build a scintillating bolometer will be given. Each detector assembly has its specifications, but it always follows the same logic: holders cleaning, thermal sensor coupling, then detector mounting.
To build a bolometer, the first step is to connect the thermal sensor to the absorber. In our case, the NTD is glued directly on the crystal, usually with glue spots where the number of spots depends on the size of the NTD. For example, for the two enriched $^{116}CdWO_4$ detectors studied in this thesis (Chapter 5), the glue (Araldite® epoxy) spots were deposited on the crystals with the help of a mechanical arm that is shown in Fig. 2.4. The spots are deposited with the help of a pogo-pin matrix to make six homogeneous spots. To have the same thickness in all the spots and to avoid their merging, a Mylar® mask is used to keep a distance between the NTD and the crystal, as shown in Fig. 2.4. The full description of the gluing procedure will be given in Chapter 5. The use of glue spots avoids stressing the NTD and the crystal, which could happen during the cooling down due to the different thermal contractions of the glue with respect to the crystal and the thermal sensor. A thermal sensor is also glued on the LD with a similar procedure. To correct the pulse amplitude [90], a heater is also glued on the crystal.

Once the gluing is done, one can proceed to the assembly of the scintillating bolometer: the crystal is kept in a copper structure (clean with a special procedure that will be described in Chapter 5) with the help of PTFE (polytetrafluoroethylene) pieces. To increase the light collection, the crystal is wrapped with a reflecting foil. After that, the electrical connections are made with the help of gold wires. The LD is mounted in a copper structure (usually in the same one as the crystal) above the crystal and facing it to collect the scintillation light. Ideally, the crystal should have two LD facing it, one above and one below, to collect more light, but it is not always possible for practical reasons. The electrical connection for the NTD of the LD is also made with the help of gold wires. An example of a scintillating bolometer mounted during this thesis is shown in Fig. 2.5. In this example, we show an enriched $^{116}CdWO_4$ crystal and a light detector mounted in the same copper holder. Both bolometers are fixed with differently shaped PTFE pieces.

2.4 Output of a bolometer

2.4.1 Readout system

As mentioned earlier, the readout of a bolometer is at a fixed current, so the voltage can vary as a function of the signal. There are two ways to register the signal: one based on DC bias and the second on AC bias. A schematic of these two circuits is shown in Fig. 2.6. For the detectors studied in this thesis, both approaches were used: AC electronics for the EDELWEISS setup and DC electronics for the CROSS setup. These two cryogenic setups are described in Sec. 2.5.1.

- DC (direct current): the difference of potential across the NTD is set by connecting two load resistors R_L in series with $2R_L > R_{NTD}$ to have a constant

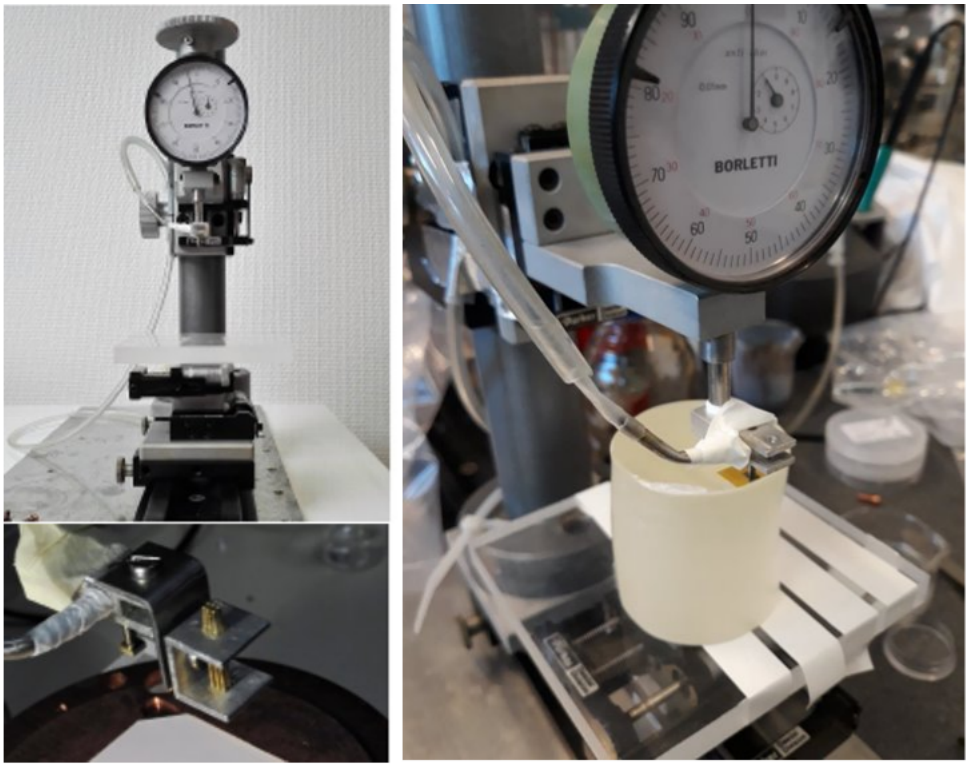

FIGURE 2.4: *Top left*: mechanical arm used to perform NTD gluing. *Bottom left*: pogo-pin matrix made of 6 pins used to deposit the glue the spots. *Right*: The mechanical arm pressing on a thermal sensor (NTD) glued on a $CdWO_4$ crystal. A Mylar® mask is used to ensure a gap between the NTD and the crystal.

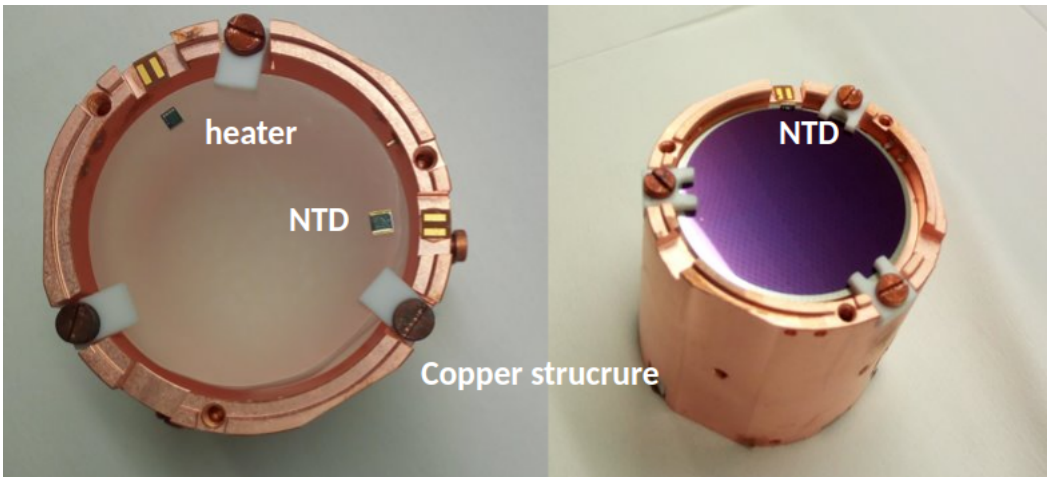

FIGURE 2.5: A scintillating bolometer assembled. *Left:* the crystal is mounted in the copper holder and fixed with the help of PTFE pieces. *Right:* the LD fixed in the same copper holder as the crystal and facing it.

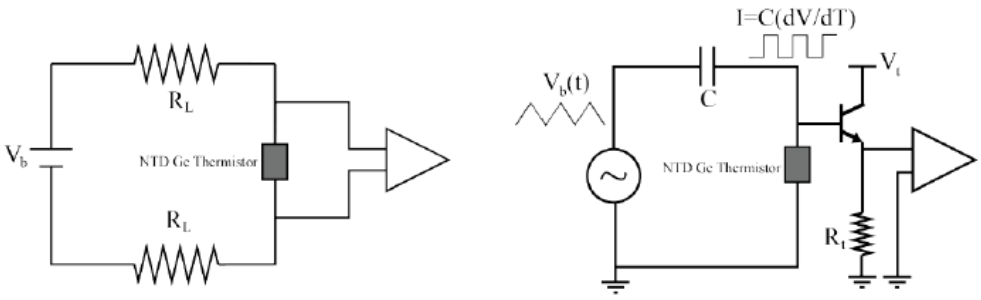

FIGURE 2.6: Scheme of the bias circuit for the NTD readout with DC circuit on the *left* and AC circuit on the *right* [102].

current flow in the circuit. The bolometer output is connected to an amplifier. In this approach, all the front-end electronics are operated at room temperature. The connection between the sensor and the front-end is made inside the cryostat using two twisted wires.

- AC (alternating current): the NTD is biased with a square wave current, which is obtained via a triangular wave through a load capacitor, as shown in Fig. 2.6. Thus, the NTD is fed with constant power. Using the modulation theorem [101], the frequency of the signal is shifted into a high-frequency range. This range is free of low-frequency noise components that deteriorate the signal. However. data processing requires deconvolution of the modulation to reconstruct the true signal.

2.4.2 Detector response

When a particle interacts in the bolometers, a temperature rise occurs, and the readout registers a thermal signal. The thermal signal has two main components. The first one is the region where the signal rises and can be described as the time needed by the deposited heat to reach the NTD. This time is called the rise time, it is measured between 10% and 90% of the total amplitude of the signal and represents about 10% of its total time length. The second component is the region where the amplitude of the signal goes back to the noise level and is measured between 90% and 30% of the total amplitude of the signal. This decay time encloses the information about the thermalization of the NTD to the heat sink. A schematic view of a thermal pulse with its two-component is given in Fig. 2.7. The shape of the pulse is influenced by the heat capacity and the conductance of the detector, the applied biased current, and the temperature of the heat sink. The output signal that we measure does not have a pure thermal pulse shape because it has an extra component due to the noise. It is time-dependent and can be written as follows:

$$s(t) = A_0 f(t) + n(t) \tag{2.13}$$

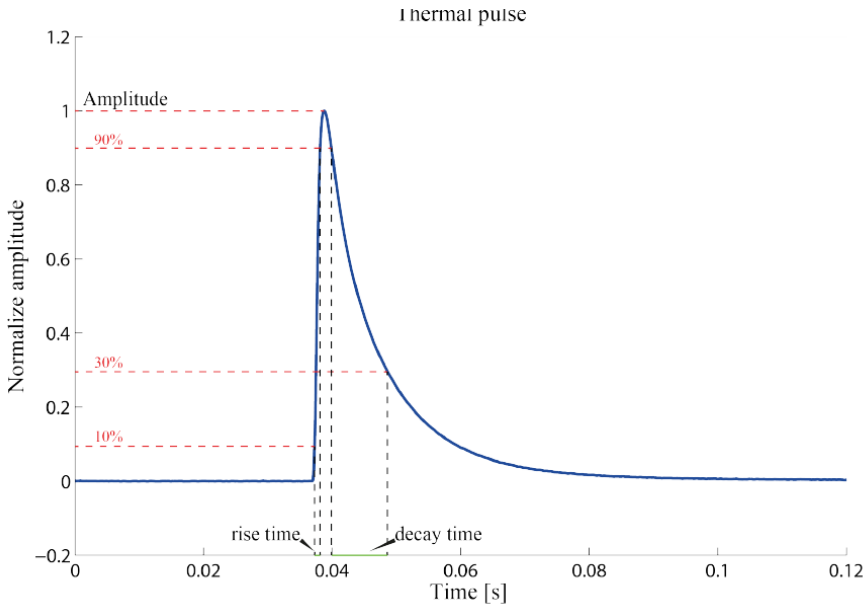

FIGURE 2.7: Scheme of a thermal pulse.

where A_0 is the amplitude of the signal and n(t) the noise component.

It is necessary to maximize the signal-to-noise ratio to extract all the valuable information from the output signal. An effective treatment to the output signal is optimal filtering.

Optimal filtering

From Eq. 2.13, the obtained signal at the end of the readout system has a noise contribution: it contains frequencies that deteriorate the information about the particle interaction in the detector. To get rid of those unwanted frequencies, we use the Optimal Filtering (OF) technique.

The OF of the data presented in this thesis was performed using the Gatti-Manfredi algorithm [103] which requires the knowledge of the detector response and noise. It is an adaptive filter that maximizes the signal-to-noise ratio. It is commonly used in the data analysis of bolometric detectors. The signal-to-noise ratio (SNR) is defined as the ratio between the maximum noise-free signal amplitude and the RMS of the noise in the frequency domain. The following equation translates this:

$$SNR = \frac{2\pi A_0 \int_{-\infty}^{+\infty} f(\omega) H(\omega) e^{i\omega t} d\omega}{\sqrt{\frac{1}{2\pi}} \int_{-\infty}^{+\infty} n(\omega) H(\omega)^2 d\omega} \tag{2.14}$$

The SNR is expressed as a function of the Fourier transform of the signal f(ω) and the noise n(ω) weighted by OF transfer function H(ω) that can be written as:

$$H(\omega) = constant \frac{f^*(\omega)}{n(\omega)} e^{i\omega t} \tag{2.15}$$

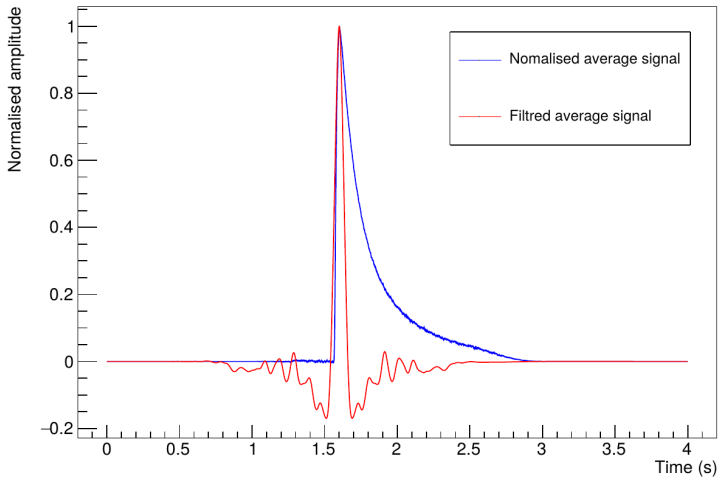

FIGURE 2.8: Average signal of the heat channel of a $CdWO_4$ scintillating bolometer before (blue) and after (red) applying the OF.

This transfer function is based on the spectral analysis of the average noise and signal of the detector. The optimal filtering does not preserve the signal shape but it permits a good reconstruction of the amplitude which contains the information about the energy of the interaction. An example of the effect of the OF on an average 2-s signal for a detector studied in this thesis is shown in Fig. 2.8 where the filtered signal has a quasi-symmetric shape.

2.5 Underground facilities

As mentioned, scintillating bolometers are cryogenic detectors that need to be kept at temperatures of the order of few tens of mK. To reach such temperatures, dilution refrigerators (DR) are required to cool a considerable amount of detectors at the same time (large mass) using the thermodynamics of a cryogenic liquid. The DR is hosted by a setup called a cryostat. It is a complicated and complex setup that makes in practice skills in cryogenics and vacuum systems.

To go down from the room temperature at 300 K to the cryogenic one at 10 mK, the heat flow between these two temperatures needs high cooling power. To reach such power, the DR must be vacuum tight and shielded with several screens. Each screen corresponds to a lower temperature stage and prevents the detectors inside the cryostat from the black body radiation. The first screen would be the 300 K one, also known as the Outer Vacuum Chamber (OVC). The second screen is the first cooling stage at the liquid nitrogen temperature (T=77 K). The third screen corresponds to the liquid helium temperature (T=4.2 K), known as the Inner Vacuum Chamber (IVC). The base temperature is reached in the lower part of the cryostat through several steps described in the text. The last screen corresponds to the base

temperature, which is supposed to be the coldest part of the system and is called the mixing chamber (MC).

2.5.1 Working principle of a cryostat

The cooling down process to 10 mK can be roughly divided into two steps: the pre-cooling to 4.2 K and the cooling down to tens of mK.

Precooling to 4.2 K step

This step can be done via two different approaches, depending on the type of the cryostat: "wet" cryostat or "dry" cryostat. The precooling in "wet" cryostat is done using cryogenic liquids to reach 4.2 K. For this purpose, the DR is placed in a liquid helium bath which is very expensive. In some "wet" cryostats, it is possible to use liquid nitrogen to cool down to 77 K. One of the advantages of such devices is that they cause less vibrational noise on the detectors.
On the other hand, the precooling in the "dry" cryostat is done using a pulse tube which avoids the cost of cryogenic liquids. It is done as follows:

- the He gas is compressed in the pulse tube. This gas has higher pressure and temperature, it drifts to the warm part of the pulse tube and exchanges heat.
- an adiabatic expansion of this gas is done, which provokes the flow of the gas towards the cold part of the pulse tube.

One drawback of pulse tube cryostat is that it causes vibration, which adds extra noise to the detectors.

Cooling down to few tens of mK

Bolometers need to be cooled down to 10-20 mK. To go to such low temperatures, we use the properties of the ^{3}He-^{4}He mixture. This mixture flows inside the DR in a closed circuit and provides cooling power.
The main property of the ^{3}He-^{4}He mixture is: two phases coexist under particular conditions. These conditions are full-filled when the total concentration of the ^{3}He is higher than 6.5%, and the mixture is cooled down to 870 mK, temperature of the tri-critical point (see Fig. 2.9). One of the two phases is rich in ^{3}He and is called the "lighter concentrated phase", the second phase, rich in ^{4}He is called the "diluted phase". The concentration of ^{3}He in each phase depends on the temperature of the mixture. The enthalpy of ^{3}He in the two phases is different, which provokes the evaporation of this isotope from a phase to another. This evaporation provides an active way of cooling down. The quantum properties of ^{3}He and ^{4}He allow this process to occur even at the lowest temperature thanks to the finite equilibrium concentration of ^{3}He in the diluted phase. The evaporation of ^{3}He from the concentrated to dilute phase is how the last stage of the cryostat is cooled to 10-20 mK: the mixing chamber where the detectors are mechanically and thermally connected.

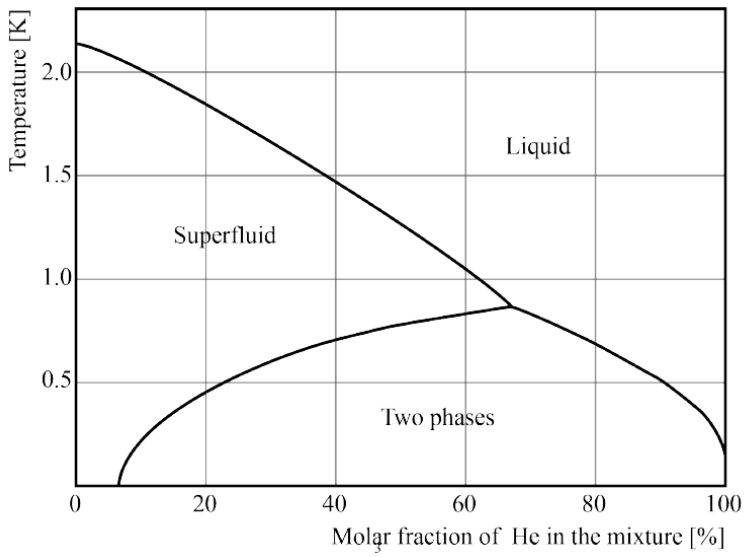

FIGURE 2.9: Phase diagram of the liquid ^{3}He-^{4}He mixtures at the saturated vapor pressure.

2.5.2 The EDELWEISS-III cryostat at LSM

The EDELWEISS-III (Experience pour DEtecter Les Wimps En Site Souterrain) cryostat [104] is located at LSM in the Frèjus tunnel that links France to Italy. This underground laboratory is one of the deepest in the world, with 1700 m of overburdened rock, which corresponds to 4800-meter water equivalent (m.w.e). This allows reducing the muon flux down to 5 muons/m^2/day.
The cryostat is installed in a clean room, and it was custom designed for dark matter searches and produced by the Néel Institute in Grenoble. It has a reverse geometry where the experimental volume is above the structure of the cryostat. This experimental volume can host up to 48 bolometers.

Concerning the cooling system, the EDELWEISS setup is a hybrid cryostat that uses the principles of both "wet" and "dry" cryostats. It needs to be periodically refilled with liquid He (LHe) during the pre-cooling phase. In addition, this cryostat is equipped with Gifford-MacMahon cryocoolers, which allows minimizing of the LHe consumption by reliquefying the cold vapor. To reach 20 mK, the setup requires about two weeks of cooling. A LHe refill is necessary every ten days, and the data acquisition needs to be stopped during this procedure. The cryostat is surrounded by active and passive shielding to protect the detectors from the natural environmental radioactivity, the neutron and the atmospheric muons that remain underground. The passive shielding consists of a first layer of 20 cm of lead with 2 cm thickness of roman lead in the inner part and a layer of polyethylene of 50 cm thickness. This shielding is enveloped by a muon veto made of 100 m^2 of plastic scintillator that acts as an active shielding. A scheme of the EDELWEISS setup shielding is shown in Fig. 2.10. Furthermore, as mentioned before, the cryostat is

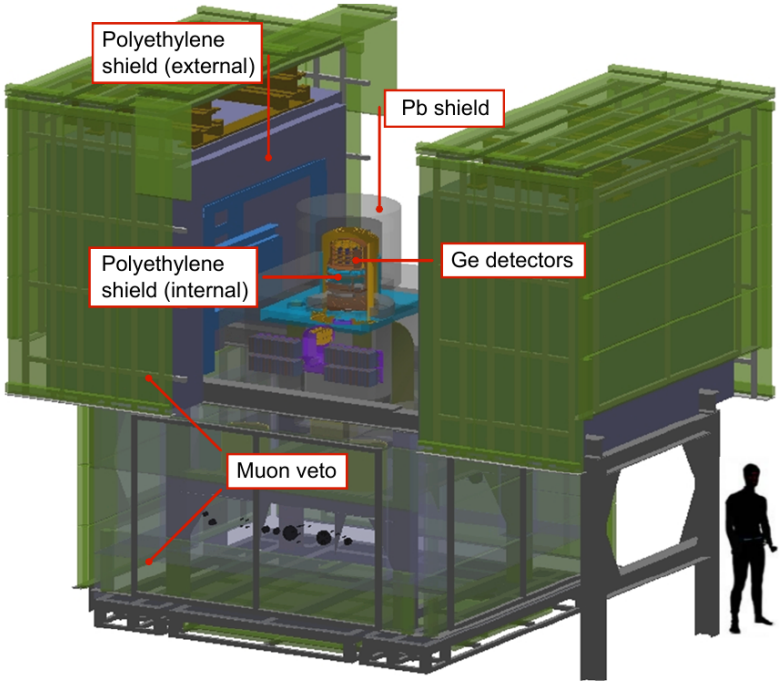

FIGURE 2.10: General view of the EDELWEISS setup at LSM [104].
The different layers of shielding are shown.

installed in a clean room where it is possible to flush radon-free air when the cryostat is open.

The calibration, in this setup, is done with an automatic system; a scheme of the position of the source is given in Fig. 2.11. It is possible to perform U/Th, ^{133}Ba and ^{60}Co calibrations with this system. The mixed U/Th is made of thorite mineral where the radioactive components are 50 Bq of ^{232}Th and 100 Bq of ^{238}U [86].
The electronics used for the data taking in this setup are AC-biased cold electronics. Room temperature electronics modules are installed outside the cryostat to have short cables to limit the noise pick-up [86]. These modules are called bolometer boxes, and they contain all the needed electronics to register the signal that comes out of the NTDs.

The CUPID-Mo detectors and one enriched $^{116}CdWO_4$ scintillating bolometer were installed in this setup and took science data from March 2019 and July 2020. The analysis and the performances of these detectors are presented in Chapter 3 and Chapter 5 of this manuscript.

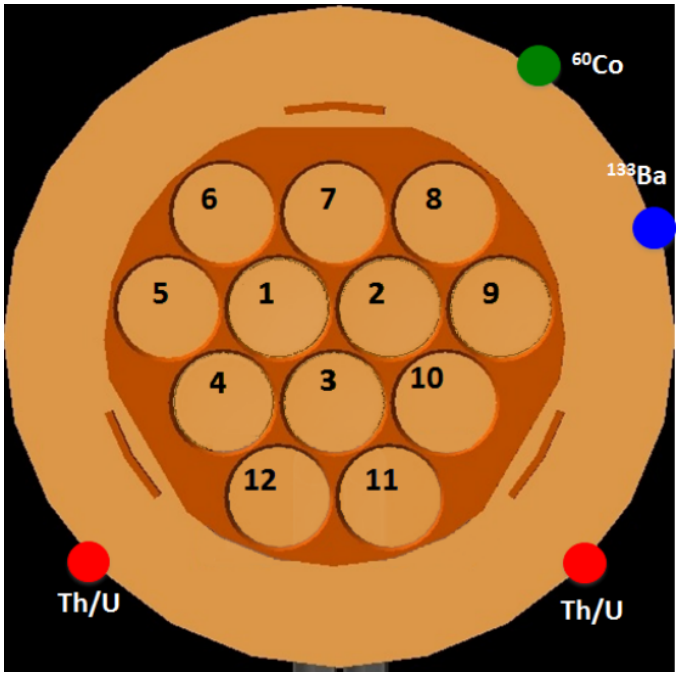

FIGURE 2.11: The position and types of calibration sources in the EDELWEISS setup [86]. The 12 slots where the detectors can be hosted are schematized, each slot can contain 4 bolometers.

2.5.3 The CROSS cryostat at LSC

The CROSS (Cryogenic Rare-event Observatory with Surface Sensitivity) Cryogenic Underground (C2U) facility is located at the Laboratorio Subterraneo de Canfranc (LSC) and was installed in April 2019. This underground laboratory is located in the Somport tunnel in the Spanish Pyrenees under 800 m of rock which corresponds to 2450 m.w.e.
The C2U setup is hosted in a Faraday cage with acoustic isolation. This cryogenic device is a pulse tube cryostat produced by Cryoconcept (France) [105]. It is coupled to an Ultra Quiet Technology (UQT) [106] where the head of the pulse tube is mechanically decoupled from the rest of the cryostat to reduce vibrations [105].
The cryostat shielding was build in several stages and is still under construction. In Fig. 2.12, one of the stages of the shielding is shown. This manuscript will describe the shielding as it is after the update done in July 2020. The experimental volume, where the detectors are placed, is surrounded by 25 cm of low radioactivity lead external shielding. To cover the gap that remains between the OVC and the lead shielding, we added 25 cm of lead bricks above the shielding around the cryostat. An additional 13 cm disk of a mix of copper and lead disk is placed between the dilution unit and the detectors. The C2U setup is also equipped with an internal lead shielding that consists of a layer of about 1 cm around the three copper screens that close the experimental space. The final C2U setup will be inside a plastic anti-radon box and surrounded by a muon veto.
In this setup, the calibration is performed using a wire of thorite inserted between

FIGURE 2.12: View of the CROSS cryostat and a 15 cm layer of lead shielding.

the external lead shielding and the OVC. The readout is done with low-noise room-temperature DC front-end electronics. Two scintillating bolometers studied in this thesis were installed in this setup and described in Chapter 5. This cryostat hosted a 12-crystal tower test for the CUPID R&D. This test will be presented in Chapter 6.

2.5.4 The Hall C cryostat at LNGS

The so-called Hall C cryostat is the CUPID R&D cryogenic facility located in Laboratori Nationali del Gran Sasso (LNGS) in Italy. It is called like that because it is installed in Hall C, one of the three main Halls at LNGS (A, B, C). The distance between each Hall is about 80 m, so the muon flux may differ from a hall to another. The muon flux in the Hall C was measured to be 3.14×10^{-4} muon/m^2/s [107].
The cryostat is a wet cryostat from OXFORD TL200 and was installed in the 1990s. It is shielded with two layers of lead of at least 10 cm each. The experimental space is protected against the radiations that could come from the dilution unit by 10 cm of roman lead. The cryostat is inside an anti-radon box and the whole system is hosted by a Faraday cage. Calibrations are performed using wires of thoriate tungsten inserted between the external lead shielding and the OVC of the dilution refrigerator. The signal readout is based on DC electronics. This cryostat hosted an 8 enriched $Li_2^{100}MoO_4$ crystals tower that will be described in Chapter 6.

2.6 Why using scintillating bolometers for $0\nu\beta\beta$ searches?

To build a scintillating bolometer for $0\nu\beta\beta$ decay searches, the absorber of the main bolometer has to be made of a crystal scintillator that contains the $0\nu\beta\beta$ decay candidate. This crystal needs to be equipped with a thermal sensor coupled to an auxiliary bolometer, the so-called light detector, to register the scintillation light. This detection technology provides excellent energy resolution and high detection efficiency since it uses the "source=detector" approach. Furthermore, the double readout heat-light allows reaching a very low background rate in the ROI at the level of 10^{-4} counts/(keV.kg.yr) [95].
In this thesis, scintillating bolometers based on $CdWO_4$ and enriched $Li_2^{100}MoO_4$ crystals are studied. In the following chapters, the results from the CUPID-Mo experiment using 20 enriched $Li_2^{100}MoO_4$ crystals on the $0\nu\beta\beta$ decay of ^{100}Mo are presented as well as the performances of three scintillating bolometers based on two enriched and one natural $CdWO_4$ crystal. Moreover, a description of two important CUPID R&D tests based on $Li_2^{100}MoO_4$ will be given in Chapter 6.

Chapter 3

The CUPID-Mo experiment

The CUPID-Mo experiment is a bolometric pilot experiment located at LSM that has taken science data from March 2019 to July 2020. There has been a commissioning run in 2018, the operation and tuning for the science data-taking campaign started in December 2018. The experiment is based on enriched $Li_2^{100}MoO_4$ scintillating bolometers to search for the neutrinoless double-beta decay of ^{100}Mo. The detectors were installed in the EDELWEISS cryostat. This chapter is dedicated to the description of the CUPID-Mo experiment, from the detector assembly and installation at LSM to the data analysis that has set the best upper limit on the half-life of the $0\nu\beta\beta$ decay of ^{100}Mo. The theoretical and experimental motivations to search for neutrinoless double-beta decay in ^{100}Mo are briefly discussed as well.

3.1 Searching for neutrinoless double-beta decay in ^{100}Mo

As presented in Chapter 1, the $0\nu\beta\beta$ decay of ^{100}Mo was investigated by several experiments. Most previous experiments studied this isotope in a foil with the help of tracking systems such as the NEMO-3 experiment. A simplified scheme of the decay for ^{100}Mo is shown in Fig. 3.1.

3.1.1 Framework and state of the art

The CUORE experiment demonstrated and emphasized two main points: it is possible to build a cryogenic ton scale experiment and it is crucial and mandatory to find a way to mitigate the background in the ROI where the surface alphas are dominant. Based on this, the CUPID experiment aims to identify and reject the background in the ROI with the help of bolometric germanium LD coupled to the crystal that contains the $0\nu\beta\beta$ decay isotope to collect the scintillation light (See Chapter 2 for a detailed description of a scintillating bolometer). In addition to the particle identification, CUPID will increase the isotopic mass of the $0\nu\beta\beta$ candidate using enriched crystals. To investigate the possibility of building a large scale experiment based on scintillating bolometers, two demonstrators have been built: CUPID-0 based on enriched $Zn^{82}Se$ crystals and CUPID-Mo based on enriched $Li_2^{100}MoO_4$ crystals.

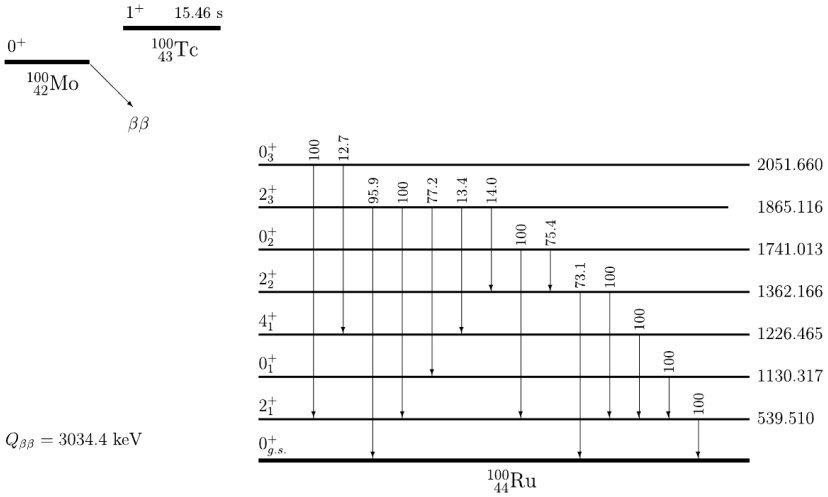

FIGURE 3.1: Decaying scheme of Mo^{100} [108].

The CUPID-0 experiment was located at LNGS and was composed of an array of 26 $Zn^{82}Se$ crystals arranged in towers [46]. This demonstrator has shown the feasibility and the robustness of dual readout calorimeters in background rejection. The measured background with 10 kg.yr of exposure was $3.5^{+1.0}_{-0.9} \times 10^{-3}$ counts/(keV.kg.yr) [46], it is the lowest background level ever achieved with a cryogenic calorimeter up to now. However, the energy resolution (20.05 ± 0.34 FWHM) at $Q_{\beta\beta}$ and the internal radioactivity level of the detectors did not fulfill the CUPID criteria (See Chapter 6).

On the other hand, the CUPID-Mo demonstrator based on the efforts and results of the LUMINEU (Luminescent Underground Molybdenum Investigation for NEUtrino mass and nature) experiment [109] has shown excellent detector performances in terms of energy resolution and radio-purity in agreement with the CUPID requirements using enriched $Li_2^{100}MoO_4$ crystals. Furthermore, using the technology developed by the LUMINEU collaboration, the CUPID-Mo demonstrator showed the ability to reproduce excellent detector performances in a large-scale 20 detector demonstrator experiment. These characteristics enable CUPID-Mo to not only demonstrate the technology for CUPID but to set leading constraints on the $0\nu\beta\beta$ decay of ^{100}Mo.

3.1.2 $Li_2^{100}MoO_4$ scintillating crystals

The experimental quest for $0\nu\beta\beta$ decay of ^{100}Mo using $Li_2^{100}MoO_4$ scintillating crystals was drawn by many tests and R&D. The first bolometric test of a Li_2MoO_4 crystal was done in 2009 at LNGS [110]. In 2012, the LUMINEU project started with the goal of developing crystals based on ^{100}Mo that could be used in a large-scale $0\nu\beta\beta$ decay experiment [109]. Two compounds containing ^{100}Mo were considered: $ZnMoO_4$ and Li_2MoO_4. They were compared in terms of crystal production, detector construction and performance [109]. Li_2MoO_4 crystals have been chosen to

be more suitable for a large-scale experiment, demonstrating better detector performances coupled to an easy production. The CUPID-Mo experiment, follow up of LUMINEU, has chosen enriched $Li_2^{100}MoO_4$ crystals.

The CUPID-Mo detector array is composed of 20 scintillating bolometers where the absorber of the main bolometer is made of enriched $Li_2^{100}MoO_4$ and the light detector is made of HP-Ge wafer. The array was installed in January 2018 at LSM where the detectors were successfully operated during the following summer (Commissioning I). During Fall 2018, several cryogenic issues occurred and cryostat maintenance was necessary. We took advantage of this delay to upgrade the assembly (see later in the text). The array was reinstalled in November 2018 and Commissioning II started over winter 2018/2019. After optimization of the detectors, CUPID-Mo collected science data successfully from March 2019 to July 2020.

3.2 The CUPID-Mo experimental setup

The 20 CUPID-Mo scintillating bolometers were arranged in five towers, each tower containing four detectors. The single module is composed of an enriched $Li_2^{100}MoO_4$ crystal and a LD, both equipped with NTD as thermal sensors. The crystal and the LD are assembled in the same copper housing. Special care was taken in choosing the materials to construct the detectors. Further cleaning is performed to avoid any additional radioactivity: the copper housing is cleaned with a procedure similar to the one described in Chapter 5 with chemical surface etching.

3.2.1 Detectors composition

3.2.1.1 $Li_2^{100}MoO_4$ crystals and Ge LD

In CUPID-Mo, each crystal has a mass of about 0.2 kg and a cylindrical shape with 44 mm of diameter and 45 mm of height. The total mass of the crystals is 4.158 kg with (2.258±0.005) kg of ^{100}Mo. Four of these crystals were previously used by LUMINEU [109]. The other sixteen crystals were fabricated with the same procedure used during the LUMINEU project [109]. All the crystals were produced at the Nikolaev Institute of Inorganic Chemistry (NIIC, Novosibirsk, Russia). A selection of high purity materials to grow the crystals were done: molybdenum, enriched at 97% in ^{100}Mo, previously used by the NEMO-3 collaboration [61] was purified, low radioactivity lithium carbonate and purified ^{100}Mo oxide was used. The crystals were grown via a double crystallization method using the low-thermal-gradient Czocharalski technique [95]. After the growing process, the crystal boules are sliced into cylindrical shapes. The surface of the crystals is polished and treated with radio-pure silicon oxide (SiO) powder [86].

Each $Li_2^{100}MoO_4$ crystal was coupled to a Ge bolometric LD to register the scintillation light. These LDs are made of high purity Ge wafer with a thickness of 175 μm and 44.5 mm. Each Ge wafer is coated with ∼70 nm of SiO as anti-reflective coating, increasing the light collection by 35% [98]. A small part on the edge of the

wafer was protected during the evaporation to leave it uncoated and facilitate the gluing of the thermal sensor.

3.2.1.2 Thermal sensors

The gluing of the sensors on the crystals and LDs was performed in 2017 in IJCLab clean room. The sensors used by CUPID-Mo for the crystals and the LDs were NTD sensors directly glued on the surface of the detectors. The NTD size for the $Li_2^{100}MoO_4$ crystals was $3\times3\times1$ mm^3. They were glued on the crystals with a tool similar to the one used by CUPID-0 [46] using a two-component epoxy resin (Araldite® rapid). As mentioned in Chapter 2, the NTD gluing on the main absorber is done with the help of six or nine glue spots to ensure a well-working detector, indeed, the performances of the bolometer are influenced by the quality of the gluing. To provide distinct glue spots, the NTD is kept 50 μm away from the crystal. The NTDs of five crystals used in LUMINEU [86] were glued with the help of six glue spots and nine spots were used for the remaining crystals.
In addition to the thermal sensor, the $Li_2^{100}MoO_4$ crystals were coupled to a silicon-based resistive chip to inject periodically a constant power that can be used offline to correct the pulse amplitude [90].

Concerning the sensors deployed for the LDs, smaller NTD sensors were used to take into account the small heat capacity of these thin wafers. The heat capacity of a $3\times3\times1$ mm^3 NTDs is reduced when diced to smaller pieces. The gluing is also performed using a two-component epoxy resin, but instead of using a spot matrix, a uniform veil of glue was applied. During Commissioning I, the size of the sensors was $3\times0.8\times0.4$mm^3. They were obtained by slicing a $3\times3\times1$ mm^3 in two directions (horizontal and vertical). The LDs equipped with these 1/6 of big NTD showed an unexpected high noise with a strong 1/f [Hz] component and high resistivity. In Commissioning II, the NTDs of LDs were replaced with NTDs of dimensions of $3\times1\times1$ mm^3 cut from $3\times3\times1$ mm^3 NTDs only in the vertical plane.

3.2.2 Detectors assembly and installation

The CUPID-Mo tower structure and the single module were designed to be compact and give the possibility to mount four single modules on a tower. The towers were designed to be suspended with the help of springs to reduce vibrations caused by the cryocoolers. Finally, the whole structure was arranged to provide a straightforward installation in the EDELWEISS cryostat. This was designed by the Service de Physique de l'État Condensé (SPEC) at CEA. The copper structure was produced by the mechanical workshop of IJCLab based on the design provided by SPEC and using highly radio-pure copper. A schematic view of the single module and towers design is presented in Fig. 3.2.

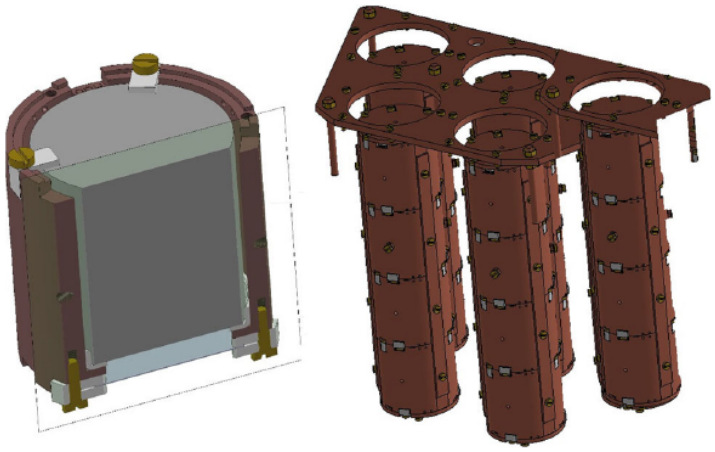

FIGURE 3.2: *Left:* CUPID-Mo single module design. *Right:* design of the CUPID-Mo towers. Each tower is composed of four single modules.

3.2.2.1 CUPID-Mo single module and tower

The CUPID-Mo single module is composed of: a single piece copper holder that hosts the $Li_2^{100}MoO_4$ crystal and the LD, PTFE pieces that keep the crystal and the LD in place, a reflecting foil to increase the light collection and Kapton gold pads to make the electrical contacts. The ingredients to construct the CUPID-Mo single module are shown in Fig. 3.3. The whole is mounted as follows:

- three small L shape PTFE pieces are placed at the bottom of the copper housing to support and decouple the $Li_2^{100}MoO_4$ crystal from the thermal bath (copper housing);
- the $Li_2^{100}MoO_4$ crystal is fixed from the top by three large L shape PTFE pieces fixed with copper screws, as illustrated in Fig. 3.4 (left);
- the LD is fixed with the help of three PTFE clamps facing the bottom of the crystal, as shown in Fig. 3.4 (right);
- Kapton with gold pads were glued on the copper holder and NTDs are bonded with 25 μm gold wires to readout the thermal signals registered by the NTD and acts as a weak thermal link to the heat bath.

The CUPID-Mo array is composed of five towers. Each tower is composed of four single modules mounted one above the other so that the three bottom crystals are facing two LDs, one from the top and one from the bottom. Only the top crystal does not have a top LD. The five towers are shown in Fig. 3.5.

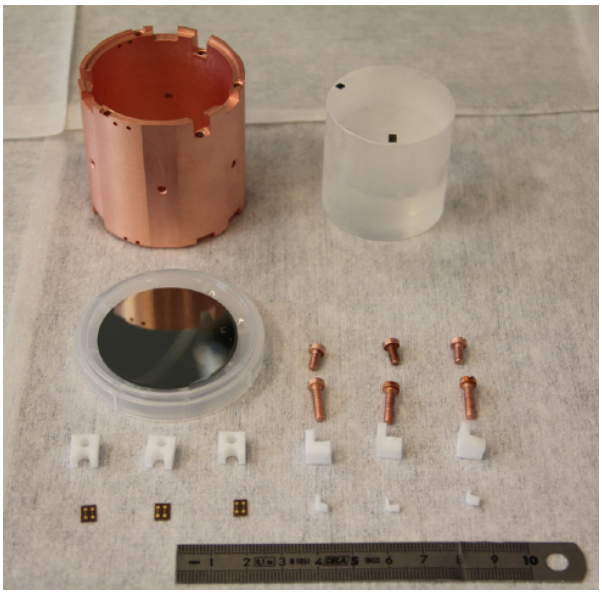

FIGURE 3.3: All components used to construct a CUPID-Mo single module: a copper housing, an enriched $Li_2^{100}MoO_4$ crystal equipped with NTD and heater, a LD equipped with NTD, different PTFE pieces to fix the detectors, copper screws, and Kapton pad for electrical contacts.

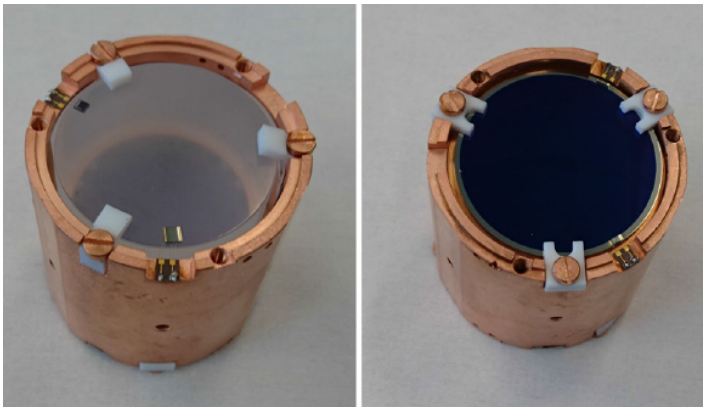

FIGURE 3.4: The CUPID-Mo single module. *Left:* the enriched $Li_2^{100}MoO_4$ crystal fixed in the copper holder with the help of PTFE pieces. *Right:* the LD mounted in the same copper holder as the crystal.

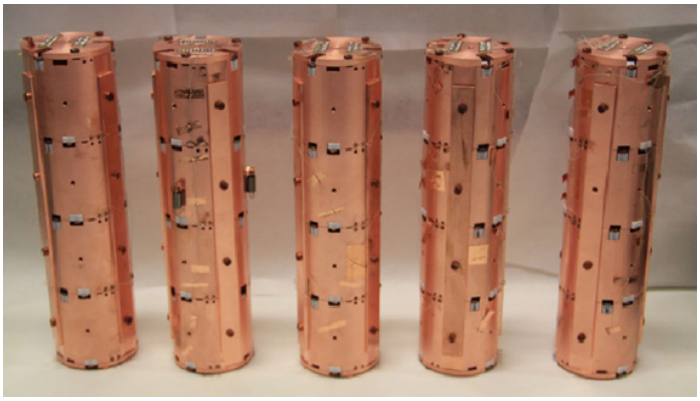

FIGURE 3.5: The five CUPID-Mo mounted towers.

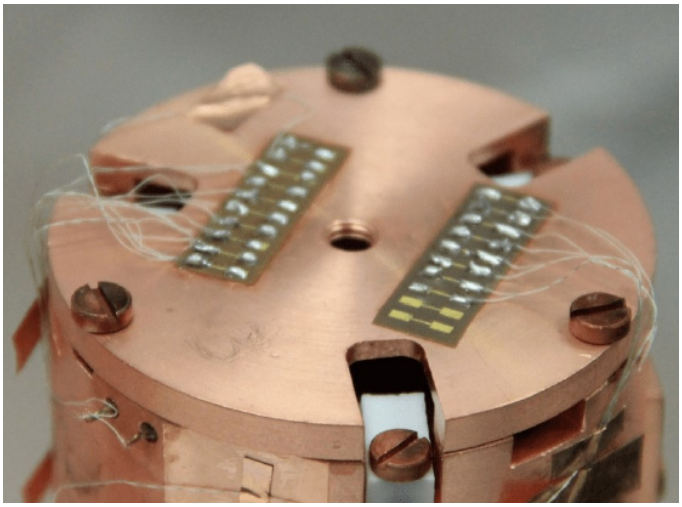

FIGURE 3.6: Details of the silk covered constantan twisted wires soldered on the top of a CUPID-Mo tower.

3.2.2.2 Wiring

The EDELWEISS wiring was updated with a dedicated wiring scheme to host the CUPID-Mo towers and 40 dual readout channels.

All the NTDs were bonded with gold wires on a flat Kapton pad glued to the holder (as mentioned in Sec. 3.2.2.1) with gold contacts to ensure the electrical signal readout. These gold wires also play the role of a weak thermal link to the heat sink. On the other side of the Kapton pads, silk-covered constantan twisted wires were soldered. These wires, three per scintillating bolometer: 1 twisted wires from NTD of $Li_2^{100}MoO_4$ crystal, one twisted wire from NTD of LD and one from the heater of each $Li_2^{100}MoO_4$ crystal, were put along with the tower and soldered on the top of it on large glued Kapton pads as illustrated in Fig. 3.6. On the other side of the pad, copper wires were soldered to be connected to the cold electronics.

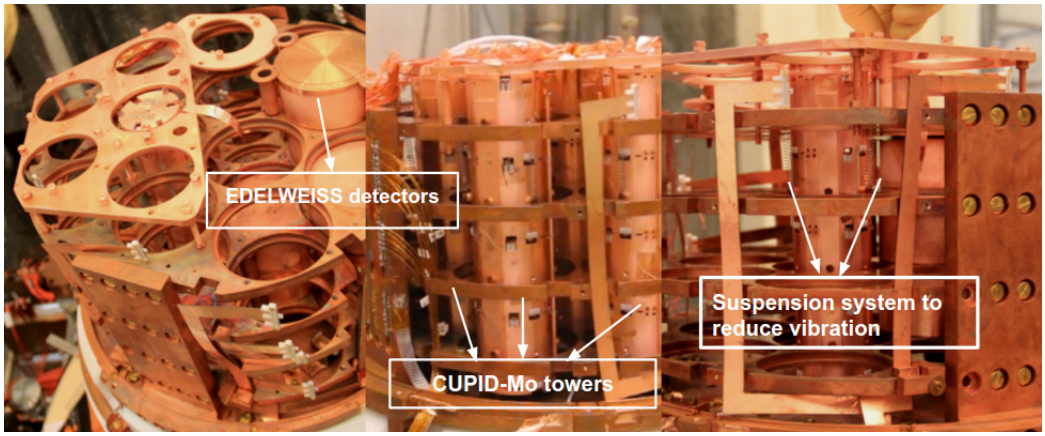

FIGURE 3.7: *Left:* EDELWEISS-III experimental space with the four floors mounted. *Middle:* the CUPID-Mo towers installed in the cryogenic facility. *Right:* the CUPID-Mo suspension system.

3.2.2.3 Installation in the EDELWEISS cryostat

The EDELWEISS setup, described in Chapter 2, contains four floors and twelve slots each, the CUPID-Mo towers were installed in five of these slots. It should be noted that a CUPID-Mo tower can only be installed in the experimental space once the EDELWEISS detectors are installed, as shown in the left panel of Fig. 3.7 and all the floors mounted. In this way, the CUPID-Mo towers can be inserted (see Fig. 3.7 middle). To mitigate the vibrational noise, the towers were mechanically decoupled from the EDELWEISS detector plate with the help of three stainless steel springs for each tower as shown in Fig. 3.7 (right).

3.3 Data analysis

In this section, a brief description of the CUPID-Mo data and its processing will be given. The results and the performances of the optimum triggering and the line-shape studies will be presented as well.

The CUPID-Mo detectors took data from March 2019 to July 2020. The data presented in this Ph.D. thesis have been acquired between March 2019 and April 2020, where the detectors were operated at 20.7 mK and 22 mK. We used 82% of the available data of this period to perform the $0\nu\beta\beta$ analysis. Data were split into 240 days of physics data and 73 days of calibration data. The physics data were divided into 10 datasets with similar operating conditions. Each dataset is about 1-2 month scale and contains background and U/Th calibration periods. We had to use 7 datasets out of these 10, reducing the number of days of physics data to 219. The 3 rejected datasets had short calibration periods. After cleaning up the data from disturbances periods and rejecting one bad performing scintillating detector [86], the total exposure used for the $0\nu\beta\beta$ analysis presented here is 2.16 kg.yr. The analysis and the results obtained from this analysis were published in [48].

3.3.1 Data production

The CUPID-Mo data were acquired as a continuous stream with a 500 Hz sampling frequency. The pulse amplitude is estimated using the optimum filtering technique [103] to maximize the signal in the 3-s pulse window used for both $Li_2^{100}MoO_4$ (LMO) crystals and LDs. The basic steps to produce calibrated data ready to be analyzed for each dataset are summarized as follows:

- data are first triggered with a specific triggering technique described later in the text;
- data are then run through a step called preprocess where few basic parameters are evaluated, such as the baseline parameters and the number of pulses. The baseline parameters are evaluated for each event in the first 3/4 of the pre-trigger. Two of the used baseline parameters in the CUPID-Mo analysis are the baseline and the baseline slope. The baseline parameter, given in mV at the end of the preprocessing, is the NTD output proportional to the operating temperature if the offset is constant. The baseline slope is computed by fitting the pre-trigger with a first-order polynomial;
- the average pulse (AP) and the average noise power spectrum (ANPS) are evaluated. To build the ideal/average pulse, good particle events are selected for each channel using calibration data. Several filters are applied to select a pure particle event. Only events with a single trigger, with a specific value of the baseline slope, are accepted to construct the AP. In addition, particle events with too low amplitude are discarded as the signal's shape is more subject to noise fluctuations. In this way, the AP is a pure particle signal template. The average noise is built using background data where a random trigger selects the noise events that do not contain any pulse;
- the signal's amplitude is evaluated by filtering the signal using the optimum filtering technique [103]. Before the filtering, the amplitude of the signal is defined as the elevation of the triggered pulse from the baseline level;
- the pulse amplitude of LMO channels is corrected with a linear stabilization using the filtered amplitude of the signal around the ^{208}Tl peak in calibration data versus the baseline. The baseline is used as a proxy for the temperature of the detectors. The temperature variations can be observed via baseline drifts. The 2615 keV peak from all calibration data of a dataset is used to establish a linear gain-temperature/baseline dependence, which is then used to correct all data for a slow thermal drift of the detector. This linear fit is then applied to background data;
- the LMO channels are calibrated using prominent peaks in the calibration data. The stabilized amplitude is calibrated with a second-order polynomial [48];
- the LDs are calibrated into two ways: cross-calibrated against the LMO signals and calibrated using the X-ray fluorescence [86] of the Mo or Cu that are

generated when the LMO crystals and the experimental setup are exposed to high intensity γ source;

- the light signals are triggered with the heat signals to search for coincidences. The detected light signals as a function of detected heat for the 20 CUPID -Mo scintillating bolometers are shown in Fig. 3.8.

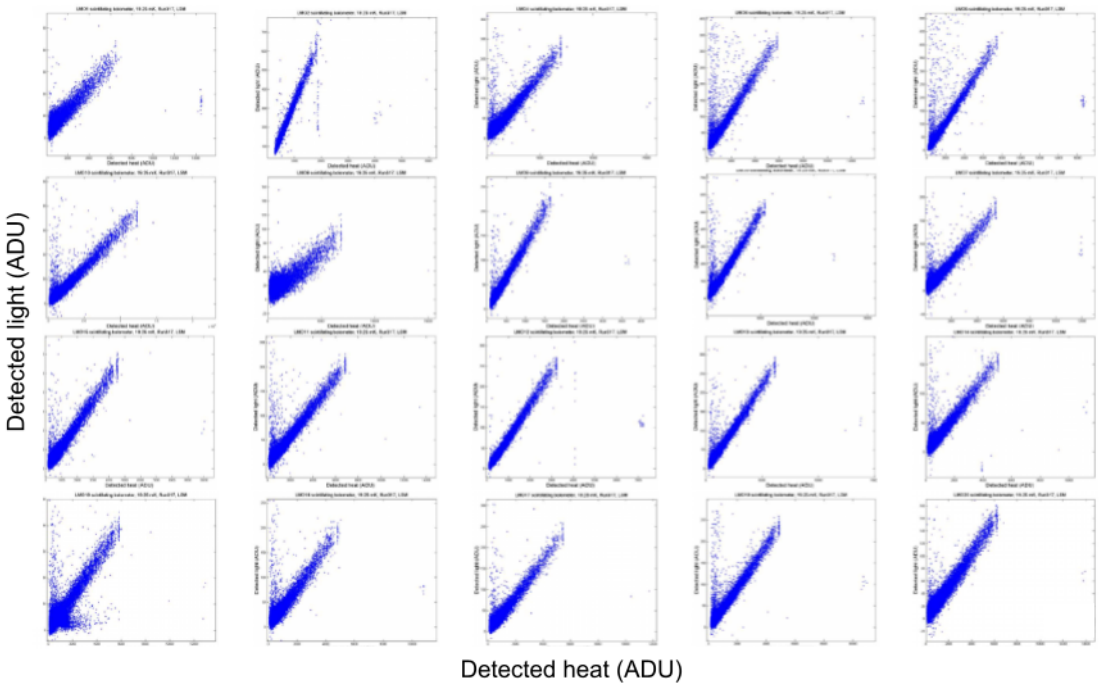

FIGURE 3.8: Light versus heat signals scatter-plots for the 20 LMO scintillating bolometers for calibration data during the commissioning.

- Pulse shape discrimination in LMO was performed using Principal Component Analysis (PCA), based on filtering the particle events from the pile-up by looking at the pulse shape. PCA is a multivariate technique that allows the analysis of a data set with correlated variables. It is based on projecting multidimensional data onto a new basis with a new coordinate system in which the components are ordered according to how strongly they explain the variance of the data. The leading PCA component explains the signal-like events and the other explains the noise-like events in the data. The details of how this analysis was performed with the CUPID -Mo detectors are presented in [111]. The cut optimization was performed with a sample of calibration data between 1 and 2 MeV. The first component of the PCA indicates the shape of the signal event. The pulse shape variable used to reject irregular pulses was defined as the reconstruction error [111] that quantifies the discrepancy between the actual pulse from the data and the reconstructed one from the PCA.

The CUPID-Mo data were analyzed using a software called DIANA. This software was developed by the CUORE-0 [112], CUORE [94] and CUPID-0 [46] collaborations. It includes a wide choice of packages that suit the analysis of a large array of detectors. It is based on C++ and uses ROOT libraries. DIANA also contains a PostgreSQL database to keep track of the detector array, electronics, and settings.

The continuous time-stream CUPID-Mo data is converted from a binary format into a specific ROOT format, used by Apollo, the triggering software of the CUORE collaboration [94]. Using Apollo, the data can be re-triggered depending on the kind of analysis one wants to perform: it is possible to set a different trigger algorithm and a different triggering threshold. During the first data analysis campaign, the CUPID-Mo data were triggered using the default trigger set in Apollo: the derivative trigger (DT) [113] in which the trigger has to be tuned channel per channel. This trigger algorithm works on the derivative of the signal waveform. When this later exceeds the threshold in a given time window for a certain number of samples, the trigger fires. However, the derivative trigger efficiency is not very satisfying at low energy as the signal-to-noise ratio decreases. To improve the energy thresholds, the Optimal Trigger (OT) algorithm was used to re-trigger the CUPID-Mo data. This algorithm is based on the matched filtering technique [103] that was briefly described in Chapter 2. This technique is designed to estimate the amplitude of a signal, maximizing the signal-to-noise ratio. The transfer function of the signal is built from the discrete Fourier transform of the average signal and the noise power spectrum constructed from the DT analysis campaign. A signal is seen by the OT when its filtered amplitude is above a certain number of σ_{noise}, the resolution of the filtered noise. The use of the OT allows lowering the energy threshold of the detectors with respect to the ones achieved with the DT algorithm since the OT is based on triggering filtered waveforms that are less noisy. To trigger the data with the OT, average pulses and average noise power spectra have to be available from the previous triggering.

3.3.2 Optimal triggering energy threshold

In this section, the analysis procedure to evaluate the trigger efficiency and the energy thresholds of the CUPID-Mo detectors developed during this thesis will be described and the results obtained. The triggering algorithm and the trigger efficiency evaluation methods used here were first developed by the CUORE collaboration [114, 115].

3.3.2.1 Why do we need to evaluate the trigger efficiency?

The goal of the OT re-triggering is to lower the energy threshold for both LMO and LD channels. To know how effective was the OT re-triggering and how much we gained in energy thresholds, we must evaluate the trigger efficiency at low energy. In addition, the knowledge of the trigger efficiency at low energy is essential to set a common analysis threshold in all the detectors, used for the anti-coincidence

analysis (evaluating whether an event is caused by a single or multiple interactions). Indeed, a lower threshold allows to better discriminate between single and multiple interactions. This is also important for the construction of the background model which is based on higher multiplicity events. Moreover, knowing the trigger efficiency and energy threshold is crucial for the low energy analysis, such as dark matter searches that will be presented in Chapter 4.

3.3.2.2 How do we evaluate the trigger efficiency?

The procedure for the evaluation of the trigger efficiency makes use of simulated events of known energies. In CUPID-Mo, we cannot exploit the heater pulses as they suffer from cross-talk from the pulse injection and show modified pulse shapes compared to regular pulses from particle interactions. Therefore, we have to rely on simulated pulses injected in the data at the analysis level for this study. The main steps of this procedure are the following:

1. choose the configuration parameters, in particular, the sigma threshold, which is the number of the σ_{noise};
2. inject simulated pulses into noise events selected randomly;
3. run the OT algorithm on matched filtered windows;
4. verify how many events were seen by the trigger and check the trigger efficiency for each energy;
5. fit the efficiency curve and evaluate the energy threshold.

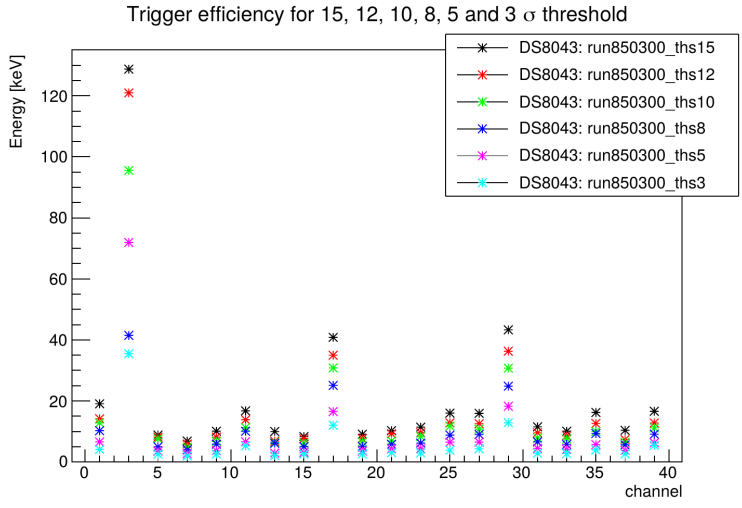

FIGURE 3.9: Energy thresholds as a function of the LMO channels for different sigma thresholds: 3 in cyan, 5 in pink, 8 in blue, 10 in green, 12 in red, and 15 in black.

The sigma threshold is the number of sigmas of the baseline noise σ_{noise} at which we want our trigger to fire for an event with this amplitude. To choose the best

suitable value to re-trigger the data for the $0\nu\beta\beta$ analysis, we evaluated the trigger efficiency for 3, 5, 8, 10, 12, and 15 σ_{noise}. In Fig. 3.9, an example of the effect of the number of sigmas of the baseline noise on the energy threshold that we obtain at 90% of the trigger efficiency. For the $0\nu\beta\beta$ analysis, we have decided to use a conservative sigma threshold and set it at 10 for both LMOs and LDs, this value can be set to a lower value at the expense of starting to trigger on noise excursion. An optimization for the low energy analysis is presented in Chapter 4.

The prerequisites before starting this study are the following: we need the AP and ANPS for each channel (both LMOs and LDs). We also need the stabilization and calibration parameters. In our case, we first used the AP, ANPS, stabilization, and calibration obtained from the DT triggering campaign to have a preliminary evaluation of the OT efficiency. Once all the data was re-triggered, we used the AP, ANPS, calibration, and stabilization parameters from the new re-triggering.

Inject simulated pulses

The pulse injection is done in the background data and is performed using a DI-ANA module where the list of the amplitudes that we want to inject into the data has to be specified in keV. The simulated pulses are artificial pulses constructed from the AP scaled a given energy. The algorithm to inject the simulated pulses in the data, for each channel, can be summarized as follows:

- the calibration and the stabilization coefficient, obtained from the previous processing, are used to compute the raw amplitude of the set of energies that will be injected;
- the average pulse is scaled to these raw amplitudes;
- in each noise event a simulated raw pulse is injected.

After that, the stabilization and the calibration coefficients used in the previous processing are applied to the simulated pulses. Examples of simulated injected pulses for LMOs and LDs are shown in Fig. 3.10.

Run the OT algorithm on a filtered windows

Once the injection part is done, the OT algorithm is applied to the simulated pulses. This step consists of building the same OF as in the re-triggering procedure and running it on the simulated pulses injected into the noise events. The OT fires when the filtered amplitude of a simulated event is detected within a ± 2 FHWM energy window of the maximum of a raw scaled AP that corresponds to one of the injected energies. At the end of the process, the number of noise events where the simulated pulses were injected and the number of simulated pulses triggered is saved for each injected energy and each detector. After that, the detection efficiency is estimated as the ratio between the total number of injected simulated events and the number of triggered simulated events at each energy.

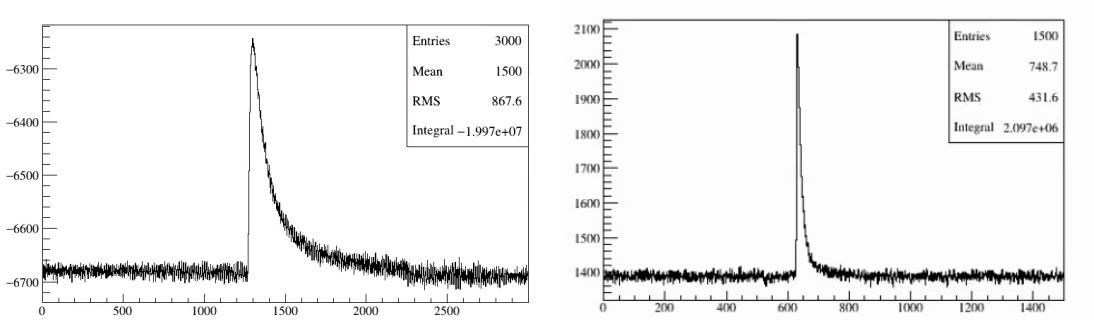

FIGURE 3.10: *Left:* simulated injected pulse at 150 keV on a LMO noise event. *Right:* simulated injected pulse at 12 keV on a LD noise event.

This pulse injection was performed in both LMO and LD detectors, first using

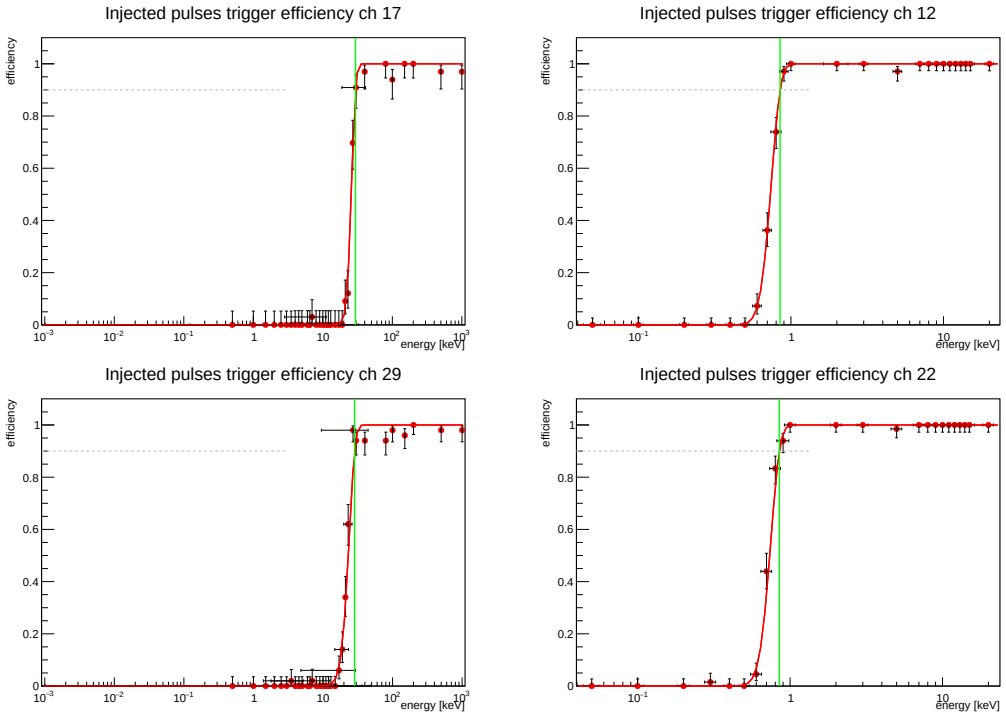

FIGURE 3.11: *Left*: example of trigger efficiency curve for LMO channels 17 and 29. *Right*: trigger efficiency curve for LD channels 12 and 22. The red dots are the trigger efficiency values for each entry, the solid red line represents the trigger efficiency fit curve and the solid green line indicates the energy threshold at 90% of the trigger efficiency.

the DT data to estimate the performances of the OT re-triggering and set the $0\nu\beta\beta$

analysis threshold. This was done on datasets 8037, 8038, 8040 and 8043. Furthermore, the evaluation of the trigger efficiency was re-performed once all the CUPID-Mo data were re-triggered using the OT algorithm in all the datasets using all the available exposure and the AP and ANPS obtained with the OT triggering.

Evaluation of the energy threshold at 90% of the trigger efficiency

To evaluate the energy thresholds for each channel on a run-by-run basis in each dataset, the saved numbers of injected pulses and triggered pulses are used. The energy threshold was computed at 90% of the trigger efficiency by fitting the energy of the injected events as a function of the trigger efficiency with an Erf(x) function and computing the optimum trigger energy threshold at 90%. Examples of trigger efficiency profiles for LMOs and LDs are shown in Fig. 3.11.

The results obtained from the evaluation of the trigger efficiency for the LMO and LD channels are reported in the following for each dataset.

LMO channels

Most of the LMO channels showed an energy threshold of less than 45 keV (except channels 3 and 25) in most datasets. In all the channels, we also observed a threshold fluctuation in the same dataset among the runs. This fluctuation is due to the fact that the noise changes from a run to another. An overview of the energy thresholds in each data set for all the LMOs channels is given in Fig. 3.12. Datasets 8040 and 8043 show a smaller spread in the energy threshold over the runs with respect to datasets 8037 and 8038 and this is due to the fact that these two datasets had more stable noise conditions. A comparison between the energy thresholds obtained with the OT and the ones obtained with the DT is shown in Fig. 3.13. The LMOs analysis and coincidence thresholds have been set to 45 keV for the $0\nu\beta\beta$ analysis well above the trigger efficiency turn on.

As mentioned, the trigger efficiency was re-evaluated once the triggering had been performed using the AP and ANPS produced during this campaign. No significant difference in the obtained energy threshold is expected when using the average pulse and average noise produced after the DT or the OT triggering. However, it is essential to know the actual energy threshold after the triggering because the two AP and ANPS produced after applying each trigger algorithm are slightly different. The results obtained are presented in Fig. 3.14. As with the DT data, a slight threshold fluctuation between the runs within one dataset is observed due to the noise fluctuations. We also find that these fluctuations are less present in some datasets thanks to more stable noise conditions.
OT energy thresholds performances can be summarized as follows:

- the threshold fluctuations for each channel are due to noise variations between runs and datasets;
- most of the LMO channels have a threshold lower than 45 keV ($0\nu\beta\beta$ analysis threshold) at 90% of trigger efficiency;

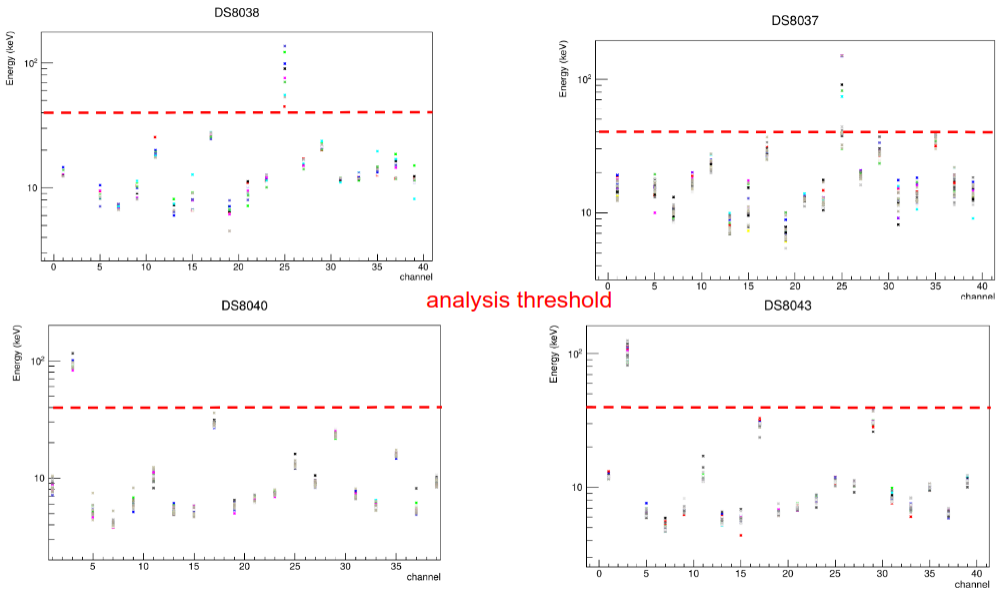

FIGURE 3.12: Energy threshold at 90% efficiency as a function of LMO channels using the DT data. The different colored points represent the different runs in the datasets. *Top left*: dataset 8038. *Top right*: dataset 8037. *Bottom left*: dataset 8040. *Bottom right*: dataset 8043.

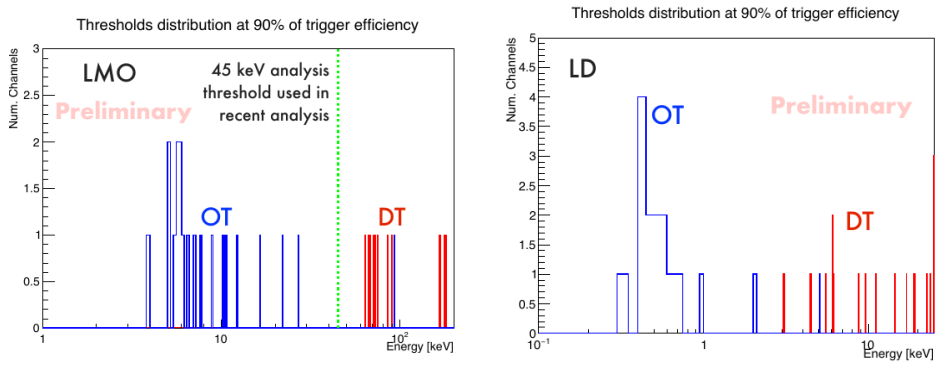

FIGURE 3.13: Comparison between the energy thresholds obtained with the OT algorithm and with the DT one. *Left:* comparison for LMO channels. *Right:* comparison for LD channels.

- the best (lowest) threshold achieved among the datasets are in datasets 8247 and 8248 (5-11 keV for most of the channels);
- channel-based thresholds show a consistent trend across the datasets.

The overall energy threshold distributions at 90% of the trigger efficiency, represented in the left panel of Fig. 3.15, for the LMOs gives a mean value of 15.4 keV and a median value of 8.5 keV. It should be noted that we had to reject one detector for having very bad performance (channel 3). Therefore, it was not taken into

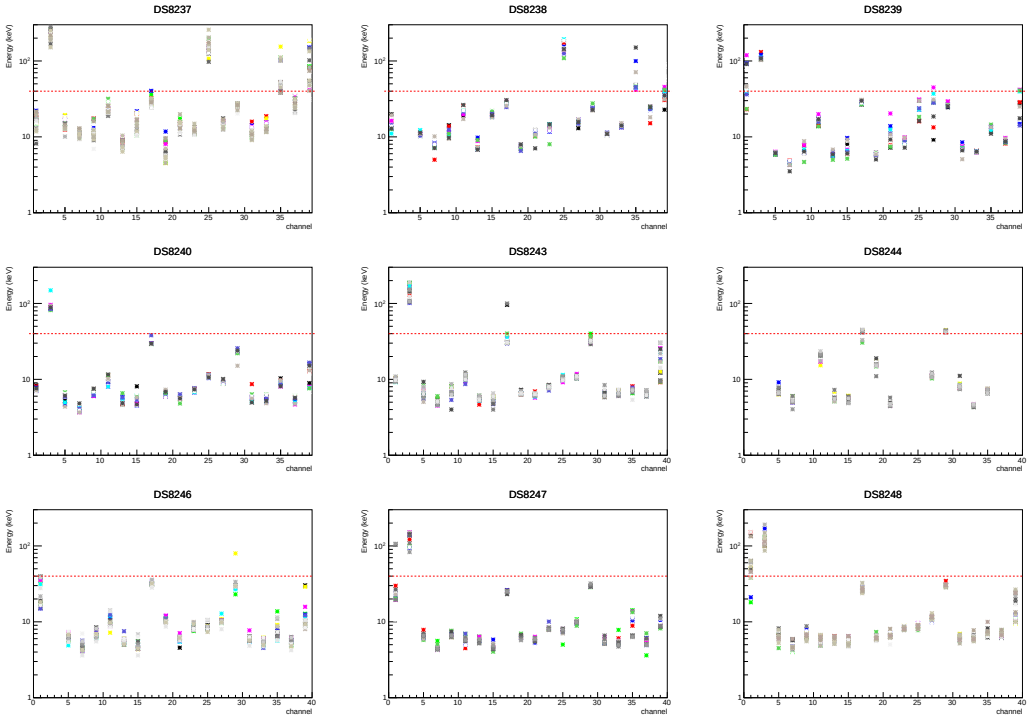

FIGURE 3.14: Energy threshold at 90% efficiency as a function of LMO channels for the all datasets where each colored points represents a run in a dataset. The horizontal red dashed line indicates the analysis threshold (45 keV). *Left column:* datasets 8237, 8240 and 8246 are represented. *Middle column:* energy thresholds for datasets 8238, 8243 and 8247. *Right column:* energy threshold for all the LMOs for datasets 8239, 8244, and 8248.

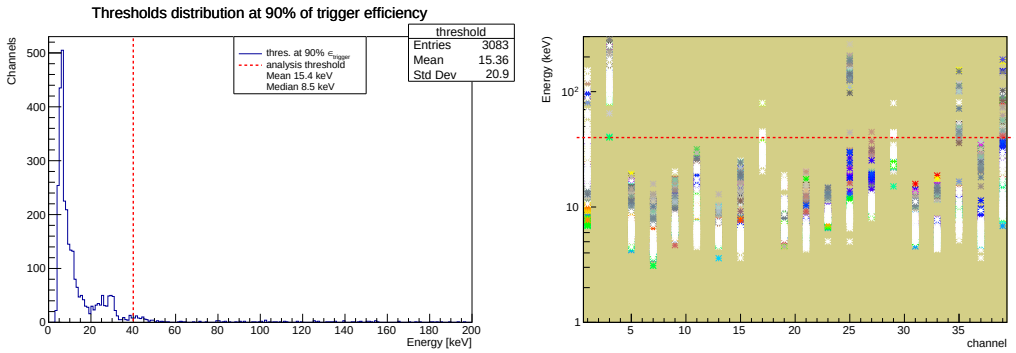

FIGURE 3.15: *Left:* overall energy threshold at 90% efficiency of the LMO channels for the all datasets. *Right:* energy threshold at 90% efficiency as a function of LMO channels for the all datasets.

account for the evaluation of the overall threshold distribution. In the right panel of Fig. 3.15, we represented the energy thresholds of all the runs in all the datasets

as a function of the LMO channels. This plot shows a slight difference in the energy thresholds between the runs due to the change of operating conditions. It also shows that some channels are relatively consistent and others have distinct populations like LMO 25, 27, 33, and 35. Given that from the data quality monitoring, we noted distinct noise sources that affect single towers.

Light Detector channels

The trigger efficiency for the light detectors was evaluated using the same method as for the LMO channels. We observed an energy threshold of the order of 1 keV in most of the channels. Small differences in the energy threshold are observed between runs, and they are due, as for LMO channels, to baseline noise fluctuations. The energy thresholds for all the LD channels for all the datasets are reported in Fig. 3.16. As for the LMOs, the lowest energy thresholds achieved are in datasets 8247 and 8248.

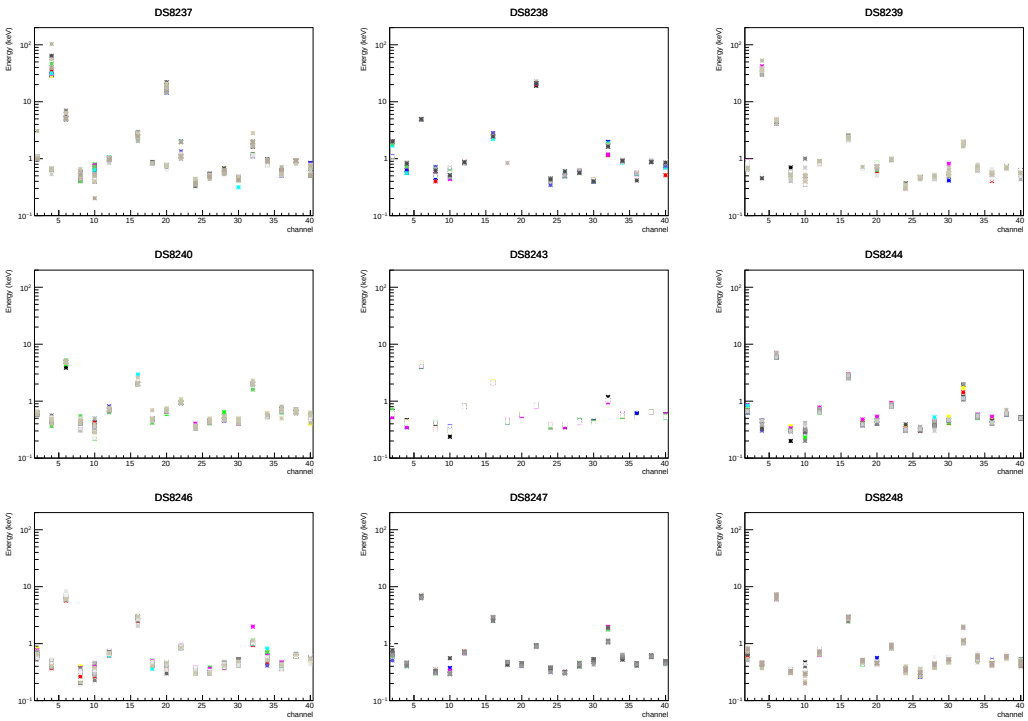

FIGURE 3.16: Energy threshold at 90% efficiency as a function of LD channels for the all datasets where each colored points represents a run in a dataset. *Left column:* datasets 8237, 8240 and 8246 are represented. *Middle column:* energy thresholds for datasets 8238, 8243 and 8247. *Right column:* energy threshold for all the LDs for datasets 8239, 8244, and 8248.

The overall threshold distribution of the LD, evaluated at 90% of the trigger efficiency, shows a mean value of 1.16 keV and a median value of 0.55 keV. This

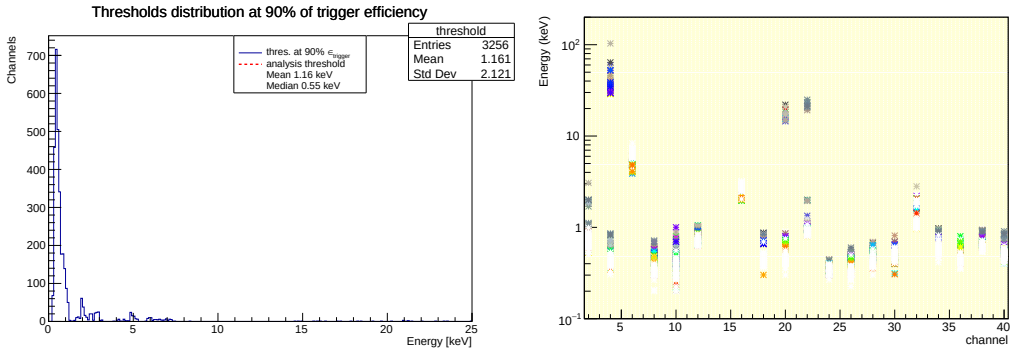

FIGURE 3.17: *Left:* overall energy threshold at 90% efficiency of the LD channels for the all datasets. *Right:* energy threshold at 90% efficiency as a function of LD channels for the all datasets.

distribution is represented in Fig. 3.17. The thresholds seem to align nicely for most channels among the datasets except for channels 20 and 22 that have a bi-modal distribution that depends on the dataset as shown on the right panel of Fig. 3.17.

3.3.3 Detector response in the ROI

To quantify the ability of the CUPID-Mo detectors in identifying the potential $0\nu\beta\beta$ decay peak at 3034 keV, it is crucial to evaluate the detector response that contains the information about the energy resolution in the region of interest (defined as 17.9 keV around the $Q_{\beta\beta}$ of ^{100}Mo [48]). For this purpose, the energy resolution of the 19 CUPID-Mo detectors used for the $0\nu\beta\beta$ analysis has to be good enough. In this section, the study about detector response will be presented. The code developed to build the line shape is based on the work done during the first triggering campaign [116].

The detector response is a function that describes an energy peak and its different components and hence its energy resolution using a specific line shape. To build this function, the γ peak at 2615 keV from ^{208}Tl is used, being the closest in energy to the $Q_{\beta\beta}$ of ^{100}Mo available in the data and having enough statistics in calibration data. However, it is important to point out that the energy peak from ^{208}Tl line and from the $0\nu\beta\beta$ of ^{100}Mo does not come from the same physical process, and therefore there are effects present in the ^{208}Tl line that would not be present in the $0\nu\beta\beta$ peak such as the Compton edge.

3.3.3.1 Line shape and fit model

We use the 2.6 MeV γ line to perform an Unbinned Extended Maximum Likelihood (UEML) simultaneous fit over all the channels in the same dataset using `RooFit` software package. The simultaneous fit is performed on each channel-dataset (ch-ds) pair.
A Probability Density Function (PDF) is built for each channel to describe the fit

model of the detector response. The PDF is the sum of three components that characterize the γ line at 2.6 MeV: the photopeak, the Compton edge, and the linear background. Therefore, the PDF is defined as follows:

$$PDF(ch, ds) = N_{sig}.Photopeak + N_{Compton}.Compton + N_{Bkg}.Background \quad (3.1)$$

where *Photopeak* is the ^{208}Tl γ line full absorption peak at 2.6 MeV, N_{sig} the number of event in the peak, *Compton* is the Compton edge of this peak and *Background* is representing the background. $N_{Compton}$ is the number of events in the Compton background and N_{Bkg} is the number of flat background events for each channel. We note that the $N_{Compton}$ and N_{Bkg} are determined by computing the common fraction of events that is the same for all the channel with respect to N_{sig}.

Shape function of the photopeak. The shape function chosen to describe the photopeak is the only component of the fit that will be propagated to the ROI for the $0\nu\beta\beta$ analysis. The choice of the shape function for the photopeak is based on phenomenological observations. In a fantasy world, the line-shape would be given by a model with perfect statistical energy to phonon conversion. However, in the experimental world, the detector response is governed by many aspects that influence the observed shape: the escape of light, crystal defects with charge-trapping, partial energy deposits in the glue of the NTD, energy mis-reconstruction due to pile-up, time-dependent excess noise and imperfections in the stabilization over time have to be added to the perfect model. Hence for the final shape, a phenomenological fit allowing for different tail-core ratios is required. For this reason, before choosing our final shape function, we tested four different shape functions to describe the photopeak: a Gaussian, a Breit-Wigner, a Crystal ball and a Voigt profile. We performed four different fits on calibration data of one dataset by using as line shape the three components of Eq. 3.1. The photopeak component was modeled by the four shape functions for each channel of the test dataset.

The results obtained are presented in Fig. 3.18. We observe that all the functions show some residuals between data and the fitted peak shape. The Breit-Weigner and Voigt functions give a small FWHM and the pulled histogram showed that the fit is not representing the data well. The Crystal ball and the Gaussian profiles give similar results. We took into account that the Crystal ball function has one more parameter than the Gaussian one, which can worsen the fit convergence combined with the degeneracy of the Compton edge. Therefore, we decided to choose the Gaussian profile to model the photopeak. We noticed that the main factor causing residuals between the data and Gaussian fit is the presence of the pile-up. Indeed, when applying a tighter pulse shape cut, the peaks tend to be more Gaussian due to a higher number of rejected pile-ups. The effect was taken into account when quantifying the signal containment due to peak shape systematic uncertainty by varying the pulse shape cut. The integral of the calibration data was compared to the integral of the Gaussian fit of the 2615 keV peak for various pulse shape cuts [48].

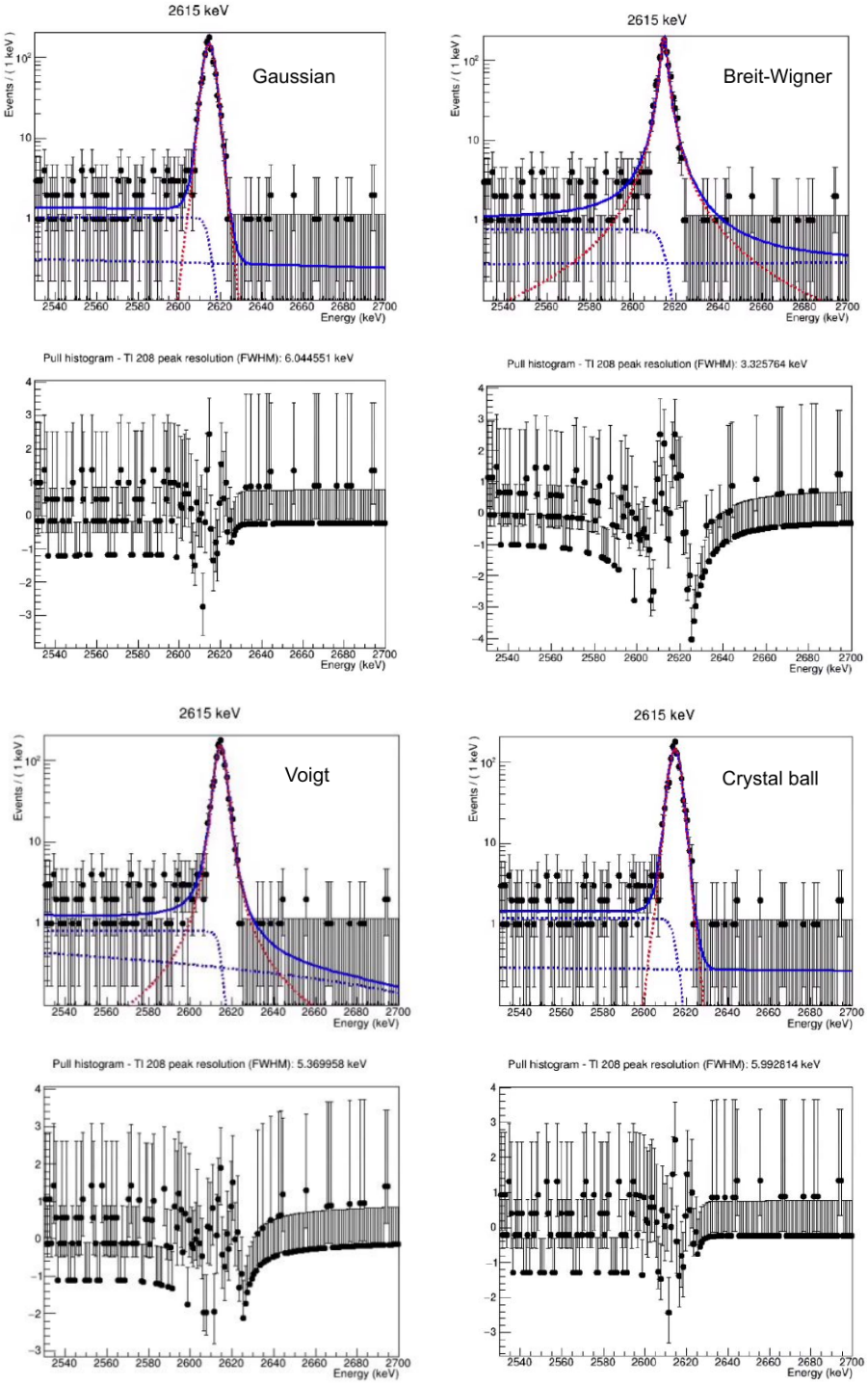

FIGURE 3.18: Fit results of the different shape functions used to describe the γ ^{208}Tl line. The black dots represent the data points. The solid blue line represents the simultaneous fit. The red dashed line is the shape function used to model to photopeak. The pulled histogram is shown for each fit result.

To summarize, the photopeak contribution of the detector response of the CUPID-Mo detectors was modeled with a Gaussian:

$$Photopeak = \frac{1}{\sqrt{2\pi}\sigma} e^{(x-\mu)^2/2\sigma^2} \tag{3.2}$$

where μ is the mean value and σ is the standard deviation of the Gaussian that represents in our model the fitted position of ^{208}Tl peak and the resolution at this energy respectively. These two parameters are both free for each ch-ds pair.

Compton Edge. This contribution is modeled by a Gaussian-smeared "step function" that mimics the Compton continuum coming from the γ of ^{208}Tl line scattering. This step function is defined as:

$$Compton = \frac{1}{2} Erfc\left(\frac{x-\mu}{\sqrt{2}\sigma}\right) \tag{3.3}$$

where σ and μ are the same from the shape function of the photopeak, which leads to having the Compton shoulder centered at 2.6 MeV. The number of events in Compton's shoulder $N_{Compton}$ is fixed to the number of events in the photopeak and is characterized by a ratio common to all channels and datasets. This ratio is a free parameter in the fit.

Background. The flat background is modeled by a first-order polynomial function. The presence of this background is due to remaining pile-up events after the pulse shape cut. The function used to model this component is:

$$Background = p1 \times x + p0 \tag{3.4}$$

where p1 is the slope and p0 is the intercepts of the first-order polynomial function. As for the Compton edge, N_{bkg} is determined by a constant fraction common to all the channels. This fraction is a free parameter in the fit.

Here we have defined our line shape with a common background ratio to all the channels in all the datasets, a Gaussian shape, and a Compton smeared step for each channel in each dataset which gives a fit with more than 60 degrees of freedom. This line shape was applied to the 19 CUPID-Mo detectors as a simultaneous UEML fit on each ch-ds pair in the energy range of [2530;2700] keV in the calibration data. The simultaneous fit runs on the sum of the ch-ds pairs PDFs defined in Eq. 3.1. There are two kinds of fit parameters involved in the simultaneous fit: global parameters and ch-ds dependent parameters. The global parameters are common to all the ch-ds pairs and are related to the nature of the fitted peak. Indeed, the background and the Compton ratios are the same for all the ch-ds couples. However, the ch-ds dependent parameters are specific to each ch-ds couple. They are the fit parameters of the shape function. To make sure that the fit converges, the parameters σ, N_{sig}, the Compton ratio, and the background ratio have

Parameter	Energy interval
σ, N_{sig}	2610-2620
Compton ratio	2530-2620
Background ratio	2650-2700

TABLE 3.1: Energy intervals used to initialize the parameters of the simultaneous fit.

to be initialized. We use the integrals in the different energy regions in the fit interval. The intervals used to initialize the corresponding parameter are reported in Table 3.1.

3.3.3.2 Fit results

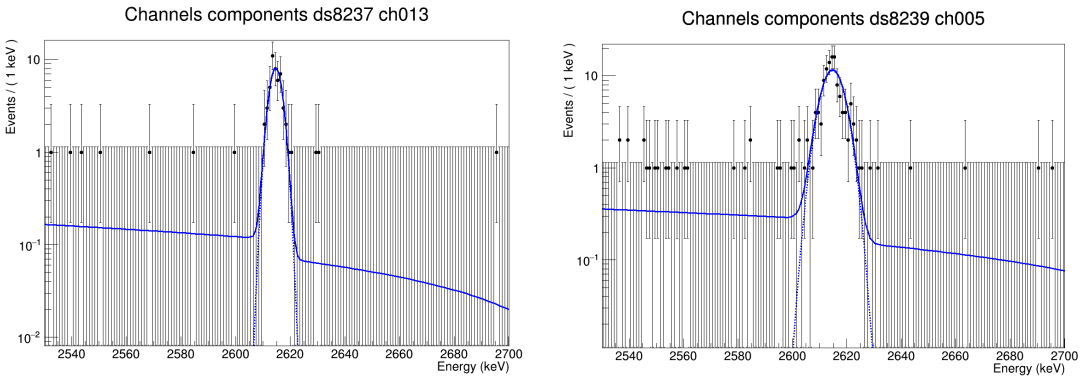

FIGURE 3.19: Example of line shape fit for channels 5 and 13 for one dataset. The solid blue line is the single channel simultaneous fit and the black dots represent the data.

The simultaneous fit was run on the 7 datasets used for the $0\nu\beta\beta$ analysis. The results obtained show that the detector response model describes quite well the data even if we observe evidence for non-Gaussian tails. These tails are dominated by unrejected pile-up events caused by the high trigger rate in calibration data. In Fig. 3.19 is reported, as an example, the ^{208}Tl line fit for two LMO channels as the fit is performed on each channel, then the PDFs of all the channels are summed to give the PDF of the simultaneous fit.
The results of the simultaneous fit on the ch-ds pairs are presented in Fig. 3.20 where the different fit components are shown. The resolutions FWHM of the simultaneous fit achieved for each dataset are between 6.3 keV and 8.3 keV at 2615 keV. We have evaluated the effective energy resolution overall for the 7 datasets to be 7.1 keV FHWM at 2615 keV.

3.3.3.3 Scaling the resolution to $Q_{\beta\beta}$

The FWHM resolution energy dependence was evaluated using the calibration data. Once the channel dataset and the overall energy resolution are obtained, they

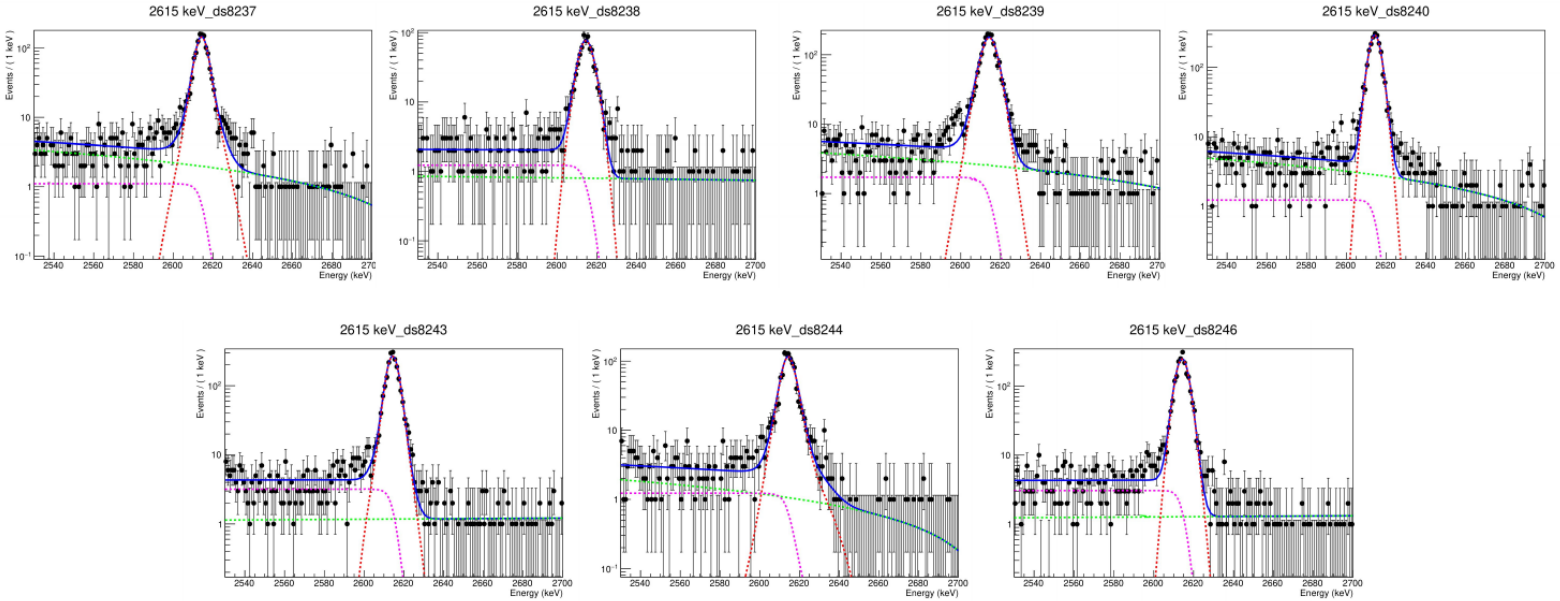

FIGURE 3.20: Fit results for the 7 datasets used for the $0\nu\beta\beta$ analysis. From left to right, top to bottom: 8237, 8238, 8239, 8240, 8243, 8244, 8246. The dashed green line is the background component one, the pink dashed line represents the Compton one and the red dashed line is the Gaussian shape function. The solid blue line is the channel-datasets simultaneous fit.

are projected with a global scaling factor common to all the datasets. This scaling factor s takes into account the extrapolation of the FWHM at 2615 keV to 3034 keV $s = \sigma_{bkg}(3034keV)/\sigma_{cal}(2615keV)$. The FWHM energy dependence was mapped with a polynomial fit of the γ peak present in the summed calibration and background spectrum [116]. The obtained FWHM projection at $Q_{\beta\beta}$ is 7.6(7) keV for all the data. The scaling energy dependence is shown in Fig. 3.21.

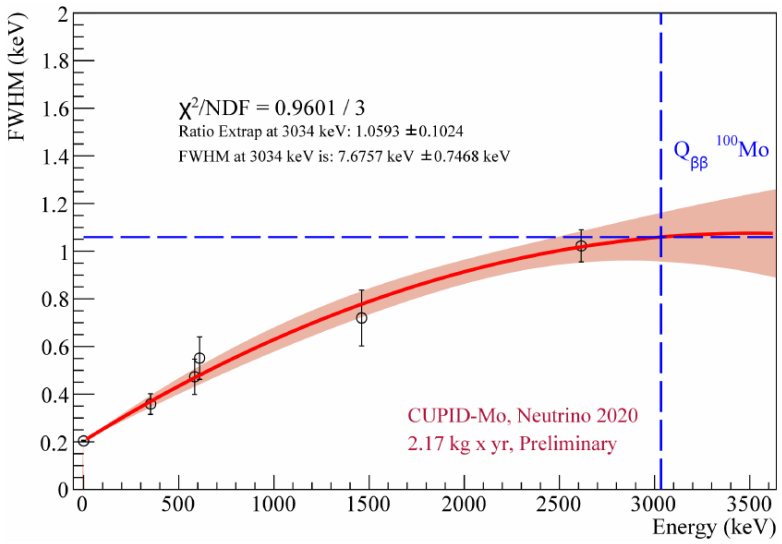

FIGURE 3.21: Scaling of the energy resolution to the $Q_{\beta\beta}$. The energy dependence of the resolution of the CUPID-Mo detectors was modeled with a polynomial function.

3.3.4 Results on $0\nu\beta\beta$ search

The search for $0\nu\beta\beta$ of ^{100}Mo was performed by blinding the data and removing all the possible events in a $\pm$50 keV energy interval around the $Q_{\beta\beta}$ to avoid any bias in the analysis and cut optimization. The accepted events after the selection cuts had to fulfill the following criteria [48]:

- each event had to be contained in a single crystal. All the events that are seen in coincidence in several crystals are rejected. In addition, an anti-coincidence cut was applied with a triple-readout trigger and a muon-veto. This cut does not depend on the energy;
- each event must have a single trigger in the 3-s pulse window;
- each event is passed through a baseline slope cut. The accepted events must have a slope of less than 15 median absolute deviations which ensure that the event has a flat pretrace;
- each event must have the expected light yield of γ and β particles within a $\pm$3 σ acceptance window based on a Gaussian fit of the light yield. In addition,

the light yield of the top and bottom light detector has to be the same with the same acceptance. An illustration of the light yield cut is presented in Fig. 3.22 where the light signals cross-calibrated against the LMO signals are plotted as a function of the energy of the LMO channels;

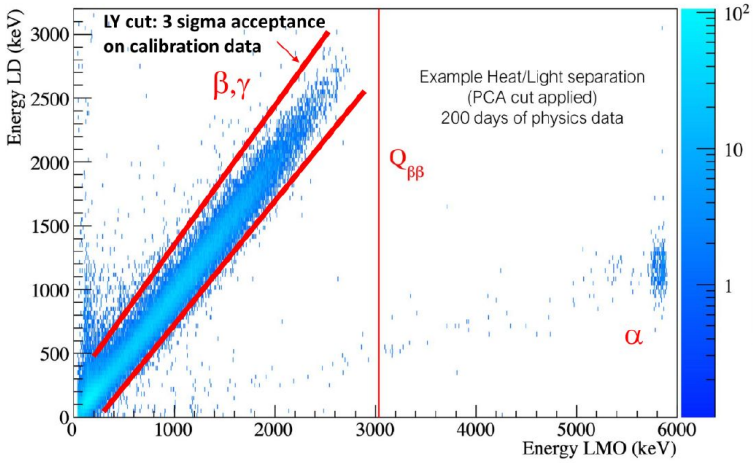

FIGURE 3.22: Cross-calibrated light signals as a function of the energy deposited in the LMO channels measured over ∼200 days of physics data. The ±3 σ acceptance window is shown in red.

- each event must have a pulse shape consistent with the PCA analysis [111] where the first component contains the main amplitude information.

The selection efficiency was evaluated to be $\epsilon = (90.6 \pm 0.4(stat.)^{+0.8}_{-0.2}(sys.))\%$. The blinded resulting background spectrum of the 19 LMO detectors for 2.16 kg.yr of exposure is shown in Fig. 3.23 as well as the summed calibration spectrum scaled to match the 2615 keV counts. In the 2.16 kg.yr background spectrum, we clearly see the contribution from $2\nu\beta\beta$ decay of ^{100}Mo continuum between 0.5 and 3 MeV. We also observe a few γ peaks (labeled in Fig. 3.23) that come from the environmental radioactive of the EDELWEISS setup. From the phenomenological background fit model, we obtained a background index of 2×10^{-3} counts/(keV.kg.yr) to 6×10^{-3} counts/(keV.kg.yr) in a 10 keV window around the $Q_{\beta\beta}$ [48]. The final background index evaluation is ongoing. The ROI was optimized on a channel-dataset basis using the background index, the detector resolution at $Q_{\beta\beta}$ and the Monte-Carlo simulations of the $0\nu\beta\beta$ decay containment.

To set the limit on the $0\nu\beta\beta$ decay of ^{100}Mo, we conducted two parallel counting analyses: a Bayesian one and a Poisson one as a cross-check [48].

After unblinding the data, we did not observe any evidence for the $0\nu\beta\beta$ decay of ^{100}Mo. We observe no event in the signal region of 17.9 keV wide (exposure weighted average width). Fig. 3.24 shows the unblinded CUPID-Mo physics spectrum for 2.16 kg.yr of data. The cyan side-band event in the spectrum was rejected after unblinding with a delayed α-β coincidence cut designed to reject high-energy

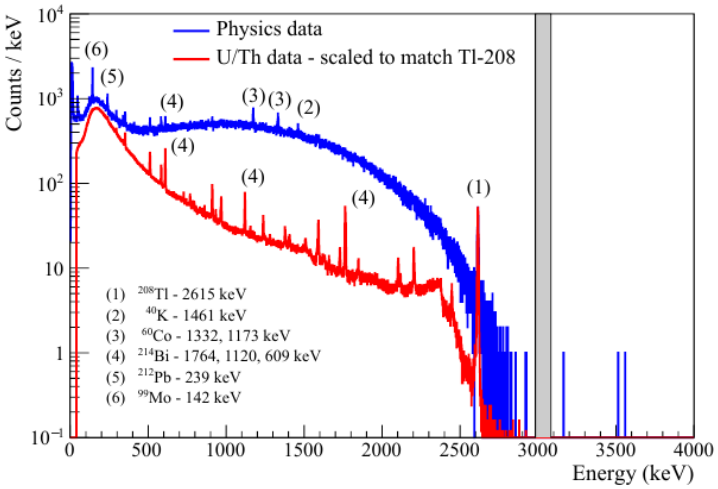

FIGURE 3.23: Summed background spectrum (blue) of 2.16 kg.yr of exposure, superimposed with the summed calibration spectrum (red) scaled to match the 2615 keV counts from ^{208}Tl. The grey band represents the blinded energy region.

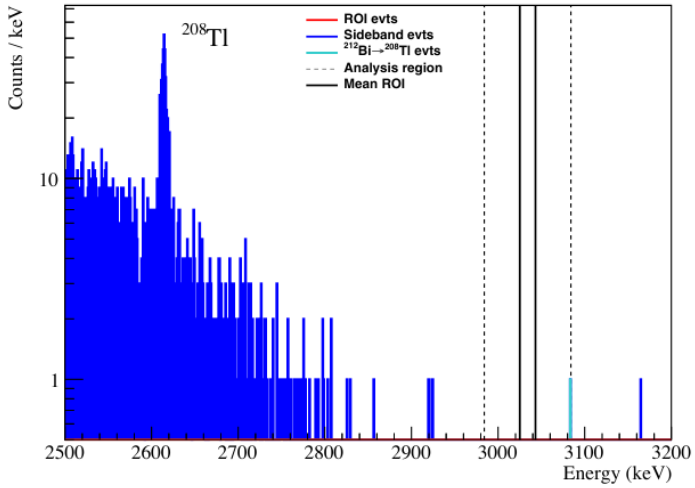

FIGURE 3.24: Unblinded CUPID-Mo physics spectrum. No event is observed in the 17.9 keV wide ROI region.

β events from ^{212}Bi [46]. The resulting upper limit on the $0\nu\beta\beta$ decay of ^{100}Mo is $T^{0\nu}_{1/2} > 1.5 \times 10^{24}$ yr at 90% C.L.. This result is the actual new world-leading limit on this decay with only 1.19 kg.yr exposure of ^{100}Mo. This obtained limit corresponds to an effective Majorana mass of $< m_{\beta\beta} > < (0.31 - 0.54)$ eV in the framework of the light Majorana neutrino exchange, depending on the NME calculations taken from [117–124] and taking $g_A = 1.27$.

Chapter 4

First dark matter searches with the CUPID-Mo detectors

Preliminary low energy analysis for dark matter searches with the CUPID-Mo detectors will be presented in this chapter. This is the first attempt to explore the potential of the CUPID-Mo detectors to search for spin-dependent dark matter interactions with ^{7}Li. First, a reminder on the dark matter problem will be introduced as well as direct dark matter searches. Then, we will describe the low energy analysis performed on the Li_2MoO_4 crystals. Finally, the preliminary exclusion limit obtained with the selected CUPID-Mo data will be presented.

4.1 A brief introduction to the dark matter problem and how to prob it

The gravitational evidence for dark matter has been known for decades, but its nature remains a mystery today. The dark matter effect has been observed via the galaxy rotational curves [125], the gravitational leansing [126] and the CMB [127]. The entity or entities constituting the dark matter are unknown. However, we know they must meet specific criteria: they must be massive, electrically neutral, stable over cosmological times and interact very weakly with the baryonic matter. Several dark matter candidates from different models are proposed: sterile neutrinos, axions and more particularly, a class of particles called WIMPs (Weakly Interacting Massive Particles).
WIMPs have been the center of interest of physicists for many years since they are considered one of the best candidates for dark matter particles. They are particles that interact very weakly with the baryonic matter with a coupling of the order of the weak interaction. The experimental search and possibly dark matter detection can be done via three different approaches: indirect detection, production, and direct detection. These approaches are schematically represented in Fig. 4.1.

The indirect detection seeks dark matter particles in the annihilation products of the dark matter particles assuming that they are Majorana particles. It is expected that the annihilation takes place in regions of high dark matter density, in the galactic center, for example. The annihilation products would be particles of the SM (photons, electrons, positrons, protons...), and therefore detectable. The indirect detection experiments are either ground-based such as H.E.S.S [128] or space-based

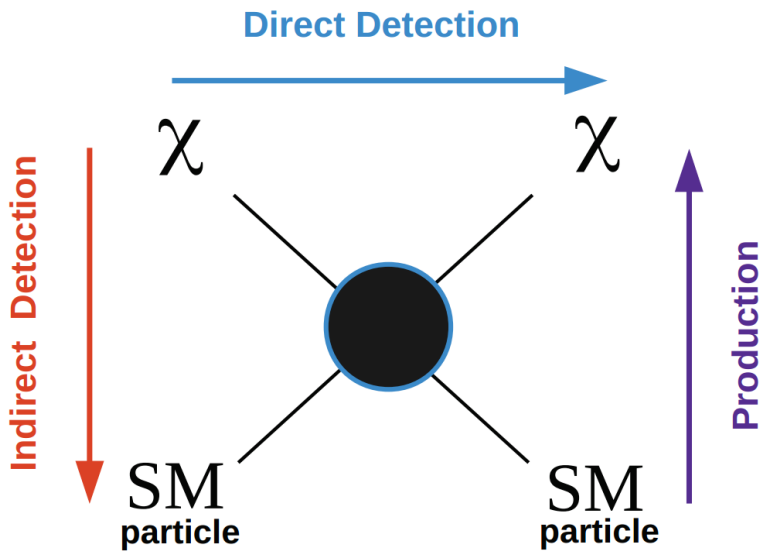

FIGURE 4.1: Schematics of the different experimental approaches to search for dark matter particles.

such as AMS [129].
Dark matter can be produced at colliders. As predicted by the dark matter models, dark matter particles can have couplings with standard model particles, so its production is possible in proton-proton collisions at the LHC. Dark matter particles interact very weakly with matter and hence are not seen by the detectors at the LHC. The search for dark matter in the LHC is done through the presence of a large missing transverse energy [130].
Finally, the detection mode that we are interested in is the direct detection mode. Direct dark matter detection experiments mainly seek to measure the recoil energy generated by elastic scattering of a WIMP with ordinary matter. This type of experiment is designed to detect the interaction of WIMPs with standard model particles via recoils off nucleons or electrons.

4.2 Direct dark matter detection

In this section a summary of the dark matter rate and cross-section calculations is given based on [131–134].
In this thesis, for kinematics reason and given the expected WIMPs masses (>1-10 GeV) [131], we will focus on the WIMPs scattering on nucleons. In contrast, other experiments look for WIMPs with lower masses via the investigation of dark matter particles scattering on electrons (PandaX-II experiment [135] for example).

The goal of direct dark matter searches is to set limits, or detect in the best scenario, nuclear recoils provoked by the scattering of a WIMP on the target nuclei

located on the surface of the earth. Therefore, the observable accessible experimentally is the nuclear recoil spectrum. The expected WIMP rate is defined as:

$$\frac{dR}{dE_R} = \frac{\rho_0}{m_N m_\chi} \int_{v_{min}}^{\infty} v f(v) \frac{d\sigma_{\chi N}}{dE_R}(v, E_R) d^3v \tag{4.1}$$

where E_R is the recoil energy, ρ_0 is the local WIMP density, m_χ the WIMP mass, m_N the target mass, $\frac{d\sigma_{\chi N}}{dE_R}(v, E_R)$ the differential cross-section for the WIMP-nucleus scattering, $f(v)$ is the WIMP velocity distribution and v_{min} is the minimum needed velocity to generate a nuclear recoil.
The interaction between the dark matter particle and the nucleon is assumed to be an elastic scattering with a WIMP velocity of the order of 300 km/s; this leads to ignore the relativistic effects and express the recoil energy as:

$$E_R = \frac{\mu_N^2 v^2 (1 - cos\theta^*)}{m_N} \tag{4.2}$$

where $\mu_N = m_\chi m_N / (m_N + m_\chi)$ is the WIMP-nucleus reduced mass and θ^* the scattering angle in the center of mass reference frame. Using the expression of E_R in Eq.4.2 at $\theta^* = \pi$, one can evaluate the minimum velocity $v_{min} = \sqrt{\frac{m_N E_R}{2\mu_N^2}}$.
The cross-section of the WIMP interaction with the target nucleus describes the physics of the process taking into account the particle and the nuclear physical properties of the entities acting in this interaction. The cross-section can be spitted into two different contributions: Spin-Dependent (SD) one and Spin-Independent one (SI) as written in Eq. 4.3.

$$\frac{d\sigma_{\chi N}}{dE_R} = \left(\frac{d\sigma_{\chi N}}{dE_R}\right)_{SD} + \left(\frac{d\sigma_{\chi N}}{dE_R}\right)_{SI} \tag{4.3}$$

In the non-relativistic limit, the total cross-section can be written as:

$$\frac{d\sigma_{\chi N}}{dE_R} = \frac{m_N}{2\mu_N^2} (\sigma_0^{SD} F_{SD}^2(E_R) + \sigma_0^{SI} F_{SI}^2(E_R)) \tag{4.4}$$

where $F_{SD,SI}$ are the nuclear form factors for the SD and the SI case, respectively and $\sigma^0_{SD,SI}$ are the WIMP-nucleus total cross-section for the zero momentum transfer.
Combining Eq. 4.1 and Eq. 4.4, we obtain the WIMP rate dependence as in Eq. 4.5.

$$\frac{dR}{dE_R} = \frac{\rho_0}{2 m_\chi \mu_N^2} (\sigma_0^{SD} F_{SD}^2(E_R) + \sigma_0^{SI} F_{SI}^2(E_R)) \int_{v_{min}}^{\infty} \frac{f(v)}{v} d^3v \tag{4.5}$$

Now, let us examine each term of the WIMP rate:

Spin-Independent interaction term $\sigma_0^{SI} F_{SI}^2(E_R)$

The SI interaction is coherent and is the same for protons and neutrons. The scalar WIMP-nucleus interaction cross-section can be expressed as:

$$\sigma_0^{SI} = \frac{4\mu_{_N}^2}{\pi} f_p^2 A^2 \tag{4.6}$$

where A is the mass number of the target nuclei and f_p is the proton effective coupling constant. Concerning the form factor, it is considered to be the Fourier transform of the density distribution of the nucleus, using Born approximation the form factor is written in this case as [131]:

$$F_{SI} = \frac{3\left[sin(qr_n) - qr_n cos(qr_n)\right]}{qr_n} \tag{4.7}$$

where $q = \sqrt{2m_N E_R}$ is the momentum transfer and $r_n = 1.2A^{1/3} fm$ is the nuclear radius.
It should be noted that the SI cross-section is proportional to A^2 which will lead the choice of the target to a heavy nucleus. On the other hand the E_R is expected to be smaller. Hence, the energy threshold of the detectors used to probe the nuclear recoils has to low.

Spin-Dependent interaction term $\sigma_0^{SD} F_{SD}^2(E_R)$

This interaction concerns only nuclei with an odd number of protons and/or neutrons since the paired nucleons does not contribute in the scattering amplitude. In this case, the WIMP will only interact with the unpaired nucleon and the cross-section can be written as:

$$\sigma_0^{SD} = \frac{32}{\pi} \mu_N^2 G_F^2 \Lambda^2 J(J+1) \tag{4.8}$$

where G_F is the Fermi constant, J is the nucleus angular momentum and Λ is a factor that takes into account the scattering amplitudes on proton a_p and on neutron a_n, and the spin matrix elements $< S_p >$ and $< S_n >$, expressed as:

$$\Lambda = \frac{1}{J}[a_p < S_p > + a_n < S_n >] \tag{4.9}$$

In the SD interaction case the form factor is expressed as:

$$F_{SD} = \frac{sin(qr_n)}{qr_n} \tag{4.10}$$

Velocity distribution term $\int_{v_{min}}^{\infty} \frac{f(v)}{v} d^3v$

This term represents the mean inverse speed that will we denote here as $\eta(E_R)$ and contains the information about the WIMP velocity distribution in the galactic halo

$f(v)$. In the standard halo model, $f(v)$ is taken to be a Maxwellian distribution and the local dark matter density is $\rho_\chi = 0.3\ \mathrm{GeV/(c^2.cm^3)}$ [136]. If we do not take into account the motion of earth and consider the target at rest, the rate becomes exponential at low energy as shown in [131]. However, the rotation of the sun in the galactic plane and the motion of the earth around the sun have to be taken into account. Considering this, it is possible to fully compute $\eta(E_R)$ by introducing a cut-off when the WIMP velocity is higher than the gravitational escape velocity $v_{esc} \sim 544$ km/s [137]. Thus, for $v < v_{esc}$, the velocity distribution becomes:

$$f(v) = \frac{1}{N_{esc}} \left(\frac{3}{2\pi\sigma^2}\right)^{3/2} e^{-3v^2/2\sigma^2} \tag{4.11}$$

where $v_0 = \sqrt{2/3}\sigma \sim 220$ km/s is the solar orbit velocity [138] and N_{esc} is a normalization written as

$$N_{esc} = erf(z) - 2ze^{-2z^2}/\sqrt{\pi} \tag{4.12}$$

with $z = v_{esc}/v_0$. Setting $x = v_{min}/v_0$ and $y = v_{obs}/v_0$, where v_{obs} is the motion of the observer with respect to the rest frame of the WIMP, the mean inverse speed $\eta(E_R)$ is written as:

$$\eta(E_R) = \begin{cases} 1/v_0 y & z < y, x < |y-z| \\ 1/(2N_{esc}v_0 y)[erf(x+y) - erf(x-y) - 4ye^{-z^2}/\sqrt{\pi}] & z > y, x < |y-z| \\ 1/(2N_{esc}v_0 y)[erf(z) - erf(x_y) - 2(y+z-x)e^{-z^2}/\sqrt{\pi}] & |y-z| < x < y+z \\ 0 & y+z < x \end{cases} \tag{4.13}$$

In this thesis, we are interested in studying the WIMP interactions with ^{7}Li via SD process. In this case and combining Eq. 4.5, 4.8 and 4.13, the differential rate becomes:

$$\frac{dR}{dE_R} = \frac{\rho_0}{2m_\chi \mu_N^2} \frac{32}{\pi} \mu_N^2 G_F^2 \frac{1}{J} [a_p < S_p > + a_n < S_n >]^2 (J+1)\eta(E_R) \tag{4.14}$$

We note here that we set the form factor squared to be 1, which is a possible approximation for light nuclei such as ^{7}Li. Usually, the differential rate is expressed as a unit of counts/(keV.kg.d). The expected rate was computed using Eq. 4.14 for the CUPID-Mo detectors for different WIMP masses and is presented in Fig. 4.2. As expected, the WIMP rate/spectrum has an exponential shape towards low energies, confirming the need for a low energy threshold detector to perform this kind of search.

4.3 Low energy analysis with the CUPID-Mo detectors

This section will present the motivations to start a dark matter analysis with the CUPID-Mo data. After that, a description of the analysis performed to lower the energy threshold of the LMO detectors will be given.

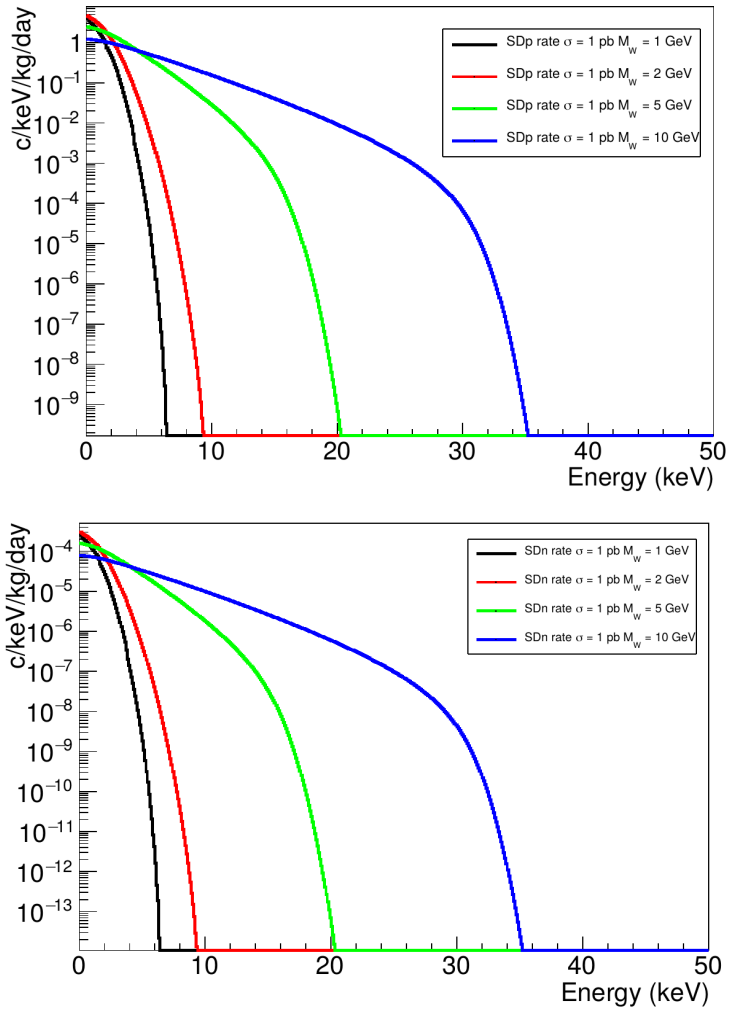

FIGURE 4.2: Expected dark matter event rate in the LMO detectors for 2 kg.yr of exposure for different WIMP masses for proton-only interactions (*top panel*) and for neutron-only interactions (*bottom panel*).

4.3.1 Motivation for dark matter searches with the CUPID-Mo detectors

We take advantage of the ^{7}Li (I.A.= 92% [69]) present in the LMO crystals to search for WIMPs interactions since this element is considered to be suitable for studying SD interactions for low WIMP masses [88]. In addition, the SI cross-section is $\sim A^2$ which penalize the use of light element to search for this type of interaction. The SD interaction leading order is carried by the $< S_{n,p} >$ whose value depends on the isotope and not its mass. An advantage of choosing a light element for SD interactions is that the kinematics of the process allows having a higher momentum transfer for light targets. Furthermore, it has been shown that the dominant contribution to the WIMP-nucleus cross-section is the SI one when A > 30 [131]. Taking

into account all the listed features, ^{7}Li with J= 3/2 and $< S_p > \sim 1/2$ is ideal for searching for SD WIMP interactions.
From an experimental point of view, the use of a double readout, registering the heat and light signals or the heat and ionization signals, cryogenic detectors for dark matter searches by several experiments (CDMS [139], CRESST[88], EDELWEISS[109]) has proven its worth in this area. Indeed, this kind of detector provides the possibility of active background discrimination and a low energy threshold. In addition, Li is the lightest element that can be embedded in crystals used as scintillating bolometers. The first test of a Li_2MoO_4 (2.66 g) crystal for dark matter searches was performed above-ground by the CRESST collaboration [140], the results obtained were very promising, opening the door for low WIMP masses searches with ^{7}Li as a target.

4.3.2 Low energy analysis optimization

As presented in the $0\nu\beta\beta$ analysis, the mean value of the trigger threshold was 13 keV at 90% of the trigger efficiency, and the analysis threshold was set to be 45 keV as the expected peak from the $0\nu\beta\beta$ of ^{100}Mo is at 3 MeV. Hence, this threshold is reasonable for such analysis.
To lower the analysis threshold and optimize the analysis below 100 keV, the CUPID-Mo data had to be re-triggered with a lower sigma threshold (see Sec. 3.3). We choose to re-trigger two datasets out of the seven available from the $0\nu\beta\beta$ analysis for this preliminary dark matter analysis. Two main arguments drove the choice of the datasets to re-trigger:

- we wanted to have a low energy peak to check our resolution and calibration at low energy, so we choose a dataset close to the AmBe calibration; in that way, the ^{99}Mo peak at 142 keV is visible in the spectrum. This dataset is denoted here as ds8437;
- we also wanted to have a dataset with a relatively low background index, so we choose to re-trigger a dataset that was far away in time from the AmBe calibration. This dataset is denoted here as ds8440.

These two datasets were re-triggered following the same procedure described in Sec. 3.3 with a sigma threshold of 4. After that, the data is reprocessed according to the steps used for the $0\nu\beta\beta$ analysis. We have evaluated the trigger efficiency of these two datasets and the results obtained are shown in Fig. 4.3. We observe that the mean value of the energy threshold at 90% of the trigger efficiency of dataset 8437 is 26.5 keV to be compared with the value obtained with a σ_{noise} threshold of 10 that was 27.9 keV in the $0\nu\beta\beta$ analysis. Concerning dataset 8440 the energy threshold moved from 9.2 keV for 10 sigmas threshold in the $0\nu\beta\beta$ analysis to 4.9 keV for 4 σ_{noise} threshold in this analysis. As we will see later in the text, not all the channels were used to perform the dark matter analysis; thus the mean effective trigger threshold is lower than the one of the whole dataset. Fig. 4.4 represents the threshold distributions of the 10 best performing channels in ds8440 and ds8437 where the mean energy thresholds were evaluated to be 4.2 and 9.7 keV at 90% of

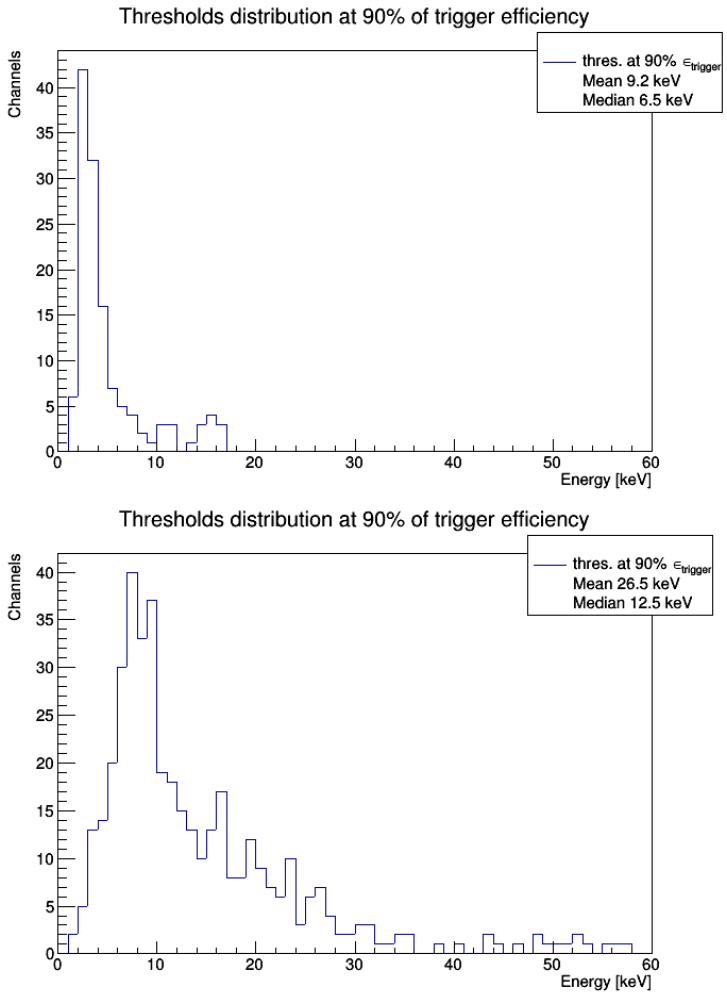

FIGURE 4.3: Energy threshold at 90% of the trigger efficiency of the LMO channels for dataset 8440 (*top panel*) and for 8437 (*bottom panel*).

the trigger efficiency, respectively.

To optimize the analysis, we introduced a new processing step to build a pulse shape parameter more suitable for low energy. This step is based on a DIANA module developed by the CUORE-0 collaboration for their dark matter analysis [114] and by the CUORE collaboration [141]. In this new processing step, the χ^2 of each filtered pulse is computed by fitting the pulse with the filtered average pulse: we will refer to this parameter as the Optimum Triggering χ^2 (OT χ^2). The OT χ^2 works correctly when the filtered pulse is well-fitted with the AP and the value of the χ^2 is low. We represent the distribution of the OT χ^2 as a function of the energy as shown in Fig. 4.5. The particle events band is spotted thanks to the ^{208}Tl peak in calibration data (top panel of Fig. 4.5), these events have a low OT χ^2. The other band present in the OT χ^2 distribution as a function of the energy contains electronic spikes, noise events, and events in the NTD (heat only events). Hence, to

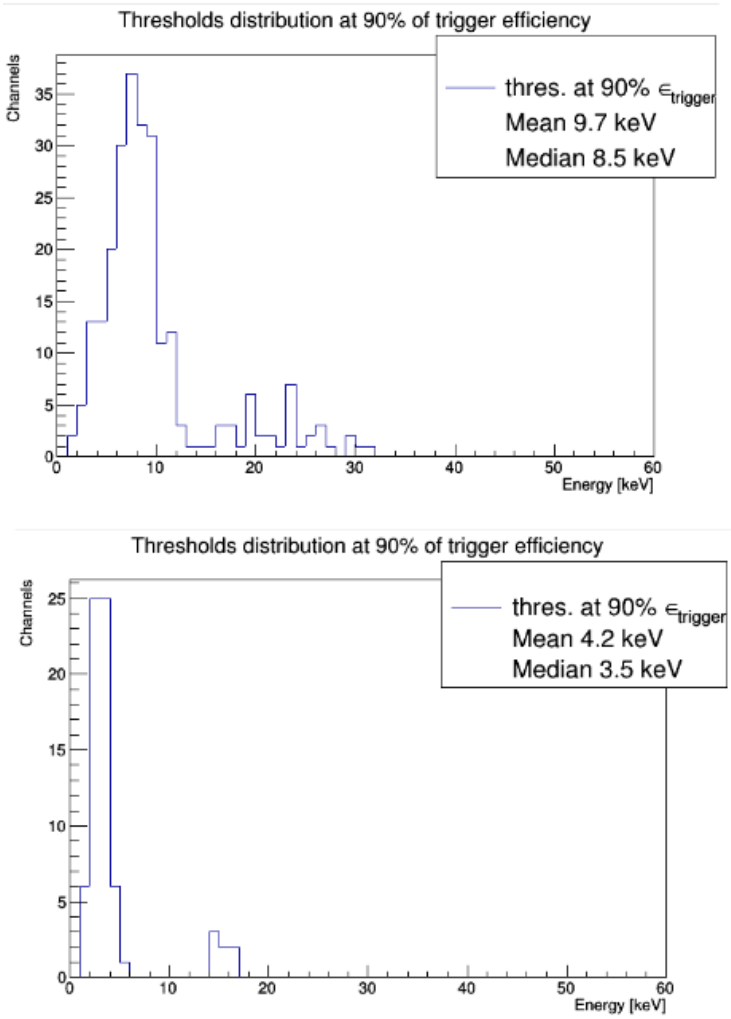

FIGURE 4.4: Energy threshold at 90% of the trigger efficiency of the 10 best performing LMO channels for dataset 8437 (*top panel*) and for 8440 (*bottom panel*).

build an OT χ^2 cut, a similar procedure to the one applied to build the light yield cut [48] is performed on the OT χ^2 distribution from background data. This procedure allows placing a reliable cut on the OT χ^2 versus energy as illustrated in Fig. 4.5. This cut is common to all the channels and hence is channel dependent. A comparison between the spectrum obtained with this analysis and the one performed for the $0\nu\beta\beta$ search is shown in Fig. 4.6. We see that the OT χ^2 works well at low energy, where the spectrum below 100 keV is reconstructed better than the $0\nu\beta\beta$ spectrum (where the cuts at low low energy are not optimized). The cut efficiency was evaluated to be $\sim$ 97% using the ^{99}Mo peak at 142 keV. A preliminary evaluation of the energy resolution at 142 keV gave 2.68 keV FWHM. For each dataset, the ten best-performing channels were selected in terms of good performing OT χ^2 and low noise.

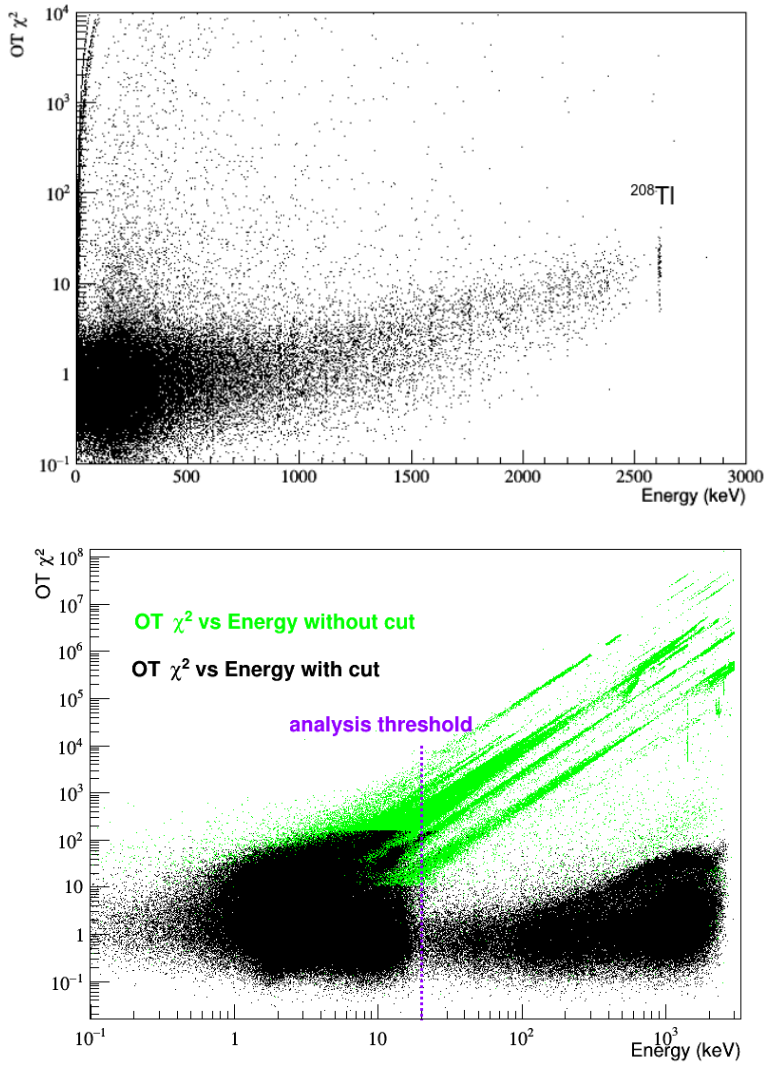

FIGURE 4.5: *Top panel:* distribution of OT χ^2 as a function of energy for one channel in calibration data. *Bottom panel* distribution of OT χ^2 as a function of energy for the 10 best channels in background data. The OT χ^2 is represented without the cut in green and in black with the cut.

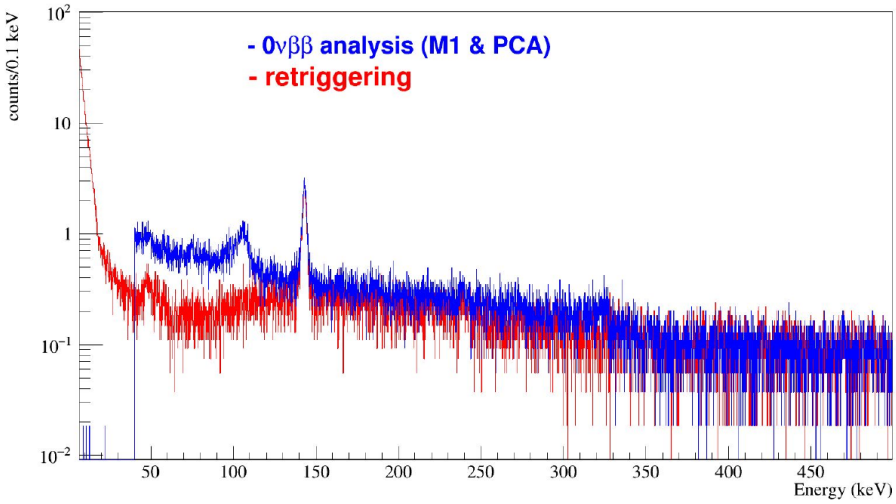

FIGURE 4.6: Comparison between the spectrum obtained in the $0\nu\beta\beta$ analysis (in blue) and the one obtained from the low energy analysis (in red) for one dataset.

It should be noted that for this preliminary analysis, the OT χ^2 shape parameter cannot distinguish particle events from spikes when the energy is lower than $\sim$ 20 keV as shown in Fig. 4.5. This is an additional constraint on setting the analysis threshold that is here different from the trigger threshold. Consequently, even if the selected channels are fully efficient at 90% above 10 keV for ds8437 and above 5 keV for ds8340, we cannot set the analysis threshold to these values because our spectrum is contaminated with non-particle events below 20 keV. Therefore, we set a conservative analysis threshold to be 20 keV for both datasets. A possible way to improve this threshold is to optimize the cut to separate the different event types below 20 keV.
The obtained spectra, without any efficiency correction, for the two datasets used in this analysis are presented in Fig. 4.7. The effect of the OT χ^2 cut is apparent, both spectra start to rise around 20 keV. The exposure corresponding to the 10 detectors selected in ds8437 is 0.15 kg.yr; we evaluated the background index in the energy interval [25-30] keV to be BI =21.3 counts/(keV.kg.d). The exposure used for ds8440 is 0.2 kg.yr (ten best channels selected) and the BI, evaluated in the same interval as for ds8437, is 12.2 counts/(keV.kg.d). Let us note that the BI in ds8437 is higher because this dataset was acquired just after an AmBe calibration, thus the spectrum was contaminated by activation products.

4.3.3 Spin-Dependent dark matter searches results

The two spectra shown in Fig. 4.7 were used to evaluate the SD dark matter interaction exclusion limits. To compute these limits, we used Yellin's optimal interval method [142] and the standard halo dark matter model, implemented in a code developed in [134] for proton and neutron only interactions. In the usual Yellin method, all the possible intervals joint and disjoint are used to search for the best

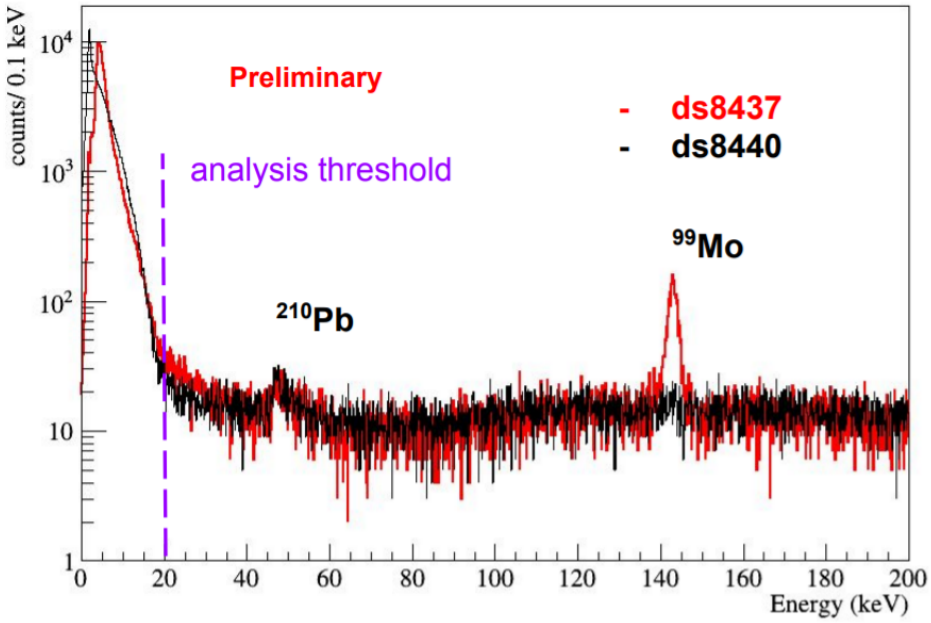

FIGURE 4.7: Energy spectra of datasets 8440 and 8437 from the CUPID-Mo low energy analysis.

one, but the disjoint intervals are not considered for practical reasons in the code that we used. The choice of using the Yellin method is lead by our approach of this analysis as this method is more conservative with respect to other methods [132]. In addition, we do not have a dedicated low-energy background model that could help understand the spectrum at low energy. Therefore, we took advantage of the Yellin method to compute our limit as it is suitable for unknown backgrounds.
The region of interest used to compute the exclusion limit goes from the analysis threshold at 20 keV to 50 keV. All events in this region are considered dark matter interaction events. To model the experimental effects, we took into account the energy dependence of the energy resolution of the detectors $FWHM(E) = \sqrt{p0 + p1 \times E}$. This resolution energy dependence was modeled using the $0\nu\beta\beta$ data and was evaluated to be 1.35 keV FWHM at the analysis threshold.

In Fig. 4.8, we present the results obtained from this CUPID-Mo preliminary low energy analysis for SD proton-only and neutron-only interactions. The exclusion limit obtained with ds8440 is slightly better due to the lower background index. We note that our limits rise below WIMPs masses of 10 GeV, this is caused by the energy resolution at the analysis threshold.
We are not competitive for WIMP masses below 10 GeV because we are limited by our experimental constraints, the analysis threshold set in this analysis is quite high compared to other dark matter experiments threshold. To show the potential of the CUPID-Mo detectors for this kind of search, we will focus on WIMP masses higher than 10 GeV to interpret the results presented here. The exclusion limit on

the cross-section for the neutron-only interaction is not competitive with other dark matter experiments. For the SD proton-only interaction, our results show the potential for being competitive with other dark matter experiments since we reached $\sigma_{SDp} \sim 10^{-34}$ cm^2.It is important to note that this analysis needs further optimization in data selection, this would help to reduce BI and lower the analysis threshold. One possible optimization would focus on improving our OT χ^2 cut below 20 keV to separate particle events from spikes. In addition, examining the analysis threshold for each channel based on the OT χ^2 cut could provide a better exclusion limit by selecting channels with the OT χ^2 cut that distinguish the different event types below 20 keV. This implies the optimization of a cut independent of the channel. Another possible optimization is to consider coincidences between events occurring in different crystals in the same tower, in order to apply an anti-coincidence cut to remove electronic spike events that are usually seen by more than one detector simultaneously. We chose not to use the LD for this analysis because we do not expect scintillation light at such a low energy ($LY \sim 0.5$ keV/ MeV).

Intending to show the potential of the CUPID-Mo detectors for WIMPs searches, we computed the expected limit using the theoretical WIMP rate for different background levels and thresholds. The projections for the spin-dependent proton-only interaction are presented in Fig. 4.9. It is possible to set a competitive exclusion limit with a 2 keV threshold and a BI of 10 counts/(keV.kg.d) for WIMP masses lower than 10 GeV.

In conclusion, this preliminary dark matter analysis with the CUPID-Mo data for spin-dependent interaction with ^{7}Li has confirmed and showed the potential of this isotope to conduct such investigations despite the relatively high BI and high analysis threshold. Of course, this analysis needs further improvements to be competitive with other dark matter experiments. In addition, we did not perform any systematic uncertainty evaluation that of course has to be taken into account in the final exclusion limit.

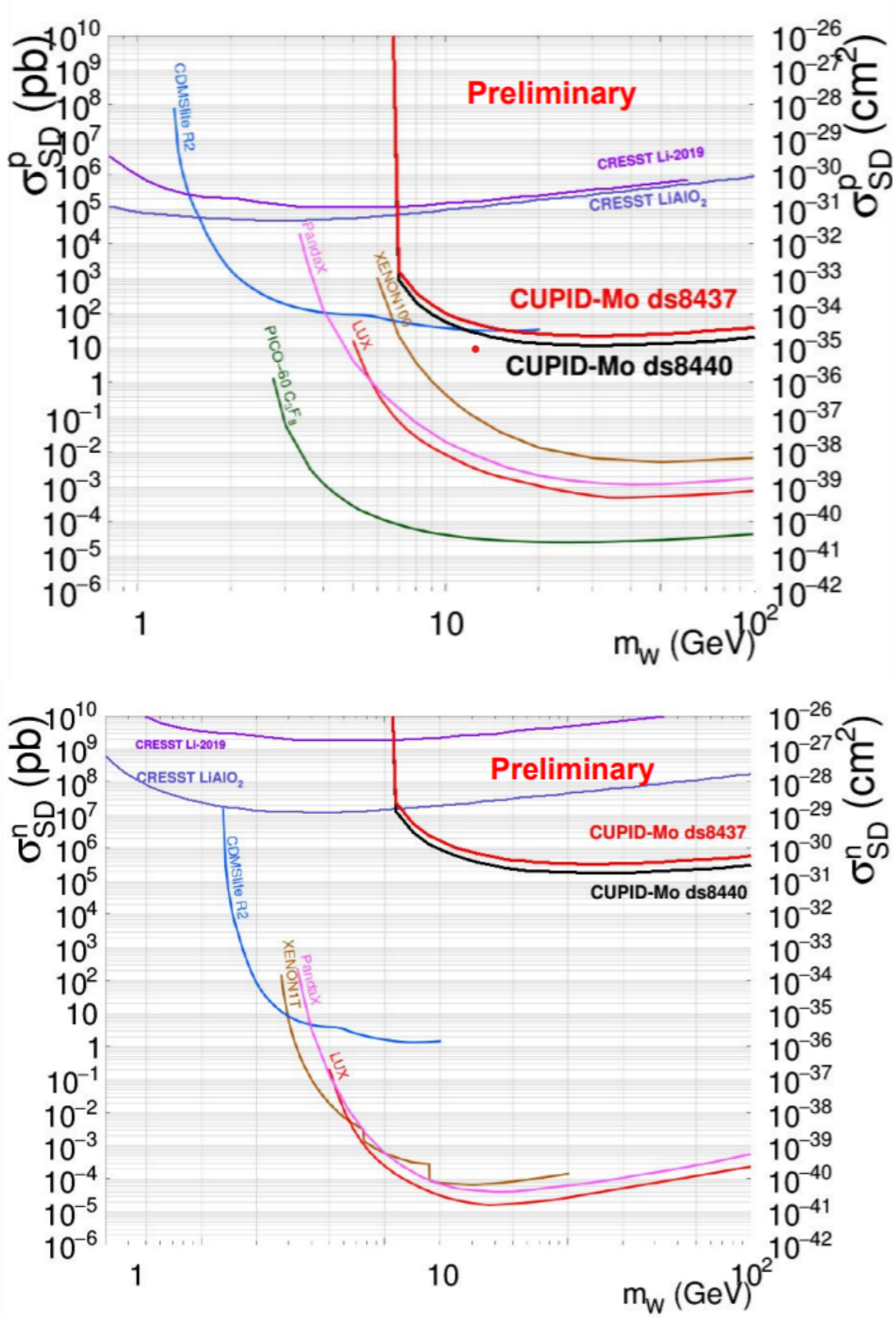

FIGURE 4.8: Exclusion limits obtained for spin-dependent dark matter with ^{7}Li proton-only interactions (*top panel*) and neutron-only interactions (*bottom panel*) for datasets 8440 (in green) and 8437 (in black). We compare our results with different experiments: CRESST [140, 143] with ^{7}Li, PICO [144], LUX [145], PandaX [146] and XENON100 [147] with ^{129}Xe+^{131}Xe, and CDMSlite [148] with ^{73}Ge.

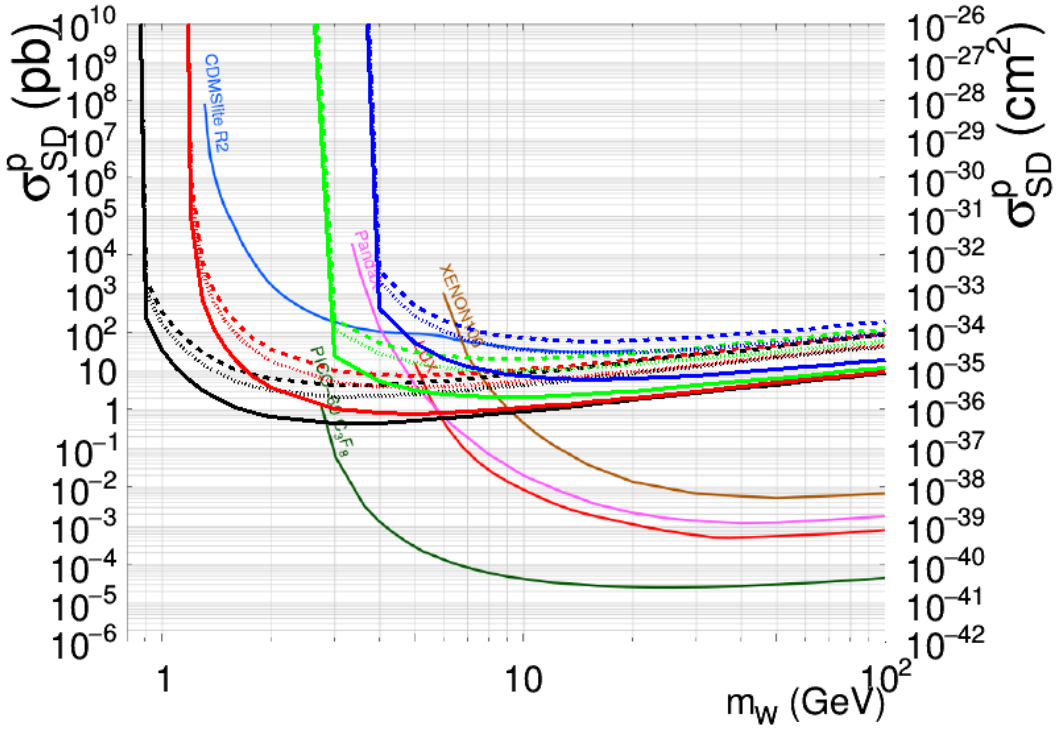

FIGURE 4.9: Expected exclusion limit for SD proton-only interactions with 2 kg.yr of exposure with the CUPID-Mo LMO crystals for background index of 1 counts/(keV.kg.d) (solid line), 5 counts/(keV.kg.d) (dotted line) and 10 counts/(keV.kg.d) (dashed line). The threshold used for this simulation are 1 keV (black), 2 keV (red), 5 keV (green) and 10 keV (blue). We compare these projections with CRESST [140], PICO [144], PandaX [146], XENON100 [147], CDMSlite [148] and LUX [145].

Chapter 5

$CdWO_4$ scintillating bolometers

5.1 Searching for double-beta decays in ^{116}Cd

The quest toward $0\nu\beta\beta$ decay investigations is of fundamental importance since its observation would answer many questions in lepton and nuclear physics. As mentioned in Chapter 1, the predictions of the half-lives of the candidate isotopes depend on the NME, for which different models apply, since no analytical calculations are available. Moreover, we cannot say today with certainty the isotope with the highest decay probability. If the $0\nu\beta\beta$ decay is observed experimentally, it would be best to confirm it in several isotopes, since this hypothetical decay is very rare. For these reasons, it is essential to study this decay in as many candidate isotopes as possible.

One possible way to confirm the detection of the $0\nu\beta\beta$ decay would be to observe it in two or more isotopes using the same detection technique to show the robustness of the discovery. As part of CUPID R&D, several $0\nu\beta\beta$ decay candidates were considered to build such an experiment. These candidates are ^{82}Se, ^{100}Mo (chosen as baseline for the CUPID experiment), and ^{116}Cd. ^{82}Se and ^{100}Mo can be embedded in scintillating crystals, while ^{130}Te can be embedded in TeO_2 crystals that emit Cherenkov light [149]. In this framework, an important part of this thesis has been devoted to the study of scintillating crystals based on enriched $^{116}CdWO_4$, with $\sim$82% of ^{116}Cd, for $0\nu\beta\beta$ decay. In this chapter, we first give a brief historical overview of the search for the double-beta decay in ^{116}Cd. The state of the art and the motivations for using scintillating crystals based on $^{116}CdWO_4$ are presented. Subsequently, the work on enriched $^{116}CdWO_4$ scintillating bolometers and the obtained results are described in detail.

5.1.1 Framework and state of the art

The history of ^{116}Cd in $0\nu\beta\beta$ decay searches is fascinating from an experimental and a theoretical point of view as this element is one of the most promising isotopes to undergo such decay. The theoretical estimations of the decay probability are very encouraging to investigate the $0\nu\beta\beta$ decay in ^{116}Cd [38]. It has a high $Q_{\beta\beta}$ of 2813.49(13) keV [150] and a relatively high isotopic abundance (I.A.=7.512(54)% [69]). A simplified scheme of ^{116}Cd double-beta decay is shown in Fig. 5.1.

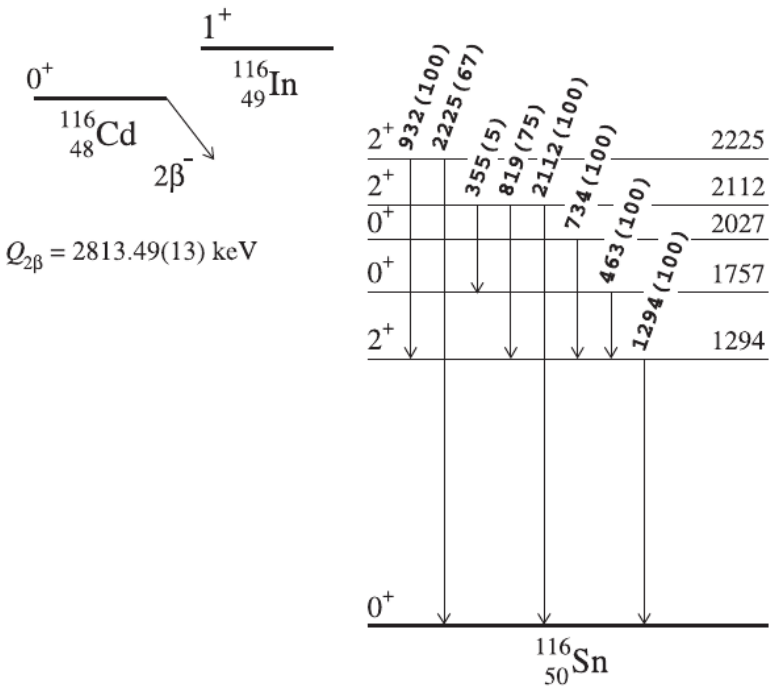

FIGURE 5.1: A simplified scheme of ^{116}Cd $0\nu\beta\beta$ decay to the ground state of ^{116}Sn [151].

The investigation of double-beta decays of ^{116}Cd began with the ELEGANT V experiment, which first observed and reported the $2\nu\beta\beta$ decay of this nucleus in 1995 [152]. The ELEGANT V experiment was located in the Kamioka underground laboratory in Japan and used drift chambers and plastic scintillators to measure the electrons emitted by the decays of ^{116}Cd nuclei present at 90.1% in the source foil. In their publication [152], the ELEGANT V collaboration reports the first measurement of $2\nu\beta\beta$ decay half-life of ^{116}Cd, which is $T_{1/2} = 2.6^{+0.9}_{-0.5} \times 10^{19}$ yr. They also give the upper limit on the $0\nu\beta\beta$ mode to be $T_{1/2} > 6.3 \times 10^{21}$ yr at 68% C.L.. In parallel, the potential of investigating these decays in ^{116}Cd was exploited by the Solotvina experiment [153], which observed the $2\nu\beta\beta$ mode using enriched cadmium tungsten ($^{116}CdWO_4$) crystals with the source isotope embedded in the crystal. The half-life measured was $T_{1/2} = 2.7^{+0.5}_{-0.4}(stat)^{+0.9}_{-0.6}(sys) \times 10^{19}$ yr. Solotvina set one of the most stringent limit on the $0\nu\beta\beta$ decay of ^{116}Cd ($T_{1/2} > 1.7 \times 10^{23}$ yr at 90% C.L.) [153]. The NEMO-2 and NEMO-3 collaborations detected the $2\nu\beta\beta$ decay as well using tracking calorimetric technology [64] at LSM. The most accurate value of the half-life of this decay was given by the NEMO-3 experiment [64]: $T_{1/2} = 2.7 \pm 0.04(stat) \pm 0.18(sys) \times 10^{19}$ yr. For the $0\nu\beta\beta$ mode, the NEMO-3 experiment set an upper limit of $T_{1/2} > 1.0 \times 10^{23}$ yr at 90% C.L. [64]. Recently, the Aurora experiment [49] with an enriched $^{116}CdWO_4$ (82%) crystal scintillator (mass of 1.162 kg) set an improved limit on the half-life ($T_{1/2} > 2.2 \times 10^{23}$ yr at 90% C.L.). The half-life of the $2\nu\beta\beta$ decay of ^{116}Cd was measured to be $T_{1/2} = 2.63 \pm 0.01(stat)^{+0.11}_{-0.12}(sys) \times 10^{19}$ yr by Aurora [49]. The measured half-lives of $2\nu\beta\beta$

decay and the limits on the $0\nu\beta\beta$ decay of ^{116}Cd are summarized in Table 5.1.

Experiment	limit on $T^{0\nu}_{1/2}$ ($\times 10^{23}$) yr	$T^{2\nu}_{1/2}$ ($\times 10^{19}$) yr	References
ELEGANT V	6.3×10^{-2}	$2.6^{+0.9}_{-0.5}$	[152]
Solotvina	1.7	$2.7^{+0.5}_{-0.4}(stat)^{+0.9}_{-0.6}(sys)$	[153]
NEMO-3	1.0	$2.7 \pm 0.04(stat) \pm 0.18(sys)$	[64]
Aurora	2.2	$2.63 \pm 0.01(stat)^{+0.11}_{-0.12}(sys)$	[49]

TABLE 5.1: Measured $2\nu\beta\beta$ half-life and limits on the $0\nu\beta\beta$ half-life for different experiments for ^{116}Cd.

5.1.2 $^{116}CdWO_4$ scintillating crystals

$CdWO_4$ is a well-known scintillator, it has a light yield of about 40% of the one of NaI(Tl) scintillators [154]. Its emission spectrum is in the visible range, peaked at 470 nm. It has a slow decaying time and hence cannot be used in high rate experiments. Of course, the element that we are interested in this crystal is cadmium that contains ^{116}Cd, candidate for $0\nu\beta\beta$ decay. The natural cadmium is composed of several isotopes with different isotopic abundance listed in Table 5.2.

Isotope	Abundance
^{106}Cd	0.012 45(22)
^{108}Cd	0.008 88(11)
^{110}Cd	0.124 70(61)
^{111}Cd	0.127 95(12)
^{112}Cd	0.241 09(7)
^{113}Cd	0.122 27(7)
^{114}Cd	0.287 54(81)
^{116}Cd	0.075 12(54)

TABLE 5.2: Isotopic abundance of the natural cadmium [69].

The first test of a scintillating bolometer based on natural $CdWO_4$ for $0\nu\beta\beta$ decay searches was reported in [92] almost two decades ago, where a 140 g crystal was coupled to a SiO-coated Ge LD. This detector was tested at the LNGS and showed the potential of using such a crystal [92] for $0\nu\beta\beta$ decay searches. The quenching factor of α particles was measured to be 0.18. A few years later, natural $CdWO_4$ crystals were used as an array of scintillating bolometers at the LNGS [155]. Four 213-g and one 426 crystals were coupled to LDs. This array provided complete separation between α and $\gamma(\beta)$ particles and the quenching factor of α particles was measured to be 0.18 [155]. In [156] the results from a test of a 510 g natural $CdWO_4$ crystal are reported, where similar performances were obtained.

However, the use of such crystal for $0\nu\beta\beta$ searches is limited by the presence of the long-lived isotope ^{113}Cd with Q_β = 322.5(1.0) keV [157] and half-life of $T_{1/2} =$

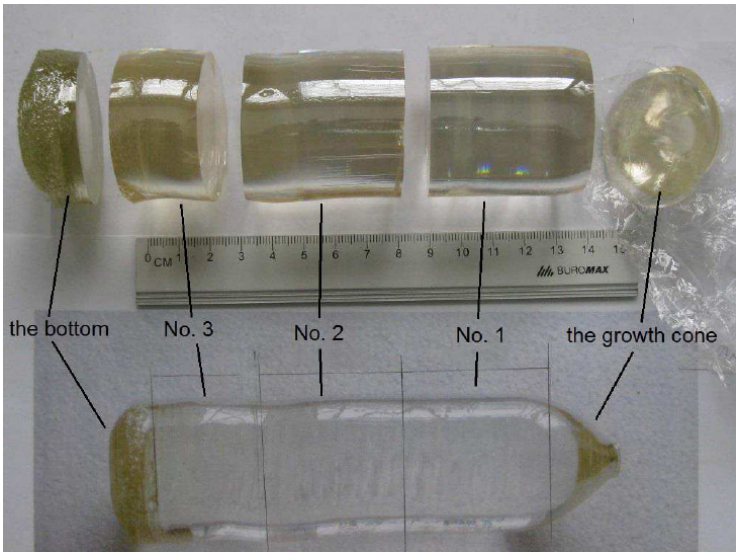

FIGURE 5.2: Photo of the crystal boule of enriched $^{116}CdWO_4$ taken from [162]. The crystals cut from the boule are: ⌀45×46.7 mm, 586.2 g, No. 1 (right), ⌀45×46.1 mm, 589.3 g, No. 2 (middle), and ⌀45.7×25.1 mm, 325.6 g, No. 3 (left). The bottom and the growth cone of the boule are indicated in the picture.

$(8.05 \pm 0.05) \times 10^{15}$ yr [158] that decays via a single beta decay. If one aims to build a $0\nu\beta\beta$ decay experiment with scintillating bolometers based on natural $CdWO_4$, the presence of ^{113}Cd will affect the background spectrum with pile-ups in the ROI of ^{116}Cd $0\nu\beta\beta$ decay. Another issue caused by this long-lived isotope present in natural crystals of $CdWO_4$ is that it has a high thermal neutron capture cross-section [159] (with a resonance at 178 meV) which provokes the emission of high energy γ between 2.81 and 9.04 MeV.

To overcome the long-lived isotope issue, it is necessary to use $CdWO_4$ crystals enriched with the $0\nu\beta\beta$ decay candidate ^{116}Cd with an enrichment close to 100%. The enrichment cost is relatively low and is done with the centrifuge separation method. The crystal growth is performed using the low-thermal-gradient Czochralski technique [160]. The first experiment to produce such crystal enriched in ^{116}Cd was the Solotvina experiment using the Czochralski technique. They published the results from 0.51 kg of enriched $CdWO_4$ crystal with 83% of ^{116}Cd in 1995 [161]. After that, they used 0.33 kg of enriched $CdWO_4$ to set the most stringent limit on the $0\nu\beta\beta$ decay of ^{116}Cd [153]. In 2011, a 1.9 kg crystal boule enriched with ^{116}Cd at 82% was produced for double-beta decay searches [68]. This crystal boule was cut in three almost cylindrical scintillating elements with a mass of 582 g, 581 g, and 334 g. In Fig. 5.2, a picture of the crystal boule and how it was cut is shown. The two crystals with larger masses (total mass of 1.116 kg) were used by the Aurora experiment as room temperature scintillators at LNGS. The collaboration achieved the most stringent limit on the $0\nu\beta\beta$ decay of ^{116}Cd [49].

The motivation to operate enriched $^{116}CdWO_4$ as scintillating bolometers is drawn by an above-ground test made at IJCLab (ex CSNSM) in Orsay with a 34 g crystal [163]. Promising and encouraging results were achieved with this small crystal in terms of energy resolution, light yield, particle discrimination, and radiopurity. As mentioned, the first test of massive enriched $^{116}CdWO_4$ crystals operated as scintillating bolometers was performed during this thesis.

5.2 Experimental setups

Two large massive $^{116}CdWO_4$ crystals (579.83 g and 582.42 g), denoted here as No. 1 and No. 2 and used previously by the Aurora experiment [49], were operated as scintillating bolometers. The twin crystals were installed in two different underground laboratories: $^{116}CdWO_4$ No. 1 at LSM and No. 2 at LSC. In this section, a detailed description of the detector construction and installation will be given.
The assembly of the two detectors was done during fall 2018 at IJCLab in France. As described in Chapter 2, the detector construction always follows the same steps: copper support cleaning, NTD, and heater gluing and assembly. Since the cleaning and the gluing procedure were the same for both samples, we will describe them once in the following.

5.2.1 Copper cleaning

The copper that keeps the crystal and the LD is the closest item to the crystal. Thus it must be clean and radio-pure. We follow a strict procedure to clean it by chemical etching using citric acid. The cleaning procedure used during this thesis can be summarized as follows:

- preliminary cleaning with soap made of a mixture of 5% of Micro-90 soap and ultrapure water. The copper is put in this mixture for about 15-20 min in an ultra-sonic bath at $\sim 50°C$, then rinse with ultrapure water. This pre-cleaning allows to remove the grease from the copper and prepare it for the chemical etching;

- a first chemical etching is done with a diluted citric acid solution $(4 \pm 2)\%$ in ultrapure water and (0.5-2%) of hydrogen peroxide (to activate the reaction). The holder is bathed in the citric acid solution for 30-45 min (the time depends on the size of the holder) in an ultrasonic bath at $\sim 50°C$. The solution should turn blue at the end of the procedure and the copper should be rinsed with ultrapure water. This step removes about 10-20 μm of the copper surface;

- the copper is bathed a second time in a citric acid solution (with the same composition) for 15 min at T $\sim 50°C$ and then rinsed with ultrapure water. This step will remove about 3-5 μm of the copper surface;

- once the copper rinsed, it should be dried and wiped very well to avoid its oxidation;

- the last step is passivation of the surface: the copper is put in the oven at $\sim$ 50°C for one hour. The time of annealing depends on the size and the shape of the pieces.

5.2.2 Thermal sensor gluing

The first step to build a bolometer is to connect the thermal sensor (the NTD, in our case) to the absorber (the crystal). NTDs are glued directly to the crystal surface. In our case, we used Araldite® rapid glue with two components. This glue was tested to have low radioactivity and to be suitable for low background experiments.
For the twin $^{116}CdWO_4$ crystals, the gluing was performed using the tool presented in Chapter 2. The gluing steps are the following:

- the NTD is kept on the mechanical arm with the help of a pump. It should be positioned according to where we want to have the gold pads to perform the bonding;
- the crystal is placed on the movable platform where we can adjust the height and the position of the x-axis;
- a Mylar® mask is placed on the crystal at the edge where we want to glue the NTD. This mask will ensure a 50 μm gap between the NTD and the crystal;
- the glue is prepared by mixing the two components for 30 s carefully to remove all the bubbles that could appear;
- the 6 pogo-pin matrix is immersed in the glue. The amount of glue has to be sufficient on the pogo-pin to ensure that enough glue will be put on the crystal;
- the pogo-pin is then lowered toward the crystal and the six distinct glue spots are deposited on the crystal inside the area delimited by the Mylar® mask;
- the NTD is lowered toward the crystal and positioned in a way that its edges will be on the two sides of the Mylar® mask as shown in the left panel of Fig. 5.3. Once the position is well-defined, the NTD is kept with the pressure of the mechanical arm for one hour.

The final results of the gluing procedure of NTD on a crystal are shown in Fig. 5.3. It should be noted that the gluing procedure for the LD is very similar to this one, except that the pogo-pin is not used, the glue is deposited on the Ge wafer as a veil.

5.2.3 $^{116}CdWO_4$ scintillating bolometer at LSM

The right panel of Fig. 5.3 shows the crystal with the heater [90] and NTD glued. We used a HP-Ge wafer (⌀44×0.175 mm) as a LD, coated with SiO to increase light absorption, on which a small NTD (3×0.9×1 mm) was glued. The crystal was mounted in a radio-pure copper holder, used previously by LUMINEU [109],

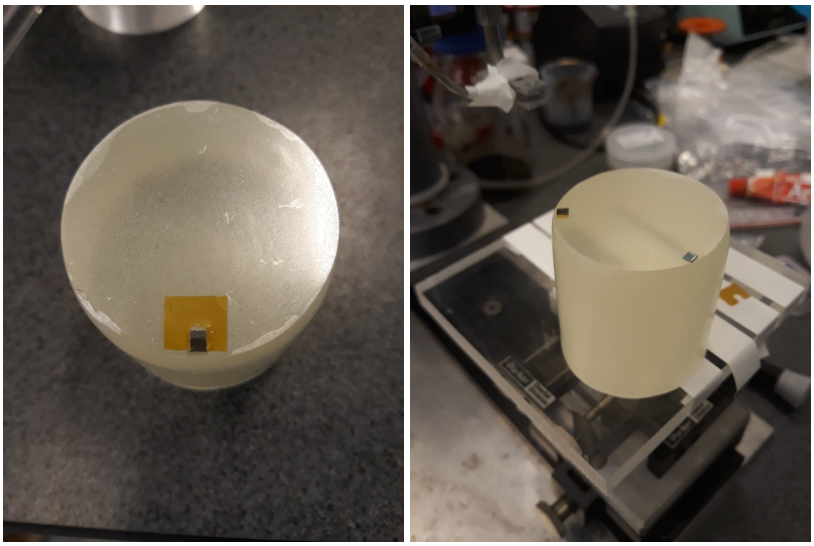

FIGURE 5.3: *Left:* $^{116}CdWO_4$ crystal with Mylar® mask that allows keeping a 50 μm gap between the NTD and the surface of the crystal. *Right:* $^{116}CdWO_4$ crystal with NTD and heater glued.

cleaned according to the procedure described above. The inner surface of the copper holder, facing the crystal, was covered with a reflecting foil to improve the light collection. The light detector was mounted in a different copper holder, as shown in Fig. 5.4.

This detector was installed in the EDELWEISS-III underground facility (described in Chapter 2) at LSM in November 2018. In addition to the cryostat external damping system, the $^{116}CdWO_4$ No. 1 is installed in a suspended tower to reduce vibrations. In Fig. 5.5, the detector position in the cryostat is shown; it was suspended with springs and placed in the bottom part of the experimental volume.

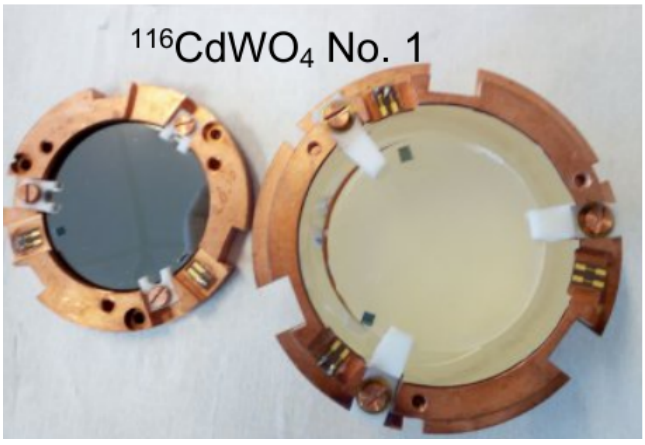

FIGURE 5.4: The $^{116}CdWO_4$ crystal in its copper holder fixed with the PTFE clamps. The Ge LD is also fixed with the PTFE clamps.

FIGURE 5.5: The $^{116}CdWO_4$ scintillating bolometer installed in the EDELWEISS cryostat.

Most of the data were collected at 20.7 mK and 22 mK. We accumulated 109 days at 20.7 mK and 119 days at 22 mK of background. The detector calibration was performed using γ quanta of a mixed $^{232}Th/^{238}U$ source available in the setup. The LD detector calibration at LSM was performed using the activation product of neutron irradiation with an AmBe source (2×10^5 neutrons/s); the ^{70}Ge was activated to ^{71}Ge that decays to ^{71}Ga through electron capture ($T_{1/2} = 11.43$ d). A detailed description of the data and the analysis performed will be presented in Sec. 5.3.

5.2.4 $^{116}CdWO_4$ scintillating bolometer at LSC

The $^{116}CdWO_4$ No. 2 ($\oslash45\times46.7$ mm) was equipped with NTD, heater, and LD in the same way as for detector No. 1. We used a CUPID-Mo like radio-pure copper holder style to mount the crystal and the LD in the same housing, as shown in Fig. 5.6. A reflecting foil was introduced in the copper holder. This detector was installed in the C2U facility located at LSC in April 2019 during the commissioning phase until July 2019. This time corresponds to what we call here RUN0 of the C2U facility. The detector was fixed on the 10 mK plate without any mechanical decoupling as shown in Fig. 5.7.

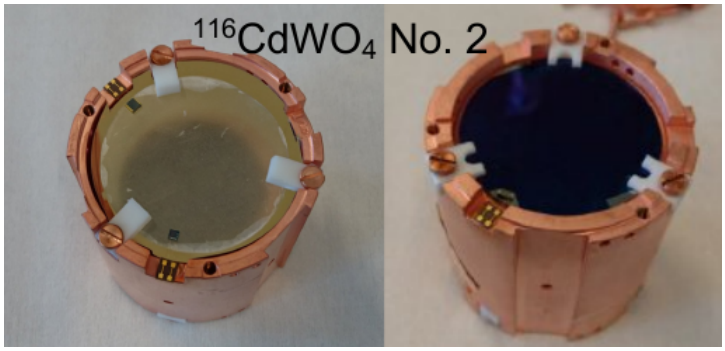

FIGURE 5.6: The $^{116}CdWO_4$ No. 2 scintillating bolometer. *Left:* the crystal is fixed with L shape PTFE pieces in the copper holder. *Right:* the LD is fixed in the same copper holder as the crystal with the help of PTFE clamps.

FIGURE 5.7: $^{116}CdWO_4$ scintillating bolometer fixed on the 10 mK plate of the C2U cryostat.

During this run, the $^{116}CdWO_4$ No. 2 scintillating bolometer has faced different configurations in terms of upgrades done on the lead shielding in the C2U facility. The shielding was built in several stages between April and July 2019. The collected data were split into three data sets according to the different upgrades. The first lead shielding stage corresponds to the first 15 cm of lead in April 2019 around the OVC (denoted here as Stage I). The second stage is with an additional 25 cm of temporary lead bricks on the top of the first layer of the lead shielding, we will refer to this stage as Stage II. The last stage is the last 10 cm of lead added to the first (denoted Stage III) around the OVC. These different stages are shown in Fig. 5.8. Table 5.3 gives a summary of the statistics registered for each stage. In this thesis, only the performances of Stage I will be presented as the performances of the other stages are very similar. The only difference between the three stages is the background level that was reduced between Stage I and Stage III.

Shielding Stage	date	Time (h)
Stage I	April 2019	408
Stage II	June 2019	115
Stage III	July 2019	18

TABLE 5.3: Data sets for each lead shielding stage.

FIGURE 5.8: Lead shielding stages. *Up left*: the first 15 cm of lead installed in April 2019 (Stage I). *Up right*: 25 cm of temporary shielding above the 15 cm in June 2019 (Stage II). *Bottom*: Complete lead shielding in July 2019 with 25 cm of lead bricks above (Stage III).

This detector was reinstalled during fall 2019 in another configuration with a scintillating bolometer based on natural $CdWO_4$ that was previously measured in Modane in 2017. This latter was constructed in the same way as the enriched one. However, as a bolometric light detector, we couple the natural $CdWO_4$ crystal to a Neganov-Trofimov-Luke Ge LD to have the possibility to enhance our signal (see Chapter 2). This detector was studied to perform a low energy threshold analysis for axial-vector coupling possible g_A quenching measurement [39], the analysis procedure and the results will be presented in Sec. 5.5.

The two detectors, mounted as a tower, were connected to the cryostat with the help of a spring to mitigate the cryostat vibrations as shown in Fig. 5.9. We will refer to this second installation of the enriched $^{116}CdWO_4$ No. 2 as RUN2. In addition to the two detectors described here, a second tower containing scintillating

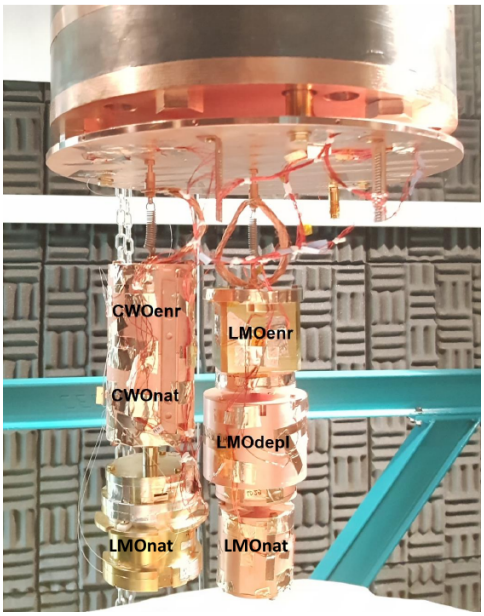

FIGURE 5.9: $CdWO_4$ and Li_2MoO_4 towers suspended to the 10 mK plate of the C2U cryostat with the help of a stainless steel spring.

bolometers based on Li_2MoO_4 crystals was installed [164], as illustrated in Fig. 5.9.

The selected data accumulated during this run corresponds to 714.5 h of background at 12 mK. A detailed description of the data and the analysis performed on the two detectors will be given in Sec. 5.3.

5.3 Data analysis

5.3.1 Data processing

Data are collected continuously as a stream with a sampling frequency of 500 Hz for the detector at LSM and 2000 Hz for the detector at LSC and they were processed offline using the optimum filtering technique [103]. The data processing is done using a tool developed at IJCLab in [102] written in MATLAB. The processing steps using this tool are the following:

- step 1: definition of the pulse window length that could contain a full thermal pulse. In Table 5.4, the window length used for the heat and light channels for the detectors at LSM and at LSC are given;
- step 2: build the template for the average pulse. This is done manually by selecting a certain number of good particle events in a given amplitude range (e.g., around 2.6 MeV for the heat channel). The same step is performed to generate the average noise. Examples of an average pulse for the heat and the light channels from the $^{116}CdWO_4$ No. 1 are given in Fig. 5.10;

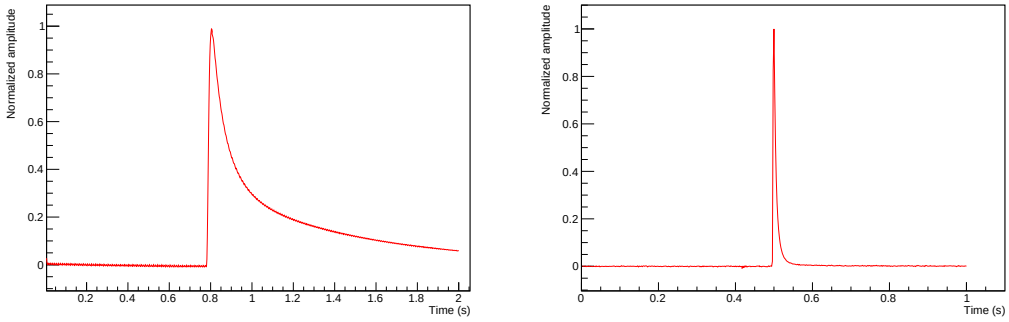

FIGURE 5.10: Examples of average pulses from the enriched $^{116}CdWO_4$ at LSM. The *left* panel represents the 2-s length average pulse of the heat channel and the *right* one the 1-s length of the light channel.

- step 3: trigger. The trigger flags an event if it has the minimum requirement based on two parameters set manually: the threshold (usually set to 5 times the standard deviation of the baseline) and the correlation. The correlation is the Pearson correlation coefficient between the event that passed the threshold and the average pulse. An event is seen as a good event if its amplitude exceeds the threshold and if its correlation parameter exceeds the value of the set one;
- step 4: filter the amplitude of the triggered events using the optimum filtering technique.

type of mean pulse	window length (s)
heat at LSM	2
light at LSM	1
heat at LSC	2.5
light at LSC	0.5

TABLE 5.4: Pulse window length analysis for the heat and the light channels at LSM and LSC.

At the end of the processing, the output file is an n-tuple containing all the evaluated parameters. They are fourteen in total, but we will use only: the trigger position, the filtered amplitude, the fitted amplitude, the correlation, the baseline level, and the baseline RMS. A description of these parameters will be given later in the text. The processing steps are applied both to the light and to the heat channels. The only difference is that light detector data were also triggered by the heat channel events to search for heat-light coincidences.

5.3.1.1 Stabilization

Once we have our n-tuple, data are not ready yet to be exploited as the amplitude needs a correction due to the thermal gain of the bolometer that depends on its temperature. The stabilization can be performed using any mono-energetic population of events, as follows:

$$Stabilized\ amplitude = constant.\frac{Amplitude}{a \times Baseline + b} \tag{5.1}$$

where a and b are the first-order polynomial fit of the *Amplitude* versus *Baseline* for the selected population. *constant* is an arbitrary value to which the stabilized amplitude is set.
The pulse amplitude of the bolometer installed at LSM was corrected into two steps on a run by run basis:

- isolating the heater with a pulse shape cut and use it to stabilize the data as a first stage [90];
- use the ^{238}U-α line present in the crystal to correct the residual slope that remains after the standard stabilization with the heater. In Fig. 5.11, an example of the ^{238}U-α line before and after the stabilization is shown.

For the detector installed at LSC, the stabilization was performed using the heater only. An illustration of this stabilization is shown in Fig. 5.12.

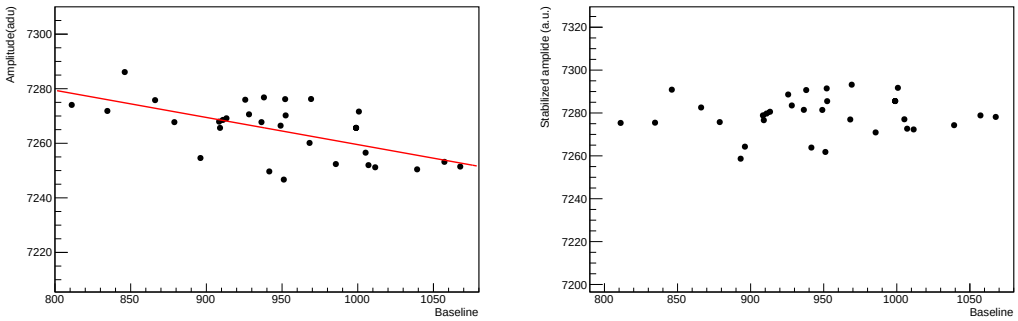

FIGURE 5.11: ^{238}U-α events of the $^{116}CdWO_4$ No. 1 before (*left*) and after (*right*) the stabilization procedure. The data points are represented in black and the fit line in red.

5.3.1.2 Calibration

Once the stabilization is performed, the amplitude is ready to be calibrated. For both detectors at LSM and LSC, the calibration is performed run by run.

For the $^{116}CdWO_4$ at LSM, the stabilized amplitude is converted to energy in keV using γ line from the ^{232}Th/^{238}U calibration source in calibration data. The

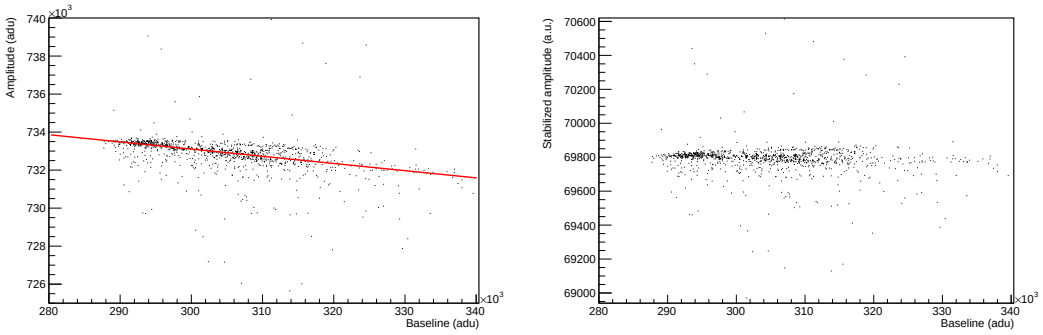

FIGURE 5.12: Heater events of the $^{116}CdWO_4$ No. 2 before (*left*) and after (*right*) the stabilization with the pulser. The data points are represented in black and the fit line in red.

stabilized amplitude corresponding to each γ line used is fitted with a first-order polynomial. It should be noted that the calibration needs an improvement when applied to background data; for this purpose, the calibration is improved (especially at low energy) using the prominent γ peaks in the background data. The LD detector calibration was done using the 10.37 keV X-rays from ^{71}Ge that decays to ^{71}Ga through electron capture ($T_{1/2} = 11.43$ d).

For what concerns data at LSC, since the lead shielding was not completed in RUN0, the background was still high enough to provide γ lines to perform the detector calibration. In RUN2, the environmental background was reduced thanks to the lead shielding upgrade. Therefore, a calibration source was needed to convert the amplitude of the detector to energy in keV. In the CROSS setup, the calibration source is a tungsten thoriated wire inserted between the lead shielding and the OVC. The calibration of the pulse amplitude was done with γ lines from ^{232}Th present in the wire. To calibrate the LD, it was permanently irradiated by a weak ^{55}Fe X-ray source.

5.3.2 Detector performances

5.3.2.1 Performances of the $^{116}CdWO_4$ crystals at LSM and LSC in RUN0

The results presented here were published in an LTD18 proceeding [165] and they correspond to 100 h of calibration and 1000 h of background data collected with the $^{116}CdWO_4$ No. 1 at 20.7 mK at LSM, and 400 h of background data collected with the sample No. 2 at 10 mK at LSC.

The baseline resolution (FWHM) was measured to be 2.3 keV for the No. 1 and 10.1 keV for No. 2. The difference in the noise between the two detectors is because sample No. 2 was not decoupled from the pulse tube cryostat in RUN0 adding vibrational noise that worsened the baseline resolution. Concerning the LD we observe a FWHM of the baseline of 150 eV and 360 eV for samples No. 1 and

No. 2, respectively.

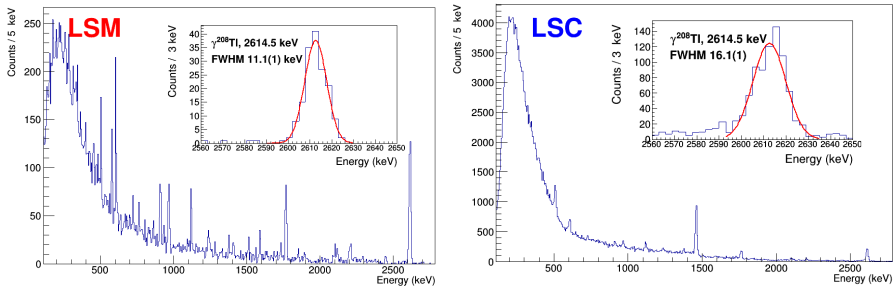

FIGURE 5.13: *Left panel*: the energy spectrum measured by the $^{116}CdWO_4$ detector No. 1 over $\sim$ 100 h of $^{232}Th/^{238}U$ calibration at LSM. The energy resolution is 11.1(1) keV FWHM at 2615 keV as shown in the inset. *Right panel*: the energy spectrum of the $^{116}CdWO_4$ detector No. 2 accumulated during $\sim$ 400 h of background measurements at LSC. The energy resolution for this detector is 16.1(3) keV FHWM at 2615 keV (inset). The lead shield is not completed, γ peaks from natural radioactivity are visible in the spectrum.

The energy spectra measured by the $^{116}CdWO_4$ scintillating bolometers are presented in Fig. 5.13. Both detectors showed a high energy resolution at 2615 keV: 11.1(1) and 16.1(3) keV FWHM for No. 1 and No. 2 respectively. This resolution is about one order of magnitude better than the energy resolution of scintillation counters based on these same crystals [49].

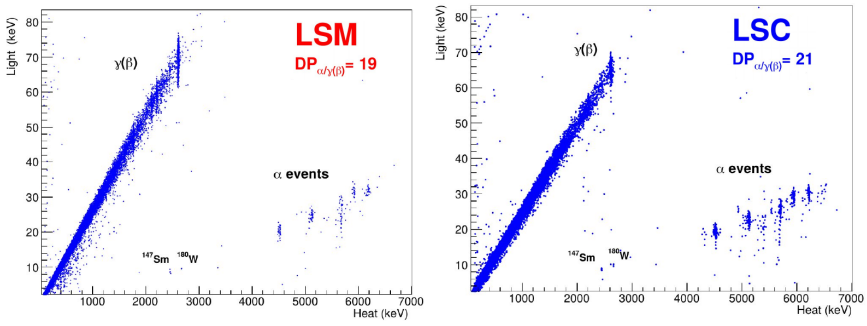

FIGURE 5.14: Scatter plots of light-versus-heat of the $^{116}CdWO_4$ detector No. 1 accumulated over $\sim$ 100 h of gamma calibration (*left panel*), and of the detector No. 2 accumulated over $\sim$ 400 h of background measurements (*right panel*).

To remove the α background, we produced the so-called scatter plot with light amplitudes in coincidence with heat ones (in keV) as presented in Fig. 5.14 where we see the separation between $\gamma(\beta)$ and α particles. It should be noted that the heat channel is calibrated with γ quanta which induce a 5% shift in energy for α

particles due to thermal quenching [166].

The light yield of $\gamma(\beta)$ particles, $LY_{\gamma(\beta)}$, between 0.5 and 2.7 MeV is 27.3(1) and 25.2(1) keV/MeV for $^{116}CdWO_4$ scintillating bolometers No. 1 and No. 2 respectively. The evaluation of the discrimination power $DP_{\alpha/\gamma(\beta)}$ between $\gamma(\beta)$ and α, using the LY in the 2.5–7 MeV energy interval, gave $DP_{\alpha/\gamma(\beta)}$ of 19 for the detector installed at LSM and 21 for the one at LSC. The difference in the $DP_{\alpha/\gamma(\beta)}$ is probably due to the difference in the LD noise.

5.3.2.2 Performance of the $^{116}CdWO_4$ in RUN2 at LSC

In this run, the detector was mechanically decoupled from the cryostat, which allows canceling the vibrational noise. This was noted in the FWHM resolution that was measured to be 3.1 keV at 12 mK. The enhancement of the performances was also observed in the LD with a baseline noise of 217 eV, which allows seeing the ^{55}Fe X-rays doublet as shown in Fig. 5.15 from the calibration source.

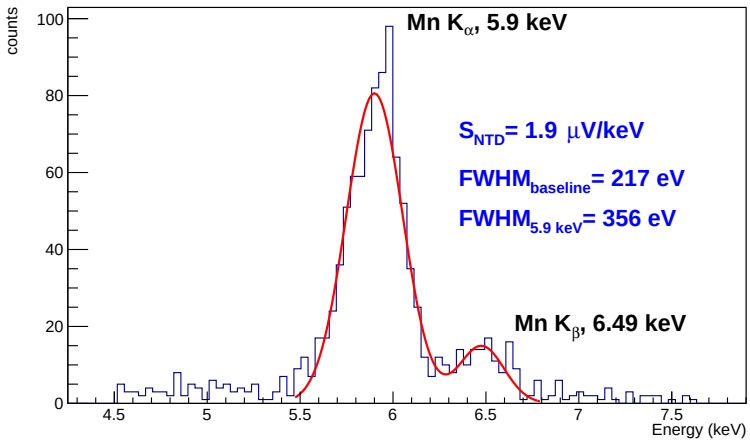

FIGURE 5.15: ^{55}Fe X-ray doublet energy spectrum of the light detector accumulated over 100 h.

The FWHM resolution of the ^{208}Tl γ line was measured to be 8.8(3) keV. An example of a calibration energy spectrum at 12 mK is shown in Fig. 5.16. The installation of an internal damping system improved the performance of the enriched $^{116}CdWO_4$ detector and showed that the UQT [106] of the CROSS cryostat efficiently reduce the noise in the vertical direction, but not much in the horizontal direction.

The measured LY in this run agreed with what was measured previously in RUN0 (25.1 keV/MeV). We also observe a similar $DP_{\alpha/\gamma(\beta)}$ of 25. The scatter plot of the LY as a function of the energy is shown in Fig. 5.17. The quenching factor of

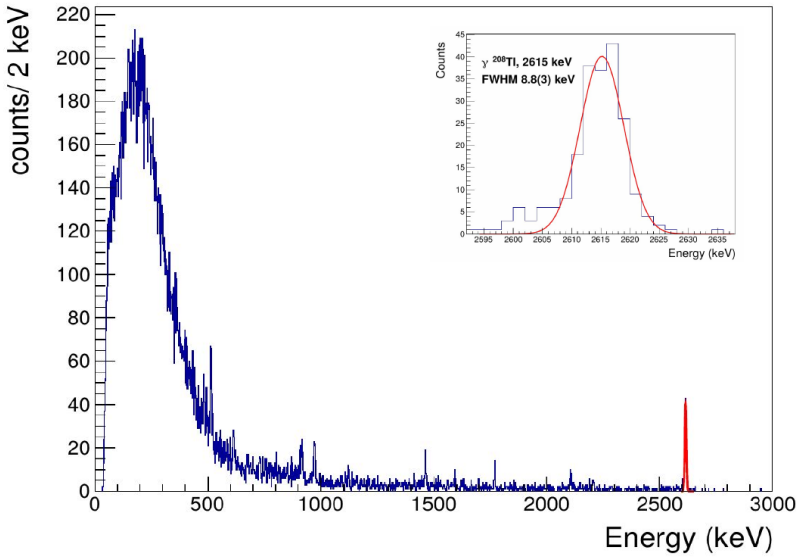

FIGURE 5.16: Example of 37 h of ^{232}Th calibration energy spectrum measured by the $^{116}CdWO_4$ detector No. 2 at LSC. The energy resolution is 8.8(3) keV FWHM at 2615 keV as shown in the inset.

α particle for γ ones is measured to be 15%, which is in agreement with what was measured in RUN0 and what was measured in $CdWO_4$ scintillating bolometers [166].

The particle events in the data are selected using a pulse shape cut based on the correlation parameter obtained at the end of the processing. The selected background data accumulated over 715 h with the $^{116}CdWO_4$ detector in RUN2 at LSC is presented in Fig. 5.18. We clearly see the contribution from the beta decays of ^{113}Cd (I.A = 2.14(6)% [68], Q_β = 324 keV [157], $T_{1/2} = 8 \times 10^{15}$ yr [158]) and ^{113m}Cd (Q_β = 583 keV [157], $T_{1/2}$ = 14.1 yr). We do not have a clear and solid explanation for the presence of ^{113m}Cd. γ peaks from the environmental background are visible in the spectrum because the CROSS shielding was not completed yet. An anti-radon box and a muon veto are foreseen to improve the C2U shielding.

We have evaluated the efficiency of this detector at the trigger level and with the quality cuts applied on the background spectrum shown in Fig. 5.18. The whole procedure to evaluate the trigger and the cut efficiency will be described in Sec. 5.5 as it was developed for the natural $CdWO_4$ scintillating bolometer. The efficiency as a function of the energy is presented in Fig. 5.19 as well as the fit of the efficiency profile.

5.3.2.3 Radioactive contamination of the crystals

One of the goals of the test of these two detectors was to evaluate their radio-purity in terms of α contamination. Thanks to the high $DP_{\alpha/\gamma(\beta)}$ (see Fig. 5.14), we distinguish several α contamination present in both crystals.

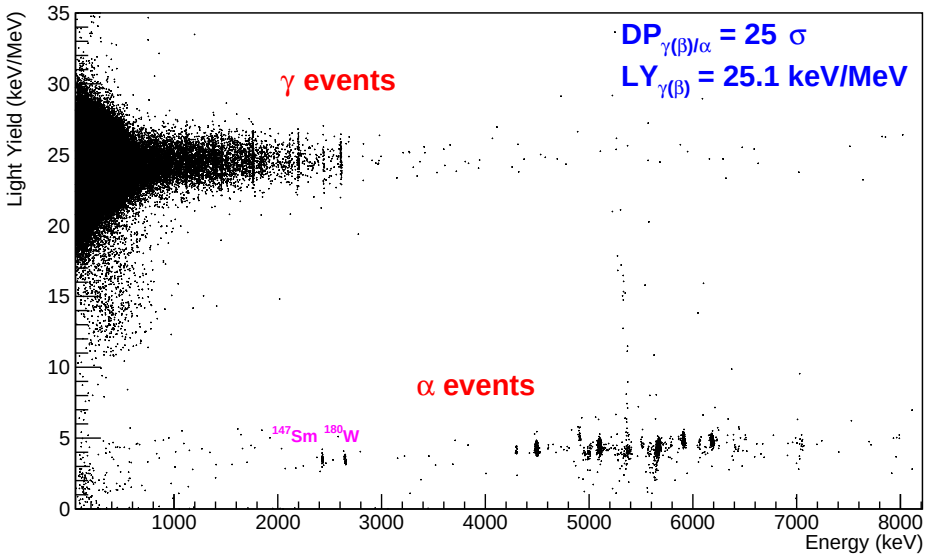

FIGURE 5.17: Light yield versus energy for background data from RUN2 at LSC. The $\gamma(\beta)$ and the α bands are separated at more than 99.99%. The measured light yield is 25.1 keV/MeV.

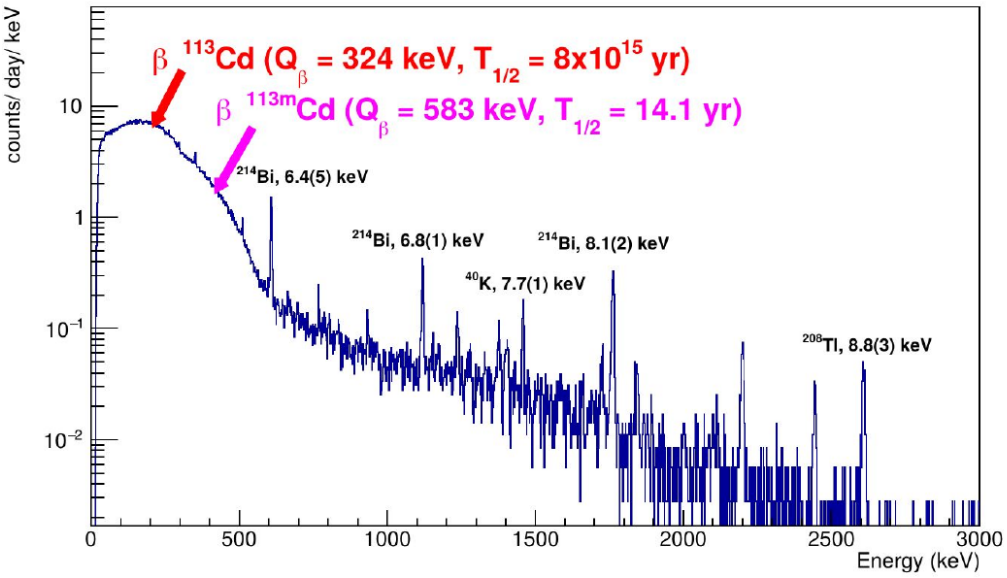

FIGURE 5.18: Background spectrum accumulated over 715 h with the enriched $^{116}CdWO_4$ at LSC. Most prominent γ peaks are labeled with their FWHM resolution.

In the 2.4–2.7 MeV energy range (calibrated by γ quanta), we observe two different populations in the twin crystals. Alpha events at 2670 keV are expected from the decay of ^{180}W, present in the crystal (I.A. = 0.12% [69]), with Q_α = 2515.3 keV [157].

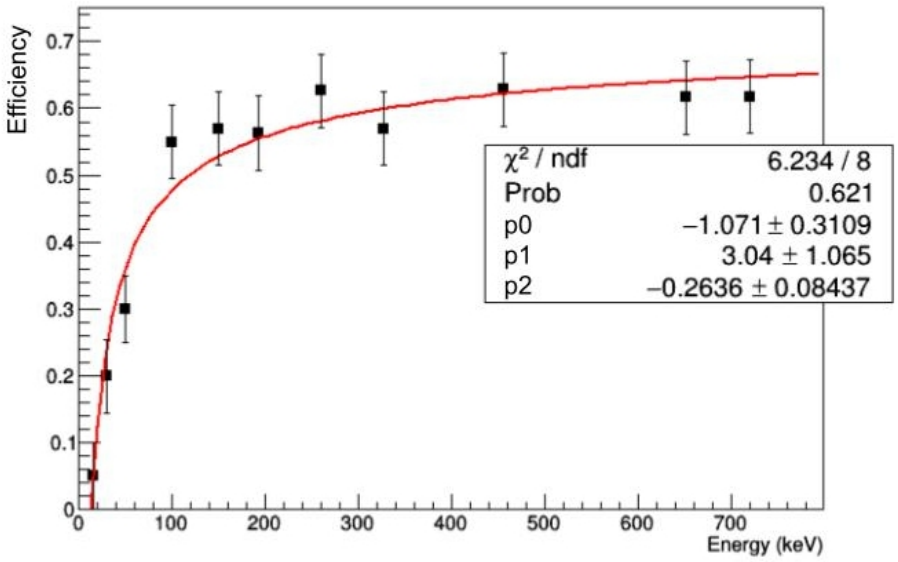

FIGURE 5.19: Efficiency of the $^{116}CdWO_4$ No. 2 measured at the trigger level and after the offline quality cuts. The black dots represent the efficiency at each energy and the red line represents the efficiency fit profile.

The second population, observed at 2455 keV, corresponds to the α decay of ^{147}Sm with Q_α = 2311.0 keV [157]. The ^{147}Sm was not detected when the two detectors were operated as room temperature scintillators [49] due to poor energy resolution. The measured activities of ^{147}Sm and ^{180}W are at the level of 0.02 mBq/kg and 0.01 mBq/kg respectively.

In the energy region above 4 MeV, α events from U/Th chains are present. We observe the chains of ^{232}Th, ^{235}U and ^{238}U and their daughters. The activities of the different α contamination are evaluated using the background spectra presented in Fig. 5.20. The radioactive contamination in ^{238}U/^{232}Th of the $^{116}CdWO_4$ crystals was observed in the Aurora experiment [49]. On top of that, thanks to the double readout of the detectors, we could distinguish other radioactive contamination in these crystals operated as scintillating bolometers. Moreover, we could improve the measurement of the radioactive contamination thanks to the high energy resolution achieved with these scintillating bolometers. We clearly see the ^{235}U line with its daughter ^{231}Pa and two other prominent peaks at 5636 keV and 5902 keV (calibrated with α events). We assume that these two populations are ^{241}Am and ^{244}Cm with Q_α = 5638 keV and Q_α = 5902 keV respectively [157]. The radioactive contamination of the $^{116}CdWO_4$ crystals by alpha-active radio-nuclides is given in Table 5.5. As expected from [49, 68], the radio-purity of the crystal No. 1 is higher because it was cut from the upper part of the crystal boule. This effect is expected because of the segregation of contaminants during the cadmium tungsten crystal growth [167].

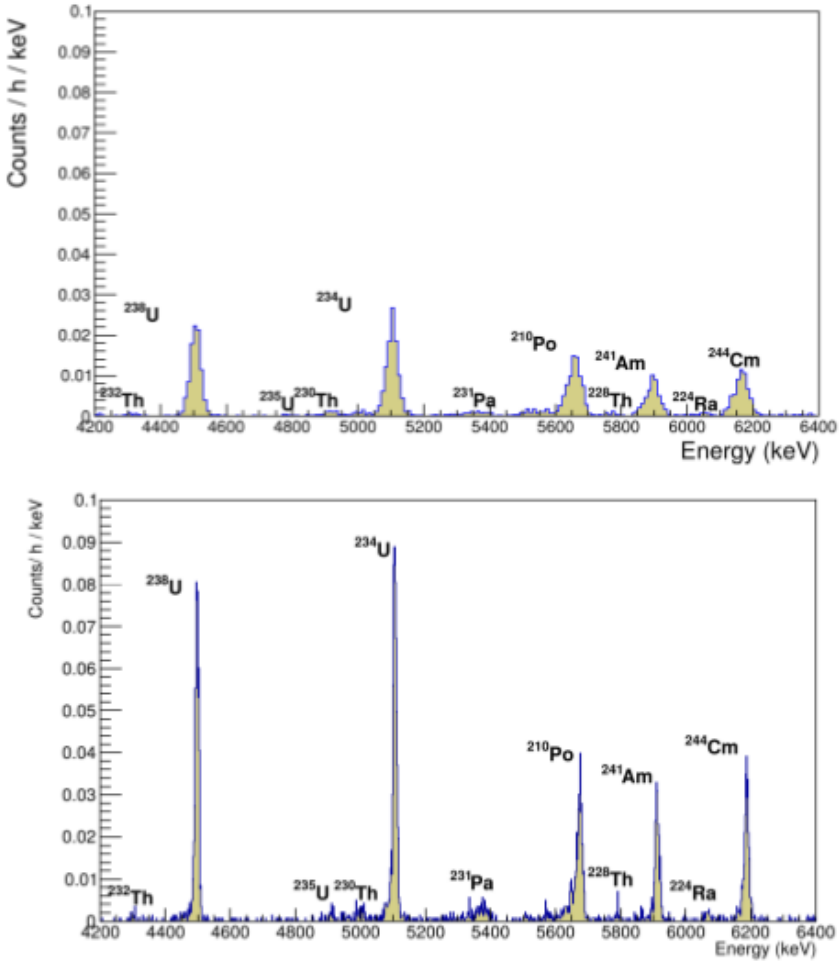

FIGURE 5.20: Energy spectra of α events accumulated in background measurements with the 0.6 kg $^{116}CdWO_4$ scintillating bolometers No. 1 (228 days, *top panel*) and No. 2 (30 days, *bottom panel*). Both spectra were calibrated with γ quanta.

A summary of the performances of the two $^{116}CdWO_4$ scintillating bolometers is given in Table 5.6 extracted from calibration data for detector No. 1 and from background data for the detector No. 2 in RUN0 and calibration data in RUN2. A small difference in the performances is observed between the data acquired at 20.7 and 22 mK. We observed a FWHM of the baseline of 2.3 keV at 20.7 mK and 3.1 keV at 22 mK. The detector showed good energy resolution at 2.6 MeV: 11.1 keV at 20.7 mK and 12.8 keV at 22 mK in calibration data. The light yield, evaluated between 0.5 and 2.6 MeV, is 27 keV/MeV.

Chain	Nuclide	Activity (mBq/kg)				
		No. 1 at LSM	No. 2 at LSC	Weighted mean	Combined value	Aurora [49]
	^{147}Sm	0.018(3)	0.019(5)	0.018(3)	0.018(2)	
	^{180}W	0.009(2)	0.010(4)	0.009(2)	0.009(2)	
	^{241}Am	0.12(1)	0.24(2)	0.14(1)	0.18(1)	
	^{244}Cm	0.19(2)	0.24(1)	0.23(1)	0.21(1)	
^{232}Th	^{232}Th	0.010(4)	0.013(4)	0.012(3)	0.011(2)	0.07(2)
^{238}U	^{238}U	0.29(2)	0.53(3)	0.36(2)	0.41(2)	0.58(4)
	^{234}U	0.32(6)	0.48(3)	0.45(3)	0.40(3)	0.60(1)
	^{210}Po	0.27(2)	0.34(2)	0.305(14)	0.30(1)	0.70(4)
^{235}U	^{235}U	0.021(2)	0.038(8)	0.022(2)	0.029(4)	
	^{231}Pa	0.037(6)	0.067(9)	0.046(5)	0.052(5)	

TABLE 5.5: Radioactive contamination of the $^{116}CdWO_4$ crystals No. 1 and No. 2 (also the weighted mean and the combined values for the whole crystal material are given). The results achieved by the Aurora experiment are given for comparison. The large different between the ^{210}Po activity measured in the present work and by the Aurora experiment is due the poor energy resolution in the Aurora experiment. The ^{210}Po activity includes also the contributions of ^{241}Am and ^{244}Cm not identified by the Aurora experiment.

	$^{116}CdWO_4$ No. 1		$^{116}CdWO_4$ No. 2	
Performance	20.7 mK	22 mK	Run0	Run2
$FWHM_{Baseline}$ (keV)	11.1	12.8	16.1	8.8
$FWHM_{^{208}Tl}$ (keV)	2.3	3.1	10	3.1
$FWHM_{Baseline}$ LD (eV)	150	–	360	217
$LY_{\gamma(\beta)}$ (keV/MeV)	27.3	–	25.2	25.1
$DP_{\alpha/\gamma(\beta)}$	19	19	21	25

TABLE 5.6: Summary of the performances of $^{116}CdWO_4$ No. 1 and $^{116}CdWO_4$ No. 2 scintillating bolometers at LSM and LSC respectively.

5.3.2.4 Description of the background data at LSM

We accumulated over 228 days of background data with the enriched $^{116}CdWO_4$ installed in the EDELWEISS cryostat at both 20.7 mK and 22 mK which corresponds to 0.36 kg.yr of physics data. To select the particle events, two types of cuts are applied offline on a run by run basis: a pulse shape cut, based on the correlation parameter to remove the pulser events and pile-ups, and a light yield cut to ensure a spectrum with only $\gamma(\beta)$ events. After that, the calibrated background is merged (data at 20.7 mK and 22 mK). The cut efficiency was evaluated to be $(91.5 \pm 1.6)\%$, we used two different γ peaks (^{208}Tl in calibration data and ^{40}K in background data) to estimate this number. In addition, we estimated the total efficiency of this detector (trigger+cuts) presented in Fig. 5.21 (for data at 22 mK) for both data at 22 and

20.7 mK to fully map the ability of the detector to see the particle interaction from the trigger level to the offline cuts. The procedure to obtain the efficiency profile will be described in Sec. 5.5. From Fig. 5.21, we note that the detector efficiency is more than 90% when the energy is higher than 700 keV. The resulting background spectrum accumulated over 228 days of physics data corrected with the measured efficiency is shown in Fig. 5.22.

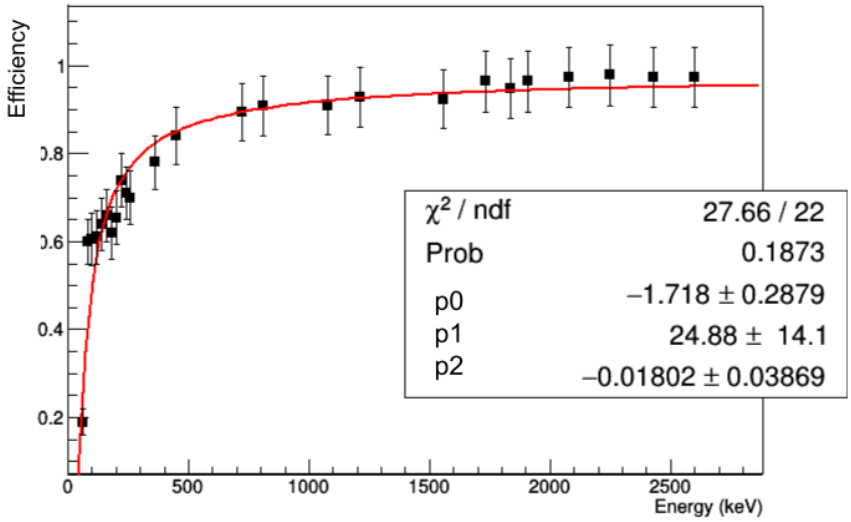

FIGURE 5.21: Efficiency curve of the enriched $^{116}CdWO_4$ No. 1 at 22 mK at LSM.

The background spectrum shows a clear contribution from the $2\nu\beta\beta$ decay of ^{116}Cd above 1 MeV. At lower energies (lower than 600 keV), the dominant contributions are from two single beta decays: the decay of ^{113}Cd and ^{113m}Cd. These two decays are also seen in the crystal installed at LSC as the two samples were cut from the same crystal boule. In addition to the internal beta decays, we observe several prominent γ peaks in the background spectrum: ^{60}Co doublet at 1170 and 1332 keV, ^{40}K at 1461 keV and ^{208}Tl at 2615 keV. This γ contamination comes from the environmental radioactivity in the experimental setup [104]. Furthermore, the EDELWEISS setup is not optimized for high-energy rare-event searches as it is a dark matter experiment [104].

We did not observe any evidence of the $0\nu\beta\beta$ decay of ^{116}Cd, zero events are observed around the $Q_{\beta\beta}$. Unfortunately, with only 0.36 kg.yr of physics data we cannot set a competitive limit on this decay where the current best one is from the Aurora experiment ($T_{1/2} > 2.2 \times 10^{23}$ at 90% C.L.) [49]. The exclusion sensitivity on the half-life of $0\nu\beta\beta$ decay of ^{116}Cd is presented in Fig. 5.23 assuming zero background. The limit obtained with the data accumulated with the enriched $^{116}CdWO_4$ at LSM is $T_{1/2} > 0.6 \times 10^{23}$ at 90% C.L.. However, it should be noted that with only

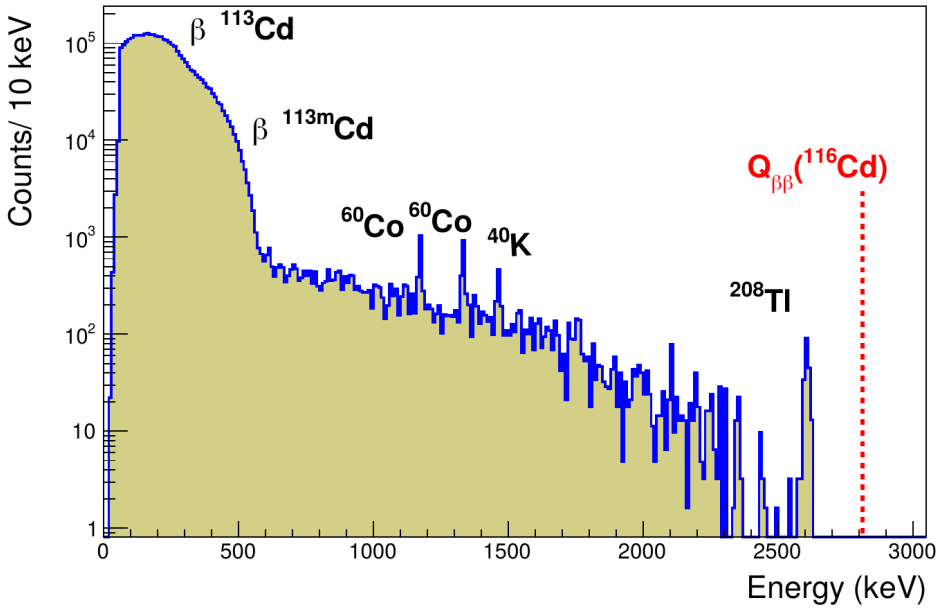

FIGURE 5.22: Spectrum of enriched $^{116}CdWO_4$ with 228 days of background at LSM. The most prominent γ peaks are labeled as well as the single beta decays of ^{113}Cd and ^{113m}Cd. The red dashed line indicates the $Q_{\beta\beta}$ of ^{116}Cd at 2813 keV.

1.31 kg.yr of exposure, it is possible to set the same limit on the half-life as the Aurora experiment [49] that used 4.68 kg.yr of exposure. The bolometric technology and the outstanding performances in terms of energy resolution and background rejection give the possibility to reduce the exposure time by a factor of $\sim$3 in the case of zero background conditions.

5.4 Preliminary results for $2\nu\beta\beta$ decay analysis

As mentioned, the main contribution in the 228 days background spectrum of the enriched $^{116}CdWO_4$ installed at LSM is the $2\nu\beta\beta$ decay of ^{116}Cd. In this section, the preliminary analysis performed to extract the half-life of this decay is described.

5.4.1 Background model

To have an estimation of the half-life of the $2\nu\beta\beta$ decay of ^{116}Cd with the $^{116}CdWO_4$ scintillating bolometer collected data, the experimental spectrum was fitted with a background model. This model is constructed based on what we observe in the data and the previous measurement of the crystal [49]. The internal α background gives indications about the beta decays that can occur at lower energy and hence contribute to the internal background of the crystal. Nevertheless, to construct the background model, we did not take into account the two main contributions to the

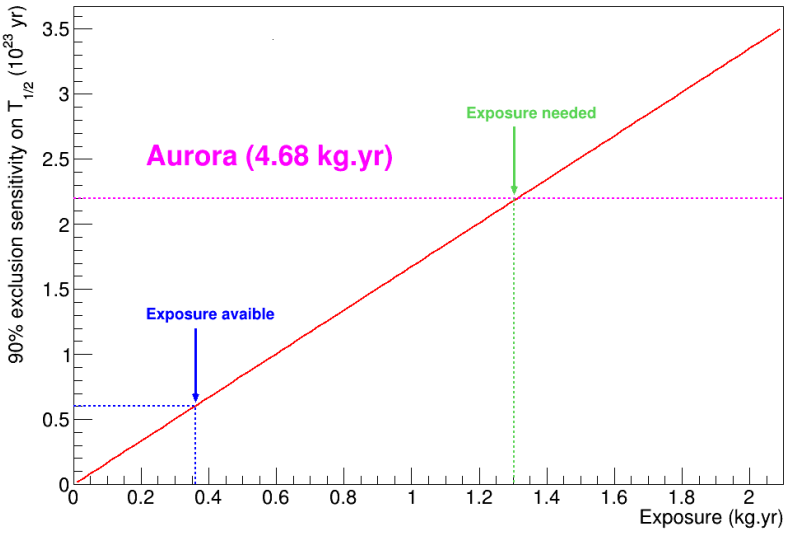

FIGURE 5.23: Exclusion sensitivity of the enriched $^{116}CdWO_4$ scintillating bolometer at LSM for zero background measured according to 228 days of physics data. The solid red line represents the exclusion sensitivity on the $T_{1/2}$ at 90% C.L., the blue dashed line is the achieved limit with 0.36 kg.yr of exposure, the pink dashed line indicates the current best limit on the $0\nu\beta\beta$ decay of ^{116}Cd, and the green dashed line illustrates the needed exposure to set a similar limit to Aurora.

spectrum for energies lower than 600 keV. These two contributions are the two single beta decay of ^{113m}Cd and ^{113}Cd with activities of 460(20)mBq/kg and 100(10) mBq/kg respectively [68]. Therefore, our model considers only the possible background contamination to the experimental spectrum for energies higher than 600 keV.

The background contributions taken into account in this model are listed in the following:

- $2\nu\beta\beta$, the signature of this decay is clearly observable in the spectrum. 10^7 events were simulated;
- the different beta decays from ^{238}U daughters that are added as internal contamination (^{210}Bi, ^{234m}Pa, ^{214}Bi, and ^{214}Pb);
- the different beta decays from ^{232}Th daughters that are added as internal contamination (^{212}Bi, ^{228}Ac, ^{208}Tl, and ^{214}Pb);
- internal ^{90}Y, ^{60}Co and ^{40}K;
- external ^{208}Tl, ^{228}Ac and ^{212}Bi (from ^{232}Th chain);
- external ^{60}Co and ^{40}K.

These different contributions are simulated using the GEANT4 package version 10.2.p02 [168] with initial kinematics given by the Decay0 event generator [169]. The obtained Monte-Carlo (MC) simulation spectrum was smeared by the FWHM as a function of energy:

$$FWHM(E) = \sqrt{c + b \times E} \tag{5.2}$$

where E is the energy and c, b are coefficients obtained from the fit of the FWHM of the γ peaks observed in the combined background spectrum versus the energy as shown in Fig. 5.24.

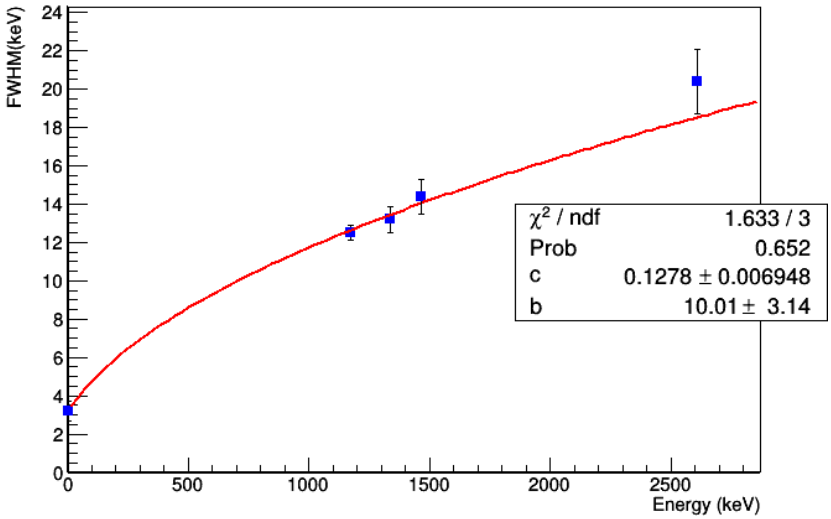

FIGURE 5.24: FWHM of $^{116}CdWO_4$ scintillating bolometer as a function of energy of the combined background spectrum at LSM.

5.4.2 Fit and result

The fit applied to the experimental background spectrum is constructed with the help of the background model described in the previous section. Each simulated MC contribution is used to fit the spectrum in a way that the global background model is constructed as the sum of all the fits of all the contributions, following:

$$Model(E) = p_0 \times MC_0(E) + p_1 \times MC_1(E) + p_3 \times MC_3(E) + ... = \sum_i p_i \times MC_i(E) \tag{5.3}$$

where, p_i is the fit parameter and $MC_i(E)$ is the MC model of each contribution. In total, to model the experimental spectrum, we used 16 MC simulated contributions. The fit parameter p_i plays the role of normalization of one MC contribution to the background model for the expected activity of this contribution. To bound the fit of each contribution, the MC is normalized to the unit and is bound according to the number of the expected event taking into account the fit interval and the binning. The expected activities are evaluated using the analysis of the α background for

the U/Th daughters and what we observe in the γ region of the physics spectrum. For example, to bound the fit of the ^{234m}Pa contribution, we used the activity of the parent ^{238}U. The fit of the external γ contribution is not bound and hence p_i is a free parameter.

The experimental spectrum was constrained using the binned Log-Likelihood

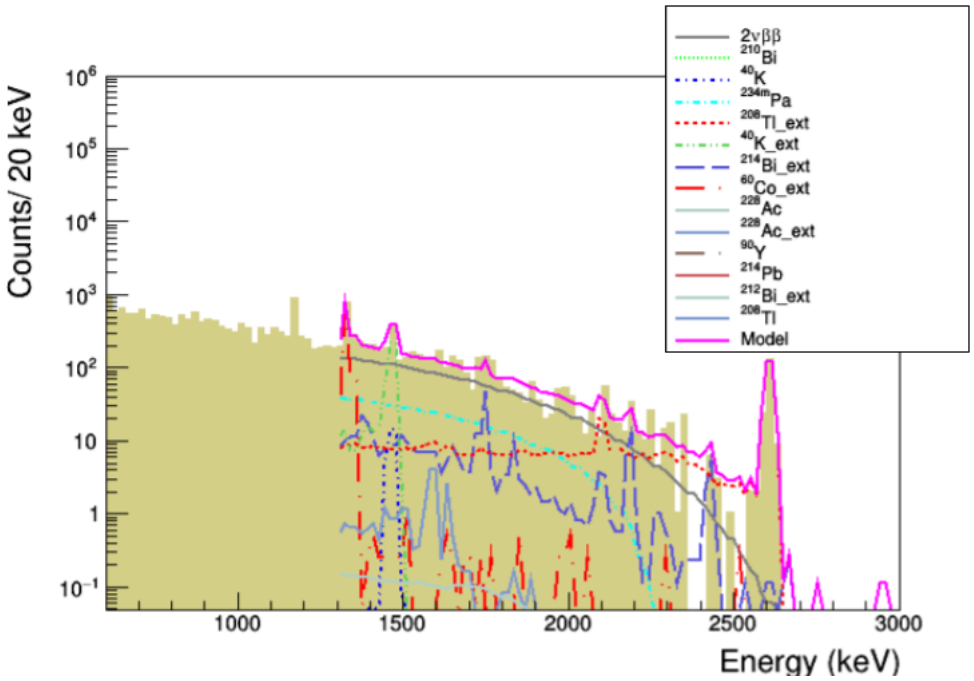

FIGURE 5.25: The energy spectrum of $\gamma(\beta)$ events accumulated over 0.36 kg.yr of physics data (golden histogram) and the background model fit in the energy range 1280–3000 keV in solid pink line. All the background contributions used to perform the fit are listed in the inset and the text.

method implemented in ROOT software package. Using the MC background model described above, we varied the fit range from the energy interval [600-1500] keV for the starting point and [2500-3200] keV for the final point with a step of 20 keV. The fit results are shown the Fig. 5.25. The best fit was achieved in the energy interval of [1280-3000] keV ($\chi^2/ndf = 4.9$), giving 5974.9 counts of the $2\nu\beta\beta$ decay of ^{116}Cd in this interval with a statistical error of 79.3 counts. The energy interval contains 29% of the $2\nu\beta\beta$ distribution. This number was evaluated considering the $2\nu\beta\beta$ containment using the MC simulation of the $2\nu\beta\beta$. The number of counts in the energy interval used for the fit is estimated and used to compute the ratio of $2\nu\beta\beta$ decay events to the total number of simulated events. Using the number of $2\nu\beta\beta$ events, the activity of ^{116}Cd in the $^{116}CdWO_4$ crystals is 1.795(7) mBq/kg. This activity was measured to be 1.138(5) mBq/kg by the Aurora experiment [49].

To estimate the half-life of the $2\nu\beta\beta$ decay of ^{116}Cd with the detector that we present here, we took into account the number of nuclei of ^{116}Cd ($N = 7.9 \times 10^{23}$) and the

$2\nu\beta\beta$ containment in the fit interval, we obtain:

$$T_{1/2} = (2.41 \pm 0.11) \times 10^{19} yr \tag{5.4}$$

Only the statistical error is taken into account obtained from the fit. This result is close to what was measured previously in the Aurora experiment [49] within the error bars. However, our background model is limited by the fact that it does not go below 600 keV where the single beta decays of ^{113}Cd and ^{113m}Cd are dominant. Furthermore, our fit model is currently not representing the data well (poor χ^2/ndf). Fit amelioration is needed as well as background model improvement. Besides, the study of systematic errors is needed to be included in the total uncertainty on the measured half-life. The nuisance parameters that should be taken into account to evaluate the systematic uncertainty are mainly caused by the uncertainty on the signal efficiency, the energy scale bias, the bin width used to fit the data, the evaluation of the bulk radioactive contamination, the number of ^{116}Cd nuclei, the exposure, and the MC model.

5.5 Low energy threshold scintillating bolometer

In this section, the detector description and data analysis of a natural $CdWO_4$ scintillation bolometer are presented. This analysis aims to characterize and optimize the threshold of a scintillating bolometer for a potential measurement of g_A. As mentioned in Chapter 1, the highly forbidden beta decays represent an excellent tool to measure the quenching of g_A via the spectral distortion of their β spectrum at low energy as described in [40].

We take advantage of the ^{113}Cd (I.A. = 12.22% [69]) present in the crystal to investigate the fourth-forbidden non-unique beta decay, which is the dominant decay for this isotope. Several studies have been done on this decay using $CdWO_4$ [158] and CdZnTe [67] crystals.

5.5.1 Detector assembly and installation at LSC

A natural $CdWO_4$ crystal (433 g), previously measured in [158], was operated as a scintillating bolometer and installed at LSC in fall 2019.
The crystal was equipped with a 3×3×1 mm NTD and a heater. It was fixed in a CUPID-Mo like copper holder (as for the $^{116}CdWO_4$ No. 2) and surrounded with a reflecting foil. The crystal was facing a Neganov-Trofimov-Luke LD (NTL-LD) used to enhance the signal. The NTL-LD was fixed in the same copper holder as the crystal. A photo of the assembled scintillating bolometer is shown in Fig. 5.26.

This scintillating bolometer, as mentioned, was mounted in a tower with the $^{116}CdWO_4$ No. 2 and installed in the CROSS cryostat. As for the $^{116}CdWO_4$ No. 2, data were collected with a sampling frequency of 2 kHz in time-stream. The selected data accumulated with this detector corresponds to 714.5 h of background at 12 mK.

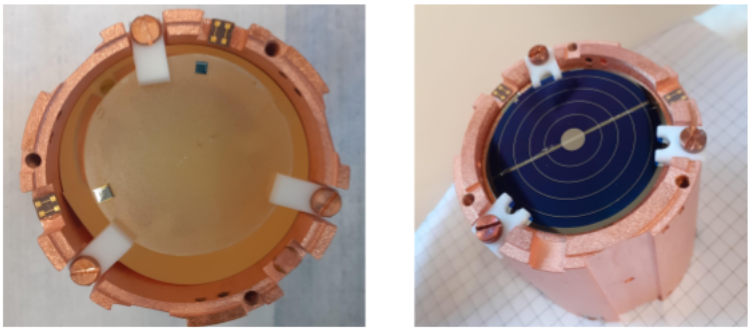

FIGURE 5.26: *Right:* natural $CdWO_4$ crystal in its copper holder fixed with PTFE pieces. *Left:* NTL-LD fixed in the same copper holder as the crystal with PTFE pieces.

5.5.2 Data analysis

As for the other detectors presented in this chapter, we used the same software to process the $CdWO_4$ data offline. We used a 2-s pulse window for the heat channel and a 0.5-s window for the light channel. The thermal response of the pulse amplitude of the heat channel was corrected with the help of heater events. This stabilized amplitude was calibrated with γ quanta from calibration data.

5.5.2.1 Detector performances

NTL-LD performance

The NTL-LD was calibrated, with a weak ^{55}Fe source that was facing it, before applying a bias on the grids as this cannot be possible when the bias is applied as explained in Chapter 2. In Fig. 5.27 we present the ^{55}Fe peak seen by the NTL-LD. The baseline resolution of the light channel was measured to be 418 eV when the NTL-LD is not biased at 12 mK.

We applied a bias of 60 volts on the grids of the NTL-LD ($\pm$30 volts). The measured baseline resolution was 30 eV. We also observe a signal amplification gain of 8 for the unbiased mode at the same noise level. An illustration of this effect is shown in Fig. 5.28 where we represent the light signal in Analog to Digit Unit (ADU) for the NTL-LD biased and unbiased versus the calibrated heat signal.

$CdWO_4$ performance

The baseline resolution (FWHM) of the heat channel was measurement to be 3.1 keV at 12 mK. The resolution at 2.6 MeV was estimated to be 8.9 keV FWHM in calibration data. We modeled the dependence of the energy resolution as a function of the energy in background data. This dependence was fitted with $\sqrt{c \times \text{Energy} + b}$ function as shown in Fig. 5.29.

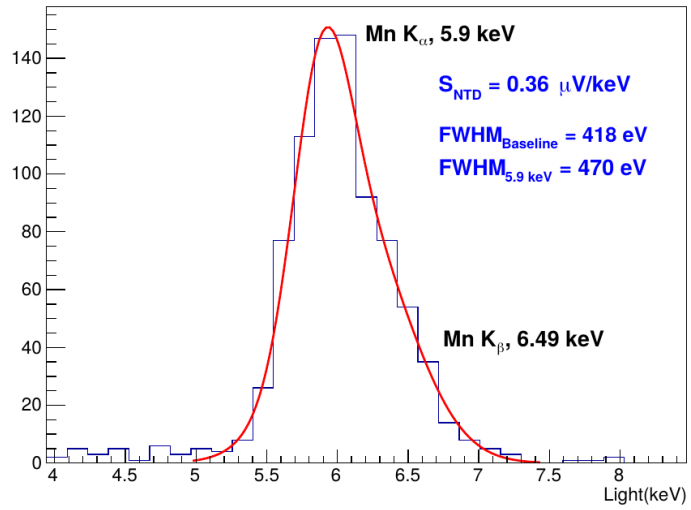

FIGURE 5.27: ^{55}Fe X-ray energy spectrum of the NTL-LD accumulated over 100 h.

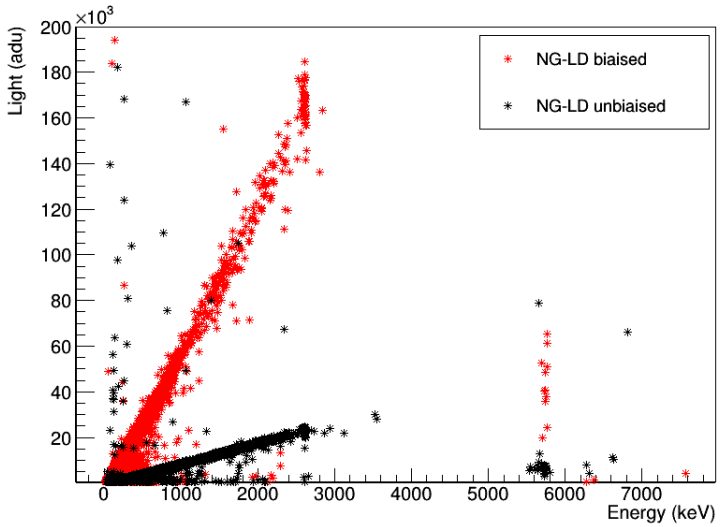

FIGURE 5.28: Light signal versus the heat signal for 37 h of ^{232}Th calibration data when the NTL-LD is biased (red) and unbiased (black).

The light yield in this detector was evaluated to be 14.3 keV/MeV at 2.6 MeV. We note that this crystal has a non-linear scintillation light response which causes a different light yield according to the γ quanta energy as shown in Fig. 5.30. The light yield is lower for γ with lower energies. Defects in the crystal could be the cause of this non-linearity. In Table 5.7, the light yield of the prominent peaks in background data are given: it varies from 11.8 keV/MeV at 609 keV to 14.3 keV/MeV at 2615 MeV.

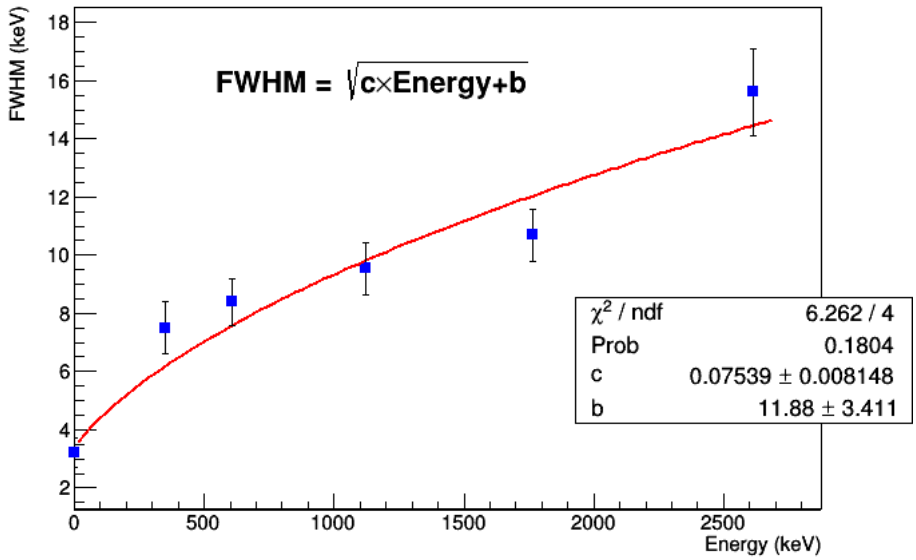

FIGURE 5.29: FWHM of $CdWO_4$ versus the energy for background data.

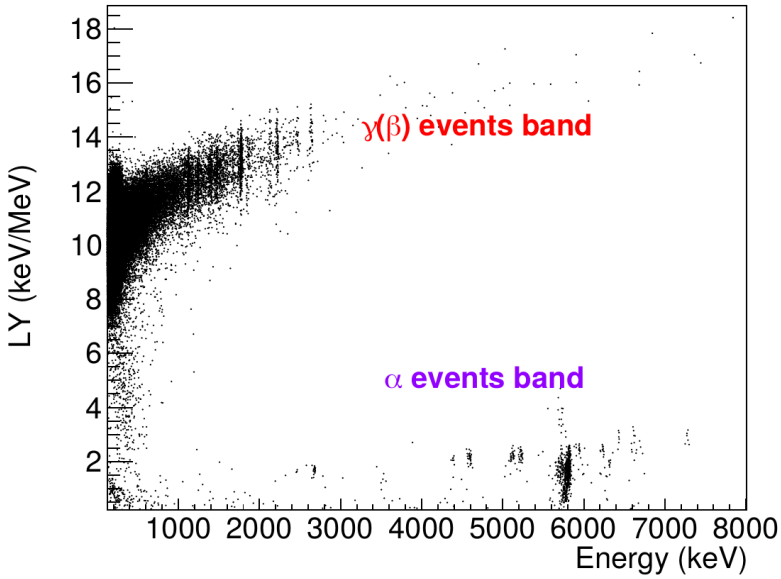

FIGURE 5.30: Light yield as a function of the energy of ∼715 h of background data from the natural $CdWO_4$ scintillating bolometer.

As this analysis was performed to be sensitive to the possible beta decay spectral distortion, we had to optimize the cuts at low energy. Indeed, we could not use the usual correlation parameter (used to select the data for the two enriched scintillating bolometers) because it tends to reject particle events with small amplitude. This is due to the pulse shape at lower energies that can be affected by noise and

Energy (keV)	LY (keV/MeV)
609	11.80
1120	12.64
1238	12.80
1460	13.02
2204	13.96
2615	14.34

TABLE 5.7: Measured light yield in the most prominent γ peaks in background data.

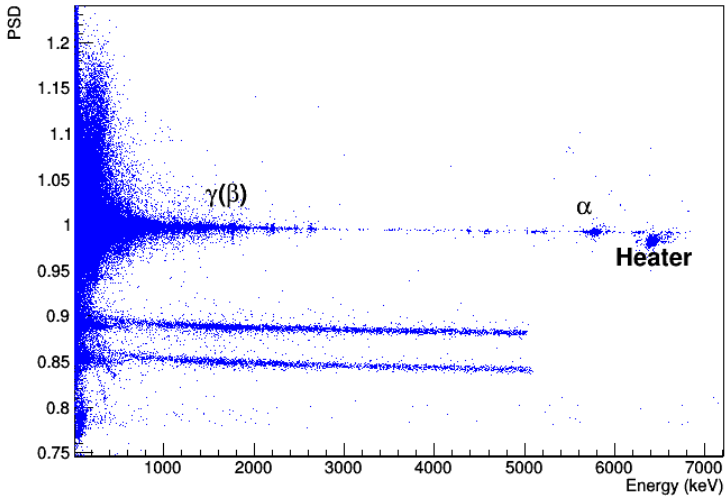

FIGURE 5.31: PSD parameter as a function of the energy.

hence lose its matching with the average pulse constructed at higher energies. To select the particle events in the data, we apply a pulse shape cut based on the ratio between the fitted amplitude and the filtered one. The filtered amplitude is the amplitude of the signal after applying the OF. The fitted amplitude is obtained by fitting the individual pulse amplitude versus the average pulse one. The individual pulse with an amplitude S_i is synchronized with the normalized average pulse A_i according to their maximum. When plotting S_i versus A_i, we obtain almost a straight line. If the individual pulse has the same shape as the average one, the amplitude of the individual pulse is the slope of this line. This pulse shape parameter, referred to as PSD in this thesis, can distinguish particle events from pile-ups and is $\sim$1 for particle events. The CROSS experiment uses the ratio between the fitted amplitude and the filtered one to discriminate bulk events from surface events [170].

The distribution of the PSD parameter as a function of the energy for the background data is presented in Fig. 5.31 where we see a different population of events separated. At PSD $\sim$ 1, the particle events are distributed.

To reject non-particle events, we used the projection of the PSD parameter on the y-axis in 25 keV energy intervals up to 200 keV and 50 keV energy starting from 200 keV. Each energy interval is fitted with a Gaussian where the mean value and the standard deviation are used to define the cut to accept only the events that belong to the particle events band. In Fig. 5.32, the green points represent $\pm 3\sigma$ of the Gaussian fit. They are fitted using (red line in Fig. 5.32): $1 - B\sqrt{x}^{A} + C$ for energies up to 200 keV and first-order polynomial for energies up to 3000 keV. The events that are not enclosed inside the red fit curve are rejected.

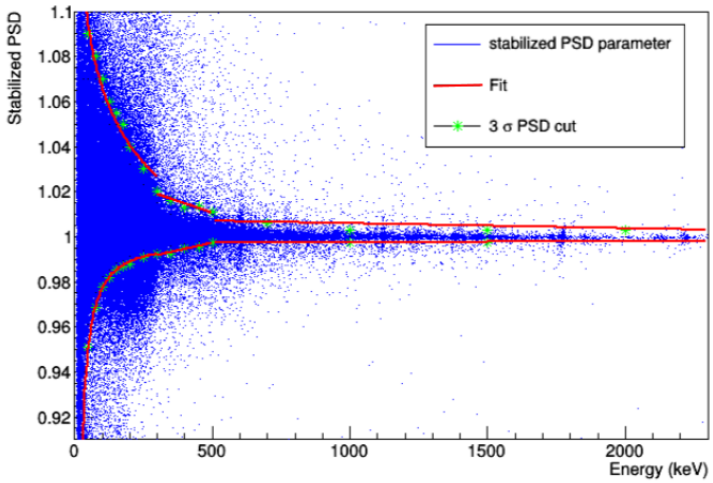

FIGURE 5.32: Stabilized PSD parameter versus the energy. The events below and above the red lines are rejected.

5.5.2.2 Efficiency evaluation

The efficiency evaluation in this analysis is crucial as it is an essential correction to the spectrum that we aim to exploit to measure its distortion at low energy. We evaluate the efficiency at the trigger level and offline with the quality cuts described above. We note that at the trigger level, with the software used to analyze this data, a pulse shape cut is applied with the correlation parameter. For the natural $CdWO_4$, we applied a loose cut with this parameter to recover the maximum number of injected events at low energy; we accept the event with a correlation parameter higher than 0.85. In addition, we trigger only events that have an amplitude higher than 5 σ_{noise} of the baseline resolution.

The procedure to evaluate the efficiency is very similar to the one used in CUPID-Mo (Chapter 3); it is based on injecting simulated events built from an average pulse scaled at given energy into data. The only difference is that for the $CdWO_4$ based scintillating bolometers, we used a MATLAB based software that allows injecting simulated events directly into stream data. Having the simulated events injected into stream data allows processing it exactly as the physics data. Therefore, we can evaluate the efficiency at the trigger level and after the quality cuts. The steps to evaluate the efficiency are the following:

- inject simulated events, based on an average pulse of particle event scaled to given energy, in the stream data. To ensure that the injected pulse recovers to the baseline and merges perfectly with is, we used a 5-s length average pulse. For each energy, 200 events were injected for the heat channel, and 400 events were injected for the light channel. An example of an injected simulated pulse into stream data for the heat channel is shown in Fig. 5.33;

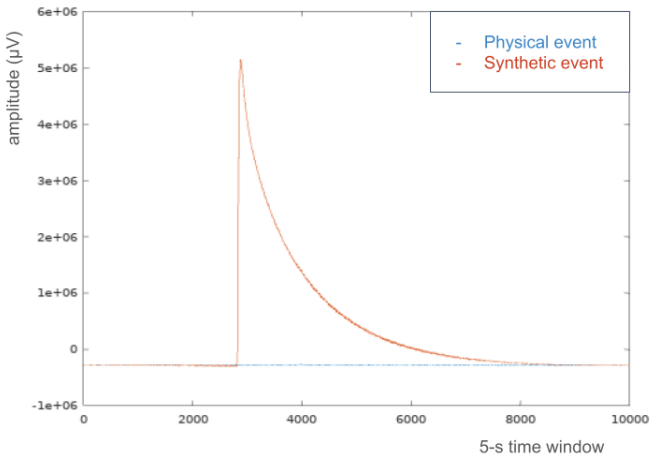

FIGURE 5.33: Example of simulated injected pulse in the stream data for the heat channel.

- process and analyze the data with the simulated pulses as particle data. The data with the simulated pulses is submitted to the same processing and analysis steps as the background data;
- subtract the data with simulated events from the background data. The spectrum with and without the injected events is shown in Fig. 5.34. We also represent the subtraction on the two;
- compute the integral of each peak that corresponds to the injected events in the subtracted spectrum;
- once the integrals of the simulated event are computed, the efficiency at each energy is evaluated to be the ratio between the number of events that survive the trigger and the cuts at a given energy, and the number of injected events.

Once the efficiency at each injected energy is evaluated, the efficiency profile is drawn and modeled with $1 - B\sqrt{x}^A + C$ fit function. The efficiency of the heat and the light channel is presented in Fig. 5.35. The efficiency of the light channel is globally higher than the heat channel one because the light channel is more efficient given its faster response. We note that for the heat channel the efficiency drops below 50% for energies lower than 20 keV because of the pulse shape cut done at the trigger level, where a significant fraction of the events with small amplitudes is rejected.

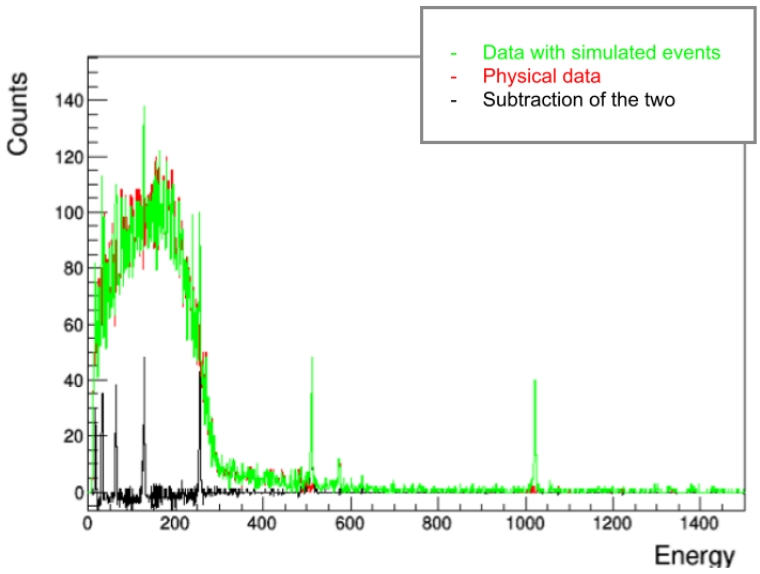

FIGURE 5.34: Energy spectrum with simulated injected events (green), without simulated injected events (red) and the subtraction of the two (black).

We used the efficiency profile of the heat channel to correct the calibrated background spectrum. A comparison between the spectrum with and without the efficiency correction is shown in Fig. 5.36.

We performed the same analysis on the light channel triggered with the light signals. In this case, the NTL-LD acts as an independent bolometer registering the scintillation light from the $CdWO_4$. It should be noted that the energy resolution of the NTL-LD for the heat channel is poor.
Fig. 5.37 shows the corrected spectra of the heat and light channels. We observe few discrepancies between the two spectra due to the different performances of the two detectors. Indeed, the NTL-LD has a faster detector response and therefore allows a better pile-up suppression. Moreover, this detector is more efficient than the light channel and has a lower energy threshold thanks to the low baseline noise. However, due to the poor energy resolution of the light channel, the β decay of ^{113}Cd endpoint is shifted.

Using the heat and light channels independently allows a direct comparison between two detection approaches for the same source. One of the advantages of using the NTL-LD is of course the pile-up rejection while the advantage of the heat channel is the high energy resolution.

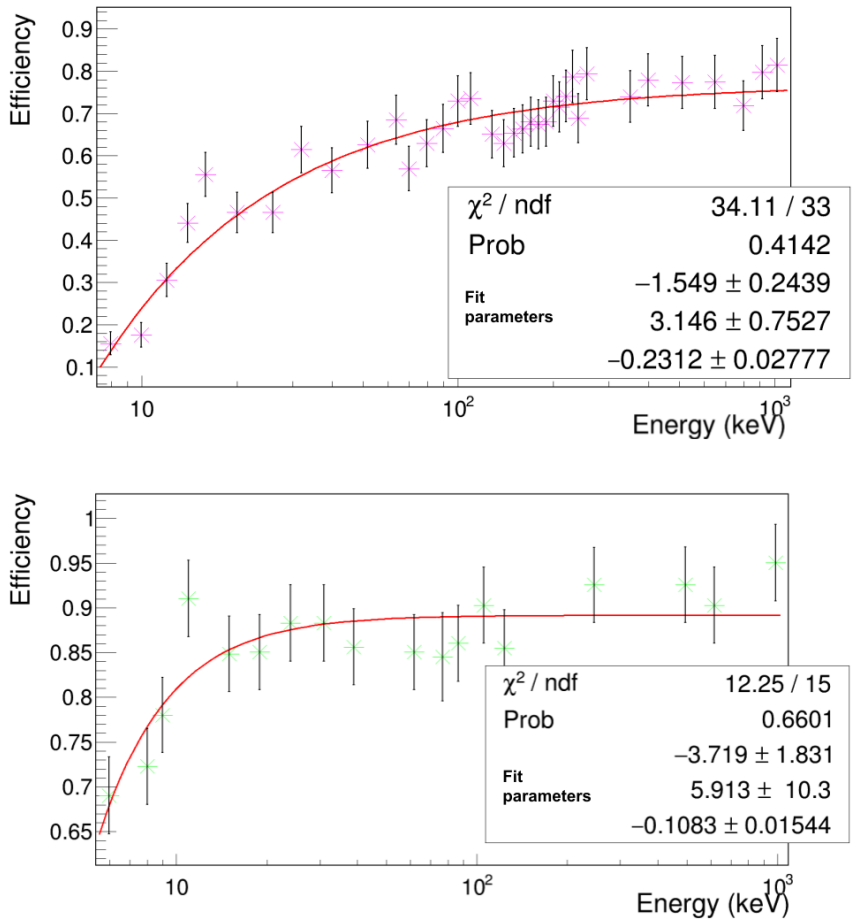

FIGURE 5.35: Efficiency of the heat channel (*top panel*) and the light channel (*bottom panel*) of the natural $CdWO_4$ scintillating bolometer.

5.5.3 Perspective of the g_A quenching measurement

This preliminary analysis aims to investigate the potential of such detector to access the g_A quenching measurement via the spectral distortion of the beta decay taking advantage of the ^{113}Cd present in the $CdWO_4$ crystal. Before diving into the spectral shape evaluation, two important factors need to be taken into account: the uncertainties on the spectrum correction and the background model to the β spectrum extraction.

We noticed that when propagating the errors from the fit of the efficiency profile to the corrected background spectrum of the heat channel, the uncertainty on the spectrum at low energy, below 50 keV, is considerable. This leads to the impossibility of being sensitive to the spectral distortion of the β spectrum. Of course, the significant uncertainty below 50 keV is due to the low number of triggered events at such energies, causing a more significant statistical error. A possible way to overcome this issue would be to increase the number of injected simulated events at

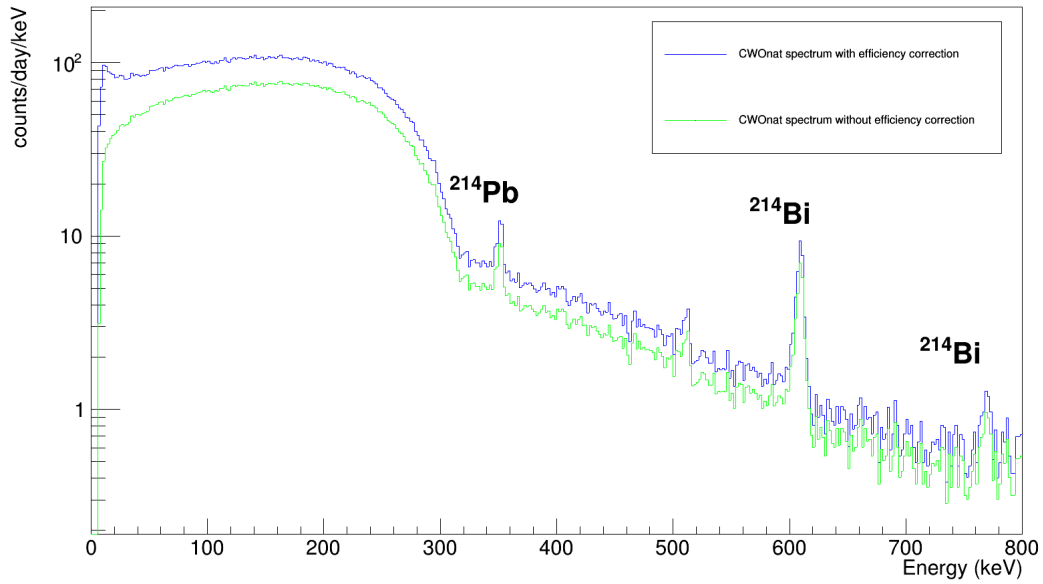

FIGURE 5.36: Energy spectrum of the $CdWO_4$ channel without (green) and with the efficiency correction (blue).

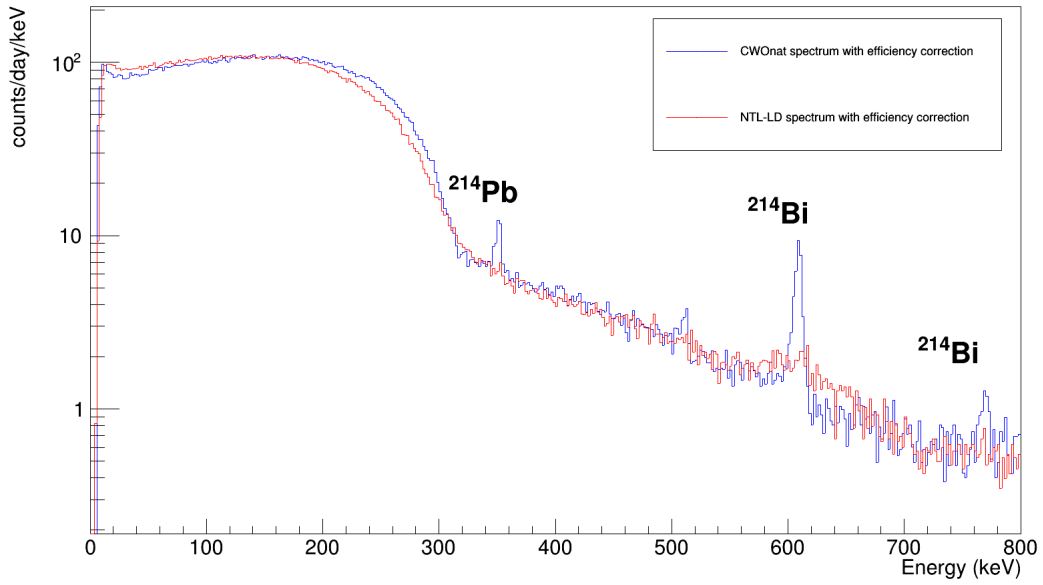

FIGURE 5.37: Energy spectrum of the $CdWO_4$ channel (blue) and the NTL-LD channel (red) corrected with the efficiency.

energies below 200 keV; in this way, the statistical error would decrease and hence the uncertainty on the spectral shape.

We are currently developing a background model, which is in a well-advanced stage. Having a background model in this analysis allows extracting the β spectrum from the experimental data. The different background external contributions

were simulated using the GEANT4 software package [168] and were smeared with the detector resolution. The MC model also takes into account the efficiency of the detector. The corrected experimental background spectrum is then fitted with the model above the endpoint of the ^{113}Cd decay (Q_β=324 keV). Later, the fit model is extrapolated in the ^{113}Cd β spectrum region (below Q_β), and the background model is subtracted from the experimental data. The preliminary extracted β spectrum is presented in Fig. 5.38. The activity of ^{113}Cd extracted from this spectrum is 623 mBq/kg which is higher than that reported in [158] (558±4 mBq/kg) for the same crystal. We explain this discrepancy by the unrejected pile-up due to the slow thermal response of the heat channel (2.5-s long pulse).

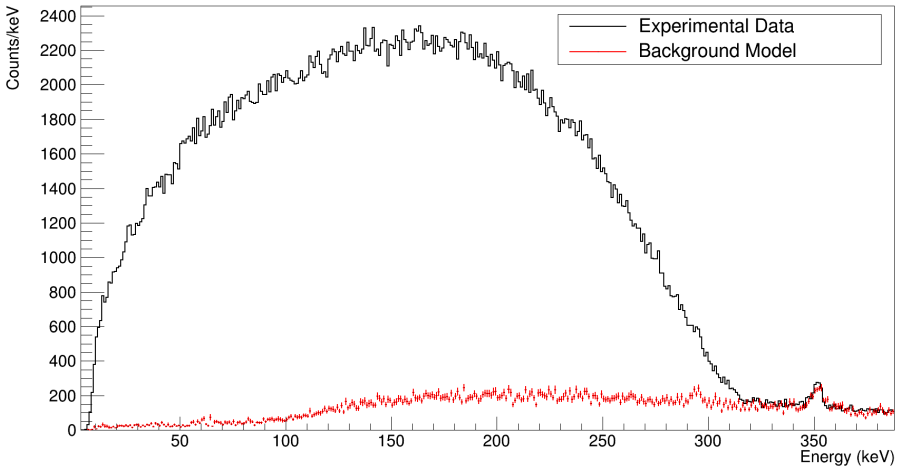

FIGURE 5.38: ^{113}Cd β spectrum extracted from the experimental background spectrum without efficiency correction (in black) and the background MC model (in red).

Chapter 6

The future ton-scale bolometric experiment CUPID

CUPID is a future ton-scale bolometric experiment currently under design. It will use the existing CUORE infrastructure and will be based on the scintillating bolometer technology that was successfully developed by several R&D (LUCIFER [171] and LUMINEU [104]) and demonstrators (CUPID-0 [46] and CUPID-Mo [48]). The goal of the next-generation experiments searching for $0\nu\beta\beta$ decays is to explore the inverted ordering region. The main physics objective of CUPID is to search for ^{100}Mo $0\nu\beta\beta$ decay with a discovery sensitivity beyond 10^{27} years which corresponds to $m_{\beta\beta}$ discovery of 12-20 meV. An illustration of the CUPID physics goal is represented in Fig. 6.1 with the well-known lobster plot. This sensitivity is reachable in background conditions close to zero. In addition, the sensitivity depends on the mass of the isotope of interest, the efficiency, the energy resolution at $Q_{\beta\beta}$ and the livetime of the experiment. For this reason, CUPID targets the deployment of an array of enriched $Li_2^{100}MoO_4$ scintillating bolometers enriched in ^{100}Mo at more than 95% with the requirement needed to be in zero background conditions.

6.1 The CUPID baseline

Several CUPID R&D tests have been performed based on cubic $Li_2^{100}MoO_4$ crystals between 2019 and 2021 [105, 164]. The detector construction of two of these tests is described as a part of the work done during this thesis. The results obtained will be presented as well.

The choice of the isotope to search for $0\nu\beta\beta$ decay is defined by experimental constraints (see Chapter 1 and Chapter 2). The crystal selection has to fulfill several criteria such as the possibility of enrichment at reasonable cost and production of high radio-purity crystals to ensure the low background level. The successful results of LUMINEU at LSM confirmed by the CUPID-Mo demonstrator lead to the choice of enriched $Li_2^{100}MoO_4$ crystals as a baseline for CUPID [95]. As described in Chapter 3, these crystals match the CUPID requirements. Different specifications for CUPID have been set and are listed in Table 6.1 [95].
In its current baseline, CUPID will consist of an array of 1596 scintillating bolome-

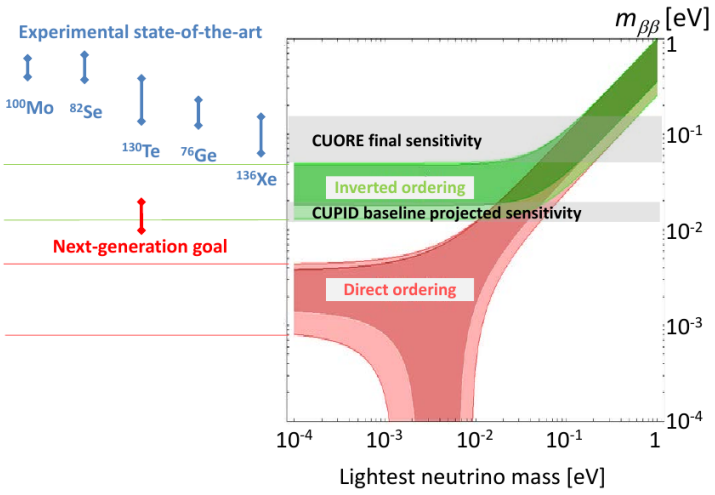

FIGURE 6.1: Effective Majorana mass $m_{\beta\beta}$ as a function of the lightest neutrino mass in the normal hierarchy (red) and in the inverted hierarchy (green) scenarios. The Final CUORE sensitivity is indicated as well as the CUPID baseline projected sensitivity [95].

Parameter	Baseline
Crystal	$Li_2^{100}MoO_4$
Crystal size	$45\times45\times45$ mm^3
Crystal mass (g)	280
Number of crystals	1596
Number of LD	1710
^{100}Mo mass (kg)	240
Energy resolution FWHM (keV)	5
BI (counts/(keV.kg.yr))	10^{-4}
Containment efficiency	79%
Selection efficiency	90%
Lifetime	10 years
Half-life limit sensitivity (90%) C.L.	1.5×10^{27} years
Half-life discovery sensitivity (3σ)	1.1×10^{27} years
$m_{\beta\beta}$ limit sensitivity (90%) C.L.	10–17 meV
$m_{\beta\beta}$ discovery sensitivity (3σ)	12–20 meV

TABLE 6.1: Main parameters for the CUPID baseline detector structure.

ters arranged in 57 towers of 14 floors hosted in the existing CUORE infrastructure. Each floor will contain two cubic enriched $Li_2^{100}MoO_4$ of about 280 g of mass each ($45\times45\times45$ mm^3). CUPID requires an enrichment level higher than 95%, which allows increasing the number of $0\nu\beta\beta$ decay emitters. The 1596 enriched crystals will contain 240 kg of ^{100}Mo, which corresponds to 1.6×10^{27} atoms of ^{100}Mo. The expected background index reachable by CUPID is $\sim 10^{-4}$ counts/(yr.kg.keV) in

the ^{100}Mo ROI. This level of background puts CUPID in almost zero background conditions to search for the $0\nu\beta\beta$ decay of ^{100}Mo, thanks to the double readout technology. Therefore, it is important to have a full α background rejection (more than 99.9%) and a very high detection efficiency close to 100%. To simplify the detector structure, CUPID will use cubic crystals to have a more compact environment optimizing the available experimental space.

6.2 Cryogenic tests towards the TDR

This thesis will focus on two tests referred to as the "8-crystal test" at LNGS and the "12-crystal test" at LSC.

6.2.1 The 8-crystal test at LNGS

The goal of this test was to characterize for the first time cubic enriched (45 mm side) $Li_2^{100}MoO_4$ crystals to check if they fulfill the CUPID criteria in terms of energy resolution and particle identification capability. The enrichment level in ^{100}Mo is $(97.7 \pm 0.3)\%$ and each crystal has a mass of $\sim$ 280 kg. The production of the crystals was performed in the framework of the CROSS project [170] using the procedure developed by LUMINEU [104]. Concerning the LDs, we used Ge disks similar to the one used in CUPID-Mo [86] coated with SiO on both sides except a small surface on which the thermal sensor and heater were glued.
We have constructed a two-floor tower composed of 8 scintillating bolometers: 8 $Li_2^{100}MoO_4$ crystals and 12 LDs arranged in a way that each crystal is facing two LDs. The design of this tower was elaborated to be compact to optimize the space and contain the less material possible around the detectors. A scheme of the tower structure is shown in Fig. 6.2. In total, the array contains two layers of crystals and three layers of LDs. In the following, we will describe the assembly procedure of this tower that was performed in the CUPID R&D clean room located in Hall A at LNGS.

Tower construction

The first step of the tower construction is very similar to what was done for CUPID-Mo (described in Chapter 3) and for the $CdWO_4$ detectors (presented in Chapter 5). For the LMO crystals, we used $3\times3\times1$mm^3 NTDs equipped with 25 μm gold wires to ensure the electrical contacts. The gluing of these thermal sensors on the LMO crystals was performed using a semi-automatic system used previously to glue the CUPID-0 detectors [46]. This system is a robot arm moving in the x-z plane that allows depositing nine glue (two-component Araldite® rapid) spots with the help of the pogo-pin matrix in a reproducible way. Concerning the LDs, two different sizes of NTDs were used: $2\times2.95\times0.5$mm^3 (CUPID-0 style NTDs) and $0.8\times0.9\times2.96$mm^3 (CUPID-Mo style NTDs). The CUPID-0 style NTDs were glued following the same procedure as the LMOs with the help of six glue spots. In contrast, the CUPID-Mo style NTDs were glued with three spots following the

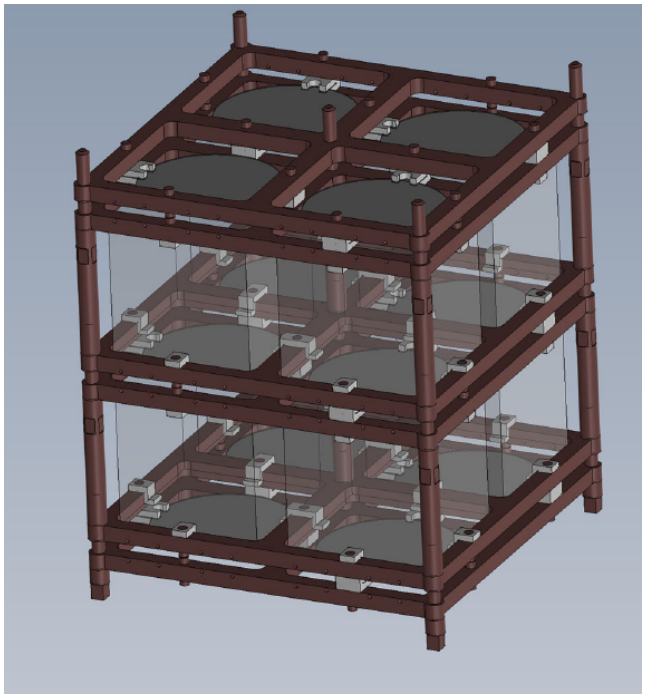

FIGURE 6.2: Schematic view of the 8-crystal array with 8 cubic crystals arranged in two floors.

procedure described in Chapter 5 using a gluing tool similar to the one presented in Chapter 2.

In Fig. 6.3, we present a picture of the tool used to glue the NTDs on the crystals and LDs. The gluing steps are summarized as follows:

- the NTD is placed on a platform equipped with a vacuum system that keeps the NTD in position. As the NTD has already the gold wires, it is important to make sure that the wires are straightened in both sides of the NTD and does not go on the NTD as shown in Fig. 6.3;
- the glue is mixed and put in a small PTFE container placed on the robot. The robot arm is programmed to dip into the PTFE container then put the glue spots on the NTD;
- once the glue is deposited on the NTD, a PTFE holder is inserted on the NTD platform. This holder is here to support the crystal/LD and ensure the 50 μm gap between the surface of the NTD and the crystal/LD. Once the holder is placed, the crystal/LD is inserted. The last thing to do is wait for $\sim$ 1.5 h to let the glue dry.

Once the thermal sensors were glued, we equipped all the detectors (crystals and LDs) with a silicon resistance (heater) to periodically inject pulses to correct the pulse amplitudes of the detector or study the pile-up caused by the random coincidences of the $2\nu\beta\beta$ events in the crystals as it was done during this run [172]. The

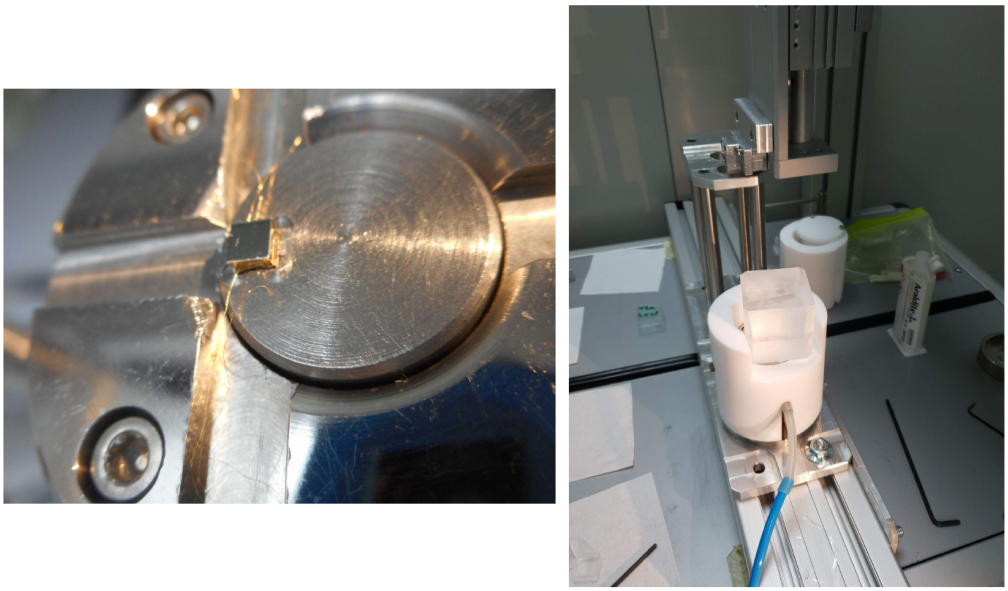

FIGURE 6.3: *Left:* NTD thermistor resting on the vacuum-tight platform. The gold wires are straightened on the side of the NTD. *Right:* general view of the gluing tool.

LDs and LMOs are now ready to be assembled in a tower. The ingredients to construct this 8-crystal tower are (see Fig. 6.5): 6 copper frames, 12 copper columns, differently shaped PTFE pieces to fix the LDs and the LMOs in the frames, and of course LMO crystals and LDs. The assembly of the tower is simple and is done layer by layer. This section will describe the first layer of LDs, the first layer of crystals, and the second layer of LDs as the two other layers are done the same as the three first. The steps are:

- the first-floor construction starts by putting five columns on the bottom side of a copper frame. The four first LDs are put in this frame. Each LD is held with two PTFE pieces shaped as crimps;
- to fix the LDs and make sure they do not slide from the PTFE crimps, a second frame is inserted and fixed with the help of five copper columns. Each copper frame contains pins on its two faces that have to be inserted inside the holes of the PTFE pieces holding the LDs;
- to make the electrical connection, each frame was equipped with copper tubes where the gold wires are inserted. After that, the copper pins are crimped as in CUPID-0 [46];
- to assemble the crystal floor, PTFE pieces are put in the middle and the edges of the copper frame. Then, the four crystals are put on these PTFE pieces;

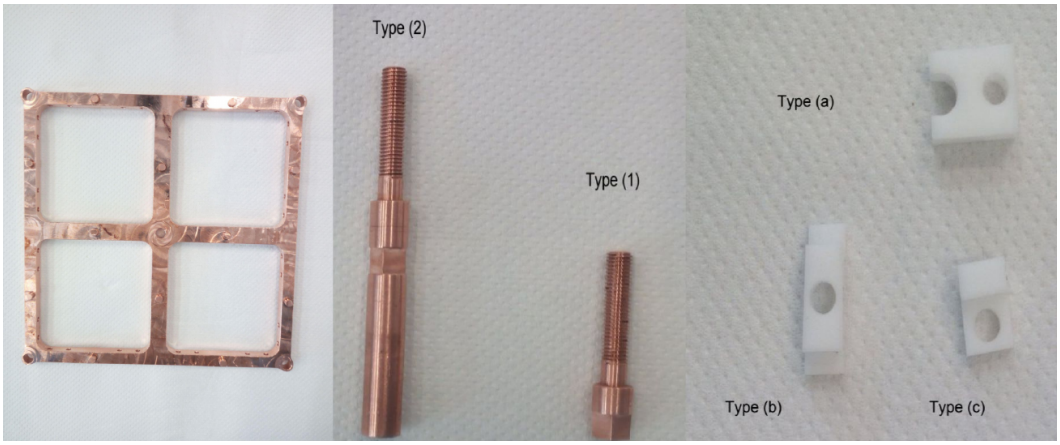

FIGURE 6.4: The different pieces used to construct the detector array. Copper frames (*left*). Two different types of copper columns (*middle*): type (1) is used for the bottom layer of the tower. PTFE pieces with different shapes (*right*): type (a) are used to fix the LDs, type (b) and type (c) are used to fix the LMOs in the middle and the edges of the copper frames.

- in another copper frame, PTFE pieces are put as in the previous step. This frame is inserted, making sure that the five holes in the frame enter simultaneously in the columns. The electrical connections are made via the copper tubes crimping technique;
- on this frame, another layer of LDs is put as described above. Then, a copper frame is inserted so that all the copper pins have to be inside the PTFE pieces of each LD. Five columns are screwed to fix this layer;
- the second floor is mounted as the first one.

In the bottom floor that we described here (see Fig. 6.5), the LMO crystals were wrapped with the Vikuiti^{TM} from 3M reflecting foil. The top floor was left without any reflector. This was done to study the effect of the reflecting foil on the light collection and see if we can run the scintillating bolometers without it since it is a source of radioactive contamination. This array was tested in the Hall C CUPID R&D cryostat described in Chapter 2 located at LNGS. The detectors were mainly operated at 18 mK.
The signal readout is based on custom front-end electronics boards. The data acquisition system is equipped with an amplifier and an active anti-aliasing Bessel filter [173]. The data were acquired continuously in time-stream with a sampling frequency of 2 kHz. An online derivative trigger algorithm was used to trigger the data [113].

Results of the 8-crystal test

The results of this test were published in [105] where the analysis procedure performed by the CUPID analysis team is described. Due to a technical issue, we had

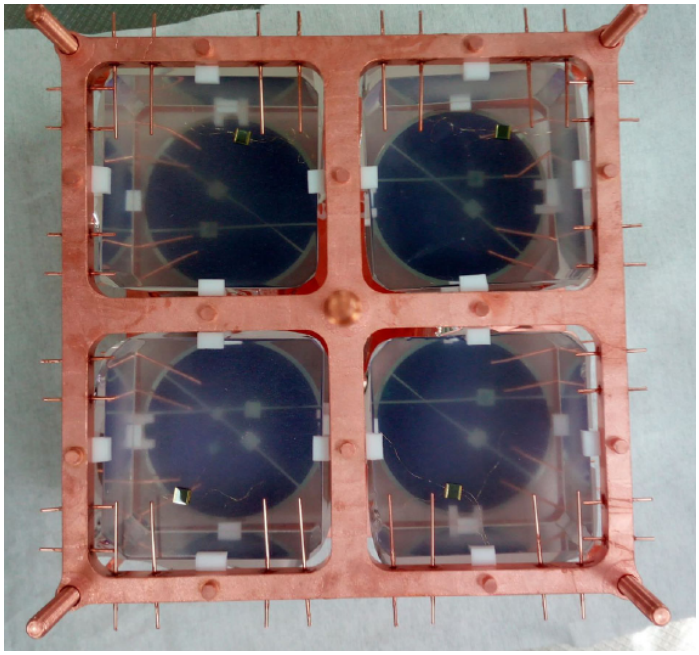

FIGURE 6.5: Top view of the first floors of the 8-crystal tower during the assembly. The crystals are surrounded with the reflecting foil.

6/8 LMO crystals working. The characterization of this array fixed several questions regarding the detector structure baseline for the ton-scale CUPID array. In the following, we will summarize the main results.

The energy resolution of the six LMO crystals was measured to be (7.5 ± 0.4) keV at 2.6 MeV extrapolated to (8.2 ± 0.5) keV at $Q_{\beta\beta}$. During the data taking, we noticed that the LMO crystals used for the pile-up studies [172] were noisy and unstable due to the artificially injected pulses, which deteriorates the overall FWHM of calibration data. With this purpose, a new estimation of the energy resolution was performed using the three other LMOs (without the pile-up injection system). The obtained resolution was (6.7 ± 0.6) keV at $Q_{\beta\beta}$ which is close to the 5 keV FWHM CUPID goal. It should be noted that the energy resolution depends on the operating temperature: the lower is the temperature, the better is the energy resolution.

Thanks to the asymmetry reflecting foil/no reflecting foil between the two floors, the effect of the reflector on the light collection was evaluated and quantified. The light collection quality defines the ability to distinguish $\gamma(\beta)$ events from α events. The scatter plot of the light yield versus the heat signal is shown in Fig. 6.6. We observe that the $\gamma(\beta)$ band is separated from the α band in both cases. The LY was evaluated for α and $\gamma(\beta)$ events higher than 1 MeV, as explained in [105]. The summed average of the top and bottom LDs was estimated to be $LY_{\gamma(\beta)} = (1.10 \pm 0.05)$ keV/MeV and $LY_{\alpha} = (0.19 \pm 0.01)$ keV/MeV for the LMOs wrapped in the reflecting foil, and $LY_{\gamma(\beta)} = (0.50 \pm 0.05)$ keV/MeV and $LY_{\alpha} = (0.085 \pm 0.004)$

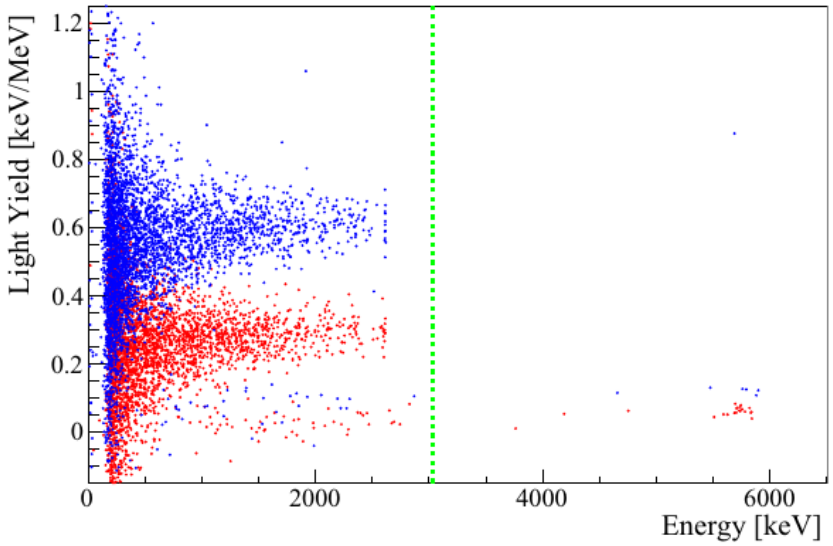

FIGURE 6.6: Light yield a function of the energy for a LMO surrounded by the reflecting foil (blue) and a LMO without a reflector (red).

keV/MeV for the LMOs without the reflecting foil. The discrimination power $DP_{\gamma(\beta)/\alpha}$ (defined in Chapter 2) was measured to be $\sim$7.3 σ on average for single LD (only top or bottom LD) when the reflecting foil is present. Concerning the crystals without reflecting foil, the average $DP_{\gamma(\beta)/\alpha}$ was evaluated to be $\sim$3.6 σ. The use of the reflecting foil guarantees a full $\gamma(\beta)/\alpha$ separation when using a single LD, while the use of two LD ameliorate the $DP_{\gamma(\beta)/\alpha}$ when the reflecting foil is not present around the LMO crystals.
In [105], a Monte Carlo simulation was performed to model the scintillation light in the CUPID crystals. This simulation showed that the light collection could be improved with a slightly different detector structure using a squared LD that fully covers the LMO crystal face and reducing the distance between the LD and the crystal.

We remind here that in the CUPID baseline, the crystals will not be surrounded by a reflector. The results obtained from this 8-crystal tower showed that this configuration fulfills the CUPID criteria in terms of background rejection. Increasing the light collection is essential to improve the background rejection. For this reason, we tested another tower structure very similar to the one presented in this section but with slight improvements taking into account the results obtained here.

6.2.2 The 12-crystal test at LSC

This test aimed to improve the structure taking into account the results and the conclusions drawn from the 8-crystal run at LNGS. This tower was designed to

be more compact than the 8-crystal, so the LDs are closer to the LMO crystals. Another important goal of this run was to investigate squared LD performance and light collection for the first time. The aluminum coating to replace the reflecting foil was considered during this run. We also wanted to study different detector configurations in the view of fixing the CUPID detector structure baseline.
The tower was composed of 12 cubics enriched LMO crystals produced for the CROSS project [170] and 16 LDs, arranged in three floors where the LD and LMO layers are alternated as shown in Fig. 6.7. The difference between the 8-crystal tower and this one is the LD geometry and the gap between the LDs and the crystals that was reduced from 6.5 mm to 0.5 mm.

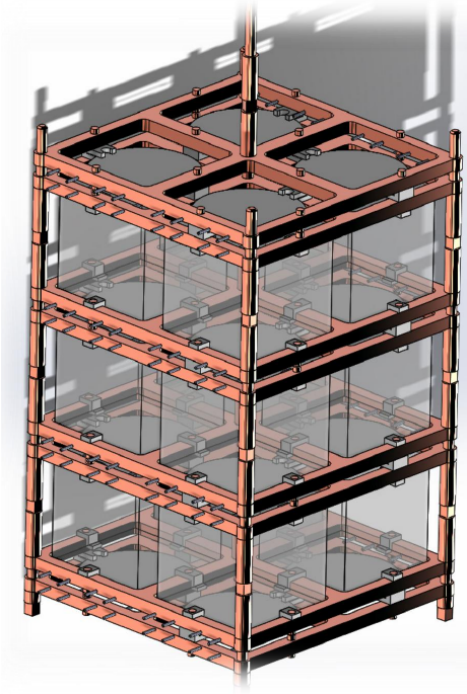

FIGURE 6.7: Schematic view of the 12 crystal array composed of 3 layers of LMO crystals and 4 layers of LD.

Tower construction

This hybrid tower was composed of crystals with and without a reflecting foil, coated with different thicknesses of aluminum, circular, and squared LDs from different producers. The detectors were equipped with different sizes of NTD. The detailed tower composition is presented in Table 6.2.
The tower construction was done in the IJCLab clean room. The NTD gluing was performed following the procedure described in Chapter 5 for the LMOs and LDs. The tower assembly follows the same steps as in Sec. 6.2.1. The wiring was done with copper pins and crimping. We used, for connection from the NTD to the cryostat electronics, as for CUPID-Mo, Constantin silk-covered wires. In Fig. 6.8, we

Layer	LD shape	Reflector	NTD size (mm)
LD	square	-	4×NTDs of 3×1×1
LMO	-	no reflector	2×NTDs of 9×3×1 2×NTDs of 3×3×1
LD	circular	-	4×NTDs of 3×1×1
LMO	-	Al coating 2 crystals with 0.2 μm 2 crystals with 2 μm	4×NTDs of 3×3×1
LD	square	-	4×NTDs of 3×1×1
LMO	-	reflector	2×NTDs of 9×3×1 2×NTDs of 3×3×1
LD	circular	-	2×NTDs of 3×0.5×1 2×NTDs of 3×0.5×1

TABLE 6.2: 12-crystal tower composition layer by layer from top to bottom.

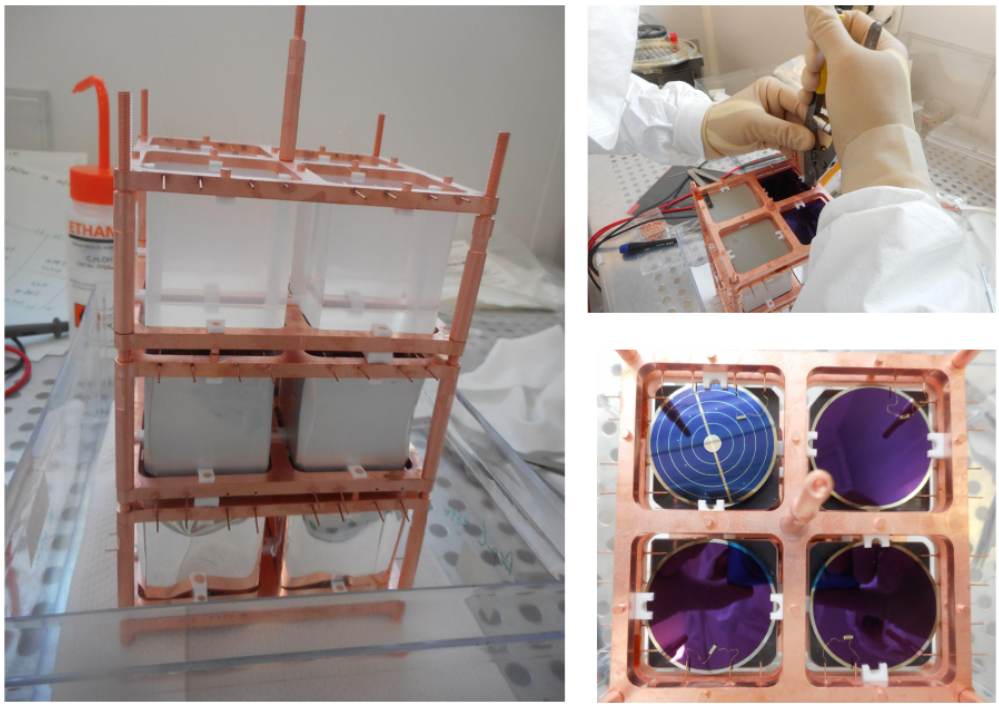

FIGURE 6.8: Photos of the assembly of the 12-crystal tower. *Left:* the tower with all the floors assembled. *Top right:* photo of a copper pin crimping to make the electrical contact. *Bottom left:* photo of one layer of LD.

present photos of the tower during the assembly where one can see that the tower is constructed layer after layer from bottom to top. The tower was then moved to LSC and installed in the CROSS cryostat with a suspension system as shown in

Fig. 6.9.

The signal readout in the CROSS facility is based on low-noise DC front-end electronics that were used by the Cuoricino experiment [174]. The data acquisition (DAQ) system is composed of 12 channels with a programmable anti-aliasing filter. This DAQ will be potentially used by CUPID and its design is described in [175]. The data were acquired as a stream with a sampling frequency of 2 kHz and were processed offline.

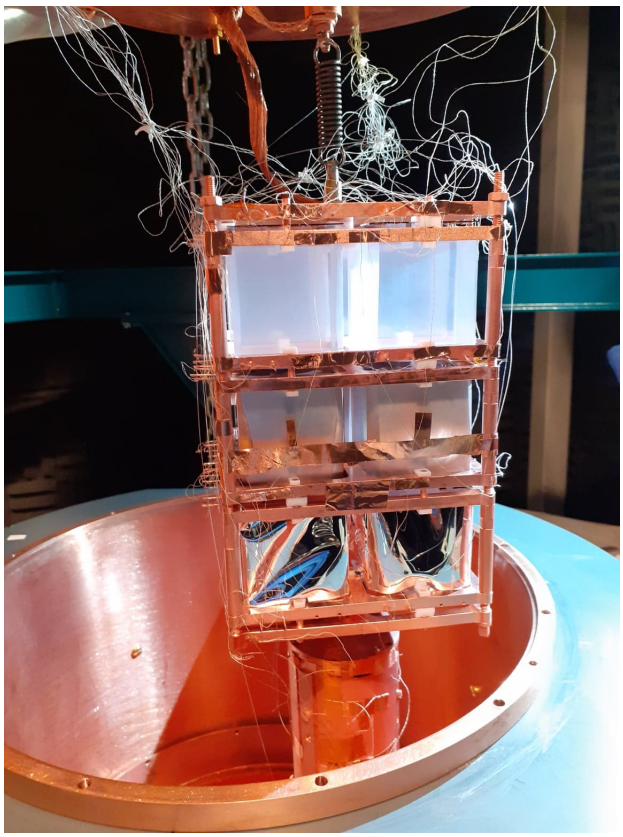

FIGURE 6.9: The 12-crystal tower suspended to the 10 mK plate of the CROSS cryostat with a stainless steel spring.

12-crystal run results

In this section, preliminary results from this test are presented. The FWHM resolution measured on the combined spectrum of 4 LMO crystals was estimated to be ∼7 keV at 2.6 keV. This result is reasonable but does not fulfill the CUPID requirement (5 keV FWHM at $Q_{\beta\beta}$). Concerning the different sizes of NTDs used for the crystals, we did not observe a big difference in the performance between standard size NTDs and the three times larger ones.

Thanks to the tower composition, we could access several light collection configurations and collected useful information for the CUPID detector baseline and the future planned tests. First, the Al coating was studied as a potential reflector to replace the reflecting foil. This coating does not provide enough light collection (three times less than the crystals surrounded with a reflecting foil). It is now discarded as a potential reflector for the CUPID baseline. Then, the LY when the crystal is facing a squared LD or a circular one was compared. In Fig. 6.10, the comparison between these configurations is presented. The LY when the crystal is wrapped in a reflecting foil and facing a squared LD (LY_{Srf} = 0.60 keV/MeV) is enhanced by 20% with respect to the case where the wrapped crystal is facing a circular LD (LY_{Crf} = 0.51 keV/MeV). When a reflector does not surround the crystal, we observe a 28% higher LY when the crystal faces a squared LD. The LY of the squared and circular LD was measured to be 0.23 keV/MeV and 0.18 keV/MeV, respectively. This result is in agreement with what was predicted in [105].

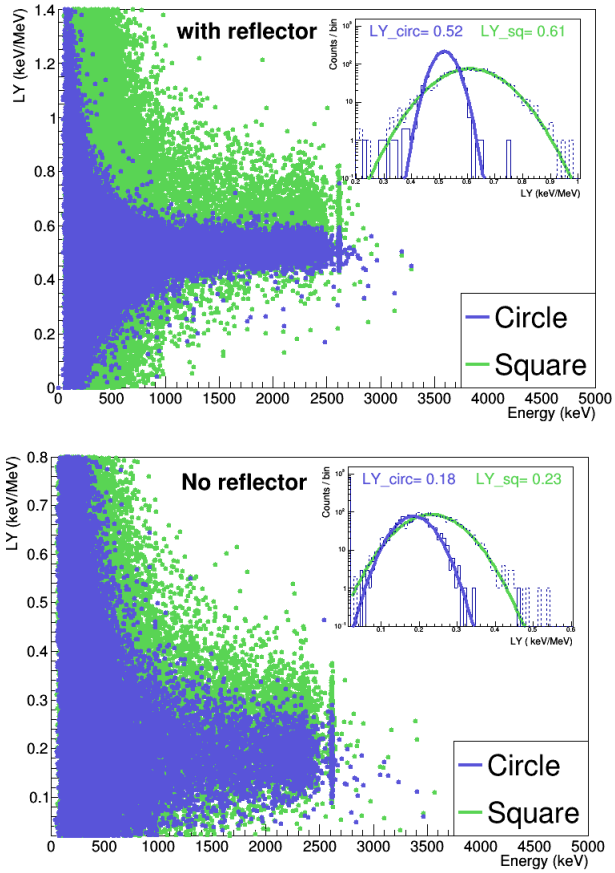

FIGURE 6.10: Light yield as a function of energy for LMO with reflecting foil (*top panel*) and for LMO without reflecting foil (*bottom panel*) when the crystal is facing a circular (purple) and a squared (green) LD.

Even if the detector structure was not optimal, the light collection was well studied and helped confirm the CUPID baseline where the bare LMO crystal should face two LDs that fully cover its surface from top and bottom. This consideration has been taken into account for the next CUPID prototype.

6.3 Perspectives and future tests

The current CUPID configuration is in a quite advanced phase where the baseline structure is defined. A schematic view of this design is shown in Fig. 6.11. The results obtained from the tests presented in this thesis were taken into account in this structure. The LD is put as close as possible to the crystal (0.5 mm gap between the LD and the crystal surface) to optimize the light collection. The CUPID detector array will be composed of 57 towers. Each tower will contain 28 crystals arranged in 14 floors with two crystals per floor. In this design, the structure is gravity stacked, and the crystals are thermally interconnected, as shown in Fig. 6.11. One floor is composed of a copper frame where the LD is fixed with PTFE pieces and the crystal is resting on the same PTFE pieces. A prototype of this design is currently being tested at LNGS and is composed of two floors of scintillating bolometers.

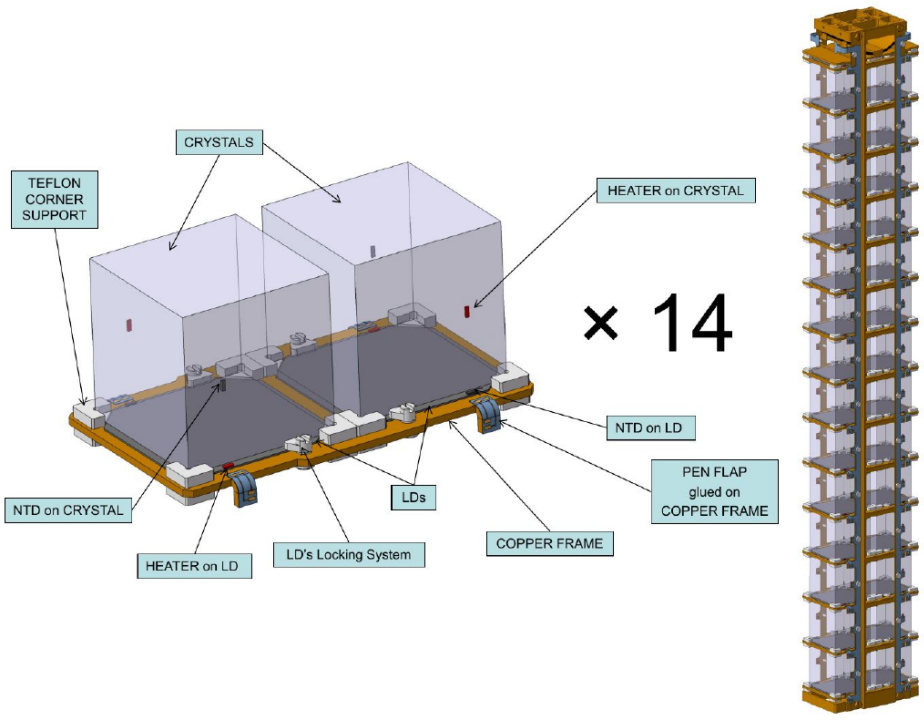

FIGURE 6.11: Schematics of the CUPID baseline tower. Each tower contains 14 floors (*right panel*) and each floor is composed of two LMO crystals and two LD (*left panel*).

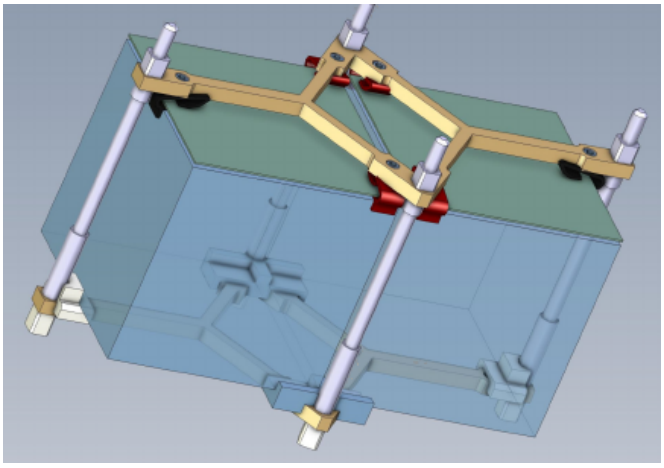

FIGURE 6.12: CUPID alternative tower design. In this configuration, the LD is in contact with the LMO and does not have a holder.

An alternative design is also being tested at LSC (summer 2021) where crystals are thermally independent and the LD does not have a copper holder but it is resting on the crystal, as shown in Fig. 6.12.

One of the goals of CUPID for the near future would be to test a full CUPID tower based on the baseline design with the 28 LMO crystals at LNGS.

Conclusions and perspectives

In this thesis, scintillating bolometers based on enriched $Li_2^{100}MoO_4$ and $^{116}CdWO_4$ crystals were investigated for searching $0\nu\beta\beta$ decay in the framework of CUPID. Promising results were obtained for the detectors based on enriched $^{116}CdWO_4$ crystals in terms of energy resolution and background suppression, confirming the robustness of the double readout technology based on scintillating bolometers. The CUPID-Mo outstanding results confirmed the feasibility of a large-scale experiment composed of an array of enriched $Li_2^{100}MoO_4$ scintillating bolometers. Moreover, the CUPID-Mo experiment has set a new world-leading limit for ^{100}Mo decay thanks to its high energy resolution and efficient background suppression. We also investigated the potential of the CUPID-Mo detectors for SD dark matter interactions with ^{7}Li.

The success of CUPID-Mo and the CUPID R&D tests allowed to establish the CUPID detector baseline design. With this baseline design, the expected background index is of the order of 10^{-4} counts/(keV.kg.yr). The main contribution to the background comes from the shields, the copper and PTFE holders, the internal contamination of the crystals, and the $2\nu\beta\beta$ pile-up. A schematic of the preliminary CUPID background budget is shown in Fig. 6.13. The background contamination from the holders depends on the final detector structure (the two different shades of blue in Fig. 6.13). The internal contamination of the crystals is well studied and known thanks to the CUPID-Mo results. The last known background contribution is the $2\nu\beta\beta$ pile-up since ^{100}Mo has one of the fastest $2\nu\beta\beta$ decays [176]. The CUPID collaboration is currently working on several methods for pile-up rejection. One of these methods was published in [172].

CUPID can be installed in its baseline version in the CUORE cryostat once CUORE data-taking is finished in 2024 and the enrichment and the crystal production is complete. This first phase of the experiment will reach the exclusion sensitivity of $T_{1/2} > 1.4 \times 10^{27}$ years with 250 kg of ^{100}Mo and 10 years of lifetime (BI=1×10^{-4} counts/(keV.kg.yr)). The second phase of the experiment, CUPID-reach, with the same mass of ^{100}Mo, will reach the background index of 2.5×10^{-5} counts/(keV.kg.yr) with the exclusion sensitivity of $T_{1/2} > 2.2 \times 10^{27}$ years. Eventually, an additional upgraded phase can be considered, CUPID-1T that would contain one-ton of ^{100}Mo. This one-ton of ^{100}Mo bolometric array would be installed in a cryostat that should be about 4-times larger than the CUORE one. In this phase the background level would be of the order of 10^{-6} counts/(keV.kg.yr) and the exclusion sensitivity of $T_{1/2} > 9.1 \times 10^{27}$ years. With such sensitivity, this ultimate CUPID phase would reach the normal ordering region. The discovery sensitivity of the different phases of CUPID and other next-generation experiments are shown

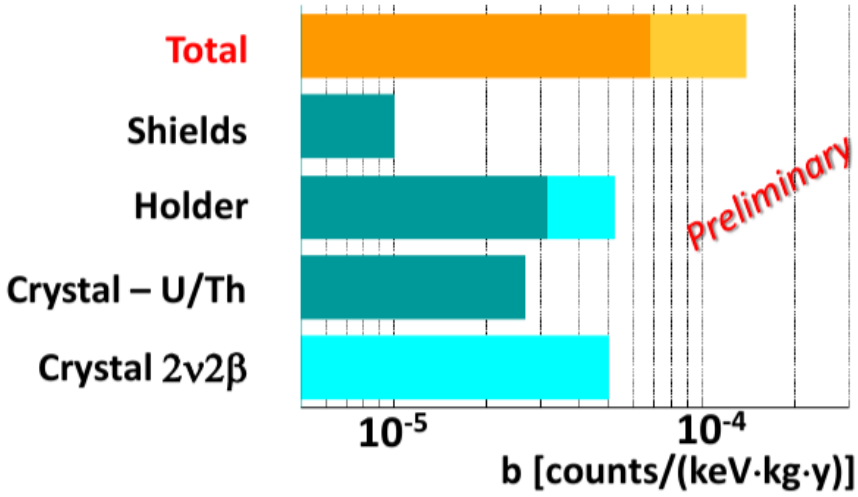

FIGURE 6.13: Scheme of the preliminary CUPID background budget with the current baseline. The darker shade of blue indicates the known and fixed background contributions. The lighter shade of blue represents the source of background that could be eliminated.

in Fig. 6.14.

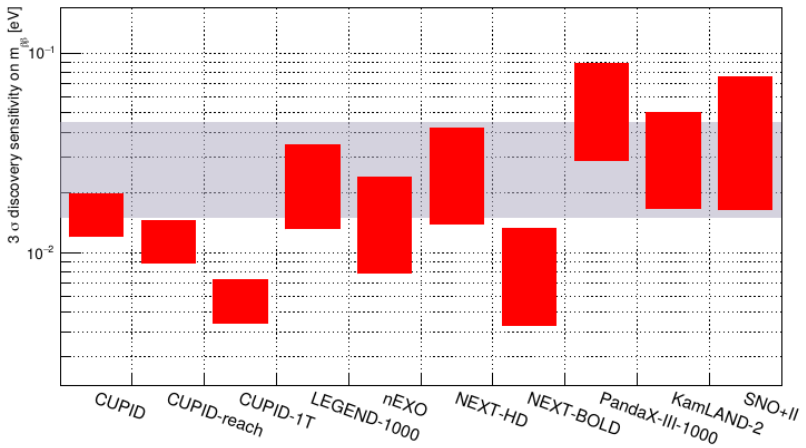

FIGURE 6.14: Discovery potential of the different CUPID phases and next-generation experiments [95].

In summary, CUPID is one of the most promising next-generation experiments searching for $0\nu\beta\beta$ decay: the cryogenic infrastructure is ready and well tested, the detector technology based on scintillating bolometers was successfully tested and validated by medium-scale demonstrators and R&D tests, and the background model is well advanced. Thanks to these features, CUPID will be able to probe the inverted ordering region.

As mentioned in this thesis, one of the experimental challenges in the search for $0\nu\beta\beta$ decay is the possible axial-vector g_A quenching, which would make the half-lives longer and hence affect the experimental sensitivity. It is of fundamental importance to understand this quenching and investigate its measurement in any beta decay (β, $2\nu\beta\beta$ or $0\nu\beta\beta$) to collect information about it. For this purpose, we investigated the single beta decay of ^{113}Cd with the help of a natural $CdWO_4$ scintillating bolometer. The goal of the analysis presented in this thesis is to use the spectral shape method to extract the quenching of g_A in the four-fold forbidden beta decay of ^{113}Cd using the experimental background spectrum of the $CdWO_4$ scintillating bolometer. In [40], the authors show the possibility to exploit the SSM to probe the g_A quenching by comparing their theoretical calculations for different models with the experimental β spectrum shape of ^{113}Cd from [158], using the same crystal, as shown in Fig. 6.15. The computed β spectra are obtained using the SSM for different NME models: MQPM [177], IBM [178], and NSM [179]. The experimental spectrum from [158] matches with the computed spectra with the IBM and the NSM models [40] with g_A values of 0.93 and 0.90 respectively.

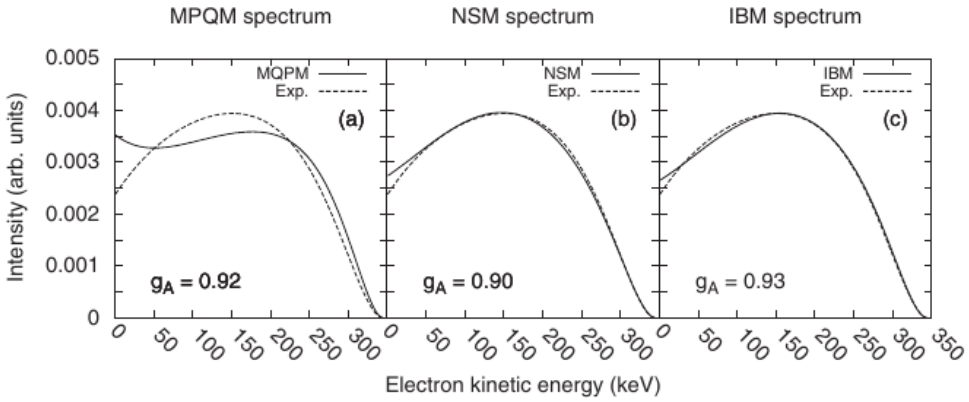

FIGURE 6.15: Comparison between the computed β spectra of ^{113}Cd with the experimental one [40].

Recently, the authors in [180], confirmed the quenching of g_A using a revised SSM in the beta decay spectrum of ^{113}Cd provided by the COBRA collaboration [67]. The spectrum was measured with high accuracy which allowed to confirm the quenching of g_A.

In summary, with the ^{113}Cd spectrum analysis presented in this thesis, we aim to measure the quenching of g_a taking advantage of both heat (good energy resolution) and light channels (low threshold, high efficiency in pile-up rejection). This allows us to have a robust spectral measurement via the comparison between the two channels. As mentioned, the next step of the analysis is to ameliorate the uncertainties on the spectrum measured by the heat channel and build a complete background model for both channels to extract with precision the beta spectra.

Bibliography

1. Group, P. D. Review of Particle Physics. *Progress of Theoretical and Experimental Physics* **2020.** 083C01. ISSN: 2050-3911. eprint: https://academic.oup.com/ptep/article-pdf/2020/8/083C01/34673740/rpp2020-vol2-2015-2092_18.pdf. https://doi.org/10.1093/ptep/ptaa104 (Aug. 2020).
2. Brown, L. M. The idea of the neutrino. *Phys. Today* **31N9,** 23–28 (1978).
3. Fermi, E. Tentativo di una Teoria Dei Raggi β. *Il Nuovo Cimento (1924-1942)* **11,** 1. ISSN: 1827-6121. https://doi.org/10.1007/BF02959820 (1934).
4. Pontecorvo, B. Inverse beta process. *Camb. Monogr. Part. Phys. Nucl. Phys. Cosmol.* **1.** [,97(1946)], 25–31 (1991).
5. Cowan, C. L., Reines, F., Harrison, F. B., Kruse, H. W. & McGuire, A. D. Detection of the free neutrino: A Confirmation. *Science* **124** (1956).
6. Reines, F. & Cowan, C. L. Detection of the Free Neutrino. *Phys. Rev.* **92,** 830–831. https://link.aps.org/doi/10.1103/PhysRev.92.830 (3 1953).
7. Davis, R., Harmer, D. S. & Hoffman, K. C. Search for Neutrinos from the Sun. *Phys. Rev. Lett.* **20,** 1205–1209. https://link.aps.org/doi/10.1103/PhysRevLett.20.1205 (21 1968).
8. Gelb, J. M., Kwong, W.-k. & Rosen, S. P. Implications of new GALLEX results for the MSW solution of the solar neutrino problem. *Phys. Rev. Lett.* **69,** 1864–1866. arXiv: hep-ph/9206228 [hep-ph] (1992).
9. Altmann, M. *et al.* GNO solar neutrino observations: Results for GNO I. *Phys. Lett.* **B490,** 16–26. arXiv: hep-ex/0006034 [hep-ex] (2000).
10. Abdurashitov, J. N. *et al.* Solar neutrino flux measurements by the Soviet-American Gallium Experiment (SAGE) for half the 22 year solar cycle. *J. Exp. Theor. Phys.* **95.** [Zh. Eksp. Teor. Fiz.122,211(2002)], 181–193. arXiv: astro-ph/0204245 [astro-ph] (2002).
11. Pontecorvo, B. Neutrino Experiments and the Problem of Conservation of Leptonic Charge. *Sov. Phys. JETP* **26.** [Zh. Eksp. Teor. Fiz.53,1717(1967)], 984–988 (1968).
12. Shiozawa, M. Evidence for neutrino oscillations in atmospheric neutrino observations. *Nucl. Instrum. Meth.* **A433,** 307–313 (1999).
13. McDonald, A. B. First neutrino observations from the Sudbury Neutrino Observatory. *Nucl. Phys. Proc. Suppl.* **91.** [21(2000)], 21–28. arXiv: hep-ex/0011025 [hep-ex] (2001).

14. Pontecorvo, B. Mesonium and anti-mesonium. *Sov. Phys. JETP* **6.** [Zh. Eksp. Teor. Fiz.33,549(1957)], 429 (1957).
15. Tanabashi, M. *et al.* Review of Particle Physics. *Phys. Rev.* **D98,** 030001 (2018).
16. Takeuchi, Y. Recent results and future prospects of Super-Kamiokande. *Nucl. Instrum. Meth. A* **952,** 161634 (2020).
17. Barros, N. Final results from SNO. *Nucl. Phys. B Proc. Suppl.* **237-238** (eds Bernardini, P., Fogli, G. & Lisi, E.) 107–110 (2013).
18. De Kerret, H. *et al.* Double Chooz θ_{13} measurement via total neutron capture detection. *Nature Phys.* **16,** 558–564. arXiv: 1901.09445 [hep-ex] (2020).
19. Berns, L. *Recent Results from T2K* in *55th Rencontres de Moriond on Electroweak Interactions and Unified Theories* (May 2021). arXiv: 2105.06732 [hep-ex].
20. Nosek, T. *NOvA Recent Results with Neutrino+Antineutrino Data* in *New Trends in High-Energy Physics* (May 2019). arXiv: 1905.09109 [hep-ex].
21. Tórtola, M. Three-flavor neutrino oscillations and beyond. *Journal of Physics: Conference Series* **1342,** 012048. https://doi.org/10.1088%2F1742-6596%2F1342%2F1%2F012048 (2020).
22. Aker, M. *et al.* An improved upper limit on the neutrino mass from a direct kinematic method by KATRIN. *Phys. Rev. Lett.* **123,** 221802. arXiv: 1909.06048 [hep-ex] (2019).
23. Sander, O. *et al.* Software-Defined Radio Readout System for the ECHo Experiment. *IEEE Transactions on Nuclear Science* **66,** 1204–1209 (2019).
24. Becker, D. T. *et al.* Working principle and demonstrator of microwave multiplexing for the HOLMES experiment microcalorimeters. *Journal of Instrumentation* **14.** ISSN: 1748-0221 (2019).
25. Giachero, A. *et al.* Measuring the electron neutrino mass with improved sensitivity: the HOLMES experiment. *JINST* **12,** C02046. arXiv: 1612.03947 (2017).
26. KATRIN. *KATRIN collaboration* https://www.katrin.kit.edu/1033.php.
27. Aghanim, N. *et al.* Planck 2018 results. VI. Cosmological parameters. arXiv: 1807.06209 [astro-ph.CO] (2018).
28. Roy Choudhury, S. & Hannestad, S. Updated results on neutrino mass and mass hierarchy from cosmology with Planck 2018 likelihoods. arXiv: 1907.12598 [astro-ph.CO] (2019).
29. Agostini, M., Benato, G., Dell'Oro, S., Pirro, S. & Vissani, F. Discovery probabilities of Majorana neutrinos based on cosmological data. *Phys. Rev. D* **103,** 033008. arXiv: 2012.13938 [hep-ph] (2021).
30. Esteban, I., Gonzalez-Garcia, M. C., Maltoni, M., Schwetz, T. & Zhou, A. The fate of hints: updated global analysis of three-flavor neutrino oscillations. *JHEP* **09,** 178. arXiv: 2007.14792 [hep-ph] (2020).
31. Capozzi, F. *et al.* Addendum to "Global constraints on absolute neutrino masses and their ordering". *Phys. Rev. D* **101,** 116013. https://link.aps.org/doi/10.1103/PhysRevD.101.116013 (11 2020).

32. De Salas, P. F. *et al.* 2020 global reassessment of the neutrino oscillation picture. *JHEP* **02,** 071. arXiv: 2006.11237 [hep-ph] (2021).
33. Goeppert-Mayer, M. Double beta-disintegration. *Phys. Rev.* **48,** 512–516 (1935).
34. Barabash, A. Precise Half-Life Values for Two-Neutrino Double-β Decay: 2020 Review. *Universe* **6,** 159. arXiv: 2009.14451 [nucl-ex] (2020).
35. Furry, W. H. On transition probabilities in double beta-disintegration. *Phys. Rev.* **56,** 1184–1193 (1939).
36. Babič, A., Štefánik, D., Krivoruchenko, M. I. & Šimkovic, F. Bound-state double-β decay. *Phys. Rev.* **C98,** 065501. arXiv: 1805.07815 [hep-ph] (2018).
37. Yao, J. M., Song, L. S., Hagino, K., Ring, P. & Meng, J. Systematic study of nuclear matrix elements in neutrinoless double-β decay with a beyond-mean-field covariant density functional theory. *Phys. Rev. C* **91,** 024316. arXiv: 1410.6326 [nucl-th] (2015).
38. Engel, J. & Menéndez, J. Status and Future of Nuclear Matrix Elements for Neutrinoless Double-Beta Decay: A Review. *Rept. Prog. Phys.* **80,** 046301. arXiv: 1610.06548 [nucl-th] (2017).
39. Suhonen, J. T. Value of the Axial-Vector Coupling Strength in and Decays: A Review. *Frontiers in Physics* **5,** 55. ISSN: 2296-424X. https://www.frontiersin.org/article/10.3389/fphy.2017.00055 (2017).
40. Haaranen, M., Kotila, J. & Suhonen, J. Spectrum-shape method and the next-to-leading-order terms of the β-decay shape factor. *Phys. Rev. C* **95,** 024327. https://link.aps.org/doi/10.1103/PhysRevC.95.024327 (2 2017).
41. Haaranen, M., Srivastava, P. C. & Suhonen, J. Forbidden nonunique β decays and effective values of weak coupling constants. *Phys. Rev. C* **93,** 034308. https://link.aps.org/doi/10.1103/PhysRevC.93.034308 (3 2016).
42. Mei, D. & Hime, A. Muon-induced background study for underground laboratories. *Phys. Rev.* **D73,** 053004. arXiv: astro-ph/0512125 [astro-ph] (2006).
43. Umehara, S. *et al.* Neutrino-less double-β decay of ^{48}Ca studied by CaF_2(Eu) scintillators. *Phys. Rev. C* **78,** 058501. https://link.aps.org/doi/10.1103/PhysRevC.78.058501 (5 2008).
44. Agostini, M. *et al.* Final Results of GERDA on the Search for Neutrinoless Double-β Decay. *Phys. Rev. Lett.* **125,** 252502. arXiv: 2009.06079 [nucl-ex] (2020).
45. Alvis, S. I. *et al.* Search for neutrinoless double-β decay in ^{76}Ge with 26 kg yr of exposure from the Majorana Demonstrator. *Phys. Rev. C* **100,** 025501. https://link.aps.org/doi/10.1103/PhysRevC.100.025501 (2 2019).
46. Azzolini, O. *et al.* Final result of CUPID-0 phase-I in the search for the ^{82}Se Neutrinoless Double-β Decay. *Phys. Rev. Lett.* **123,** 032501. arXiv: 1906.05001 [nucl-ex] (2019).
47. Argyriades, J. *et al.* Measurement of the two neutrino double beta decay half-life of Zr-96 with the NEMO-3 detector. *Nucl. Phys.* **A847,** 168–179. arXiv: 0906.2694 [nucl-ex] (2010).

48. Armengaud, E. *et al.* New Limit for Neutrinoless Double-Beta Decay of ^{100}Mo from the CUPID-Mo Experiment. *Phys. Rev. Lett.* **126,** 181802. arXiv: 2011.13243 [nucl-ex] (2021).
49. Barabash, A. S. *et al.* Final results of the Aurora experiment to study 2β decay of ^{116}Cd with enriched $^{116}CdWO_4$ crystal scintillators. *Phys. Rev.* **D98,** 092007. arXiv: 1811.06398 [nucl-ex] (2018).
50. Adams, D. Q. *et al.* High sensitivity neutrinoless double-beta decay search with one tonne-year of CUORE data. arXiv: 2104.06906 [nucl-ex] (Apr. 2021).
51. Gando, A. *et al.* Search for Majorana Neutrinos near the Inverted Mass Hierarchy Region with KamLAND-Zen. *Phys. Rev. Lett.* **117.** [Addendum: Phys. Rev. Lett.117,no.10,109903(2016)], 082503. arXiv: 1605.02889 [hep-ex] (2016).
52. Anton, G. *et al.* Search for Neutrinoless Double-β Decay with the Complete EXO-200 Dataset. *Phys. Rev. Lett.* **123,** 161802. arXiv: 1906.02723 [hep-ex] (2019).
53. Arnold, R. *et al.* Measurement of the $2\nu\beta\beta$ decay half-life of ^{150}Nd and a search for $0\nu\beta\beta$ decay processes with the full exposure from the NEMO-3 detector. *Phys. Rev. D* **94,** 072003. https://link.aps.org/doi/10.1103/PhysRevD.94.072003 (7 2016).
54. López-Castaño, J. M. & Guinn, I. Current status of LEGEND: Searching for Neutrinoless Double-Beta Decay in 76Ge: Part II. *PoS,* 162. arXiv: 1912.03308 [nucl-ex] (2019).
55. Zeng, Z. *et al.* Characterization study of a broad-energy germanium detector at CJPL. arXiv: 1603.01782 [physics.ins-det] (2016).
56. Agostini, M. *et al.* Probing Majorana neutrinos with double-β decay. *Science* **365,** 1445. arXiv: 1909.02726 [hep-ex] (2019).
57. Arnold, R. *et al.* Technical design and performance of the NEMO 3 detector. *Nucl. Instrum. Meth.* **A536,** 79–122. arXiv: physics/0402115 [physics] (2005).
58. SuperNEMO. *SuperNEMO collaboration* https://supernemo.org/about.html.
59. Arnold, R. *et al.* Final results on ^{82}Se double beta decay to the ground state of ^{82}Kr from the NEMO-3 experiment. *Eur. Phys. J.* **C78,** 821. arXiv: 1806.05553 [hep-ex] (2018).
60. Jeremie, A. The SuperNEMO demonstrator double beta experiment. *Nucl. Instrum. Meth. A* **958** (eds Krammer, M. *et al.*) 162115 (2020).
61. Arnold, R. *et al.* Results of the search for neutrinoless double-β decay in ^{100}Mo with the NEMO-3 experiment. *Phys. Rev. D* **92,** 072011. https://link.aps.org/doi/10.1103/PhysRevD.92.072011 (7 2015).
62. Alenkov, V. *et al.* First Results from the AMoRE-Pilot neutrinoless double beta decay experiment. *Eur. Phys. J.* **C79,** 791. arXiv: 1903.09483 [hep-ex] (2019).

63. Lee, M. H. AMoRE: A search for neutrinoless double-beta decay of 100Mo using low-temperature molybdenum-containing crystal detectors. *JINST* **15,** C08010. arXiv: 2005.05567 [physics.ins-det] (2020).
64. Arnold, R. *et al.* Measurement of the $2\nu\beta\beta$ Decay Half-Life and Search for the $0\nu\beta\beta$ Decay of ^{116}Cd with the NEMO-3 Detector. *Phys. Rev.* **D95,** 012007. arXiv: 1610.03226 [hep-ex] (2017).
65. Ebert, J. *et al.* The COBRA demonstrator at the LNGS underground laboratory. *Nucl. Instrum. Meth.* **A807,** 114–120. arXiv: 1507.08177 [physics.ins-det] (2016).
66. Ebert, J. *et al.* Results of a search for neutrinoless double- decay using the COBRA demonstrator. *Phys. Rev.* **C94,** 024603. arXiv: 1509.04113 [nucl-ex] (2016).
67. Bodenstein-Dresler, L. *et al.* Quenching of g_A deduced from the β-spectrum shape of ^{113}Cd measured with the COBRA experiment. *Phys. Lett.* **B800.** arXiv: 1806.02254 [nucl-ex] (2020).
68. Barabash, A. S. *et al.* Low background detector with enriched $^{116}CdWO_4$ crystal scintillators to search for double β decay of ^{116}Cd. *JINST* **6,** P08011. arXiv: 1108.2771 [physics.ins-det] (2011).
69. Meija, J. *et al.* Isotopic compositions of the elements 2013 (IUPAC Technical Report). *Pure and Applied Chemistry* **88,** 293–306. https://doi.org/10.1515/pac-2015-0503 (2016).
70. Alduino, C. *et al.* The CUORE cryostat: An infrastructure for rare event searches at millikelvin temperatures. *Cryogenics* **102,** 9–21 (2019).
71. Aharmim, B. *et al.* Combined analysis of all three phases of solar neutrino data from the Sudbury Neutrino Observatory. *Phys. Rev. C* **88,** 025501. https://link.aps.org/doi/10.1103/PhysRevC.88.025501 (2 2013).
72. Albanese, V. *et al.* The SNO+ Experiment. arXiv: 2104.11687 (Apr. 2021).
73. Paton, J. *Neutrinoless Double Beta Decay in the SNO+ Experiment* in *Prospects in Neutrino Physics (NuPhys2018) London, United Kingdom, December 19-21, 2018* (2019). arXiv: 1904.01418 [hep-ex].
74. Auger, M. *et al.* The EXO-200 detector, part I: Detector design and construction. *JINST* **7,** P05010. arXiv: 1202.2192 [physics.ins-det] (2012).
75. Albert, J. B. *et al.* Sensitivity and Discovery Potential of nEXO to Neutrinoless Double Beta Decay. *Phys. Rev.* **C97,** 065503. arXiv: 1710.05075 [nucl-ex] (2018).
76. Renner, J. *et al.* Initial results on energy resolution of the NEXT-White detector. *JINST* **13,** P10020. arXiv: 1808.01804 [physics.ins-det] (2018).
77. Martín-Albo, J. *The NEXT experiment for neutrinoless double beta decay searches* in *31st Rencontres de Blois on Particle Physics and Cosmology Blois, France, June 2-7, 2019* (2019). arXiv: 1910.07314 [physics.ins-det].

78. Giuliani, A. *et al.* Double Beta Decay APPEC Committee Report. arXiv: 1910.04688 [hep-ex] (2019).
79. Vissani, F. Signal of neutrinoless double beta decay, neutrino spectrum and oscillation scenarios. *JHEP* **06.** [,700(1999)], 022. arXiv: hep-ph/9906525 (1999).
80. Langley, S. P. The Bolometer and Radiant Energy. *Proceedings of the American Academy of Arts and Sciences* **16,** 342–358. ISSN: 01999818. http://www.jstor.org/stable/25138616 (1880).
81. P., C. & A., L. Sur la chaleur dégagée spontanément par les sels de radium. *Compt. Rend* **136,** 673–675 (1903).
82. Simon, F. Application of Low Temperature Calorimetry to Radioactive Measurements. *Nature,* 135–763 (1934).
83. Fiorini, E. & Niinikoski, T. Low Temperature Calorimetry for Rare Decays. *Nucl. Instrum. Meth. A* **224,** 83 (1984).
84. Novati, V. *Sensitivity enhancement of the CUORE experiment via the development of Cherenkov hybrid TeO bolometers* PhD thesis (CSNSM, Orsay, 2018).
85. L'Hote, D. *Les bolomètres pour la détection de particules* École thématique. Lecture. Maubuisson, (France), du 12-17 septembre 1994 : 13ème session, Sept. 1994. https://cel.archives-ouvertes.fr/cel-00648817.
86. Armengaud, E. *et al.* The CUPID-Mo experiment for neutrinoless double-beta decay: performance and prospects. *Eur. Phys. J.* **C80,** 44. arXiv: 1909.02994 [physics.ins-det] (2020).
87. Adams, D. Q. *et al.* Improved Limit on Neutrinoless Double-Beta Decay in ^{130}Te with CUORE. *Phys. Rev. Lett.* **124,** 122501. arXiv: 1912.10966 [nucl-ex] (2020).
88. Abdelhameed, A. *et al.* First results from the CRESST-III low-mass dark matter program. *Phys. Rev. D* **100,** 102002. arXiv: 1904.00498 [astro-ph.CO] (2019).
89. Haller, E. E., Palaio, N. P., Rodder, M., Hansen, W. L. & Kreysa, E. in *Neutron Transmutation Doping of Semiconductor Materials* (ed Larrabee, R. D.) 21–36 (Springer US, Boston, MA, 1984). ISBN: 978-1-4613-2695-3. https://doi.org/10.1007/978-1-4613-2695-3_2.
90. Alessandrello, A *et al.* Methods for response stabilization in bolometers for rare decays. *Nucl. Instrum. Methods Phys. Res. A,* **412,** 454 –464. ISSN: 0168-9002 (1998).
91. Gonzalez-Mestres, L. & Perret-Gallix, D. Detection of Low-energy Solar Neutrinos and Galactic Dark Matter With Crystal Scintillators. *Nucl. Instrum. Meth. A* **279,** 382–387 (1989).
92. Pirro, S. *et al.* Scintillating double beta decay bolometers. *Phys. Atom. Nucl.* **69,** 2109–2116. arXiv: nucl-ex/0510074 (2006).
93. Pirro, S. & Mauskopf, P. Advances in Bolometer Technology for Fundamental Physics. *Ann. Rev. Nucl. Part. Sci.* **67,** 161–181 (2017).

94. Adams, D. Q. *et al.* Improved Limit on Neutrinoless Double-Beta Decay in ^{130}Te with CUORE. arXiv: 1912.10966 [nucl-ex] (2019).
95. Armstrong, W. R. *et al.* CUPID pre-CDR. arXiv: 1907.09376 [physics.ins-det] (July 2019).
96. Bizarri, G. Scintillation mechanisms of inorganic materials: From crystal characteristics to scintillation properties. *Journal of Crystal Growth* **312,** 1213 –1215. ISSN: 0022-0248. http://www.sciencedirect.com/science/article/pii/S0022024809011609 (2010).
97. Birks, J. B. Scintillations from Organic Crystals: Specific Fluorescence and Relative Response to Different Radiations. *Proc. Phys. Soc. A* **64,** 874–877 (1951).
98. Mancuso, M. *et al.* An experimental study of antireflective coatings in Ge light detectors for scintillating bolometers. *EPJ Web Conf.* **65** (eds Danevich, F. & Tretyak, V.) 04003 (2014).
99. Neganov, B. & Trofimov, V. Colorimetric method measuring ionizing radiation. *Otkryt. Izobret.* **146,** 215 (1985).
100. Luke, P. N. Voltage-assisted calorimetric ionization detector. *J. Appl. Phys,* 64:6858 (1988).
101. Press, W. H., Teukolsky, S. A., Vetterling, W. T. & Flannery, B. P. *Numerical Recipes in C* Second (Cambridge University Press, Cambridge, USA, 1992).
102. Mancuso, M. *Development and optimization of scintillating bolometers and innovative light detectors for a pilot underground experiment on neutrinoless double beta decay* PhD thesis (CSNSM, Orsay, 2016).
103. Gatti, E. & Manfredi, P. Processing the Signals From Solid State Detectors in Elementary Particle Physics. *Riv. Nuovo Cim.* **9N1,** 1–146 (1986).
104. Armengaud, E. *et al.* Performance of the EDELWEISS-III experiment for direct dark matter searches. *JINST* **12,** P08010. arXiv: 1706.01070 (2017).
105. Armatol, A. *et al.* Characterization of cubic $Li_2^{100}MoO_4$ crystals for the CUPID experiment. arXiv: 2011.13656 [physics.ins-det] (Nov. 2020).
106. Olivieri, E., Billard, J., De Jesus, M., Juillard, A. & Leder, A. Vibrations on pulse tube based Dry Dilution Refrigerators for low noise measurements. *Nucl. Instrum. Meth. A* **858,** 73–79. arXiv: 1703.08957 [physics.ins-det] (2017).
107. Bellini, G. *et al.* Cosmic-muon flux and annual modulation in Borexino at 3800 m water-equivalent depth. *JCAP* **05,** 015. arXiv: 1202.6403 [hep-ex] (2012).
108. Singh, B. Nuclear Data Sheets for A = 100. *Nuclear Data Sheets* **109,** 297–516. ISSN: 0090-3752 (2008).
109. Armengaud, E. *et al.* Development of ^{100}Mo-containing scintillating bolometers for a high-sensitivity neutrinoless double-beta decay search. *Eur. Phys. J. C* **77,** 785. arXiv: 1704.01758 [physics.ins-det] (2017).
110. Barinova, O. P. *et al.* First test of Li_2MoO_4 crystal as a cryogenic scintillating bolometer. *Nucl. Instrum. Meth. A* **613,** 54–57 (2010).

111. Huang, R. *et al.* Pulse Shape Discrimination in CUPID-Mo using Principal Component Analysis. *JINST* **16,** P03032. arXiv: 2010.04033 [physics.data-an] (2021).

112. Alduino, C. *et al.* Analysis techniques for the evaluation of the neutrinoless double-β decay lifetime in ^{130}Te with the CUORE-0 detector. *Phys. Rev. C* **93,** 045503. arXiv: 1601.01334 [nucl-ex] (2016).

113. Di Domizio, S. *et al.* A data acquisition and control system for large mass bolometer arrays. *JINST* **13,** P12003. arXiv: 1807.11446 [physics.ins-det] (2018).

114. Di Domizio, S., Orio, F. & Vignati, M. Lowering the energy threshold of large-mass bolometric detectors. *JINST* **6,** P02007. arXiv: 1012.1263 [astro-ph.IM] (2011).

115. Branca, A. Performance of the low threshold Optimum Trigger on CUORE data. *J. Phys. Conf. Ser.* **1468** (ed Nakahata, M.) 012118 (2020).

116. Schmidt, B. *et al.* First data from the CUPID-Mo neutrinoless double beta decay experiment. *J. Phys. Conf. Ser.* **1468** (ed Nakahata, M.) 012129. arXiv: 1911.10426 [hep-ex] (2020).

117. Fedor Šimkovic Vadim Rodin, A. F. & Vogel, P. $0\nu\beta\beta$ and $2\nu\beta\beta$ nuclear matrix elements, quasiparticle random-phase approximation, and isospin symmetry restoration. *Phys. Rev. C* **87,** 045501. https://link.aps.org/doi/10.1103/PhysRevC.87.045501 (4 2013).

118. Vaquero, N. L., Rodríguez, T. R. & Egido, J. L. Shape and Pairing Fluctuation Effects on Neutrinoless Double Beta Decay Nuclear Matrix Elements. *Phys. Rev. Lett.* **111,** 142501. https://link.aps.org/doi/10.1103/PhysRevLett.111.142501 (14 2013).

119. Barea, J., Kotila, J. & Iachello, F. $0\nu\beta\beta$ and $2\nu\beta\beta$ nuclear matrix elements in the interacting boson model with isospin restoration. *Phys. Rev. C* **91,** 034304. https://link.aps.org/doi/10.1103/PhysRevC.91.034304 (3 2015).

120. Hyvärinen, J. & Suhonen, J. Nuclear matrix elements for $0\nu\beta\beta$ decays with light or heavy Majorana-neutrino exchange. *Phys. Rev. C* **91,** 024613. https://link.aps.org/doi/10.1103/PhysRevC.91.024613 (2 2015).

121. Song, L. S., Yao, J. M., Ring, P. & Meng, J. Nuclear matrix element of neutrinoless double-β decay: Relativity and short-range correlations. *Phys. Rev. C* **95,** 024305. https://link.aps.org/doi/10.1103/PhysRevC.95.024305 (2 2017).

122. Rath, P. K. *et al.* Neutrinoless $\beta\beta$ decay transition matrix elements within mechanisms involving light Majorana neutrinos, classical Majorons, and sterile neutrinos. *Phys. Rev. C* **88,** 064322. https://link.aps.org/doi/10.1103/PhysRevC.88.064322 (6 2013).

123. F. Šimkovic, A. S. & Vogel, P. $0\nu\beta\beta$ and $2\nu\beta\beta$ nuclear matrix elements evaluated in closure approximation, neutrino potentials and SU(4) symmetry. *Phys. Rev. C* **98,** 064325. https://link.aps.org/doi/10.1103/PhysRevC.98.064325 (6 2018).

124. Rath, P. K., Chandra, R., Chaturvedi, K. & Raina, P. K. Nuclear Transition Matrix Elements for Double- Decay Within PHFB Model. *Frontiers in Physics* **7,** 64. ISSN: 2296-424X. https://www.frontiersin.org/article/10.3389/fphy.2019.00064 (2019).

125. Zwicky, F. Die Rotverschiebung von extragalaktischen Nebeln. *Helv. Phys. Acta* **6,** 110–127 (1933).

126. Gilman, D. *et al.* Strong lensing signatures of self-interacting dark matter in low-mass halos. arXiv: 2105.05259 [astro-ph.CO] (May 2021).

127. Kawasaki, M., Nakatsuka, H., Nakayama, K. & Sekiguchi, T. Revisiting CMB constraints on dark matter annihilation. arXiv: 2105.08334 [astro-ph.CO] (May 2021).

128. Abdallah, H. *et al.* Search for dark matter annihilation in the Wolf-Lundmark-Melotte dwarf irregular galaxy with H.E.S.S. *Phys. Rev. D* **103,** 102002. arXiv: 2105.04325 [astro-ph.HE] (2021).

129. Weng, Z. Latest Results from the AMS Experiment on the International Space Station. *PoS* **ICHEP2020,** 045 (2021).

130. Sirunyan, A. M. *et al.* Search for dark matter produced in association with a leptonically decaying Z boson in proton-proton collisions at $\sqrt{s} = 13$ TeV. *Eur. Phys. J. C* **81.** [Erratum: Eur.Phys.J.C 81, 333 (2021)], 13. arXiv: 2008.04735 [hep-ex] (2021).

131. Lewin, J. D. & Smith, P. F. Review of mathematics, numerical factors, and corrections for dark matter experiments based on elastic nuclear recoil. *Astropart. Phys.* **6,** 87–112 (1996).

132. Billard, J. *Détection directionnelle de matière sombre avec MIMAC* PhD thesis (Laboratoire de Physique Subatomique et de Cosmologie, France, 2012).

133. Lisanti, M. *Lectures on Dark Matter Physics* in *Theoretical Advanced Study Institute in Elementary Particle Physics: New Frontiers in Fields and Strings* (Mar. 2016). arXiv: 1603.03797 [hep-ph].

134. Pérez, M. L. M. *Diseño de un prototipo para un experimento de detección directa de materia oscura mediante modulación anual con centelleadores de ioduro de sodio.* PhD thesis (Universidad de Zaragoza, 2006).

135. Cheng, C. *et al.* Search for Light Dark Matter-Electron Scatterings in the PandaX-II Experiment. *Phys. Rev. Lett.* **126,** 211803. arXiv: 2101.07479 [hep-ex] (2021).

136. Salucci, P., Nesti, F., Gentile, G. & Martins, C. F. The dark matter density at the Sun's location. *Astron. Astrophys.* **523,** A83. arXiv: 1003.3101 [astro-ph.GA] (2010).

137. Smith, M. C. *et al.* The RAVE Survey: Constraining the Local Galactic Escape Speed. *Mon. Not. Roy. Astron. Soc.* **379,** 755–772. arXiv: astro-ph/0611671 (2007).

138. Kerr, F. J. & Lynden-Bell, D. Review of galactic constants. *Monthly Notices of the Royal Astronomical Society* **221,** 1023–1038. ISSN: 0035-8711 (Aug. 1986).

139. Alkhatib, I. *et al.* Constraints on Lightly Ionizing Particles from CDMSlite. arXiv: 2011.09183 [hep-ex] (Nov. 2020).

140. Abdelhameed, A. H. *et al.* First results on sub-GeV spin-dependent dark matter interactions with ^{7}Li. *Eur. Phys. J. C* **79,** 630 (2019).

141. Alduino, C. *et al.* Low Energy Analysis Techniques for CUORE. *Eur. Phys. J. C* **77,** 857. arXiv: 1708.07809 [physics.ins-det] (2017).

142. Yellin, S. Finding an upper limit in the presence of unknown background. *Phys. Rev. D* **66,** 032005. arXiv: physics/0203002 (2002).

143. Abdelhameed, A. H. *et al.* Cryogenic characterization of a $LiAlO_2$ crystal and new results on spin-dependent dark matter interactions with ordinary matter. *Eur. Phys. J. C* **80,** 834. arXiv: 2005.02692 [physics.ins-det] (2020).

144. Amole, C. *et al.* Dark Matter Search Results from the Complete Exposure of the PICO-60 C_3F_8 Bubble Chamber. *Phys. Rev. D* **100,** 022001. arXiv: 1902.04031 [astro-ph.CO] (2019).

145. Akerib, D. S. *et al.* Limits on spin-dependent WIMP-nucleon cross section obtained from the complete LUX exposure. *Phys. Rev. Lett.* **118,** 251302. arXiv: 1705.03380 [astro-ph.CO] (2017).

146. Fu, C. *et al.* Spin-Dependent Weakly-Interacting-Massive-Particle–Nucleon Cross Section Limits from First Data of PandaX-II Experiment. *Phys. Rev. Lett.* **118.** [Erratum: Phys.Rev.Lett. 120, 049902 (2018)], 071301. arXiv: 1611.06553 (2017).

147. Aprile, E. *et al.* XENON100 Dark Matter Results from a Combination of 477 Live Days. *Phys. Rev. D* **94,** 122001. arXiv: 1609.06154 [astro-ph.CO] (2016).

148. Agnese, R. *et al.* Low-mass dark matter search with CDMSlite. *Phys. Rev. D* **97,** 022002. arXiv: 1707.01632 [astro-ph.CO] (2018).

149. Tabarelli de Fatis, T. Cerenkov emission as a positive tag of double beta decays in bolometric experiments. *Eur. Phys. J. C* **65,** 359–361 (2010).

150. Wang, M. *et al.* The AME2016 atomic mass evaluation (II). Tables, graphs and references. *Chinese Physics C* **41,** 030003. https://doi.org/10.1088/1674-1137/41/3/030003 (2017).

151. Blachot, J. Nuclear Data Sheets for A = 116. *Nuclear Data Sheets* **111,** 717–895. ISSN: 0090-3752. https://www.sciencedirect.com/science/article/pii/S0090375210000281 (2010).

152. Ejiri, H. *et al.* Double beta decays of Cd-116. *J. Phys. Soc. Jap.* **64,** 339–343 (1995).

153. Danevich, F. A. *et al.* Search for 2β decay of cadmium and tungsten isotopes: Final results of the Solotvina experiment. *Phys. Rev. C* **68,** 035501. https://link.aps.org/doi/10.1103/PhysRevC.68.035501 (3 2003).

154. Knoll, G. F. *Radiation Detection and Measurement, 3rd ed.* 3rd edition. ISBN: 978-0-471-07338-3, 978-0-471-07338-3 (John Wiley and Sons, New York, 2000).

155. Gironi, L. *et al.* $CdWO_4$ bolometers for double beta decay search. *Opt. Mater.* **31** (eds Di Stefano, P. & Petricca, F.) 1388–1392. arXiv: 0809.5126 [nucl-ex] (2009).

156. Arnaboldi, C. *et al.* CdWO4 scintillating bolometer for Double Beta Decay: Light and heat anticorrelation, light yield and quenching factors. *Astroparticle Physics* **34,** 143–150. ISSN: 0927-6505. https://www.sciencedirect.com/science/article/pii/S0927650510001210 (2010).

157. Wang, M., Huang, W. J., Kondev, F. G., Audi, G. & Naimi, S. The AME 2020 atomic mass evaluation (II). Tables, graphs and references. *Chin. Phys. C* **45,** 030003 (2021).

158. Belli, P. e. *et al.* Investigation of β decay of ^{113}Cd. *Phys. Rev. C* **76,** 064603. https://link.aps.org/doi/10.1103/PhysRevC.76.064603 (6 2007).

159. Pritychenko, B. & Mughabghab, S. F. Neutron Thermal Cross Sections, Westcott Factors, Resonance Integrals, Maxwellian Averaged Cross Sections and Astrophysical Reaction Rates Calculated from the ENDF/B-VII.1, JEFF-3.1.2, JENDL-4.0, ROSFOND-2010, CENDL-3.1 and EAF-2010 Evaluated Data Libraries. *Nucl. Data Sheets* **113,** 3120–3144. arXiv: 1208.2879 [astro-ph.SR] (2012).

160. Galashov, E. N., Gusev, V. A., Shlegel, V. N. & Vasiliev, Y. V. The growth of $ZnWO_4$ and $CdWO_4$ single crystals from melt by the low thermal gradient Czochralski technique. *Crystallography Reports* **54,** 689–691 (July 2009).

161. Danevich, F. *et al.* The research of 2β decay of ^{116}Cd with enriched $^{116}CdWO_4$ crystal scintillators. *Physics Letters B* **344,** 72–78. ISSN: 0370-2693. https://www.sciencedirect.com/science/article/pii/037026939401528K (1995).

162. Barabash, A. S. *et al.* Improvement of radiopurity level of enriched $^{116}CdWO_4$ and $ZnWO_4$ crystal scintillators by recrystallization. *Nucl. Instrum. Meth. A* **833,** 77–81. arXiv: 1607.04117 [physics.ins-det] (2016).

163. Barabash, A. S. *et al.* First test of an enriched $^{116}CdWO_4$ scintillating bolometer for neutrinoless double-beta-decay searches. *Eur. Phys. J. C* **76,** 487. arXiv: 1606.07806 [physics.ins-det] (2016).

164. Armatol, A. *et al.* A CUPID $Li_2^{100}MoO_4$ scintillating bolometer tested in the CROSS underground facility. *JINST* **16,** P02037 (2021).

165. Helis, D. L. *et al.* Neutrinoless Double-Beta Decay Searches with Enriched $^{116}CdWO_4$ Scintillating Bolometers. *J. Low Temp. Phys.* **199,** 467–474 (2020).

166. Arnaboldi, C. *et al.* $CdWO_4$ scintillating bolometer for Double Beta Decay: Light and Heat anticorrelation, light yield and quenching factors. *Astropart. Phys.* **34,** 143–150. arXiv: 1005.1239 [nucl-ex] (2010).

167. Barabash, A *et al.* Improvement of radiopurity level of enriched $^{116}CdWO_4$ and $ZnWO_4$ crystal scintillators by recrystallization. *Nucl. Instrum. Meth. A* **833,** 77–81. ISSN: 0168-9002. https://www.sciencedirect.com/science/article/pii/S0168900216307422 (2016).

168. *GEANT4 user documentation* https://geant4.web.cern.ch/support/user_documentation.

169. Ponkratenko, O. A., Tretyak, V. I. & Zdesenko, Y. G. The Event generator DECAY4 for simulation of double beta processes and decay of radioactive nuclei. *Phys. Atom. Nucl.* **63,** 1282–1287. arXiv: nucl-ex/0104018 (2000).

170. Bandac, I. C. *et al.* The $0\nu2\beta$-decay CROSS experiment: preliminary results and prospects. *JHEP* **01,** 018. arXiv: 1906.10233 [nucl-ex] (2020).

171. Beeman, J. W. *et al.* Current Status and Future Perspectives of the LUCIFER Experiment. *Adv. High Energy Phys.* **2013,** 237973 (2013).

172. Armatol, A. *et al.* A novel technique for the study of pile-up events in cryogenic bolometers. arXiv: 2011.11726 [physics.ins-det] (Nov. 2020).

173. Arnaboldi, C. *et al.* A front-end electronic system for large arrays of bolometers. *JINST* **13,** P02026. arXiv: 1710.06365 [physics.ins-det] (2018).

174. Arnaboldi, C. *et al.* The programmable front-end system for CUORICINO, an array of large-mass bolometers. *IEEE Transactions on Nuclear Science* **49,** 2440–2447 (2002).

175. Carniti, P., Gotti, C. & Pessina, G. High resolution digitization system for the CROSS experiment. *J. Low Temp. Phys.* **199,** 833–839. arXiv: 1908.11242 [physics.ins-det] (2019).

176. Armengaud, E. *et al.* Precise measurement of $2\nu\beta\beta$ decay of ^{100}Mo with the CUPID-Mo detection technology. *Eur. Phys. J. C* **80,** 674. arXiv: 1912.07272 [nucl-ex] (2020).

177. Toivanen, J. & Suhonen, J. Microscopic quasiparticle-phonon description of odd-mass 127- Xe-133 isotopes and their beta decay. *Phys. Rev. C* **57,** 1237–1245 (1998).

178. Iachello, F. & Isacker, P. V. *The Interacting Boson-Fermion Model* (Cambridge University Press, USA, 1991).

179. Heyde, K. L. G. *The Nuclear Shell Model* (Springer, Berlin, 1990).

180. Kostensalo, J., Suhonen, J., Volkmer, J., Zatschler, S. & Zuber, K. Confirmation of g_A quenching using the revised spectrum-shape method for the analysis of the ^{113}Cd β-decay as measured with the COBRA demonstrator. arXiv: 2011.11061 [nucl-ex] (Nov. 2020).

université PARIS-SACLAY

ÉCOLE DOCTORALE
Particules, hadrons, énergie et noyau : instrumentation, imagerie, cosmos et simulation (PHENIICS)

Titre : Recherche de la double désintégration bêta sans neutrinos avec des bolomètres scintillants
Mots clés : basse radioactivité, bolomètres, double désintégration bêta sans neutrinos

Résumé : La double désintégration bêta sans neutrinos ($0\nu\beta\beta$) est une transition nucléaire hypothétique ($T_{1/2}>10^{26}$ ans). Si elle est observée, elle prouvera la violation du nombre de leptons et confirmera la nature de Majorana des neutrinos. Pour étudier cette désintégration, nous utilisons des bolomètres scintillants. Ce sont des détecteurs cryogéniques constitués d'un absorbeur scintillant (où a lieu la libération d'énergie) couplé à un détecteur auxiliaire pour lire en coïncidence la lumière émise. Cette double lecture, chaleur et lumière, est utilisée pour déterminer l'origine de la particule. Dans cette thèse, deux cristaux enrichis ont été étudiés : le $Li_2^{100}MoO_4$ et le $^{116}CdWO_4$ exploités comme bolomètres scintillants, où le ^{100}Mo et le ^{116}Cd sont candidats à $0\nu\beta\beta$. CUPID-Mo comprend un réseau de 20 bolomètres scintillants cryogéniques recherchant la $0\nu\beta\beta$ du ^{100}Mo basés sur des cristaux enrichis de $Li_2^{100}MoO_4$ fonctionnant à 20 mK. Nous présentons l'analyse des données qui a conduit à établir une nouvelle limite de record mondial sur la demi-vie du ^{100}Mo ($T_{1/2}>1.5\text{x}10^{24}$ ans à 90% C.L.). Nous présentons également la première analyse à basse énergie pour la recherches de matière noire avec les détecteurs CUPID-Mo. CUPID est une future expérience à l'échelle de la tonne en cours de conception. Dans cette thèse, les résultats de différents tests de R&D visant à établir la structure finale des détecteurs sont présentés. De plus, deux cristaux de 0,6 kg de $^{116}CdWO_4$, enrichis à 82% en ^{116}Cd, ont été testés pour la première fois sous terre comme bolomètres scintillants cryogéniques. Des résultats prometteurs ont été obtenus, montrant les perspectives de la technologie bolométrique pour des recherches à haute sensibilité de la $0\nu\beta\beta$ du ^{116}Cd. Nous présentons également une analyse préliminaire d'un bolomètre scintillant à bas seuil basé sur un cristal naturel de $CdWO_4$ pour extraire l'extinction du facteur de couplage axial g_A dans la désintégration bêta du ^{113}Cd.

Title : Searching for neutrinoless double-beta decay with scintillating bolometers
Keywords : low radioactivity, bolometers, neutrinoless double-beta decay

Abstract : Neutrinoless double-beta decay ($0\nu\beta\beta$) is a hypothetical nuclear transition ($T_{1/2}>10^{26}$ yr) which, if observed, will prove the lepton number violation and confirm the Majorana nature of neutrinos. To study this decay, we use scintillating bolometers. They are cryogenic detectors consisting of a scintillating absorber (where the energy release takes place) coupled to an auxiliary detector to read in coincidence the emitted light. The dual readout, heat and light, is used to discriminate the origin of the particle. In this thesis, two crystals have been studied : enriched $Li_2^{100}MoO_4$ and $^{116}CdWO_4$ operated as scintillating bolometers, where ^{100}Mo and ^{116}Cd are the candidates for $0\nu\beta\beta$. CUPID-Mo comprises an array of 20 cryogenic scintillating bolometers searching for $0\nu\beta\beta$ of ^{100}Mo based on enriched $Li_2^{100}MoO_4$ crystals operating at 20 mK. We present the data analysis that led to the new world-leading limit on the half-life of $0\nu\beta\beta$ of ^{100}Mo ($T_{1/2}>1.5\text{x}10^{24}$ yr at 90% C.L.). We also present the first low energy analysis for dark matter searches with the CUPID-Mo detectors. CUPID is a future ton-scale experiment under design. In this thesis, results from different R&D tests to establish the baseline of the detector structure are presented. In addition, two 0.6 kg $^{116}CdWO_4$ crystals, enriched to 82% in ^{116}Cd, were tested for the first time underground as cryogenic scintillating bolometers. Promising results were obtained, showing the prospects of the bolometric technology for high-sensitivity searches for $0\nu\beta\beta$ of ^{116}Cd. Moreover, we present a preliminary analysis of a low-threshold scintillating bolometer based on a natural $CdWO_4$ crystal to extract the quenching of the axial-vector coupling g_A in the beta decay of ^{113}Cd.

Maison du doctorat de Université Paris-Saclay
2e étage, aile ouest, École normale supérieure Paris-Saclay
4 avenue des Sciences
91190 Gif-sur-Yvette, France